annual report 1979-1980

Biology & Medicine Division

MARCH 1981

Lawrence Berkeley Laboratory
University of California, Berkeley

PREPARED FOR THE U.S. DEPARTMENT OF ENERGY UNDER CONTRACT W-7405-ENG-48

DISCLAIMER

BIOLOGY AND MEDICINE DIVISION
ANNUAL REPORT 1979–1980

Lawrence Berkeley Laboratory
University of California
Berkeley, California 94720

This work was supported by the Office of Environment of the U.S. Department of Energy under Contract W-7405-ENG-48. Portions of this work were also supported by the National Institutes of Health, Department of Health and Human Services; the Environmental Protection Agency; and the National Aeronautics and Space Administration. Contracts and grants are listed in Appendix A.

CONTENTS

DNA and Genetic Studies

Lipoprotein Studies

APPENDICES

INTRODUCTION

Edward L. Alpen

This year's annual report marks a time during which important intellectual and medical milestones have been achieved and major steps taken toward new and expanding research goals for the Division.

Speaking first on the subject of research achievements, I find it hard to imagine a year in which more significant research advances could have been made by a laboratory group of this size. It is obviously impossible to mention all of them in a brief introduction—and, of course, the body of the report includes more detailed descriptions of these accomplishments. The following, however, are some of the highlights of this remarkable year:

- The radioimmunoassay for erythropoietin, an important hormone that regulates blood production, has now come fully into its own as a tested method of clinical assay. The method is finding worldwide acceptance and utilization.

- In a joint effort with the Materials and Molecular Research Division, a new class of compounds has been developed that shows great promise for removing toxic metal ions, including plutonium, from the body.

- The Research Medicine Group has now been able to fully demonstrate the utility of the positron emission tomograph for evaluating cardiac function and disease.

- Especially satisfying is the brilliant success of the Radiotherapy Group in treating choroidal melanoma, a cancer of the eye that would otherwise be treated by removal of the eye.

- For the first time, two patients have been treated with cyclotron alpha particle beams to control disease states in the vascular architecture of the brain. This milestone study marks a transformation of the former pituitary irradiation program into a new effort, namely, a focus on work with the brain. The pituitary program had fully met its goal to demonstrate the feasibility of using cyclotron beams in pituitary disease. This method is now in the domain of accepted medical procedures for treating pituitary disorders.

For several years we have been building up the skills, facilities, and competence to grow in new areas. This report will show that we are achieving major headway.

- One of these new program areas, mutagenesis and carcinogenesis research, is now well established, with a competent staff, including recent distinguished additions. We will continue to emphasize this area of research.

- The Structural Biophysics Group continues to build its research leadership in intracellular and subcellular structure and function. We are adding a new, large-capacity VAX 780 computer to speed its efforts.

- Research medicine continues to be marked by special emphasis on positron imaging and the development of positron-emitting radiopharmaceuticals. As part of this program we plan to push ahead on the development of a multiplanar positron emission tomograph and a small package cyclotron to assist in the production of positron-labeled radiopharmaceuticals.

The successful and smooth operation of the Division depends upon a quiet and efficient administrative staff. This staff often goes about its work unnoticed while the scientists accept their rightfully deserved honors for research achievement. I wish to take this opportunity to express my appreciation to our Division staff for their unobtrusive efficiency. I also wish to thank Dr. Thomas Hayes for agreeing to accept appointment as my Deputy to share with me not only the responsibilities and burdens, but also the satisfaction of achievement that are part of the Biology and Medicine Division.

2. RESEARCH MEDICINE

The Research Medicine Group has as its objective the direct application of physics, chemistry, and mathematics to human disease investigations and treatment. The emphasis over the past few years has been upon two approaches: (1) nuclear instrumentation and radioisotopes in the study of brain and heart disorders; and (2) investigation of human blood diseases, particularly those concerning platelet disorders.

The major accomplishments of the last year are:

- First quantitative studies of heart muscle perfusion using constant infusion.
- A 100-fold improvement in the capability of the rubidium-82 generator over its first development in 1968.
- First human brain tumor and brain blood flow studies with ^{82}Rb.
- Preliminary studies of brain metabolism of methionine in schizophrenia.
- Autoradiography studies of taurine and choline uptake in animals in preparation for human studies.
- New synthesis of ^{11}C-taurine.
- First high-resolution brain sugar metabolism studies in the disease of early aging.
- Completion of the data acquisition system for heart motion studies.
- Completion of a major revision of the Donner tomograph (twofold improvement in sensitivity) by incorporation of bismuth germanate crystals.
- Adoption of a blood gas method for evaluation of patients with blood disorders.
- Perfection of a method for platelet sizing.
- Development of a new model for measurement of platelet production.
- New insights into bone marrow transfusion.
- Development of a whole body autoradiographic facility for investigation of the fate of labeled tracers.

Two major relocations were accomplished this year as part of the Divisional plan to consolidate patient diagnosis and treatment facilities at one site. In spring 1980, the Donner Clinic, founded in the early 1940s by Dr. John Lawrence for the treatment of blood disease and thyroid cancer, moved to Building 55, the Research Medicine Facility. In September, the 280-crystal positron emission tomograph also was moved to Building 55 for an expanded program of brain and heart clinical studies with patients referred from East Bay physicians as well as from physicians at the University of California Medical Centers at San Francisco and Davis. While the clinical work is going on with the present ring, an advanced system comprised of four layers and 2000 crystals is being built at Donner Laboratory. This new system will provide approximately 10 times the efficiency of the present system.

The highlights of the research efforts conducted during the past year are summarized in the following reports.

BRAIN AND HEART DISEASE STUDIES

Thomas F. Budinger, Thornton W. Sargent III, Chi-Kwan Yen, Robert F. Friedland,* and Brian R. Moyer

When the Donner 280-crystal positron ring tomograph was completed two years ago, it showed the highest resolution and the highest speed of any positron emission tomograph in the world. The characteristics of this imaging device are discussed in S.E. Derenzo's report. The figures shown here illustrate highlights of important studies accomplished with the tomograph over the past year. The studies are obtaining both fundamental physiological and clinical diagnostic information, and their investigative protocols follow Laboratory and University guidelines for control of radiation dose and risks to patients.

*University of California at Davis Medical Center and Veterans Administration Medical Center, Martinez, CA.

Figure 1(a) shows a brain tumor image obtained by the use of a positron-emitting isotope, rubidium-82. Normally, ^{82}Rb does not go into brain cells unless there is some kind of breakdown; in this case the breakdown is associated with a brain tumor. The rubidium-82 was produced by the world's largest ^{82}Sr-^{82}Rb generator (see following report), which has been constantly improved over the past 12 years since its introduction in 1968 by Y. Yano. Rubidium-82 is an ideal isotope because its 75-second half-life is sufficient for the testing procedures while keeping patient exposure to a minimum. This is the first study to demonstrate the utility of this table-top positron source for diagnosis of the presence or absence of brain tumors. C.-K. Yen of Donner Laboratory and associates at the University of California Medical Center at Davis and the Martinez Veterans Administration Hospital intend to use this approach for following the therapy of brain tumors.

Figure 1(b) is also a rubidium-82 image of an arteriovenous malformation (abnormal connection of the blood vessels in the brain) in a patient treated at Lawrence Berkeley Laboratory's Heavy Ion Facility by J. Fabrikant and associates. This picture obtained by the Research Medicine Group demonstrates for the first time the ability to noninvasively evaluate the degree of vessel abnormality. The plan of the Division is to follow a number of patients receiving heavy ion treatment to study its efficacy. Only patients for whom there is no other method of treatment are receiving it.

Figure 1(c) demonstrates uptake of methionine (an essential amino acid) in a patient with schizophrenia. The purpose of this project, led by T. W. Sargent III, is to determine the metabolic basis of serious mental disorders such as schizophrenia, manic-depression, and depression.

Figure 1(d) reflects sugar metabolism in the brain of a man who has Alzheimer's disease, or early mental aging, an affliction that is the fifth most widespread disease in the world today. In a project led by R. Friedland of UC Davis, we are trying to understand the cause of this disease. Figure 1(d) is one of the first images to demonstrate a defect in sugar metabolism that may be part of this metabolic disorder.

Coronary disease is also being studied by the nuclear medicine part of the Research Medicine Group. This disease is the major cause of death in this country (1.5 million deaths per year).

Figure 2 shows the uptake of rubidium-82 in a subject before and after exercise. Rubidium behaves like potassium and accumulates in muscle more or less in proportion to blood flow. Our major experimental work involves calibrating ^{82}Rb positron tomography as a quantitative heart muscle flow detector. In addition, with B. Moyer, L. Sherman, J. Davis, and Y. Yano, development of a new method of evaluating heart muscle metabolism using dynamic positron tomography, ^{11}C-palmitic acid, and ^{18}F-deoxyglucose is well under way.

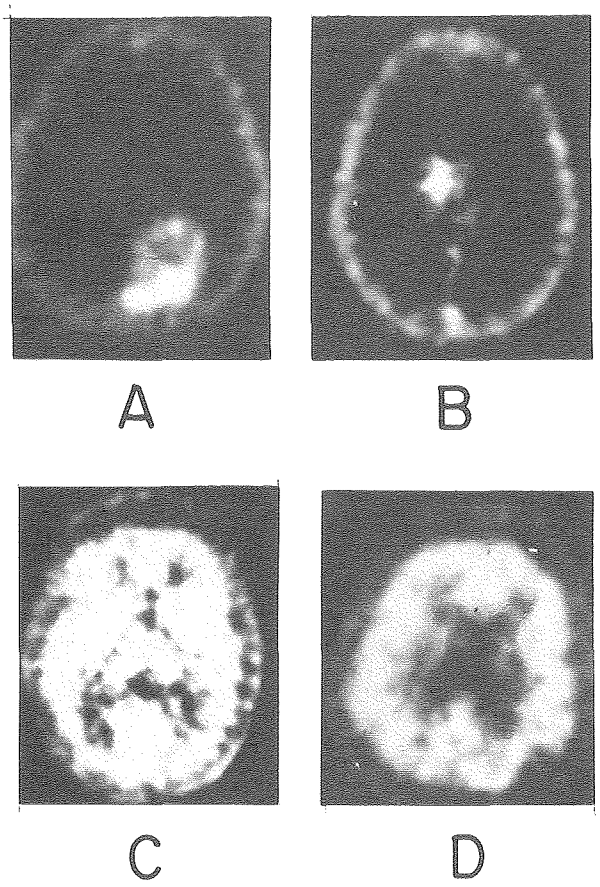

Figure 1. Brain study images: (a) Brain tumor; (b) arteriovenous malformation; (c) methionine uptake in schizophrenic subject; (d) sugar metabolism in subject with Alzheimer's disease. *XBB 800-12727*

A new development this year was the establishment of the whole body autoradiographic facility with the assistance of C.-T. Peng of the University of California Medical Center at San Francisco. In order to understand the distribution of various radionuclides and the compounds which these nuclides are used to tag, a technique was developed to examine the whole body distribution by investigations in animals. One of the more important discoveries using this technique was the distribution of choline in the

brain of subhuman primates as shown in Fig. 3. This is the first time the choline uptake in muscle brain cortex and brain white matter has been demonstrated in detail in mammals.

In addition to the synthesis of new radiopharmaceuticals shown in the human studies, and the development of a new synthesis of ^{11}C-taurine by J. Davis, an automated procedure for the production of ^{11}C palmitic acid was introduced by L. Sherman, J. Davis, and Y. Yano. This fatty acid will be used to study the metabolism of the human heart after the completion of a series of animal studies.

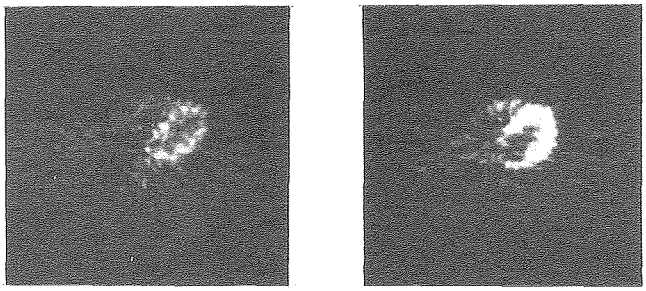

Figure 2. Rubidium-82 uptake in the heart before and after exercise. *XBB 793-3582A*

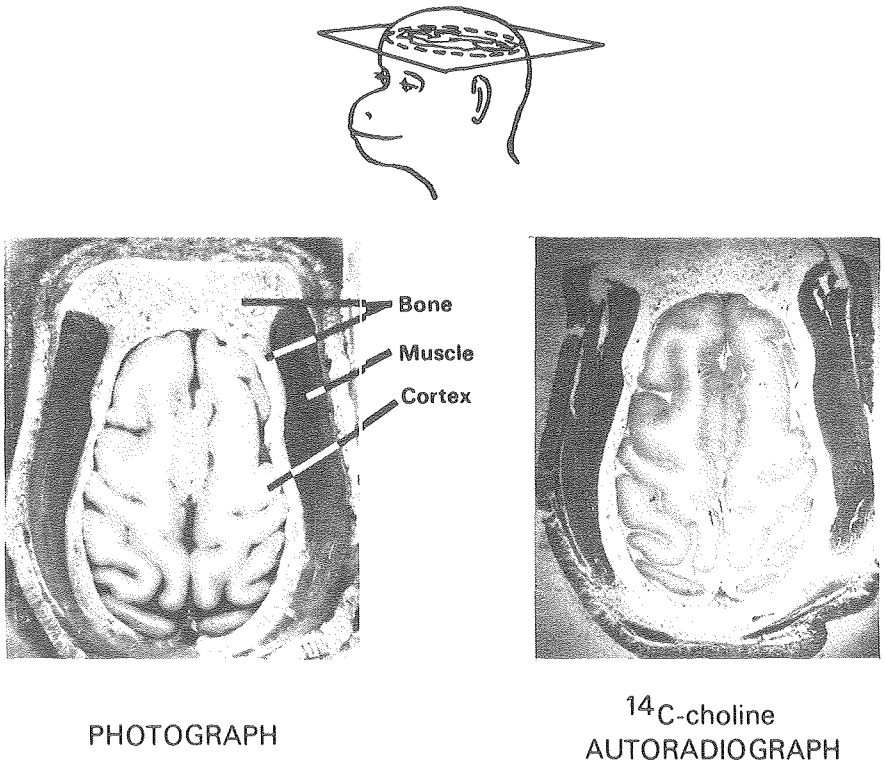

Figure 3. Choline distribution in monkey brain. *XBB 800-11908*

A PRECISION FLOW-CONTROLLED RUBIDIUM-82 GENERATOR FOR BOLUS AND CONSTANT INFUSION STUDIES

Yukio Yano

Generator-produced ^{82}Rb can be infused intravenously at bolus infusion (BI), constant infusion (CI), or variable infusion (EI) rates. When ^{82}Rb is used with the positron ring detector (tomograph), extraction or flow information can be obtained in studies of the heart, head or kidneys.

To accomplish these studies, we have developed a unique flow rate controller and large-volume (150 ml) reservoir pumping system for delivery of a sterile solution of 75-sec ^{82}Rb in saline from an alumina column ^{82}Sr generator operating at extremes of either slow or fast elution rates and pressures of 100 psi or more. The elution yield is about 80% of the ^{82}Sr at a 1.1 cc/sec flow rate for 20 sec. The breakthrough of ^{82}Sr from the alumina column is 10^{-7} to 10^{-6} of the dose of Rb even after several months of generator use and a flow of 3 to 4 liters of 2% NaCl at pH 8 through the column. The useful life of the generator is 2 to 3 months.

Sterility and pyrogen testing of periodic elutions from the generator show the eluate to be safe for human studies.

Electrocardiogram-gated myocardial studies have been done with this new system, which contains 150 mCi ^{82}Sr. Other studies include brain blood flow and brain tumor imaging.

Figure 1 is a schematic of the ^{82}Rb generator showing the stepping motor drive with a wide speed range interfaced to a microprocessor that reads flow rate and quantity of eluent injected. Thumb-wheel switches on the control panel are set to predetermined values for CI, BI, or EI studies. The flow rate is a function of a pulse rate sent to the stepping motor. A belt drive connects the motor drive to a recirculating ball nut and screw that moves the piston inside of a machined Lexan barrel. A Bellofram rolling diaphragm around the piston allows extremely low friction. The entire pumping system is

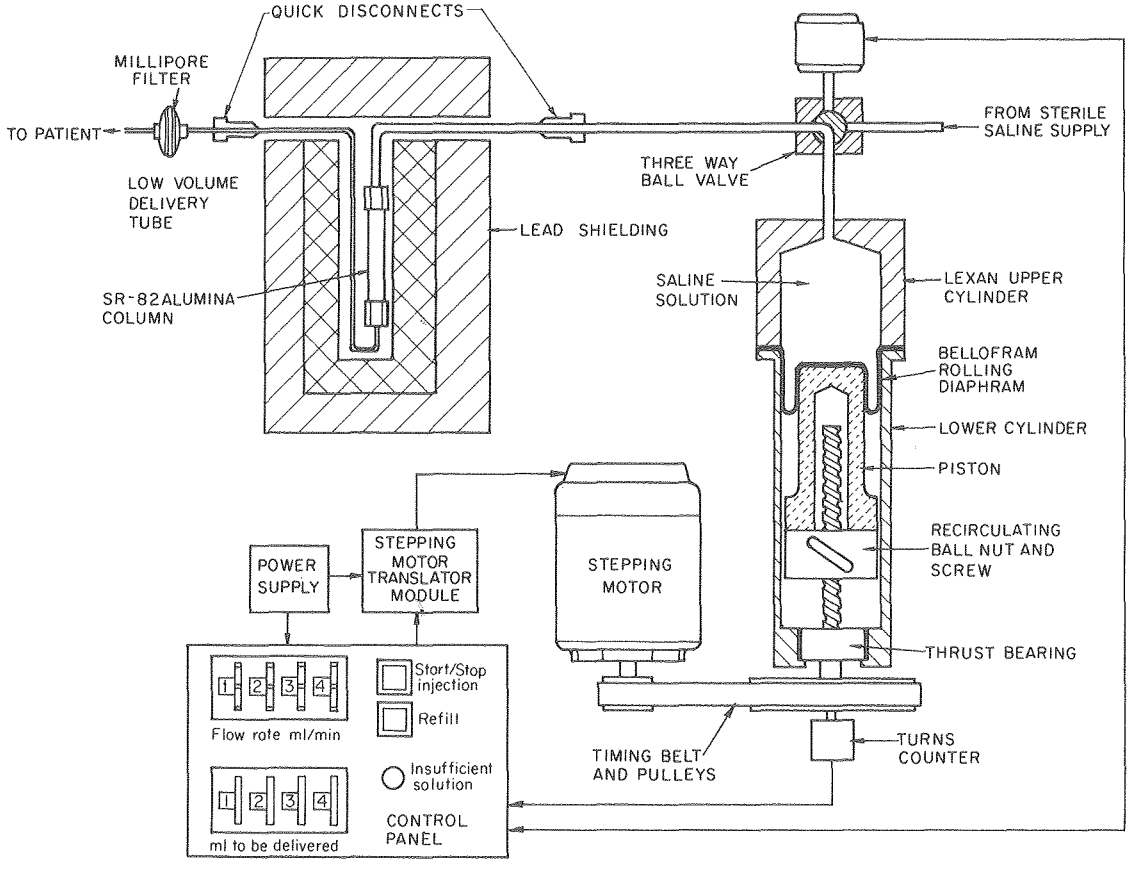

Figure 1. Schematic diagram of rubidium-82 generator. XBL 801-3026

mounted in FR-4 glass-epoxy for electrical isolation from the patient.

The pumping unit, consisting of the Lexan cylinder, piston, Bellofram diaphragm (neoprene or silicone rubber), stainless steel lines and column quick connects, are autoclaved before the generator is loaded with ^{82}Sr. Note the inner and outer lead shielding for the alumina column. This shielding arrangement allows transporting only the column and its primary shielding to the "hot cell" for reloading with fresh ^{82}Sr, while the pumping system, electronic controls, and secondary shielding remain at the clinical site.

DATA ACQUISITION, RECONSTRUCTION, AND DISPLAY

Ronald H. Huesman

A special emphasis of the Research Medicine program is the development of methods for acquiring and manipulating data from the Donner 280-crystal positron emission tomograph. This past year, we completed development of a system capable of taking 1 million events per second while simultaneously correcting for unwanted accidental coincidence events (Fig. 1). The system permits the simultaneous acquisition of data for eight different time-slices of the cardiac cycle. A microprocessor responds to the patient's electrocardiogram (EKG) signal, routing data to the histogram memory corresponding to the phase of the cardiac cycle indicated by the signal (Fig. 2).

Additional work completed this year includes quantitation of the signal-to-noise ratio to be expected when imaging the human head. Effort is continuing on the more complicated problem of noise propagation in reconstructions of the human thorax.

Researchers working on the mathematical physics and data acquisition and reconstruction projects include J. Cahoon, G. Gullberg, and L. Woods.

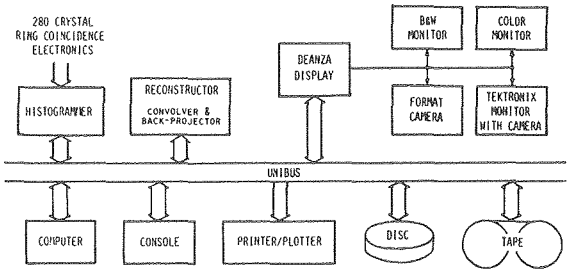

Figure 1. Schematic diagram of the data acquisition, reconstruction, and display system for the Donner 280-crystal positron tomograph. XBL 8010-3775

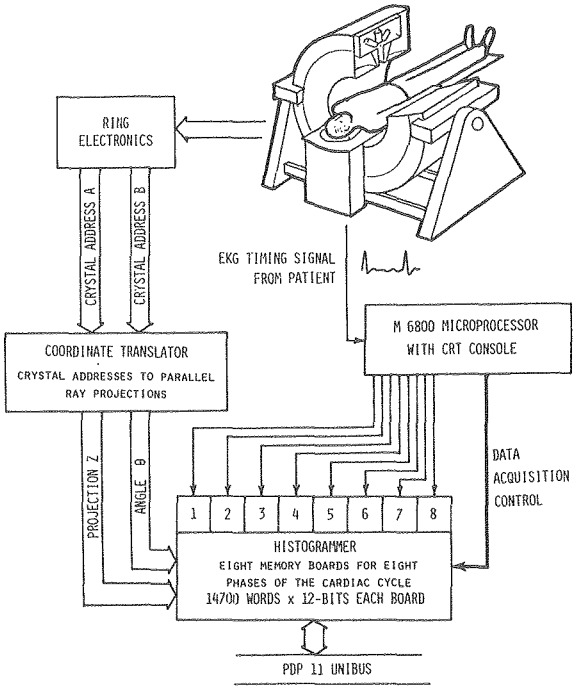

Figure 2. Control for gated cardiac imaging. XBL 7910-3845

INSTRUMENTATION FOR THREE-DIMENSIONAL TOMOGRAPHY

Stephen E. Derenzo

The Donner 280-crystal positron tomograph was designed and built at LBL to image the three-dimensional distribution of positron-labeled compounds in the human body. The system consists of a continuous ring of 280 rectangular (9.5 mm × 32 mm × 32 mm) bismuth germanate detector crystals that completely encircle the patient. When a positron is emitted, it travels a few millimeters and annihilates with an electron to produce two 511-keV photons that fly off in nearly opposite directions. Each crystal is coupled to a phototube, and electronic circuits determine whenever any crystal has detected an an-

nihilation photon in time coincidence (within 20 nanoseconds) with any of the opposing 105 crystals.

Events are accumulated in high-speed semiconductor memory. In a typical high-resolution study (9-mm full width at half-maximum), 1 million events are collected in 2 minutes and the image is reconstructed in 10 seconds by a hard-wired arithmetic unit (see R.H. Huesman report). Dynamic processes can be imaged with lower resolution (2 cm) by collecting a 100,000-event data set every 2 seconds.

The tomograph became operational with sodium iodide (thallium) detectors in July 1978, and has been converted to the more efficient bismuth germanate detector material over the past year. In September 1980 the tomograph was moved (Fig. 1) to the Research Medicine Facility Building 55, where further clinical studies will be conducted. The system is used to study blood flow, and amino acid, fatty acid, and sugar metabolism in man and animals (see T.F. Budinger report). Using the rubidium-82 generator developed at Donner Laboratory (see Y. Yano report), we have this 75-second half-life isotope available to image the blood flow in human heart muscle with a low radiation dose. The size and location of sick heart muscle can be accurately determined in three dimensions.

Future work will center on a 2000 crystal, four-layer system able to image the entire heart or brain in nine transverse sections without mechanical motion.

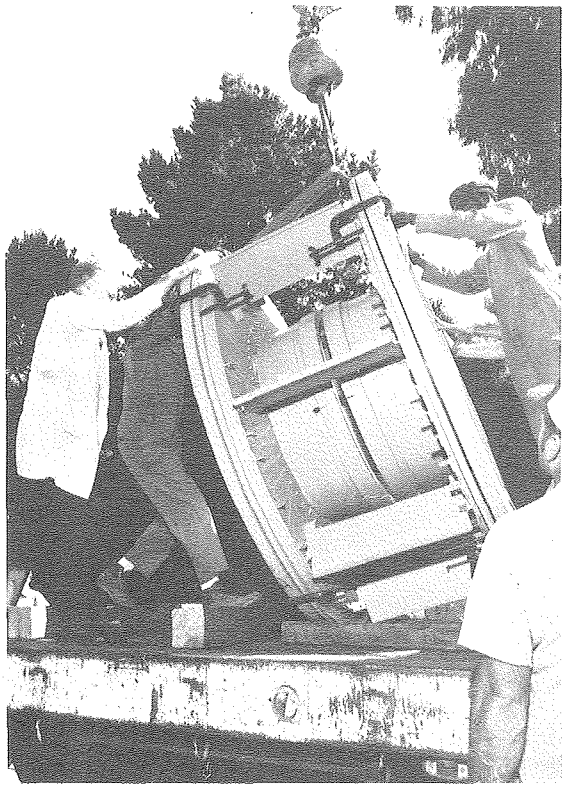

Figure 1. The Donner 280-crystal positron tomograph being moved to Building 55 where further clinical studies will be conducted. *CBB 809-11464*

HEMATOLOGY

Shirley N. Ebbe, George Brecher, Ruth A. Cohen, Gregory A. Threatte, Cathryne C. Allan, Carol S. Bohlen, Dorothy A. Carpenter, Carol Fong, Patricia A. Garbutt, Elizabeth A. Phalen. Attending Physicians: James L. Born, Hunter O. Cutting, Lester Hollander, Henry H. Stauffer

The hematology program of the research Medicine Group includes the Donner Clinic, a laboratory for experimental megakaryocytopoiesis (the production of giant bone marrow cells that are the precursors of blood platelets), and a training program for pre- and postdoctoral fellows, the latter a cooperative project with investigators in other groups.

During the past year, the Donner Clinic moved from Donner Laboratory (Building 1) to new quarters in Building 55, the Research Medicine Facility. For many years, the clinic has specialized in the diagnosis, treatment, and study of patients with myeloproliferative disorders, diseases characterized by an overproduction of blood cells. Most notably, patients with red blood cell overproduction (erythrocytosis) have been followed; in some patients, the erythrocytosis is due to intrinsic disease of the bone marrow (polycythemia vera), and in others it is secondary to other abnormalities. Studies are being initiated to analyze blood gases and acid-base balance in patients with erythrocytosis and to correlate these measurements with levels of erythropoietin, the hormone that regulates red cell production, in the blood and urine of these patients. These parameters will be monitored as patients undergo treatment to determine if patients with erythrocytoses of different etiologies may respond differently to reduction in their red cell mass and also to mild perturbation of their acid-base balance, which, in turn, may affect tissue oxygenation. If their responses dif-

fer, it will help to elucidate pathogenetic mechanisms and physiological responses to erythrocytosis, and the differences may provide the basis for improvement of diagnostic tests. A laboratory source of erythropoietin is important in order to be able to do these and other experiments. Two clinic patients who are severely anemic produce an excess of erythropoietin and they voluntarily collect their urine, which is then processed here as a potent source of erythropoietin.

Many of the patients in the clinic have abnormalities of their platelet counts, and studies are underway to apply concepts gained from animal studies to some of these patients in an effort to understand the regulation of platelet production in human beings and the ways in which it may be aberrant in disease states. New technology, consisting of a sensing device that features a hydrodynamically focused aperture tube, is being applied to measurements of platelet volume, thus permitting sizing of the small blood platelets in the presence of the much larger red and white blood cells and avoiding some of the artifacts introduced by more conventional instruments. This instrumentation, when connected to a multichannel analyzer and a minicomputer, permits rapid assessment of platelet size with a minimum of blood-sample handling, thus potentially preserving physiological platelet volumes and avoiding many of the *in vitro* artifacts that are known to change platelet size and ultrastructure. With this technique we have found that anticoagulants have a profound influence on platelet volume and that conditions previously thought to be optimal are not. Under these supposedly optimal conditions, platelet volumes had been reported to be lognormally distributed, and various physiological implications of such a distribution were postulated. We have found that lognormality is not the rule and are searching for the ideal conditions of platelet-volume measurement, conditions that will preserve platelets in the size and shape that they have in the blood. When this is accomplished, platelet size and number will be correlated with megakaryocyte size and ploidy (their DNA content) in both human beings and experimental animals to evaluate some of the megakaryocytic determinants of platelet production.

Platelet production, in experimental animals, is also commonly measured by determining the incorporation of radioactively-labeled tracer substances that are incorporated primarily into megakaryocytes. The tracer substances usually used are ^{75}Se-selenomethionine and ^{35}S-sodium sulfate. We have used both traces to study platelet production in W/W^{v} mice, a strain of genetically anemic mice that produces normal numbers of platelets in spite of having only about half the normal number of megakaryocytes in the bone marrow and spleen. Different results were obtained with the two tracers when the percentage of the injected dose that was incorporated into platelets was calculated, as is usually done; the results with ^{75}Se were normal, but those with ^{35}S suggested, paradoxically, that platelet production was greater than normal. The discrepancy was corrected by using plasma radioactivity as an independent measurement of radioisotope availability, rather than assuming that all mice handled a given dose of tracer substance identically. In addition to providing a new concept relative to the measurement of platelet production with radioactive tracers, these results indicated that W/W^{v} mice have an intrinsic abnormality of sulfate metabolism that may or may not be linked to their hemopoietic defect.

Megakaryocytopoiesis is clearly regulated, in part, by the level of circulating platelets. However, there may be other mechanisms by which it is regulated. In addition to the numbers of megakaryocytes in hemopoietic tissues, the mass of platelets they produce is also partly controlled by the size of individual megakaryocytes. Under several experimental conditions platelet counts can be maintained at a normal level even though megakaryocyte numbers are substantially reduced and there is an apparently reciprocal increase in megakaryocyte size. The mechanisms responsible for these adjustments in megakaryocytopoiesis are the subject for continuing experiments in animals. In spite of the evidence that the level of circulating platelets feeds back information to hemopoietic tissue to regulate the rate of platelet production, the nature of the feedback messenger is not clearly understood. Research to evaluate the role of platelet interaction with endothelia cells and of a humoral thrombopoietin in this process is underway.

SYNGENEIC MARROW TRANSFUSION INTO NORMAL RECIPIENTS

George Brecher

Bone marrow transplantation is a potential therapy for certain anemias and leukemias. Bone marrow can be readily transplanted after doses of radiation that destroy some or all of the recipient's own hemopoietic stem cells, the precursors of all blood cells. Lethal doses produce sufficient degrees of immunosuppression that both syngeneic (histocompatible) and allogeneic (histoincompatible) marrow can proliferate in the irradiated recipients and replace their own marrow. With lesser doses of irradiation, allogeneic marrow is rejected.

It was formerly assumed that transfused marrow cells would go to the marrow and proliferate there even without prior irradiation. However, in the limited instances in which this assumption has been tested, very few proliferating donor cells (as identified by marker chromosomes) were found in the recipients. We have confirmed this observation repeatedly.

In contrast, in animals given lethal doses of radiation and restored to hematologic normalcy by an initial bone marrow transfusion, marrow cells from a syngeneic donor in a second transfusion could subsequently proliferate and replace, on the average, 10% of the recipient's own marrow, although the marrow and spleen appeared histologically normal and the peripheral blood cells were normal in number and appearance. In previously non-irradiated recipients, the maximum proliferation of transfused cells was 0% to 2%.

It was suggested that the normal turnover of hemopoietic stem cells is so slow, or their entry into more the mature compartment of the marrow so rare an event, that stem cells transfused all at one time had little chance of entering the proliferating compartment of the recipient's marrow. A possible explanation for our observation, therefore, was that irradiation altered the turnover of stem cells, so that transfused stem cells could replace endogenous cells. The basic observations appeared worthy of further study, both for new insights into the kinetics of stem cells and for possible clinical application. These added studies were made possible by a Director's Grant for October 1979 to September 30, 1980.

As a marker for these studies, the Y chromosome has been useful because it can be fairly readily identified in all strains of mice. Consequently, in all our previous experiments we had used male mice as donors and females as recipients, and examined the recipients two weeks or more after the transfusion. By two weeks the progeny appeared to have reached its maximum and subsequently stayed at that level, provided that the donor cells were syngeneic.

Normal recipients did not appear to allow the proliferation of transfused marrow cells to the same extent as mice previously irradiated, though apparently hematologically normal. This raised the question whether the transfused cells actually reach the recipient marrow in normals. We therefore harvested the recipients' marrow at 2 and 24 hours after transfusion and injected it into pairs of secondary recipients, one male and one female, that had been given lethal doses of radiation. The ratio of male to female cells in the secondary recipients should then reflect the proportion of transfused to endogenous stem cells in the primary recipient, provided the secondary recipient was entirely repopulated by the marrow of the primary recipient.

That this was indeed the case could be concluded because the ratios were identical in each pair of male and female recipients. These equal ratios indicated that the secondary recipients did not contribute any of their own cells; if they had, the proportion of male:female cells would have been greater in male recipients and smaller in females. Using this technique, we found transfused male cells in normal female recipients to vary from 0% to 70% at 2 hours after transfusion, and to be an almost uniform 4% at 24 hours. The spleen at 24 hours contained 40% of donor cells. We tentatively conclude that while the initial distribution of transfused stem cells is probably random, only 4% are retained in the marrow, and even fewer proliferate. Other studies have shown that the high percentage of transfused cells in the spleen persists for only one week and is not self-sustaining.

To explore the possibility that the control of seeding into the marrow was under local control, we irradiated one hind limb with 1,000 roentgens. Six weeks later, when recovery of the irradiated femoral and tibial marrow was expected to be complete, a transfusion of male cells into female recipients resulted in 10% to 15% proliferation of donor cells, not only in the irradiated, but also in the shielded portions of the marrow. Since we had previously observed that animals given 500 R, a sublethal dose, will not support the proliferation of subsequently transfused stem cells after complete recovery, the

possibility that inadequate shielding and scatter radiation is responsible appears unlikely. It must be assumed that local radiation of 1,000 R in some fashion alters the turnover in the stem cell compartment throughout the skeleton. Local irradiation of one part of the body has indeed been reported to alter cell turnover in shielded portions of the marrow, but only during the first few days after irradiation. The problem is being reinvestigated with different combinations of radiation dosages and shielding.

3. DONNER PAVILION

The Donner Pavilion Program has long been associated with the cyclotron irradiation treatment of pituitary lesions and metabolic diseases mediated through the pituitary. Successes in the treatment of pituitary tumors established by this research program have proven its therapeutic advantages. In recognition of DOE's continuing commitment to the applications of nuclear science to medicine, pituitary irradiation is now being made available to patients referred here by physicians on a fee-for-service basis. An LBL Pituitary Committee has been set up to coordinate this activity.

Research effort is now being strongly directed to the creation of focal lesions in the brain and central nervous system as a means of treating or controlling pathological disease, particularly where surgery is difficult or impossible. Especially suitable for this type of research are arteriovenous malformations of various types in the brain where irradiation to the vessels may prevent life-threatening disasters. The first patient in this series has been treated and other patients are being evaluated. Concomitantly, small animal studies are being conducted. These studies are expected to extend the therapeutic applications of this program.

Epidemiological studies are in progress on the entire series of patients who have received alpha particle pituitary irradiation (APPI) as well as those who received radioisotope therapy for thyroid and various hematologic diseases.

Follow-up studies are being maintained on the endocrine patients who have had cyclotron irradiation of the pituitary for treatment of their diseases. These are now being done primarily through their private physicians. In the patients with diabetic retinopathy, a definitive evaluation of pituitary irradiation with respect to the preservation of visual acuity will soon be completed.

Three additional primates have received pituitary irradiation with carbon-12 ions from the Bevalac. Information from this study, along with the histological studies on previously irradiated animals that have recently been killed, is providing data to evaluate the potential advantages of the carbon beam.

The research efforts of this program are summarized in the following reports.

FOCAL LESIONS IN THE CENTRAL NERVOUS SYSTEM—STEREOTAXIC RADIONEUROSURGERY

Jacob I. Fabrikant, Thomas F. Budinger, Yoshio Hosobuchi,* James L. Born and Cornelius A. Tobias

The application of heavy-ion beams for fundamental and applied brain research has unusual potential. Methods are being developed in our laboratory for producing focal lesions in the central nervous system (e.g., the hypothalamus, thalamus, pituitary gland) to investigate nerve pathways and neuroendocrine responses, and for treating certain pathological disorders of the brain with stereotaxic Bragg peak heavy-ion radiosurgery.

Studies in animals are demonstrating the value of this neuroscience tool for investigating mammalian brain response to induction of discrete focal lesions in the hypothalamus or in the cerebral cortex. These studies are also elucidating the neuroendocrinological response following ablation of various portions of the midbrain, without requiring complex neurosurgical preparations.

Clinical studies are demonstrating the feasibility of stereotaxic neurological radiosurgery for treating certain inoperable vascular disorders of the brain [e.g., arteriovenous malformations (AVM), internal carotid artery–cavernous sinus fistulas and other cerebrovascular disorders] in patients who are already demonstrating progressive neurological deficit. Further applications of focal lesion production with the Bragg ionization peak can be extended to include localized radiation to centers of the brain and spinal cord for treatment of such disorders as Parkinson's disease, pituitary microadenomas, acoustic neuromas, and the control of pain. The

*University of California at San Francisco Medical Center.

eventual application of radioactive beams will provide accurate localization of the stopping points of the beam, thereby making it feasible to stop the beam accurately at a defined depth within the central nervous system.

STEREOTAXIC BRAGG PEAK RADIOSURGERY IN THE CENTRAL NERVOUS SYSTEM

Surgical excision or ablation is the treatment of choice for intracranial AVM, vascular fistulae, and acoustic neuromas. However, when the lesion is inoperable or when other factors preclude surgery, neurosurgeons must turn to alternative methods of treatment. For inoperable intracranial AVM and certain other vascular disorders in the brain (e.g., carotid–cavernous sinus fistulae or cavernous hemangiomas) and large, inoperable acoustic neuromas (nonmalignant expanding tumors of the eighth cranial nerve), radiosurgery has become a potentially successful experimental therapeutic procedure at three university centers in the world: Professor Kjellberg's group at Massachusetts General Hospital at Harvard University; Professor Leksell's group at the Karolinska Institute, Sweden; and Professor Barcia-Salorio's group at University Hospital, Valencia, Spain. The results, using cyclotron-produced protons, intense high-dose gamma radiation, or linear-accelerator x rays, have been encouraging. Approximately 150 patients have been treated in this fashion during the past decade in these three centers, and with only minimal morbidity arising from the radiation treatments. Conventional radiotherapy has been tried in the past, but abandoned.

During the past year at Donner Pavilion, we have initiated a program of stereotaxic Bragg peak radiosurgery in the central nervous system. The use of the Bragg-ionization peak is a non-invasive surgical tool to induce radiation damage in a defined region in the brain; the charged particle beam is precisely directed and delivered to the predetermined region in the nervous system by a multiplanar technique.

The patients comprise three groups, all of whom have brain disorders that cannot be treated by neurosurgical procedures without increased morbidity or mortality: (a) patients with AVM or other vascular disorders who would most likely suffer progressive brain damage and paralysis or ultimately bleed to death unless treated; (b) patients with internal carotid artery–cavernous sinus fistulae who would become blind from progressive glaucoma unless treated; and (c) patients with large tumors of the acoustic nerve who would become deaf and suffer progressive brain damage unless treated.

Figure 1 illustrates a 26-year-old patient with a very large arteriovenous malformation in the right thalamus and extending into the right cerebral cortex. There is evidence of peri-malformation infarction with progressive brain damage which has re-

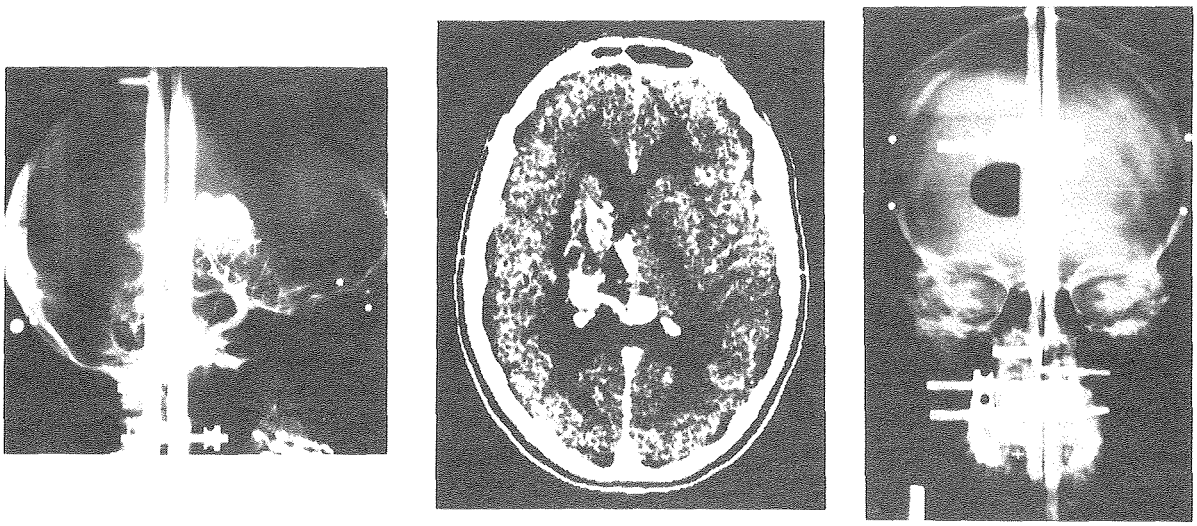

Figure 1. Patient with very large arteriovenous (blood vessel) malformation in the brain involving the right thalamus and extending into the right cerebral cortex. (A) Cerebral angiogram demonstrating the large right thalamic arteriovenous malformation. (B) X-ray computerized tomogram of the brain showing extension of the vascular malformation into the right lateral ventricle with evidence of old right frontoparietal cerebral infarction. (C) Treatment field showing stereotaxic-directed Bragg peak helium-ion radiation delivered through large posterior occipital and axial ports. *XBB 809-10582A*

sulted in left-sided hemiplegia from repeated subarachnoid hemorrhage. Figure 1(A) is the cerebral angiogram demonstrating the right thalamic arteriovenous malformation; Fig. 1(B) is the computerized tomogram of the brain and demonstrates the extension of the malformation into the right lateral ventricle with evidence consistent with an old right frontoparietal cerebral infarction. Stereotaxic-directed Bragg peak helium-ion irradiation was carried out; a fractionated-schedule, total dose of 2500 rem, was delivered through large axial and posterior occipital ports, as shown in Fig. 1(C). Obliterative changes of the feeder arterial vessels and their communicating structures are anticipated within six to seven months, to be followed by arrest of neurological degeneration and bleeding.

Baseline studies of intracerebral blood flow patterns in transverse section using the Donner-280 crystal dynamic positron emission tomograph were carried out by C.-K. Yen, T.F. Budinger, and their colleagues. In the report of Budinger et al. (p. 4), Fig. 1(b) illustrates a study in which rubidium-82 is used as an intravascular tracer to evaluate the response of the malformation to Bragg peak therapy. The tomograph study demonstrates clearly the dynamic changes of increased intracerebral blood flow and shunting of blood through the large, dilated, tortuous vessels. The precise quantitative measures of blood flow determined from the reconstruction of the images are used to evaluate the therapeutic response of the arteriovenous malformation to Bragg ionization peak stereotaxic radiosurgery.

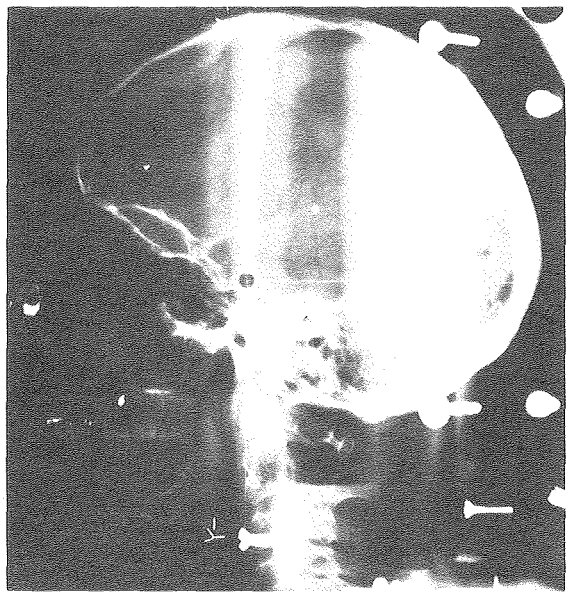

Figure 2. Radiographic treatment port film of the head of a patient with a vascular fistula in the brain, demonstrating use of narrow (6 mm) helium-ion Bragg peak beam (at center of cross lines) for stereotaxic radiosurgery. Bragg ionization peak is used to obliterate right internal carotid artery–cavernous sinus fistula, and to restore normal vision. *XBB 800-12345*

Figure 2 illustrates the use of the very narrow helium-ion Bragg peak beam for stereotaxic radiosurgery to obliterate a right internal carotid artery–cavernous sinus fistula in a 67-year-old woman who is experiencing progressive blindness. The 6-mm beam was precisely directed to the region of the fistula, and 4000 rem was delivered through four ports in a single treatment procedure. The 90° lateral port film identifies the size and location of the target volume (approximately 250 mm^3) treated. It is anticipated that her progressive loss of sight will be arrested, and over a period of three to four months, she will be regaining her eyesight.

FUTURE STUDIES

Recently at the Bevalac, high-energy particle beams of carbon and neon became available for clinical applications in medical research. The carbon Bragg ionization peak has particularly good potential for use in the application of focal lesions in the central nervous system. This is because the carbon beam has less scattering and straggling than helium ions and protons. The obtainable Bragg ionization curves—depth versus dose curves—have greater peak-to-plateau ratios, enabling more accurate positioning, thereby protecting sensitive adjacent neural structures, such as the hypothalamus, thalamus, and brain stem. Furthermore, near the peak of the Bragg curve, the biological effectiveness of the carbon-ion beam is much greater than at the plateau. If the peak is stopped in a lesion, such as in a small vascular disorder in the brain, relatively greater radiobiological effects are achieved with much less dose.

Thus, heavy-ion beams, particularly carbon, allow improved dose-delivery for localized irradiation in the central nervous system. It can be expected that small vascular lesions, vascular fistulae, pituitary microadenomas, and similar radiosurgically amenable disorders can be approached. Furthermore, large vascular lesions, such as arteriovenous malformations of the midbrain, which cannot be approached by invasive neurosurgical procedures, can readily be treated with stereotaxic carbon-ion Bragg peak radiosurgery.

A technique is being developed in our laboratory by E. L. Alpen, A. Chatterjee, and C. A. Tobias to achieve precise localization of the stopping points

of the beam inside the head by use of a radioactive beam. This will make it feasible to stop the beam accurately at the appropriate depth in the central nervous system in the head. Carbon-11 ion beams, for example, provide the potential of accurate positioning not available with helium or protons. Tobias and Chatterjee demonstrated that radioactive carbon-11 nuclei comprise about 1% of the total carbon-ion beam, emitting positrons with a half-life of 20.5 min. These positrons are detected with a specially constructed gamma camera. Recent studies have made it possible to form a small beam of pure carbon-11 particles which permit determination of the stopping points in an absorber with an accuracy of 1 mm. In one possible scheme for delivering focal lesions in the brain via radioactive heavy particle beams, the positron camera would continually monitor the precise location of the stopping points of the beam in the patient's head. The data would be fed back on-line to a variable absorber controlling the range penetration of the beam, thereby fully controlling the location and depth dose of the carbon beam.

PITUITARY IRRADIATION PROGRAM

John A. Linfoot, Peter Linfoot, Jacob I. Fabrikant, Jeanette Nakagawa, and Tokuko Saito

The alpha particle pituitary irradiation program continues to be a major research project at Donner Pavilion. A study to determine the incidence of hyperprolactinemia in a large series of acromegalic subjects was undertaken. The relationships between plasma levels of growth hormone and prolactin, sellar volume, duration of acromegaly, and age at time of evaluation were investigated.

An examination of 179 acromegalic patients revealed a high incidence of hyperprolactinemia representing either mixed or multiple pituitary tumors. Prolactin determinations were made on fasting plasma samples previously assayed for growth hormone. Results indicated a 40% incidence of hyperprolactinemia in this series. Patients are divided into two groups: Those without prior treatment and those having had unsuccessful prior surgery. The expected positive correlation between sellar volume, as defined by di Chiro and Nelson,[1] and growth hormone was observed. Sellar volume and prolactin did not correlate well, nor was there a relationship between prolactin and growth hormone. There was a negative correlation for both prolactin and growth hormone in the nonsurgical patients. Duration of disease had little relationship to hormone levels. The mean prolactin levels for nonsurgical males was 15.85 ng/ml compared to 27.54 ng/ml for nonsurgical females. Mean prolactin values for the surgical group were 23.44 ng/ml and 17.78 ng/ml for males and females, respectively. Differences in prolactin values between nonsurgical and surgical groups were insignificant (see Table 1). We concluded that: (1) The incidence of mixed tumors in acromegaly, as evidenced by hyperprolactinemia, is the same for males and females. (2) The incidence of hyperprolactinemia is not higher in patients who have undergone prior surgery. (3) There is no correlation between sellar size and the presence or absence of hyperprolactinemia. (4) The volume of the sella containing mixed or multiple tumors is correlated to the growth hormone level rather than to the prolactin level in acromegalic patients.

The follow-up of these patients to determine

Table 1. Statistical analysis of clinical parameters in 179 acromegalic patients to determine incidence and relationship of hyperprolactinemia prior to treatment with alpha particle pituitary irradiation.

	Nonsurgical (NS)		Surgical (S)	
N	males (78)	females (60)	males (26)	females (15)
log GH:volume	0.45 ($p < 0.001$)	0.33 ($p < 0.01$)	0.38 ($p < 0.052$)	0.42 (ns)
log PRL:volume	−0.08 (ns)	0.29 (ns)	0.27 (ns)	0.09 (ns)
log PRL:log GH	0.16 (ns)	−0.08 (ns)	0.07 (ns)	−0.26 (ns)
log GH:age	−0.19 (ns)	−0.22 (ns)	0.15 (ns)	0.26 (ns)
log PRL:age	−0.28 ($p < 0.025$)	−0.27 ($p < 0.05$)	0.48 ($p < 0.015$)	0.45 (ns)
log GH:duration	0.08 (ns)	−0.06 (ns)	−0.11 (ns)	−0.10 (ns)
log PRL:duration	−0.08 (ns)	−0.38 ($p < 0.005$)	0.24 (ns)	−0.46 (ns)

ns = $p > 0.05$

the long-term benefits and side effects of pituitary irradiation continues to be of major research interest.

REFERENCE

1. Di Chiro, G. and Nelson, K. B. 1962. "The volume of the sella turcica." *Amer. J. Roent. Radium Therapy and Nucl. Med.* 87:989–1007.

RECENT ADVANCES IN PITUITARY RESEARCH

John A. Linfoot and John T. Lyman

It has been previously determined that the low Bragg-peak-to-plateau ratio of helium ions[1] largely eliminates helium ions as a source of Bragg-peak high energy radiation necessary for rapid destruction of normal pituitary tissue in man. Heavy ions available at the Bevalac, however, such as carbon (^{12}C) and neon (^{20}Ne), have this potential biological advantage.[2] Using heavy ions and the Bragg peak, single or multiple laminar lesions or larger lesions using the spread peak should produce focal or total destruction of normal or abnormal pituitary tissue because of this radiation's high relative biological effectiveness (RBE). The spatial localization of hormone secreting cells within the pituitary of primates[3] and man[4] offers a physiological parameter to determine the effects of localized radiation on the pituitary *in vivo*.

While 910 MeV helium ions have been highly successful in treating hormone-secreting pituitary tumors, e.g., those associated with acromegaly,

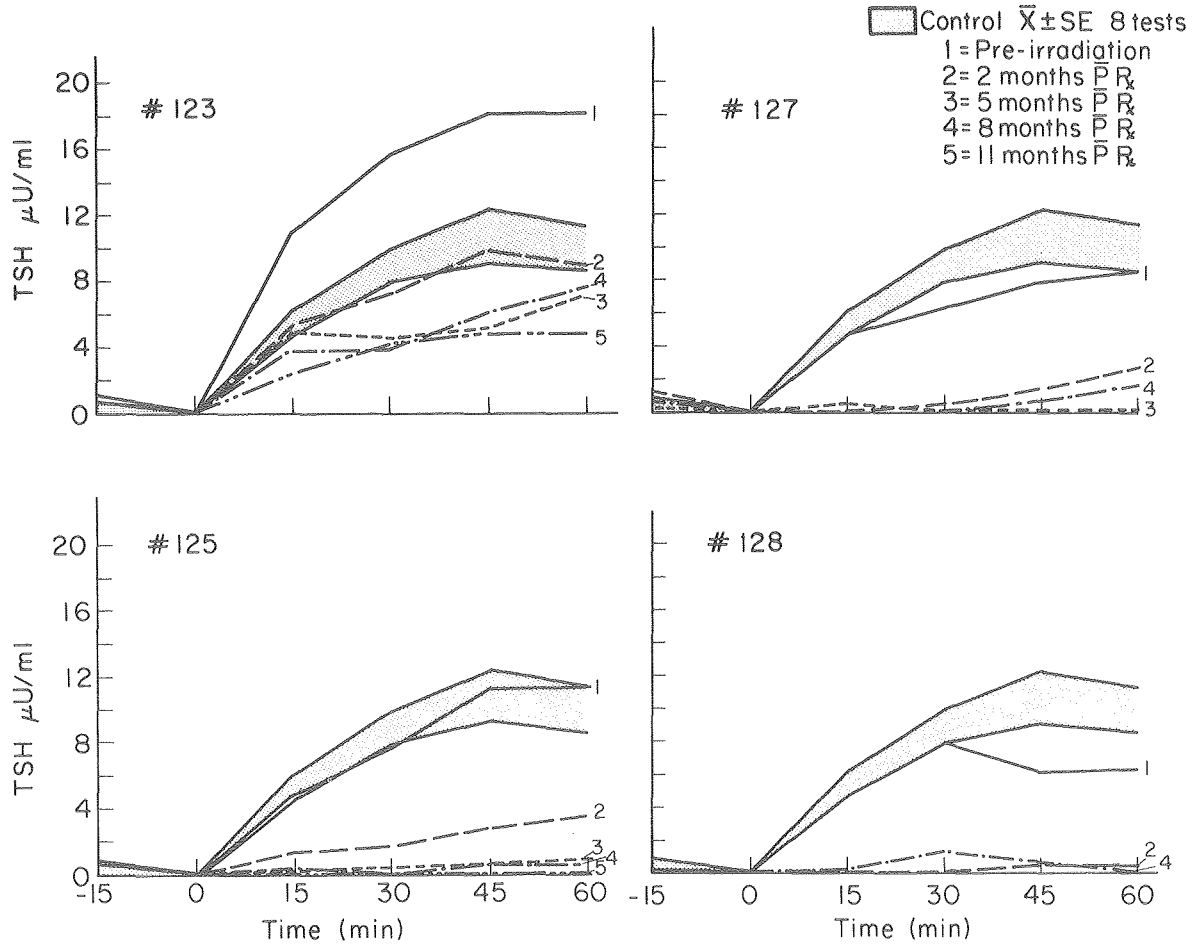

Figure 1. Changes in mean maximum thyroid-stimulating hormone (TSH) responses in Cynomolgus monkeys before and after 250 MeV/amu ^{12}C irradiation of the pituitary. Pharmacological stimulation of the pituitary peptide was produced using thyroid-releasing hormone (TRH) administered by rapid intravenous injection. XBL 806-3376

Cushing's disease, and amenorrhea-galactorrhea syndromes,[5] there are many patients who would benefit from the hormonal effects of either rapid ablation of a small selected portion of the pituitary gland or its total destruction by a nonsurgical technique, performed on an ambulatory basis.

The aims of this study, in which we irradiated Cynomolgus monkeys with carbon-12 ions from the Bevalac, were to investigate the neuroendocrine, neuroanatomical and other effects of irradiation on defined regions of the pituitary and to correlate the onset of specific hormonal changes with anatomical localization of the focal lesions as well as with dose and mode of heavy-ion delivery. Autopsy data from these experiments will be used in the development of a methodology for total pituitary destruction without producing localized or widespread radionecrosis of surrounding neural and neuroendocrine structures such as the cranial nerves, temporal lobes, and hypothalamus.

From these initial experiments with 250 MeV/amu carbon ions and the use of sensitive radioimmunoassay hormone measurements, effects of the *in vivo* secretion of the pituitary peptide hormones by high-LET (linear energy transfer) carbon ions has been demonstrated. A greater and more rapid hormonal ablative effect was observed for lateral Bragg peak with combined peak doses of approximately 14,000 rad in the lateral margins of the pituitary than when either higher central doses or lower spread peak doses were employed. The *in vivo* differences observed at 38 days suggest that the location of the lesion as well as the dose and volume of irradiated tissues determine the magnitude of the effect on hormone secretion. The greater hormonal effect of Bragg peak lesions in the lateral lobes of the pituitary conforms to our anatomical data and confirms that spatial distribution of cells in the pituitary can be used as an *in vivo* means of confirming accurate localization of high-LET irradiation in the pituitary. Provocative hormone testing is a very sensitive measure of radiation effects, as demonstrated in Fig. 1.

Further experiments employing *in vivo* hormonal studies and correlating them with gross anatomical and immunocytochemical studies of the pituitary after irradiation with even heavier ions, e.g., silicon, are planned.

REFERENCES

1. Tobias, C. A. 1979. Pituitary irradiation: radiation physics and biology. In *Recent Advances in the Diagnosis and Treatment of Pituitary Tumors,* J. A. Linfoot, ed., pp. 221–243. New York: Raven Press.
2. Tobias, C. A. 1973. Pretherapeutic investigations with accelerated heavy ions. *Radiology* 108:145–158.
3. Herbert, D. C. and Hayashida, T. 1974. Histologic identification and immunochemical studies of prolactin and growth hormone in the primate pituitary gland. *Gen. Comp. Endocr.* 24:381–397.
4. Hardy, J. 1979. Transsphenoidal microsurgical treatment of pituitary tumors. *Recent Advances in the Diagnosis and Treatment of Pituitary Tumors,* J. A. Linfoot, ed, pp. 375–388. New York: Raven Press.
5. Linfoot, J. A. 1980. Alpha particle pituitary irradiation in the primary and post-surgical management of pituitary microadenomas. In *Proceedings of the International Symposium on Pituitary Microadenomas,* pp. 515–529. London: Academic Press, Inc.

DIABETES RESEARCH

John A. Linfoot and Harrison Stubbs

A recent review of the long-term effects of alpha-particle pituitary irradiation (APPI) on patients treated for diabetic retinopathy continues to confirm the apparent improved survival in this patient group. Although a certain number of our diabetic population die of microangiopathic (capillary) complications, specifically of nephropathy (kidney disease), this group may have a more favorable prognosis than is reported in the literature. The rate of deterioration in the glomerular filtration rate was slower in APPI-treated patients.

The factors influencing the rate of progression of diabetic renal disease are not known. Using constant proteinuria as the criterion for diabetic renal disease (DRD), we defined three groups of patients: ≤ 1, 1–4, and >4 gm of protein in urine per 24 hours. All groups showed a slower decline in glomerular filtration rate, measured by endogenous creatinine clearance, and the observed differences were significantly less than predicted by Mogensen,[1] i.e., ~1 ml/min/mol. To further assess deterioration of renal function, the reciprocal of serum creatinine

(μmol/l) was analyzed in each of the three groups (see Fig. 1). Although there is great variability between diabetics, the decline in renal function in any given diabetic is linear after the serum creatinine reaches 200 μmol/l (2.3 mg/dl). We found that the rate of development of moderately advanced or severe renal failure was significantly reduced in our patients, in spite of proliferative diabetic retinopathy (PDR) and renal angiopathy, and was correlated with improved survival.

The collaborative study with B. Klein at the Diabetic Retinopathy Center at the University of Wisconsin under the direction of M. Davis will provide a unique opportunity to determine the effects of APPI on the patients treated for PDR, particularly whether the altered hormonal environment influenced vision, renal function, and survival.

REFERENCE

1. Mogensen, C. E. 1971. Glomerular filtration rate and renal plasma flow in short-term and long-term juvenile diabetes mellitus. *Scand. J. Clin. Lab. Invest.* 28:91–100.

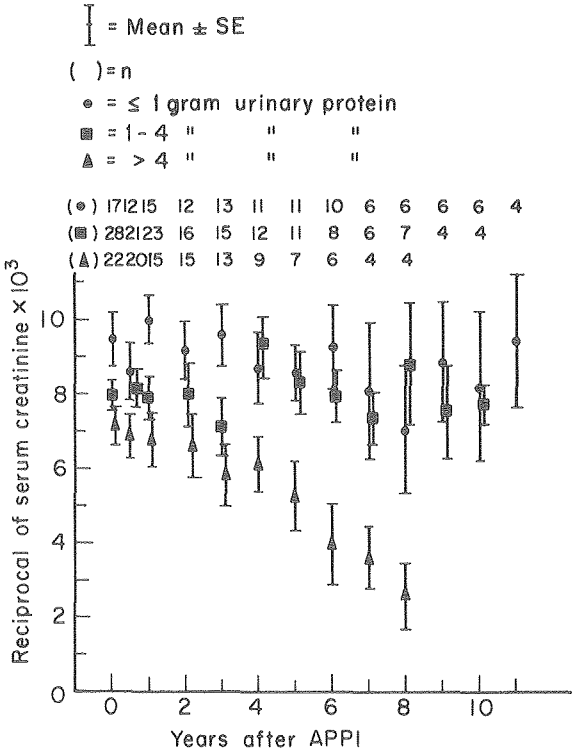

Figure 1. Reciprocal of serum creatinine measured in μmol/l (1/cr × 10³) versus time after irradiation, reflecting decline in renal function. The number of patients who developed early renal failure was surprisingly low and the rate of decline less than expected. (2.3 mg/dl = 200 μmol/l; reciprocal of 200 μmol/l × 10³ = 5.0.) *XBL 801-3001*

LIPOTROPIN AND ENDORPHIN RESEARCH

Eckehart Wiedemann, Tokuko Saito, and Kathleen Harris

Beta-lipotropin (β-LPH) and adrenocorticotropin (ACTH) are derived from the same precursor molecule, which has a molecular weight of 31 K and is present in brain, pituitary, and probably some peripheral sites. This "31 K" precursor contains the complete amino acid sequences of at least six different pituitary hormones. Several of these, including β-endorphin, serve also as neurotransmitters or neuromodulators. Some fragments of β-endorphin, named α-, γ-, and δ-endorphin, are also neuropeptides. The endorphins are involved in pain perception and in the control of behavior and of hypothalamic functions such as the regulation of appetite, body temperature, blood pressure and pituitary function. Although our interest in β-LPH began when it was recognized only as a pituitary hormone of unknown function, the subsequent unraveling of its relationship to the endorphins led us to investigate these peptides as well.

DEVELOPMENT OF ASSAYS FOR LIPOTROPINS AND ENDORPHINS

We had previously developed the first radioimmunoassays for β-lipotropin and β-endorphin suitable for use with unextracted plasma and have measured these hormones in healthy subjects and in patients with certain diseases. During the past year, in order to study lipotropin and endorphin metabolism, we have raised antisera directed against specific regions of the β-LPH molecule. By immunizing rabbits with antigens, coupled to thyroglobulin to increase their antigenicity, we have obtained useful antisera against Met-enkephalin or β-LPH (61–66), β-melanocyte-stimulating hormone (β-MSH) or β-LPH (37–58), and γ-endorphin or β-LPH (61–78), and have developed radioimmunoassays for these peptides. The β-MSH assay may be used for the diagnosis of certain types of cancer that sometimes

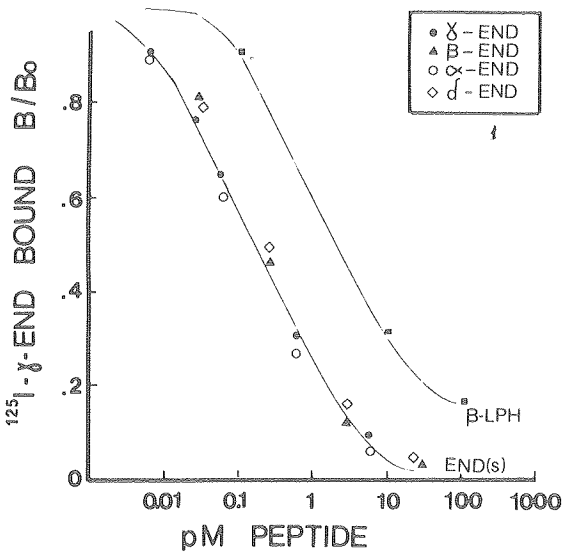

Figure 1. Displacement curves of ^{125}I-γ-endorphin bound to antiserum R-3. This antiserum shows 100% crossreactivity with four endorphins and 6.5% crossreactivity with β-LPH. *XBL 8010-12278*

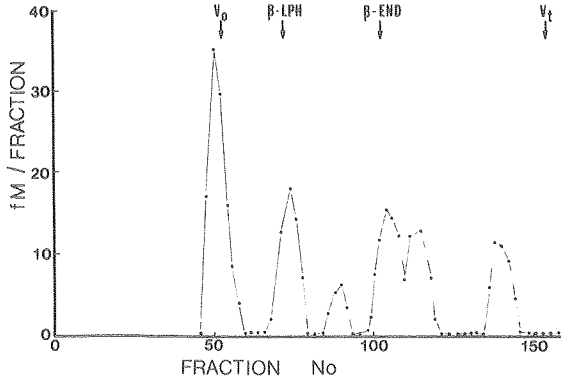

Figure 2. Endorphins and related peptides in an extract of human plasma fractionated on Sephadex G50. Fractions are assayed using antiserum R-3. The extract contains several endorphins as well as β-LPH and the 31 K precursor (first peak). *XBL 8010-12276*

secrete this peptide, which is not detectable in the blood of healthy subjects. Particularly useful is our antiserum R-3, which shows 100% crossreactivity with all four endorphins (Fig. 1). This allows measurement of "total endorphins" in a single step, or, in combination with appropriate fractionation procedures, quantitation of each endorphin with the same assay procedure. The latter approach has proved very useful in determining which lipotropins and endorphins are present in body fluids and tissue extracts.

LIPOTROPINS AND ENDORPHINS IN PLASMA AND CEREBROSPINAL FLUIDS

We have found that both human plasma and cerebrospinal fluid contain not only β-LPH and β-endorphin, but also γ-LPH, γ-endorphin, and smaller β-endorphin fragments as well as a high-molecular-weight component that may represent the 31 K precursor. (Figure 2 shows human plasma fractions.) Studies are in progress to determine which of these peptides are actually secreted into the blood and which, if any, represent breakdown products generated in the periphery.

FUNCTION OF β-LIPOTROPIN

Although there is no doubt that β-LPH is a hormone secreted by the anterior pituitary, usually together with ACTH, its function remains unknown. In order to get a clue to the possible function, we have searched for and have detected apparently specific binding sites ("receptors") for β-LPH in various tissues. Binding sites were most numerous in the adrenal cortex, suggesting that β-LPH may be involved in the regulation of adrenal function. Several observations lead us to suspect that β-LPH may specifically stimulate adrenal androgen production. We are now developing protocols to test this hypothesis in animal models.

ENDORPHINS, OBESITY, AND DIABETES

Studies by several investigators suggest that β-endorphin stimulates appetite and may be responsible for the development of genetically determined obesity and diabetes in certain strains of rats and mice. Other workers have shown that β-endorphin can stimulate insulin secretion by the isolated perfused dog pancreas and have detected β-endorphin-like immunoreactivity in total pancreas extracts. Such observations implicate abnormal β-endorphin metabolism in pathogenesis of obesity and diabetes, disorders which very commonly occur together. We have started several investigations to study these possible relationships. With J. Givens of the University of Tennessee, we have detected a positive correlation between body weight and plasma endorphin concentration in women who have hirsutism and elevated levels of adrenal androgens in their blood. Since hirsutism (abnormally increased body hair) is commonly associated with obesity, glucose intolerance, and hyperinsulinism, this entire syndrome could be simply explained by increased secretion of β-LPH and β-endorphin.

In a related project with G. Grodsky of the University of California, San Francisco, we have looked for β-endorphin in the islets of Langerhans, the endocrine portion of the pancreas. By assaying gel chromatography fractions of acid extracts of isolated perfused rat islets of Langerhans with various antisera, we have indeed detected both β-endorphin and its precursor, β-LPH, as well as smaller endorphin fragments (Fig. 3). Together with our recent demonstration of β-endorphin secretion by the isolated perfused rat pancreas, this observation suggests synthesis of β-endorphin by the rat islet cells themselves, and is consistent with a role for β-endorphin in insulin secretion. On the basis of these results, we have now developed the working hypothesis that adult-onset insulin-independent diabetes mellitus associated with obesity may, at least in part, result from an overproduction of β-endorphin in the hypothalamus, pituitary and islet cells. This hypothesis will now be tested in the rat model.

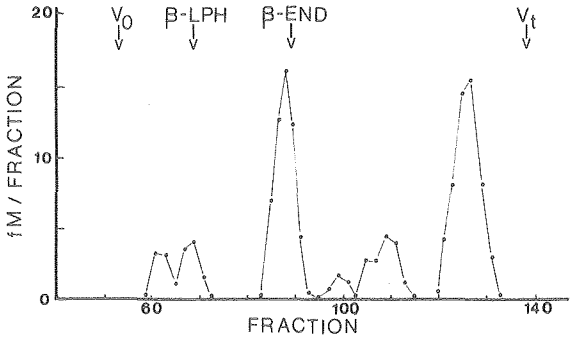

Figure 3. Endorphins and related peptides in an extract of rat islets of Langerhans fractionated and assayed as indicated in Fig. 2. The extract contains β-endorphin, smaller endorphins, and β-LPH. Because β-LPH shows only 6.5% crossreactivity with antiserum R-3, the β-LPH peak is actually 15 times as large as indicated. XBL 8010-12277

4. PERALTA CANCER RESEARCH INSTITUTE

The Peralta Cancer Research Institute (PCRI), directed by Dr. Adeline J. Hackett, was formed in May 1974 as an association of Peralta Hospital, Oakland, with the University of California, Berkeley. The institute's goal is to encourage mutually beneficial interactions between basic researchers and clinicians practicing oncology. Thus, the tumor biologist gains clinical information needed to design new and perhaps more relevant model systems, and the clinician can be provided with important and effective new tools for the early diagnosis of disease and improved patient care. Since July 1977, PCRI has been affiliated with the Biology and Medicine Division of Lawrence Berkeley Laboratory. The institute runs programs in cell biology, cancer diagnosis, and cancer treatment.

Investigators in the cell biology program at PCRI have pioneered in the development of techniques for culturing human mammary epithelial cells. This achievement is particularly important because approximately 99% of human breast cancers are malignancies of this cell type but, until recently, only minimal growth of these cells could be achieved in culture. Techniques developed at PCRI can now provide mammary epithelial cells in numbers large enough to perform studies on the mechanisms of cancer induction and the identification of characteristics marking the progression from normal to malignant.

The cancer diagnosis program has been concerned with researching new techniques for early diagnosis of breast cancer in women. Studies have concentrated on developing and evaluating breast fluid and fine needle aspiration cytology for early detection of breast tumors. Further plans include working with biologists and physicists to evaluate heavy-ion radiation technology as a potential modality for early diagnosis of breast cancer. The concept of the Breast Diagnostic Center, which brings together in one place all current modalities for breast cancer diagnosis, treatment, and education, is being tested with the financial assistance of the Clorox Company.

The cancer treatment program has been concerned with applying cell biology and biochemistry advances to improve cancer management. Using the expertise developed at the institute in culturing human cells, this group has begun testing cancer cells for sensitivity to chemotherapeutic drugs. It is hoped that this approach will optimize chemotherapy effectiveness by determining the most effective drug combinations and by ruling out ineffective agents, thus eliminating unnecessary patient toxicity.

These programs demonstrate how effectively the Lawrence Berkeley Laboratory can work together with the local medical community to apply basic research advances for improved patient care.

CANCER DIAGNOSIS PROGRAM

Adeline J. Hackett, Helene S. Smith, Otto W. Sartorius,* Lisa Snow, and Martha R. Stampfer

The Peralta Cancer Research Institute has organized the Breast Diagnostic Center (BDC) to make available to women information about the breast, and to conduct clinical research to improve methods for early diagnosis and treatment of breast disease. Women entering the center are educated about the anatomy and physiology of the breast, signs of both benign and malignant disease, and factors that influence the risk of developing cancer. The BDC program proposes to demonstrate that the combined use of various diagnostic modalities, when each modality is used at maximum potential, can detect cancers at an earlier stage. Emphasis is placed on the physical examination, using nipple aspiration cytology, contrast ductography, fine-needle aspirations, and mammography. With the financial participation of the Clorox Company, we have shown that the concept of the BDC is economically sound and fills a need in our community.

*Peralta Cancer Research Institute.

CANCER TREATMENT PROGRAM

Adeline J. Hackett, Helene S. Smith, Tom K. Lee,* and Martha R. Stampfer

The cancer treatment program has begun studies to determine whether it will be possible to evaluate a patient's response to chemotherapeutic drugs by seeding second-passage epithelial cells in culture with irradiated fibroblasts. The resulting colonies of epithelial cells grow up in approximately 10 days (see Fig. 1). Using this assay, the toxic effect of chemotherapeutic drugs on cells from a number of different tumors has been found to vary from drug to drug. Although the assay has yet to be tested clinically, it is an important breakthrough for studies on the effects of chemical carcinogens, hormones, drugs, nutritional variables, and low-dose irradiation on human cells.

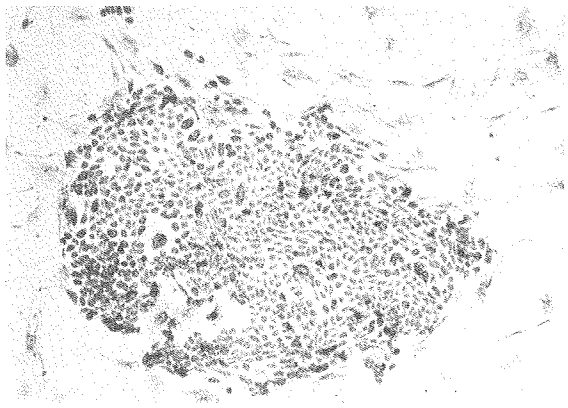

Figure 1. Colonial growth of human mammary epithelial cells. Single cells are plated onto irradiated fibroblasts. Note extensive growth after 10 days in culture. Efficiency of colony formation ranges from 6% to 35%.

XBB 809-10355

*Peralta Hospital.

CELL BIOLOGY PROGRAM

Adeline J. Hackett, Helene S. Smith, Martha R. Stampfer and Jack C. Bartley

Many relevant assays have been developed to evaluate the carcinogenicity of various compounds, including *in vivo* studies with rodents, and *in vitro* studies assaying mutagenicity using various eukaryotic and prokaryotic systems or transformation of rodent tissue culture cells. However, a major concern about such tests for chemical carcinogens is the applicability of their results to humans.

Since many differences have been observed between human and murine rodent cells that may be relevant to carcinogenesis assays (i.e., variability in enzyme populations, metabolic pathways, and growth properties, as well as differences in the incidence of cancer among various species), it is extremely important to study the effects of carcinogens on human cell substrates to directly validate results obtained with other transformation systems.

Furthermore, most murine tissue-culture transformation systems have utilized fibroblastic rather than epithelial substrates. Since approximately 90% of human cancers are carcinomas, that is, tumors derived from epithelial cells, it is also important to test for chemical carcinogenesis on epithelial cell substrates, as there may be significant differences in the effect of chemicals upon cell types.

One of the chief difficulties with developing an assay to test carcinogens on human cells has been the inability to grow human cells in culture. During the past few years the cell biology group at the institute has achieved a major breakthrough in this important problem. We have developed a medium that uses various hormones and growth factors and that readily supports the rapid replication of very large numbers of human mammary epithelial cells derived from reduction mammoplasties. The cooperation of local surgeons in providing tissue specimens necessary for this work further illustrates the way in which PCRI has become a catalyst for promoting cooperation between LBL staff and the medical community.

We have begun to use this newly developed culturing technology to study the effect on human mammary cells of benzo(a)pyrene (BaP), a combustion-produced carcinogen found in cigarette smoke, coal tar, and polluted air. We have found that BaP is readily metabolized by mammary epithelial cells and that repair of the altered cellular DNA is not detectable. This suggests the possibility that BaP may play a role in mammary carcinogenesis. Current attempts to demonstrate the induction of malignant proper-

ties in cells exposed to BaP may lead to a quantitative assay for transformation of human epithelial cells. Studies on the effect of hormonal and nutritional factors on the metabolic patterns of BaP may provide information on the risk for breast cancer and, ultimately, control of the disease. Other studies include: development of techniques to isolate colonic crypts as a prelude to culturing epithelial cells of the colon; the interaction between different cell types in culture; hormonal and nutritional control of cell growth; and identification of malignant markers.

5. ENVIRONMENTAL PHYSIOLOGY

The changes in physiological activity that take place when living organisms attempt to maintain a constant internal environment in spite of the assault of external environmental pollutants continues to be the focal point of research in the Environmental Physiology Group, led by Dr. Joseph F. Garcia. In seeking to understand how environmental pollutants exert their effects on the body's internal environment, these investigators hope to develop methods for the early detection of adverse effects as well as a scientific basis for their successful treatment. This knowledge would also allow appropriate exposure standards to be established for the general population.

One area of research effort involves studies with erythropoietin, the primary hormone controlling the production of red blood cells. With the purification of erythropoietin, a sensitive radioimmunoassay for detecting its presence in the blood stream has become available. Erythropoietic tissue is affected by a variety of influences, including nuclear and non-nuclear energy pollutants. The measurement of circulating erythropoietin levels in the blood stream of pollutant-exposed laboratory animals may provide an early sign of the pollutant's effect on erythropoiesis before it is manifested as a change in the blood picture—possibly even before the erythropoietic response actually begins. This sensitive assay for measuring erythropoietin blood levels may also allow the early detection of exposure to pollutants such as oxides of carbon, nitrogen, and sulfur, as well as to nuclear and certain metal pollutants. The erythropoietin radioimmunoassay is currently being used on human plasma and serum samples as well as on animal material. Erythropoietin values for normal humans have been established and the uses of this assay as a diagnostic tool are being explored in the hematology clinic. For example, the radioimmunoassay is already being used to distinguish patients with primary polycythemia (excess red blood cells) from those with polycythemia of secondary origin.

Another area of research concerns the acute and chronic effects of gaseous and metal pollutants, as observed in laboratory animals. Effects on the steroid hormone mechanism, on the hypothalamo-pituitary-thyroid axis, and on tumor incidence are being studied. The effects of gaseous pollutant exposure on the biochemical integrity of lung tissue continue to be studied in an attempt to develop immunologic methods for assessing lung damage at the cellular level and to understand the role of enzymes released from damaged tissue on the pathophysiological development of lung disease.

A research center for the analysis and interpretation of data from short-term tests for carcinogens and mutagens is being developed in the Biology and Medicine Division. During the past few years various short-term testing methods for detecting potential chemical carcinogens and mutagens have emerged and are now being incorporated into the package of required or recommended toxicological tests for chemicals controlled by major regulatory agencies. Such tests have been proposed as part of the regulatory decision-making policy of the Occupational Safety and Health Administration (OSHA) for classification of chemical carcinogens in the workplace, by the Food and Drug Administration (FDA) for the regulation of new animal drugs, and by the Environmental Protection Agency (EPA) for regulating pesticides, the disposal of toxic wastes, and air pollutants. Animal cancer tests require longer testing periods, and consequently there is an expanding list of suspected chemicals identified by short-term tests which have not been subjected to animal cancer tests. The effort of this center will be important in determining how relevant the short-term test results are in establishing the genetic and human cancer risks.

The highlights of achievements during the past year in these and other areas of investigational interest are presented in the papers that follow.

EFFECTS OF ENVIRONMENTAL POLLUTANTS ON STEROID HORMONE MECHANISMS

Gerald M. Connell

Research in our laboratory continues the investigation of the health effects of man-made alterations to our environment. We have examined atmospheric pollution with ozone as a model pollutant and also examined some subtle mammalian reproductive biochemical perturbations caused by the heavy metal cadmium, a waste product of oil shale refinement and other industries. Furthermore, we have studied some basic testicular biochemical changes promoted by exposure to dibromochloropropane (DBCP), an agricultural nematocide. Although its use in California is at present restricted, it is still a problem because of its contamination of ground water and water wells in many agricultural regions.

We have previously reported that chronic exposure to ozone, a common atmospheric pollutant, is more detrimental to the health of male rodents than female rodents. Mortality of male mice within a three-month exposure period is significantly greater than that observed for female mice. We concluded that some sex-related factor, possibly a hormone or a hormone-dependent mechanism, was responsible for facilitating the survival of female mice. To further investigate this unusual phenomenon, we chose to gonadectomize male and female mice. This surgical procedure removed the endogenous sources of the male and female sex steroids, the testes and ovaries. A large population of male mice without testicular androgens and of female mice without ovarian estrogens could thus be tested for their responses to a chronic ozone environment.

Exposure conditions within the environmental chambers were the same as in our earlier studies with intact male and female mice, and combined results are illustrated in Fig. 1. The general responses to the chronic 1.5 ppm ozone environment were similar to those observed previously. An "ozone syndrome"—the appearance of weight loss, fluid-filled lung tissue accompanying enlarged lungs, deformed spinal configuration, brittle bones, thinning and dry coats with diffuse hair-loss patterns, and a general cyanotic appearance—evolves; however, the onset of this generalized syndrome was much accelerated in the castrate population compared to a normal population. The striking difference observed in this study, compared to our earlier ones with intact mice, was that ovariectomized female mice are significantly more sensitive to the ozone environment than castrate male mice. These experiments clearly indicate that an ovarian product, probably a sex steroid, facilitates the greater survival of the intact female mice. At present, experiments with gonadectomized mice receiving sex hormone replacement therapy are underway. It is anticipated that these studies will provide information as to which sex hormone or hormones are critical, and concomitant biochemical studies will seek to identify the mechanisms by which this protection is mediated.

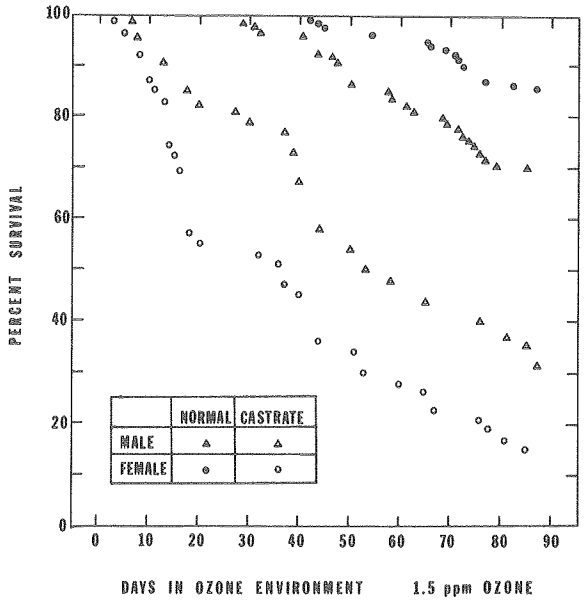

Figure 1. Contrasts in the survival of male and female mice in a chronic ozone environment (1.5 ppm). Symbols are explained in the inset. Each symbol represents the death of an animal during the experiment, its position showing the percent surviving at that point in time. XBL 809-11705

Another area of interest has included the effects of heavy metals on reproductive biochemistry and morphology of the mammalian testis. It has long been known that cadmium, a waste product of many industries, has a deleterious effect on the structural integrity of the testicular tubular compartment, where sperm is produced. We have demonstrated in a mammalian testicular *in vitro* system that low doses of cadmium will also inhibit testosterone production. More recently, we have examined the cadmium content of rodent testes after chronic low dose administration of cadmium. Quantities of cadmium used in these studies were too low to evoke

any structural alterations that conventional light microscope techniques could reveal. Also, surprisingly, no differences in the cadmium content of the testes of untreated, 0.5 ppm and 5.0 ppm cadmium-treated rodents were observed. All testes, including those from untreated animals, showed significant concentrations of this metal, whereas other organs, for example the liver, showed a dose-dependent response to cadmium treatment. This unusual response may possibly be a normal sequestering of cadmium by the testis, and may in some way be related to the decline of sperm production normally observed with advancing age.

Dibromochloropropane (DBCP) is a very potent pesticide that effectively controls nematodes, which are extremely destructive to the root systems of economically valuable agricultural products. Tremendous quantities of this compound had been formulated and used on crops throughout the world until the recent discovery of reproductive complications among factory formulators and farm workers. Although its use has been restricted in California, its presence is still detected routinely in water wells and ground water of California's Central Valley farming regions. The ultimate consequences of such chronic low-level exposure to DBCP remain to be determined. The apparent action of this structurally very simple agent on the testis aroused our interest several years ago. Laboratory experiments with rodents showed that microgram quantities of this compound would alter the normal production of the male hormone, testosterone. Further studies with the mammalian testis in an *in vitro* system have indicated that the conversion of androstenedione into testosterone may specifically be affected. This biochemical transformation is mediated by the enzyme 17-β steroid hydroxylase, and additional studies of the metabolic pathway of steroid hormone formation may yield some valuable information on the action of DBCP in the mammalian testis.

HORMONE STUDIES IN RATS EXPOSED TO ENVIRONMENTAL POLLUTANTS

Gisela K. Clemons and Joseph F. Garcia

The main objective of our project is to study the effect of non-nuclear energy pollutants on the production, secretion and metabolism of protein and polypeptide hormones in laboratory animals. A variety of gaseous and metal pollutants, presented both acutely and chronically, are being studied. The radioimmunoassay technique for hormone measurements has been extensively employed. Initial work into the effects of ozone on hormonal systems has led us to an extensive study of the hypothalamo-pituitary-thyroid axis of rats perturbed with this pollutant.

Ozone concentrations as low as 0.8 ppm for a period of 8 hours will result in a highly significant decrease in circulating thyroxine (T4), triiodothyronine (T3), thyroid-stimulating hormone (TSH), and protein-bound iodine (PBI). However, this depression in pituitary TSH secretion was not part of a general depression in pituitary activity since serum levels of growth hormone and gonadotropins were not depressed and, in fact, serum prolactin was concomitantly increased.

To understand the primary effect of ozone on this hormonal system, a variety of *in vivo* and *in vitro* studies were initiated. *In vivo* and *in vitro* studies with the hypothalamic thyrotropin releasing hormone (TRH) indicated that the anterior pituitary was capable of normal function. The thyroid gland itself appears to respond normally to its stimulatory hormone, and the response of rats to cold immediately following ozone exposure indicated normal function of the hypothalamus. Administration of TSH (1U/rat; i.v.) prior to a 9-hour exposure at 1 ppm did prevent the ozone-induced reduction in circulating thyroxine levels, and intravenous administration of radioiodine-labeled TSH immediately following ozone exposure showed the same clearance half-time as control animals. This indicates that there is no increased metabolism or damage to circulating TSH to account for the observed reduction in serum TSH seen following such pollutant exposure.

The thyroid weight of ozone-exposed rats is always significantly increased. This weight increase is attributable to an increase in both water content and total protein content. This edema is reminiscent of the well-documented observation of lung edema in ozone-exposed animals, yet unlike the lung tissue, the thyroid tissue is not the object of as direct an insult by ozone exposure as is the lung.

There is a striking similarity between ozone and hypoxic (low-oxygen) environments, in that survival is decreased by the administration of thyroid hormones and increased by thyroidectomy. Because of this we have initiated work with hypoxia to explore its possible effect on the pituitary-thyroid axis. When rats are exposed to a hypoxia equivalent to

that existing at a 22,000-foot altitude for 2 to 48 hours, the circulating TSH, T4, and T3 are all significantly depressed, as in ozone exposure.

Whether the observed disturbance of the hypothalamo-pituitary-thyroid axis is attributable to peripheral changes of thyroid hormone metabolism or possibly to a lowered hypothalamic setpoint of TRH release is currently being investigated. Indications are that lowered thyroid hormones are beneficial for the protection of the animals during ozone exposure and, therefore, that changes in peripheral hormone metabolism or a reduced hypothalamic setpoint are an adaptive mechanism or induced homeostasis.

The occurrence of edema in the lung and the thyroid after ozone exposure indicates that there are significant fluid shifts within the animals. Since prolactin has been implicated as an osmoregulatory factor, the increased prolactin levels seen after ozone exposure may play such an osmoregulatory role, and the ozone-exposed rat may provide a model for studying osmoregulation in mammals. We have begun work using an *in vitro* system in which water transport is measured across the inverted small intestine of ozone-exposed and normal rats. Our initial studies indicate that after ozone exposure there is an increased transport of fluid across the jejunum (part of the small intestine). This fluid uptake was increased by 68% in ozone-exposed rats as compared to control rats and corresponded to a 90% increase in the circulating prolactin levels of such ozone-exposed rats. These studies will be pursued, as they may relate to the observed edema in lung and thyroid tissue following ozone exposure.

Endocrine disturbances following chronic and acute administration of metal pollutants are also currently being investigated. The sensitivity of the endocrine system is ideally suited to show early biological indications of environmental pollution even at trace amounts. Metals have been shown to influence the endocrine system in different ways, depending on whether there is an excess or a deficiency of the metal. In excess, lead, mercury, iron, cadmium, cobalt, nickel, and arsenic have been reported to affect the endocrine system adversely. Chronic administration of methyl-mercury (3 and 10 ppm) and cobalt (30 and 100 ppm) in drinking water for ten months generally reduced the circulating levels of most pituitary hormones. For both metals, tissue uptake was proportionately kidney >> liver > heart > brain. Chronic exposure to cadmium (5 and 0.5 ppm) and arsenic (25 and 5 ppm), administered with drinking water, is currently also being studied in rats.

The acute administration of nickel and cobalt chloride shows both interesting similarities and differences in their action upon the endocrine system. Injection of either metal has been reported to cause prompt hyperglycemia, hyperglucagonemia and subsequent hyperinsulinemia in rats, rabbits, and guinea pigs. Nickel has also been shown to specifically inhibit prolactin secretion from the pituitary *in vivo* and *in vitro* within two hours after administration, and it has been suggested that nickel is part of the hypothalamic prolactin-inhibiting factor (PIF). By measuring the hormone levels for up to 28 days after a single injection of either nickel chloride or cobalt chloride, we observed the immediate metal-induced effects on glucose metabolism and prolactin inhibition. However, from 1 to 7 days, nickel chloride caused a profound hypersecretion of prolactin from the pituitary. This hyperprolactinemia is associated with higher *in vitro* release of prolactin from the pituitaries and reduced PIF activity in the extracts of hypothalami obtained during this period. On the other hand, cobalt chloride administered at the same dose led to a progressive reduction of circulating prolactin levels throughout the experiment. Another endocrine system in which both metals have different actions is erythropoiesis. Cobalt stimulates erythropoietin and red blood cell production, while nickel seemingly has no effect.

POLLUTANTS AND THE IMMUNE SYSTEM

Joan Wright Goodman and Sarah Garner Shinpock

Rapidly dividing cells, including myelo- and lymphopoietic tissues (those in the marrow and lymph nodes) are exceptionally vulnerable to the damaging effects of agents such as radiation and other pollutants. Because of the body's continuing need for blood formation and for immune defenses, these tissues must be kept functional. It is necessary, therefore, to study the behavior of these cellular systems when the whole animal is exposed to pollutants. We are studying mice that have been acutely exposed to lead in an attempt to corroborate and broaden scattered reports in the literature that pollutants such as lead, cadmium, and ozone affect certain immune parameters, including antibody for-

mation and responsiveness to mitogens, agents inducing cell division and proliferation. We have studied proliferative responses to T lymphocyte (phytohemagglutinin and Concanavalin A or ConA) and B lymphocyte (lipopolysaccharide or LPS) mitogens after intravenous injection of 1% lead acetate (0.2 ml per mouse) in 5% dextrose in water. After 3 or 4 days, when spleen and blood CFU-S (colony-forming unit—in the spleen) would be elevated, spleens were removed aseptically and prepared for *in vitro* culture with the mitogens.

Early experiments with B6D2F mice confirmed that, insofar as response to mitogens reflects cell populations in the spleen, acute lead exposure causes no decrease in T and B lymphocytes. One difficulty with interpreting mitogen response data is the background (unstimulated culture, or NIL) ^{3}H-thymidine uptake by spleen cells. Spleens from mice acutely exposed to lead regularly have very high (20–50 ×) background counts per minute (CPM). True stimulation indices (stimulation index: CPM mitogen/CPM NIL) are therefore obscured. In the past year we have attempted to find out to what extent myelopoietic (non-lymphoid) cellular division was contributing to the high NIL's. Recipient mice were exposed to a large dose of gamma irradiation and then treated intravenously with isogenic lymph node cells and thymocytes (1 donor/recipient). Seven days later they were acutely exposed intravenously to 0.2 ml lead acetate (1% in dextrose and water). As controls, other groups were either untreated from the beginning (normal) or irradiated and treated with the same cell suspension but injected seven days later with sodium acetate. Spleens were removed 3 or 6 days after lead injection and cultured with mitogens. All chimeras of both experimental groups had very low NIL's, although their spleens contained many lymphocytes in the regenerating white pulp. This result indicates that non-lymphoid elements, stimulated into cell division (or at least DNA synthesis) by lead, had indeed been responsible for much of the background activity in the unirradiated mice studied earlier.

Although marrow CFU-S of lead-exposed mice are stimulated into cycle, the actual concentration (or absolute number) of them does not appear to change. We have transplanted isogenic bone marrow from exposed mice and followed thymus weight and CFU-S recovery in resultant chimeras. Preliminary data show no remarkable changes from the usual pattern of recovery seen after normal (or other control) marrow is given.

Mitogen stimulation in two studies of splenic cells from ozone-exposed (1 ppm, for 7 days) B6 mice have shown a depressed response to LPS. These studies need to be repeated in the more hardy B6D2F$_1$ hybrid and should be broadened to cover a larger range of exposures.

EFFECTS OF TOXIC AIR POLLUTANTS ON TUMOR INCIDENCE IN MICE

Margaret R. White, Beverly G. S. McCalla, and Jerome A. Moore

Toxic gases and known chemical carcinogens occur in our environment as by-products of modern technology and especially from the use of fossil fuels. Some of the chemical carcinogens are known to induce lung tumors in mice. There is some evidence[1,2] that at least one of the toxic gases, sulfur dioxide (SO_2), when superimposed on the effects of a chemical carcinogen, may increase the incidence of tumors in animals. Since humans are exposed to both toxic gases and chemical carcinogens in the environment, information is needed with respect to the possible interactions of these air pollutants.

An experiment to test the interactions of SO_2 and urethan on the yield of lung tumors (adenomas) in mice was performed. Urethan is a chemical carcinogen and was chosen for the first experiment with SO_2 because its tumor dose-response relationships are well known (e.g., Refs. 3,4,5), although it is not found widely in the environment. Future experiments will be done with carcinogens that are more frequently found (initially benzopyrene).

Mice were injected intraperitoneally with urethan either 24 hours before or 24 hours after exposure to SO_2. Exposure to SO_2 was done in stainless steel chambers and was continuous for the planned duration, except for short shutdowns to change food and water. The SO_2 exposures were: (1) 40 ppm for 3 days, (2) 20 ppm for 6 days, or (3) 10 ppm for 12 days. SO_2 controls were exposed to chamber air for 6 days. The urethan dose was 0.5 mg/g of body weight for all mice except controls. Urethan controls were injected with the equivalent volume of distilled water (the solvent for urethan).

The data are presented in Figs. 1, 2 and 3. As seen in Fig. 1, for all SO_2 exposures after injection and urethan, the yield of tumors was lower than that in air controls. Conversely, Fig. 2 shows that when SO_2 was given prior to urethan, almost all SO_2-ex-

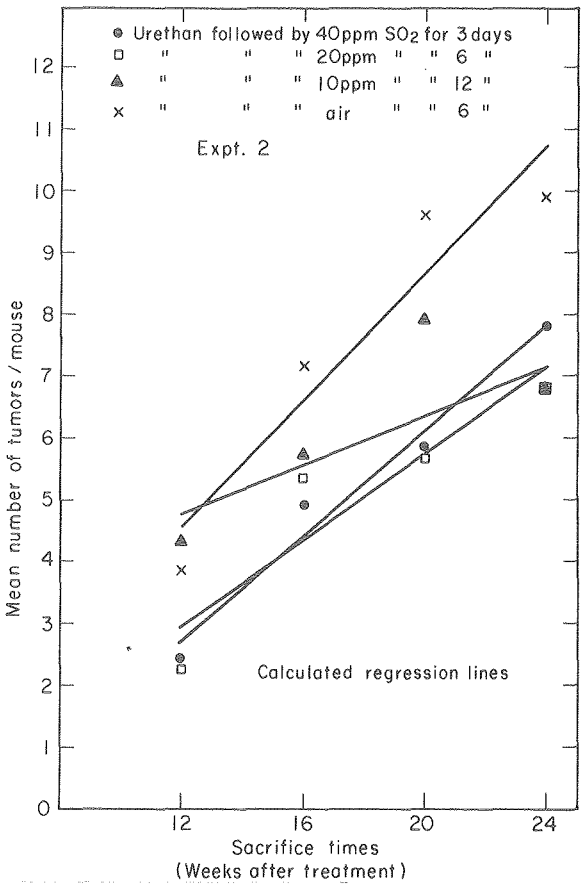

Figure 1. Effects of SO_2 exposure after urethan administration on tumor induction in mice. For each group of SO_2-exposed mice, the tumor yield was lower than that for the air controls. *XBL 801-3044*

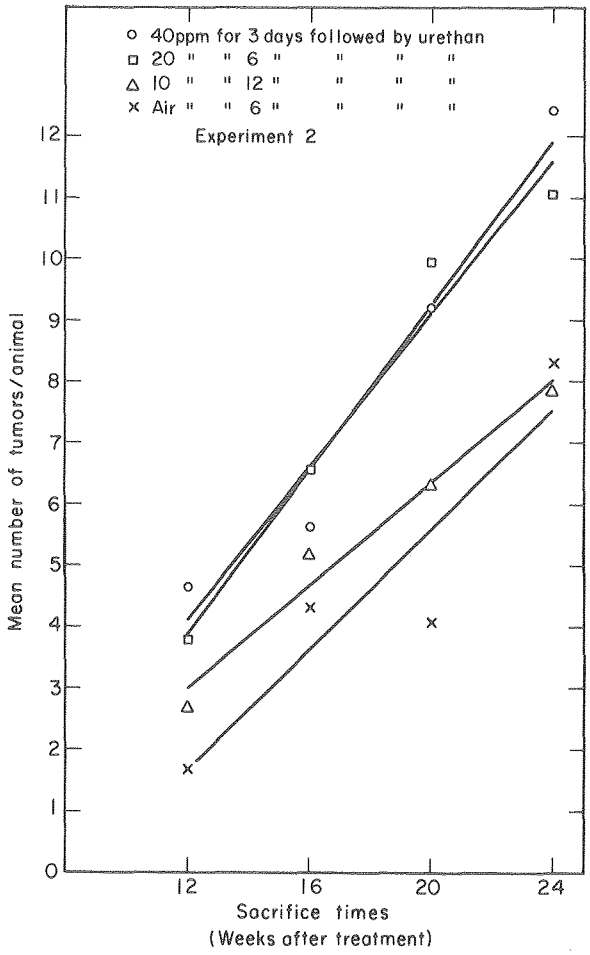

Figure 2. Effects of SO_2 exposure before urethan administration on tumor induction in mice. For each group of SO_2-exposed mice, the tumor yield was higher than for the air controls. *XBL 801-3043*

posed animals had more tumors than air controls. In both cases, the animals exposed to 10 ppm for 12 days were less affected compared to controls (chamber air for 6 days) than those exposed to 20 ppm of SO_2 for 6 days or 40 ppm of SO_2 for 3 days.

There appears to be a chamber effect on the yield of tumors. The animals given urethan and then put in the chamber with air only for 6 days had more tumors (at all sacrifice times) than those receiving urethan after chamber air exposure. The animals appeared not to eat well during the first few days in the chamber and lost weight initially. This may have changed the rate of cell proliferation in the target lung cells and thus modified the urethan effects. Unfortunately, when the experiment was planned, no appreciable chamber effect was anticipated, and therefore only one air exposure period (6 days) was done; no animals were exposed to chamber air for 3 or 12 days. Thus, only the animals exposed to 20 ppm of SO_2 for 6 days are strictly comparable to the air controls. The chamber effects are being looked at in current experiments, the results of which are not yet available.

In Fig. 3 the data are combined for the animals exposed to SO_2 or air before and after urethan. These data show a probable increase in numbers of tumors for those exposed to 20 and 40 ppm of SO_2 and a possible decrease of tumors for those exposed to 10 ppm of SO_2.

Further experiments, some of which are in progress, will be needed for understanding the interactions of: (1) gas concentration, (2) length of time in chamber, and (3) timing of injection of urethan with respect to SO_2 exposure. It is, however, evident that SO_2 exposure does modify the yield of tumors following urethan treatment.

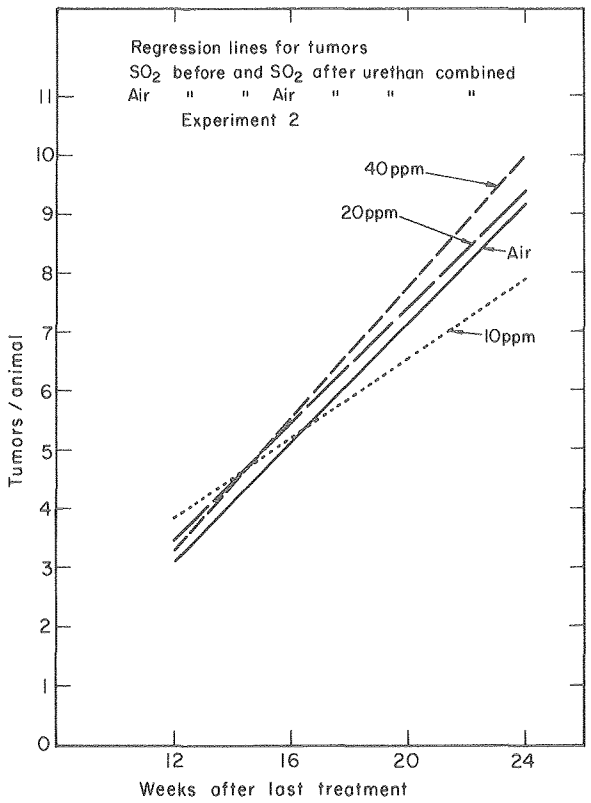

Figure 3. Effect of SO_2 exposure on tumor induction in mice. When data from SO_2 exposures before and after urethan administration are combined, and compared to the combined data for air controls, there is a probable increase in tumor yield for groups of mice exposed to 20 and 40 ppm SO_2 and a possible decrease in the group exposed to 10 ppm SO_2. XBL 801-3042

The mean number of lung tumors in animals given distilled water and exposed to SO_2 was low and did not differ statistically from that of distilled water/air controls. Thus, for the treatment schedules tested here, SO_2 appears not to initiate these lung tumors.

REFERENCES

1. Peacock, P.R. and Spence, J.B. 1967. Incidence of lung tumors in LX mice exposed to (1) free radicals; (2) SO_2. *British J. Cancer* 21:606–618.
2. Laskin, S., Kuschner, M., Sellakumar, A., and Katz, G.V., 1975. Combined carcinogen-irritant animal inhalation studies. In *Air Pollution and the Lung,* E. F. Aharonson, ed., pp. 190–213. New York: John Wiley and Sons.
3. White, M., Grendon, A., and Jones, H.B. 1967. Effects of urethan dose and time patterns on tumor formation. In *Proceedings of the Fifth Berkeley Symposium on Mathematical Statistics and Probability,* vol. 4, *Biology and Problems in Health.* L. LeCam and J. Neyman, eds., pp. 707–719. Berkeley: University of California Press.
4. White, M.R., Grendon, A., and Jones, H.B. 1970. Tumor incidence and cellularity in lungs of mice given various dose schedules of urethan. *Cancer Res.* 30:1030–1036.
5. White, M.R. 1972. Studies of the mechanism of induction of pulmonary adenomas in mice. In *Proceedings of the Sixth Berkeley Symposium on Mathematical Statistics and Probability, vol. 4, Biology and Health,* L. LeCam, J. Neyman and E.L. Scott, eds., pp. 287–307. Berkeley: University of California Press.

ROLE OF PROTEASES AND ANTIPROTEASES IN THE PATHOGENESIS OF POLLUTANT-EXPOSED LUNG DAMAGE

John C. Schooley and Robert J. Webber

The lung is one of the first major organ systems exposed to toxic gaseous pollutants. Our specific aim is to develop immunologic methods for assessing lung damage at the cellular level and to understand the role of enzymes released from damaged tissue on the pathophysiological development of lung disease.

The lung is a complex organ comprised of many cell types. Only during the last decade has it become clear that the lung has a complex metabolic function in addition to its respiratory function. The cells of the lung, particularly those of the alveoli, are severely damaged following exposure to airborne gaseous pollutants. The aleveolar capillary is composed of a continuous layer of squamous, alveolar Type I cells, interspersed with alveolar Type II cells separated from the underlying capillaries by a basement membrane. Macrophages are found within the alveoli. The endothelial cells of the capillaries also rest on a basement membrane. The capillary endothelium is continuous, and in the interstitial space between the basement membrane of the endothelial and epithelial cells are found fibroblasts, macrophages, polymorphonuclear leukocytes, and collagenous and elastic fibers.

A "protease pathogenesis" hypothesis of lung

disease has been advanced by some investigators. In this view, proteolytic (protein-digesting) proteases, released from damaged lung cells such as polymorphonuclear leukocytes and pulmonary macrophages, digest lung proteins and produce anatomical changes in the lung, leading to the development of lung disease. It has been demonstrated that the instillation of such proteases into the lung do produce lesions characteristic of lung disease, but this protease activity is inhibited by substances termed antiproteases.

In blood plasma, about 10% of the total proteins are antiproteases, and at least six specific antiproteases have been described. The two major types are the Alpha-1 antitrypsin, having a molecular weight of about 54,000, and the Alpha-2 macroglobulin, with a molecular weight of about 725,000. It is known that if sufficient amounts of antiproteases are present at the site of protease release, the development of respiratory lesions is minimized. It is also known that human beings with a decreased level of Alpha-1 antitrypsin are prone to the development of pulmonary emphysema. Because of these findings, we have begun studies to determine the behavior of antiproteases in mice exposed to 1 ppm ozone for various periods of time.

Elastase is a protease found in a number of lung cells, but particularly in the polymorphonuclear leukocytes, where it comprises about 5% of the total soluble proteins. We have found, following the injection of I^{125}-labeled elastase into normal mice, a multiphasic pattern of elimination of this protease. Analysis of this multiphasic curve has demonstrated that the enzyme is almost immediately bound to Alpha-1 antitrypsin and Alpha-2 macroglobulin. The macroglobulin rapidly sweeps the enzyme from blood plasma (the half-life of this inhibitor complex is only 6 to 8 minutes), whereas the combination of the protease with Alpha-1 trypsin disappears much more slowly, with a half-life of about 1.5 hours.

A significant transfer of injected protease from the slowly disappearing antitrypsin molecule to the rapidly disappearing Alpha-2 macroglobulin normally occurs. Transfer of the enzyme in the opposite direction also occurs in some instances. Furthermore, the disappearance of the enzyme inhibitor complex from the plasma is decreased when the amount of injected enzyme is increased. We have also found in rodents exposed continuously to ozone that a 5% to 10% drop of the inhibitor concentration in the general circulation occurs.

The large-molecular-weight Alpha-2 macroglobulin is not normally found outside the vascular system, so its role in neutralizing the proteolytic action of proteases released in tissues is unclear. When the integrity of the vascular system is compromised in an injured tissue, such as a lung exposed to pollutants, it is likely that these plasma protease inhibitors move outside of the vessels. One phase of our experiments is to determine the magnitude of this movement.

We are now attempting to determine the processes involved in regulating the synthesis and destruction of the two major serum antiproteases in experimental animals and to clarify whether the synthesis and destruction of these proteins is altered in pollutant-exposed animals. We have isolated and purified the two antiproteases from the serum of mice and rats and have produced antibody against them in rabbits. We can also quantitate the levels of these proteases in blood and lymph. To follow their elimination from the blood, we initially labeled the purified proteins with I^{125} but discovered that iodination altered their ability to combine with proteases. We now label the proteins with C^{14} by a reduction methylation reaction, and this appears to let the proteins retain their biochemical activities. We intend to continue with our studies of the rate of synthesis and destruction in normal and pathophysiological states. The normal physiological role of antiproteases is unclear, although it is thought that they play a role in delineating blood clotting and other proteolytic cascade processes, such as hormone production and elimination.

Another aspect of our study is concerned with the hypothesis that the damaged lung releases proteins that enter the bloodstream to initiate an immune response. Membrane proteins characteristic of the alveolar lining cells of the lung are not normally exposed to the immune mechanisms of an animal, so it is possible that these native proteins initiate an immune response only when absorbed into the bloodstream after lung damage. But it is also possible that these proteins have been altered by the action of proteases, leading to unrecognized foreign protein, or that pollutant gases such as ozone react directly with the lung tissue proteins, leading to a foreign protein.

A number of clinical observations, including studies of emphysema and Goodpasture's disease, have indicated that humans may have rather high titers of antibody against some lung proteins. These proteins generally derive from the basement membrane; in most cases, the antibodies attack collagen or denatured varieties of collagen or elastin. We consider it possible that at least two proteins found only in the lung might initiate an immune response that would thus specifically characterize lung dam-

age. These are: (1) the apoprotein believed to be produced by the alveolar Type II cell, an apoprotein that leads to the formation of surfactant and (2) a specific antiprotease protease produced by lung cells. Our investigations to date have used polyacrylamide-gel electrophoretic separations to determine whether changes occur in the lung protein of animals exposed to ozone, and we have observed distinct changes in some protein classes. We are now attempting to identify these proteins and to determine to what lung cell types these proteins are related. To do this, we have begun experiments to separate and purify the major cellular types of the lung and characterize their membrane proteins.

MEGAKARYOCYTE DIFFERENTIATION

Mary E. Barker and Carol J. Mortensen

Megakaryocytes, the precursors of blood platelets, constitute less than 0.5% of the nucleated cells of the bone marrow. Nevertheless, their large size and multilobulated polyploid nucleus make them conspicuous in bone marrow preparations. In contrast, platelets, which are produced by fragmentation of the megakaryocyte cytoplasm, are the smallest formed elements of the blood (2 to 3 μm in diameter); they function chiefly in hemostasis and repair of blood vessel injury.

Like all other hemopoietic cells, megakaryocytes originate from pluripotential stem cells. However, at some point in their maturation they cease dividing while continuing to synthesize DNA and thus become polyploid. The cytoplasmic volume likewise increases, producing a cell that is enormous by comparison with other hemopoietic cell types. As seen in Fig. 1, the cytoplasm of a mature megakaryocyte is divided by an elaborate system of membranes into thousands of small regions (estimates range from 1000 to 7000), each of which eventually becomes a platelet. Although megakaryocyte fragmentation has been observed by cinematography as well as in sectioned material, almost nothing is known about the subcellular reorganization that transforms the cytoplasmic fragment into the biconvex disc-shaped platelet (Fig. 2).

In spite of its minute size and lack of a nucleus the platelet is a highly organized cell with an impressive array of enzymes, clotting factors, contractile proteins, and numerous other components in its granules and membrane systems. Except for the dense granules containing serotonin, all elements of the normal circulating platelet so far investigated can also be found in the parent megakaryocyte. Furthermore, the relative proportion of various cytoplasmic components, as well as general cell size, appears to be controlled in some way by the ploidy of the cell. Ploidy values, which may range from 8 N to 64 N, are in turn altered when platelet counts are low (thrombocytopenia) or high (thrombocytosis). Besides increasing ploidy, thrombocytopenia also causes megakaryocytes to become larger, mature faster, and eventually increase in number; platelet size also undergoes significant changes. These alterations are accompanied by morphological changes visible in the electron microscope, and possibly by functional changes as well. (Fig. 3).

Since all blood cells apparently originate from the same pluripotent stem cell, one would expect variations in one line to be reflected in other lines. A reciprocal relationship between red cell and platelet counts is indeed found under certain conditions, especially some types of anemia. We are attempting to discover what changes occur in megakaryocytes in response to certain types of fluctuations in the erythroid (red cell) line. It has been shown that during hypoxia, which causes a large increase in red cells, platelet counts first increase and then decrease to below normal. The mechanisms by which these changes are mediated are not known. We hope that an analysis of megakaryocyte size, ploidy, maturation rate, and fine structure will give some clues as to how platelet size and number are related to megakaryocyte size and ploidy and whether subcellular morphological differences accompany size variations.

Two other naturally occurring systems that should also provide insights into the relationship between the erythroid and megakaryocyte platelet lines are mice of the genotypes S1/S1^{d} and W/W^{v}. These mice have a hereditary macrocytic anemia. The number of circulating platelets in both mutants are normal, but bone marrow megakaryocytes are reduced in number. Mature megakaryocytes in W/W^{v} mice are about 20% larger than those of normal littermates, and in S1/S1^{d} mice they are increased about 75% in size. Average platelet size in S1/S1^{d} mice, however, is smaller than normal.

In collaboration with S. Ebbe, we are studying

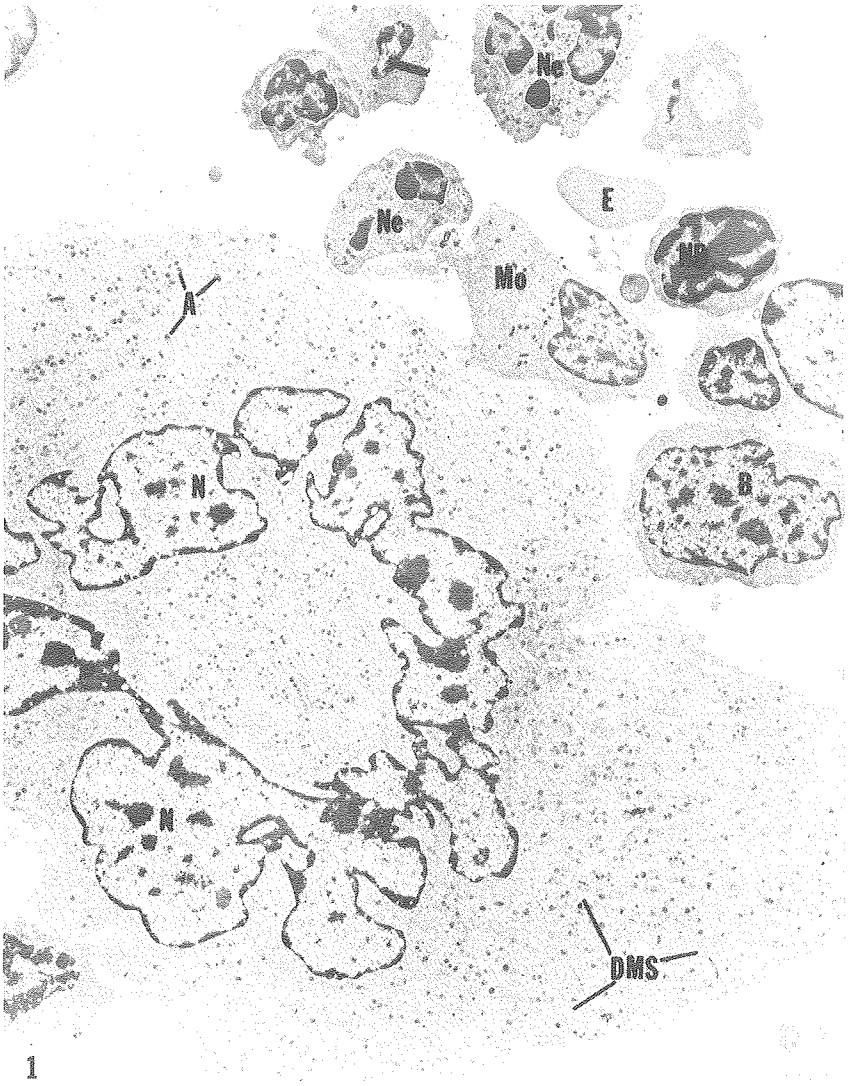

Figure 1. Nearly mature megakaryocyte from normal littermate of an S1/S1^d mouse. The nuclear lobes (N) form a ring near center of cell. The entire cytoplasm is divided into "platelet fields" by the demarcation membrane system (DMS). Alpha granules (A) are distributed uniformly throughout platelet fields. Compare size of megakaryocyte with other typical bone marrow cells at upper right; shown are two mature neutrophils (Ne), an early monocyte (Mo), red cell precursors (NB), mature erythrocyte (E), and undifferentiated blast cell (B). Magnification: 2800×. *XBB 809-10958*

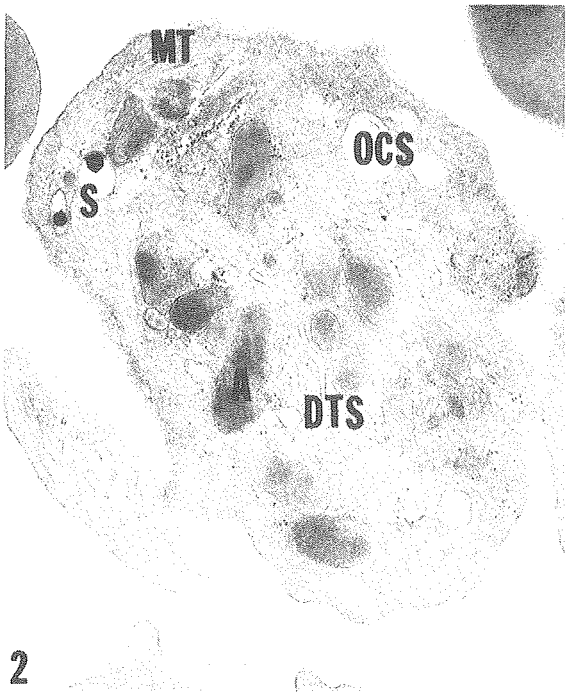

Figure 2. Oblique section through platelet of normal rat. The most conspicuous organelles are pleomorphic alpha granules (A), which contain a heparin-neutralizing factor, at least one growth factor, β-thromboglobulin, and probably fibrinogen; two serotonin-containing granules (S) are also present. Near center of cell are membranes of the dense tubular system (DTS), where prostaglandin synthesis occurs during platelet activation; more peripherally are vacuoles of the open canalicular system (OCS), through which granule contents are discharged when platelets aggregate. Part of the peripheral bundle of microtubules (MT), which maintains cell shape, is at upper left. Magnification: 10,250×. *XBB 809-10959*

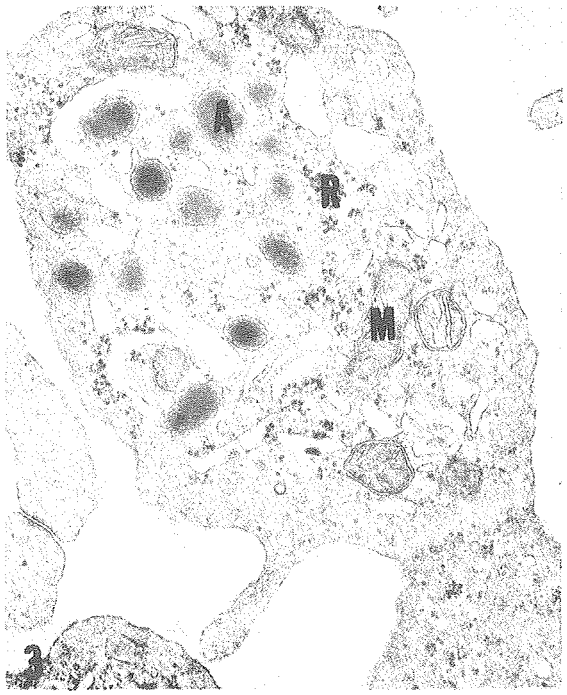

Figure 3. Platelet from a thrombocytopenic rat. Although approximately same size as platelet in Fig. 2, it appears more irregular, and the microtubule bundle does not seem to be organized. Alpha granules (A) are generally smaller, and the numerous ribosomes (R) suggest a newly formed platelet. M, mitochondrion. Magnification: 10,250×.
XBB 809-10960

the fine structure of megakaryocytes and platelets in these two mutants. Megakaryocytes of both S1/S1^d mice and their normal littermates have ultrastructural characteristics similar to those of "stimulated" megakaryocytes of rats, i.e., those produced in response to thrombocytopenia. Morphological differences between mutants and normals are minimal, although megakaryocytes from the anemic mice appear to show more variability in number and distribution of organelles and possibly more asynchrony in maturation in various parts of the voluminous cytoplasm. Morphometric analysis will be necessary to validate subjective impressions.

We are also beginning to investigate the growth of megakaryocytes *in vitro*. Clonogenic assays of red blood cell precursors, including megakaryocytes, are beginning to be used in the study of hematologic disorders. However, the assay for megakaryocyte precursors is one of the most recently developed, and little is known about the differentiation of these cells outside the living animal. We are culturing megakaryocytes in soft agar and following their maturation by electron microscopy and cytochemistry to determine how maturation *in vitro* compares with this process in the intact animal.

PHYSIOLOGICAL STUDIES USING AN ERYTHROPOIETIN RADIOIMMUNOASSAY

Joseph F. Garcia

Blood is one of the most critical tissues in the body. Red blood cells are its major cellular constituent. Blood loss causes the bone marrow to respond by increasing its production of red blood cells. It is now generally accepted that the mechanism controlling this response is a humoral one mediated by the hormone erythropoietin (Ep). The ability to accurately measure the concentration of this important hormone in circulating blood should add significantly to our understanding of the nature of its control over the production of red blood cells.

Using pure human Ep (kindly supplied by E. Goldwasser of the University of Chicago) as the labeled reactant, we have developed a radioimmunoassay (RIA) specific for Ep capable of measuring not only normal plasma and serum concentrations, but also the depressed levels seen in rats and mice following physiological conditions known to depress erythropoiesis (fasting, hypertransfusion, hyperoxia, or hypophysectomy, removal of the pituitary). Also, the RIA shows increased circulating levels of Ep associated with stimuli known to increase erythropoiesis, such as bleeding, hypoxia and cobalt administration. Such consistency in observations correlating appropriate increases and decreases with physiological states plays a significant role in validating the Ep RIA. Correlations with the *in vivo* polycythemic mouse bioassay (Fig. 1) and the *in vitro* fetal mouse liver cell bioassay, as well as parallel dilution curves of serum Ep concentrations with the accepted Ep standard, also support the validity of the Ep RIA. Such a study is shown in Fig. 2, where dilutions of various rat sera are parallel to the respective part of the Ep standard curve, indicating that, in addition to normal rat serum, even the small amount measured in hypophysectomized and fasted rat sera is consistent with the standard Ep. Such studies, although not proof, support identity between the standard hormone and the immunoreactive material present in serum. This is a necessary requirement for a valid RIA.

Preliminary studies have been made using the Ep RIA on tissue homogenates. Rat tissue homogenates were prepared from liver, spleen, kidney, lung, heart, brain, and salivary gland and assayed with the Ep RIA. Surprisingly, although the kidney is generally considered the source for Ep, the tissue with the highest concentration of radioimmunoassayable Ep was the salivary gland. Exposure of rats to hypoxic environment equivalent to 22,000 feet for 24 hours resulted in an increase in kidney concentration by a factor of 10 with no change in the salivary gland concentration. The material in both the kidney and salivary gland showed a parallel dilution curve with the second International Reference Preparation (IRP) of Ep. A time-hypoxic exposure study was initiated in adult male rats in order to make observations on the earliest possible Ep changes. Because of the results for the salivary gland, it was assayed along with the kidney and the serum in this

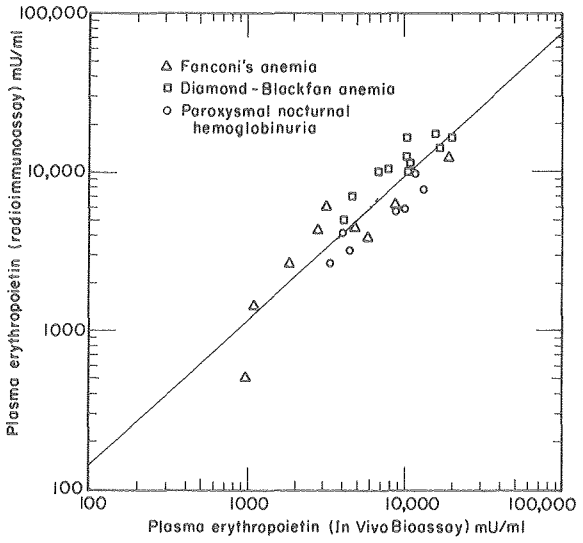

Figure 1. Correlation of the erythropoietin radioimmunoassay with results obtained from in vivo polycythemic mouse bioassay on plasma from three anemic patients. XBL 804-3255

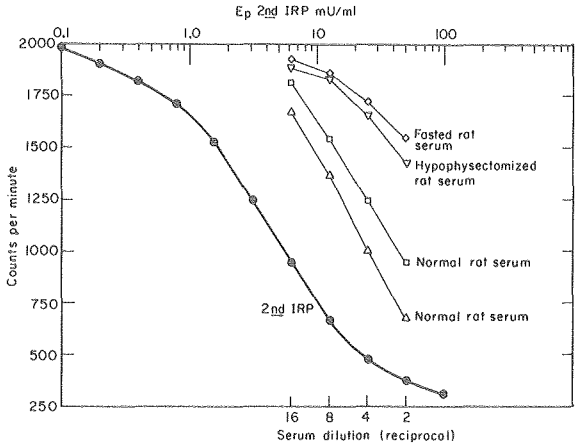

Figure 2. Comparison of the effect of various rat serum dilutions with standard erythropoietin in the radioimmunoassay. XBL 808-3619

Table 1. Hypoxic-exposure study in adult male rats.

Time exposed to	Erythropoietin levels, determined by RIA		
	Serum	Kidney	Salivary
6% oxygen	mU/ml	mU/gm	mU/gm
0 min*	21.3	20.4	1863
5 min	22.9	19.2	1367
10 min	22.5	18.3	1553
15 min	21.4	23.4	1807
30 min	21.1	23.9	1533
45 min	19.1	25.5	1482
60 min	21.1	45.9	1761
120 min	64.8	199.4	1413

**Control*

study. The results are presented in Table 1 and indicate the magnitude of the level seen in the salivary gland.

Although very high RIA values are observed in the salivary gland homogenate, they do not appear to change with hypoxic exposure. The first indication of an increase in serum Ep concentration occurs after 120 minutes at 6% O_2. Interestingly, the kidney concentration is already significantly increased after 60 minutes of exposure. In another study, exposure of rats to hypoxia equivalent to 22,000 feet for periods of up to seven days indicated a peak in serum Ep concentration of 2196 mU/ml at 12 hours. The kidney reached its peak value of 1367 mU/gm at six hours, while the salivary gland concentration remained essentially unaltered. The fact that the kidney concentration increases before any increase is seen in the serum supports the kidney as the source of Ep and undercuts the erythrogenin hypothesis. The nature of the material in the salivary gland will be further investigated, but it has been reported that Ep is reduced following salivary gland removal.

Other studies in rats show a peak at six hours in serum Ep concentration following the injection of cobalt. Irradiation studies in mice with 700 R (total body) show peak levels of serum Ep between five and seven days after irradiation.

Because of the insensitivity of previous Ep assay systems, physiologists have had to resort, in many cases, to extensive manipulation of animal preparations to observe the basic phenomena dealing with the secretion of Ep. With the greater sensitivity of the Ep RIA and the small amount of material required, many of these phenomena are now open to direct assessment. The Ep RIA will play a major role in verifying and extending our knowledge concerning the physiology of this hormone.

REMOVAL OF ^{238}Pu(IV) FROM MICE BY TETRAMERIC CATECHOYLAMIDES: INITIAL RESULTS FOR 3,4,3-LICAMC

Patricia W. Durbin, E. Sarah Jones, Nylan Jeung, Frederick L. Weitl* and Kenneth N. Raymond*

Our research is directed at finding chelating (sequestering) agents specific for toxic ions—compounds that will safely remove poisonous metal ions from the body. Some highly promising compounds for the sequestering of plutonium—derivatives of a naturally occurring iron-chelating agent—are reported.

The structure of enterobactin (EB), an efficient FE(III)-chelating agent elaborated by enteric bacteria (e.g., *E. coli*), and the chemical and biological similarities of Fe(III) and Pu(IV) suggested that tetrameric ligands containing the EB functional group (catechoyl, 2,3,-dihydroxybenzoic acid) would form stable Pu(IV) chelates at pH 7, but would not react with essential divalent metals.[1] That hypothesis is being applied to develop efficient agents for actinide removal therapy. Tests of acute toxicity of the test ligands and excretion of Pu(IV) in mice guided the design of tetrameric catechoylamide (CAM) ligands in a stepwise manner, from 3,3,3,3-CYCAM, a cyclic, uncharged EB analogue that formed a Pu(IV) complex that could not be excreted, to 3,4,3-LI-

*Materials and Molecular Research Division.

CAMS a linear (LI), sulfonated (S), anionic ligand capable of forming a charge cavity suitable for Pu(IV).[2,3] The two most effective compounds, 3,4,3-LICAMS and 4,4,4-LICAMS, promoted more than 60% excretion of ^{238}Pu(IV), as much as an equimolar amount of $CaNa_3$ diethylenetriamine pentaacetic acid ($CaNa_3$DTPA), the broad-spectrum chelating agent used most often for actinide therapy. In addition, both CAM ligands removed more of the Pu present in the skeleton at 1 hour than did $CaNa_3$DTPA.

A sample of 3,4,3-LICAMS was sent to the Radiobiology Laboratory at the University of Utah for testing in dogs.[4] Six beagles were injected intravenously with a mixture of ^{237,239}Pu(IV), and 30 minutes later pairs of dogs received (i.v.) 30 μmole/kg of 3,4,3-LICAMS or $CaNa_3$DTPA, or an equimolar amount of both ligands. At 7 days the whole-body retentions of ^{237}Pu in percent of injected dose were as follows: 3,4,3-LICAMS, 13.7%; $CaNa_3$DTPA, 20.1%; 3,4,3-LICAMS + $CaNa_3$DTPA, 11.6%; controls, 87.3%.

No acute deaths occurred in mice after five daily injections of 30 μmole/kg/injection of 3,4,3-LICAMS, but there was weight loss and focal emaciation in liver and kidneys. Renal toxicity was seen in two of the four dogs given 3,4,3-LICAMS, but there is no information on the permanence of the injuries.

The toxic side effects of 3,4,3-LICAMS at the test dosage of 30 μmole/kg led us to prepare dosage-effectiveness curves in mice for 3,4,3-LICAMS, 4,4,4-LICAMS, and $CaNa_3$DTPA.[5] It is apparent from Fig. 1 that as little as 0.4 μmole/kg, possibly a non-toxic amount, of the structurally similar LICAMS ligands promoted up to 50% excretion of *newly injected* Pu(IV), but a low dosage, 3 μmole/kg/day, of 3,4,3-LICAMS did not enhance excretion of *deposited* Pu(IV). The structure of the CAM ligands needed modification to make them less toxic, so that an effective dosage level could be administered for prolonged therapy.

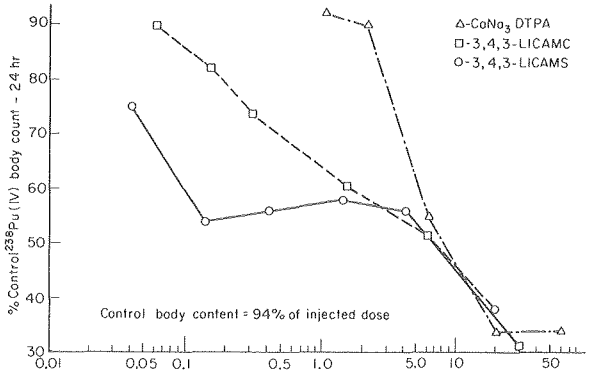

Figure 1. Effectiveness in adult mouse of a single intraperitoneal injection of test ligand in promoting excretion of ^{238}Pu. Test ligands were injected at 1 hour and excreta collected and body contents measured at 24 hours after intravenous injection of ^{238}Pu(IV) citrate. XBL 8010-3772

TEREPHTHALIC ACID LIGANDS (CAMC)

Dihydroxybenzoic acid (DHBA) is a low toxicity monomer; given orally or parenterally, it enhances excretion of iron from chronically transfused animals.[6] Those observations suggested that CAM ligands containing carboxyl ($-CO_2H$) groups might be as effective for Pu(IV) binding as the sulfonated analogues, and less toxic. Several CAMC ligands (Figs. 2,3) have been designed and synthesized.[7] The functional group of these derivatives of terephthalic acid is p-substituted 2,3-dihydroxybenzoic acid, and in our abbreviated nomenclature they are designated CAMC compounds. They are otherwise identical to the prototype CAM ligands,[2] and the DHBA units are connected by amide linkages to linear or cyclic alkaline backbones.

The terephthalic acid (CAMC) compounds are expected to be less selective for the actinides and less hydrophilic than their sulfonated analogues and therefore to be less rapidly excreted and to have a lower tendency to penetrate cells. The $-CO_2H$ group of the LICAMC molecules is ortho to one $-OH$ group, and an additional, and perhaps biologically advantageous, mode of chelation (salicyl) is available.

Several synthetic macromolecular CAMC ligands have been tested for their ability to promote Pu(IV) excretion in mice, and the results of the 24-hour Pu(IV) excretion tests are collected in Table 1. Overall, the CAMC ligands promoted more Pu(IV) excretion than their sulfonated analogues. The linear tetramer, 3,4,3-LICAMC, elicited prompt excretion of 70% of newly injected Pu(IV). The effectiveness of the cyclic ligand, 3,3,3,3-CYCAMC, was much greater than its sulfonated analogue. The trimer, 3,4-LICAMC, which cannot fully coordinate with Pu(IV), still was capable of promoting about 50% excretion of Pu(IV). A sample of 3,4,3-LICAMC was sent to the University of Utah, and the experimental conditions were the same as for the test of 3,4,3-LICAMS.[4] In two dogs, retention of Pu(IV) at 7 days was 11.8%, somewhat less than after treatment with the sulfonated analogue (C.W. Mays *et al.*, unpublished).

There is a major qualitative difference in the biological actions of the carboxylated and sulfon-

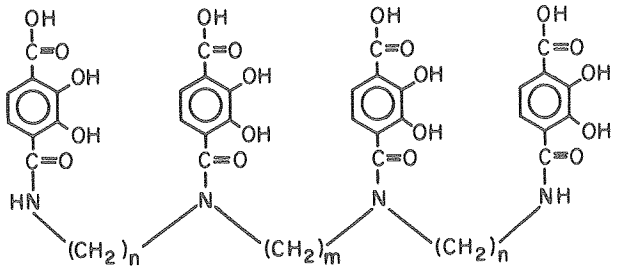

3,4,3-LICAMC

Abbreviation	m,n	Molecular formula	Weight	IUPAC name
3,4,3-LICAMC	3,4	$C_{42}H_{42}N_4O_{20}\cdot 3H_2O$	980	N^1,N^5,N^{10},N^{14}-tetra(2,3-dihydroxy-4-carboxybenzoyl)-tetraazatetradecane

Figure 2. Structure and formula of 3,4,3-LICAMC. *XBL 8012-13615*

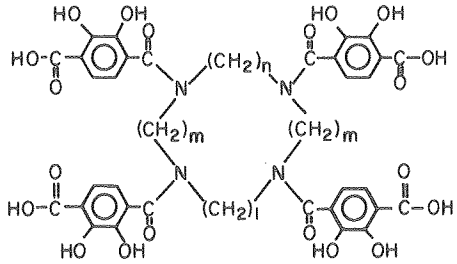

3,3,3,3-CYCAMC

Abbreviation	l,m,n	Molecular formula	Weight	IUPAC name
3,3,3,3-CYCAMC	3,3,3	$C_{44}H_{44}N_4O_{20}\cdot 2.5H_2O$	994	N^1,N^5,N^9,N^{13}-tetra(2,3-dihydroxy-4-carboxybenzoyl)-tetraazacyclohexadecane

Figure 3. Structure and formula of 3,3,3,3-CYCAMC. *XBL 8012-13616*

Table 1. Retention of $^{238}Pu(IV)$ in tissues of mice treated with various chelating agents. Results are expressed as percent of injected dose ± S.D. normalized to 100% recovery.*

Tissue	Control (N = 34)+	$CaNa_3DTPA$ (N = 5)	3,4,3-LICAMS (N = 5)	3,4,3-LICAMC (N = 10)	poly-LICAMC (N = 4)
Liver	51 ± 7.0	17.7 ± 4.4	23.8 ± 7.9	8.7 ± 3.0	29.5 ± 10.7
Skeleton	31 ± 6.3	10 ± 1.4	6.6 ± 1.0	9.7 ± 2.0	10.0 ± 1.0
Soft tissues	5.1 ± 0.8	3.3 ± 1.4	1.9 ± 0.4	2.7 ± 0.9	9.1 ± 1.8
GI (full)	4.6 ± 1.1	5.2 —	2.5 —	8.0 —	11.5 —
Kidneys	2.6 ± 2.6	0.5 —	1.3 —	2.0 —	2.5 —
Excreta	6.1 ± 2.0‡	63.0§ —	64.1 —	69.0‖ —	37.1** —

**Ligands (30 μmole/kg) were injected (i.p.) 1 hour and mice sacrificed 24 hours after $^{238}Pu(IV)$ citrate (i.v.). Methods were described previously.[2]*

+N = number of mice.

‡Mean ± S.D. for 7 groups of 5 mice. For 10 of those mice urine, 1.0%; feces, 1.9%.

§Urine, 59%; feces 4%.[8]

‖For 5 mice urine, 50.2%; feces, 14.1%.

***Urine, 30.5%; feces 7.0%.*

ated CAM ligands. No CAMS ligand appeared to be capable of removing Pu from the liver or improving biliary excretion of Pu. In marked contrast, 3,4,3-LICAMC appears to be capable of accelerating elimination of Pu(IV) from the mouse liver, via biliary excretion, to a greater degree than an equimolar amount of $CaNa_3DTPA$. (Compare the amounts of Pu in liver, gastrointestinal (GI) tract, and feces for DTPA and the two CAM ligands shown in Table 1.)

The dosage-effectiveness curve for 3,4,3-LICAMC is compared to the curves for 3,4,3-LICAMS and $CaNa_3DTPA$ in Fig. 1. The stoichiometry of the Pu(IV)-LICAMC complex is believed to be 1:1, although the curve for 3,4,3-LICAMC lies close to the 3,4,3-LICAMS curve, and 3,4,3-LICAMC is more concentration-dependent, in agreement with the expectation that some 3,4,3-LICMAC may be lost to competition with other metals.

Three replications of a delayed test of ligand effectiveness were conducted in mice: a single intraperitoneal (i.p.) injection of 3,4,3-LICAMC was given 24 hours after the injection of $^{238}Pu(IV)$, and the mice were killed 24 hours later (48 hours after the ^{238}Pu). On the average, a 20% increase in urinary Pu excretion and a 200% increase in fecal Pu excretion occurred, indicating that a prolonged course of administration of 3,4,3-LICAMC at that daily dosage may be effective in promoting excretion of Pu recirculated from tissue deposits.

Two preliminary tests have been made of the toxicity of 3,4,3-LICAMC: (1) A five-day acute toxicity test was extended to 20 injections of 30 μmole/kg/injection in 28 days. The treated mice gained weight at the same rate as controls, and no tissue changes were visible at autopsy. (2) The test of efficiency for Pu removal in dogs at the University of Utah was accompanied by clinical tests of renal function, a gross autopsy, and preparation of sections for histology. The clinical tests yielded normal values, and there were no visible gross tissue lesions at autopsy. (Visible lesions were found in the dogs given 3,4,3-LICAMS.)

The CAMC ligands appear to have achieved both major design goals—they are more effective for *in vivo* complexation and promotion of Pu(IV) excretion as the sulfonated analogues, and they are significantly less toxic.

POLYMERIC LICAMC

Starting materials and synthetic methods were available with which to prepare large polymers containing many DHBA functional groups, and a polymer containing 14 CAMC units linked by ethylene bridges was prepared (F.L. Weitl, unpublished). The molecular weight of poly-LICAMC is 3000, and the tetrameric structure is repeated 3.5 times (see Fig. 2). Results of the 24-hour Pu(IV) excretion test in mice are shown in Table 1. Total 24-hour Pu excretion was less after the polymeric ligand than after treatment of mice with the smaller 3,4,3-LICAMC molecule. However, poly-LICAMC prevented deposition of Pu(IV) in the skeleton to the same degree as equimolar amounts (of the functional groups) of either 3,4,3-LICAMC or $CaNa_3DTPA$. The large amount of Pu that was still present in soft tissues suggests excretion will be delayed; and the large amounts of Pu and feces and the GI tract at 24 hours suggest that liver clearance via biliary excretion will be accelerated.

Poly-LICAMC must still be tested for toxicity. It is expected to be a broad spectrum agent, and may be less selective for Pu(IV) than the tetrameric compounds. We also need to follow Pu excretion for several days in mice given a single injection of poly-LICAMC to investigate excretory delay. Studies with suitable stable metal-chelates of poly-LICAMC are also needed to determine the completeness of excretion of this large molecule.

REFERENCES

1. Raymond, K.N., Smith, W.L., Weitl, F.L., Durbin, P.W., Jones, E.S., Abu-Dari, K., Sofen, S.R., and Cooper, S.R., 1980. Specific sequestering agents for the actinides. In: *Lanthanide and Actinide Chemistry and Spectroscopy,* N.M. Edelstein, ed., pp. 143–172. Proc. of a Symposium, Washington, D.C., Sept. 1979. ACS Symposium Series 131, Am. Chem. Soc., Washington, D.C.
2. Durbin, P.W., Jones, E.S., Raymond, K.N., and Weitl, F.L., 1980. Specific sequestering agent for the actinides. 4. Removal of ^{238}Pu (IV) from mice by sulfonated tetraminic catechoyl amides. *Radiat. Res. 81,* 170–187.
3. Durbin, P.W., Jones, E.S., Weitl, F.L., and Raymond, K.M., 1980. Removal of $^{238}Pu(IV)$ from mice by sulfonated tetrameric catechoyl amides. Biology and Medicine Division, Lawrence Berkeley Laboratory, Annual Report 1978–1979, pp. 37–39. LBL-10022.
4. Lloyd, R.D., Bruenger, F.W., Atherton, D.R., Jones, C.W., Weitl, F.L., Durbin, P.W., Raymond, K.N., Taylor, G.N., Stevens, W., and Mays, C.W. 1979. Decorporation of Pu or Am in beagles by 3,4,3-LICAMS, pp. 151–160. In: *Research in Radiobiology, Annual Report, Radiobiology Divi-*

sion, Department of Pharmacology, University of Utah, C00–119–254.
5. Durbin, P.W., Jones, E.S., Weitl, F.W., and Raymond, K.N. 1980. Dosage-effect relationships for $^{238}Pu(IV)$ removal from mice by sulfonated tetrameric catechoyl amides (3,4,3-LICAMS and 4,4,4-LICAMS), Diethylene-triaminepenta-acetic acid (DTPA) and o-dihydroxy-1,5–benezenedisulfonic acid (Tiron). *Radiat. Res.* 83:434. Abstract.
6. Grady, R.W., Graziano, J.H., Akers, H.A., and Cerami, A., 1976. The development of new iron-chelating drugs. *J. Pharmacol. Exptl. Therap.* 196:478–485.
7. Weitl, F.L., Raymond, K.N., and Durbin, P.W. In press. Synthetic enterobactin analogues. Carboxyamido-2,3-Dihydroxyterephthalate conjugates of spermine and spermidine. *J. Med. Chem.*
8. Schubert, J., Fried, J., Rosenthal, M.W., and Lindenbaum, A., 1961. Tissue distributing of monomeric and polymeric plutonium as modified by a chelating agent. *Radiat. Res.* 15:220–226.

DEVELOPMENT OF A RESEARCH AND INFORMATION CENTER FOR THE ANALYSIS AND INTERPRETATION OF DATA FROM SHORT-TERM TESTS FOR CARCINOGENS AND MUTAGENS

Joyce McCann, Linda Hayashi, Laura Horn, Holly Hurd, John Kaldor, Praveena Lal, Gerry Litton,* Philip Presentation, and Vicki Santiago*

In the last 5 to 10 years increasing awareness of the importance of environmental factors in cancer causation (and possibly heritable effects) has led to a greater emphasis on prevention and on attempts to minimize human exposure to hazardous chemicals. With this new focus on prevention, methods for identifying potentially hazardous chemicals have assumed a key role. The traditional long-term animal cancer tests are costly (now almost $300,000 for each chemical) and time-consuming (about three years). Tests for heritable germline mutations in animals take somewhat less time (under two years), but can require very large numbers of animals (up to 50,000), and may detect only a small proportion of potential human mutagens.

A number of varied and imaginative "short-term" testing methods for detecting potential chemical carcinogens and mutagens have, in the past several years, emerged from the diverse fields of cancer biochemistry, nucleic acid research, genetics, and molecular and cell biology. In a recent review[1] we identified over 100 assays that use a variety of cell types *in vitro,* from bacteria and phage to human cells, as well as assays that can be done directly in animals or people. With these methods a test can take from as little as a few hours to as much as a few weeks, and the cost ranges from a few hundred to a few thousand dollars. An enormous number of chemicals have already been tested using these methods. In the most widely used of these assays, the *Salmonella* (Ames) test (Figs. 1 and 2), results on over 2,600 chemicals have been published, and hundreds of additional chemicals have been tested in industrial or commercial testing laboratories.†

New mutagens are being found by short-term tests at an ever increasing rate. Since animal cancer tests cannot be conducted at such a rapid pace, society will be faced with an expanding list of chemicals identified as potential carcinogens by short-term tests that have not been tested in animal cancer tests. It will therefore be essential to determine the degree of relevance of short-term test results to human cancer and genetic risk. We are approaching this general problem from the point of view that assessing the relative value of these diverse methodologies will best proceed from a quantitative analysis of the data. We are, therefore, establishing an analyzed data base of results from about 25 major short-term tests. As part of this effort we are: (1) developing statistical methods (in collaboration with M. Pike at the University of Southern California) for the analysis of data from the major short-term assays and (2) establishing a "potency index" for expressing results of short-term tests. The potency index will serve as a standard basis for comparison be-

*Computer Applications, Engineering and Technical Services Division.

†Short-term tests are also being incorporated into the package of required or recommended toxicological tests for chemicals regulated by all of the major regulatory agencies. They have recently been proposed as part of regulatory decision-making policy by the Occupational Safety and Health Administration (OSHA) for classification of chemical carcinogens in the workplace, by the FDA for the regulation of new animal drugs, and by the Environmental Protection Agency for regulating pesticides, the disposal of toxic wastes, and air pollutants.[3]

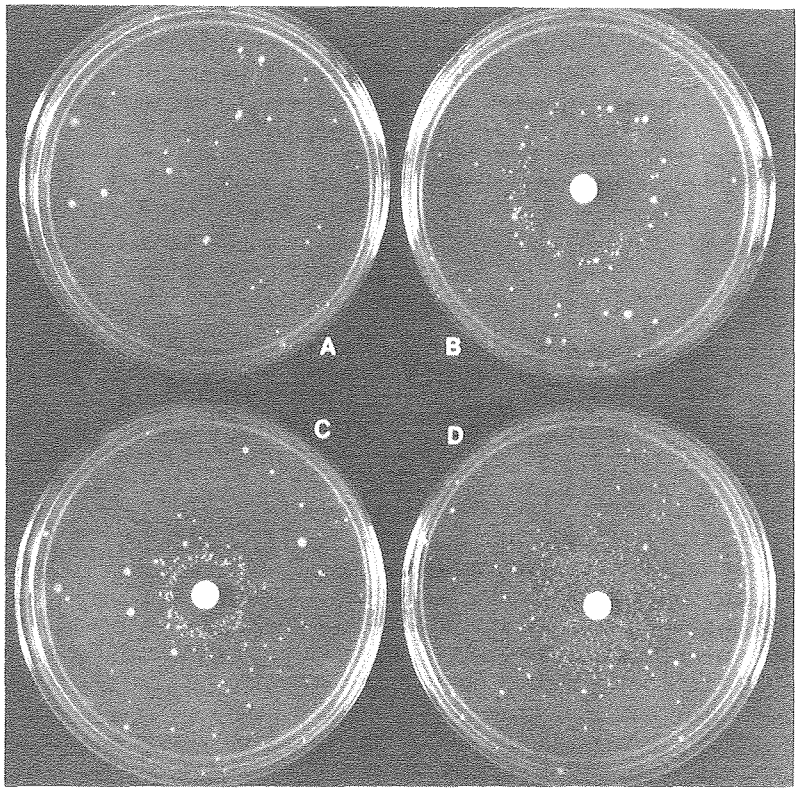

Figure 1. The Salmonella (Ames) test. Several specially constructed strains of bacteria are used, in combination with homogenates from rat (or human) tissue, to detect reverse mutations induced by chemical carcinogens and mutagens. A small amount (usually a few micrograms) of test chemical, a bacterial tester strain (about 10^8 bacteria), and the tissue homogenate (usually liver) are added in top agar to the surface of a Petri dish (2 ml), and revertant colonies are counted after incubation at 37°C for 2 days. Shown is the "spot test," in which the test chemical diffuses outward from a small paper disk (results from earlier work[2]): (A) a control plate; (B) AF-2, a food additive formerly used in Japan; (C) aflatoxin B1, a fungal toxin, and (D) 2-aminofluorene. Courtesy N.Y. Academy of Sciences.[2] *XBB 800-11504*

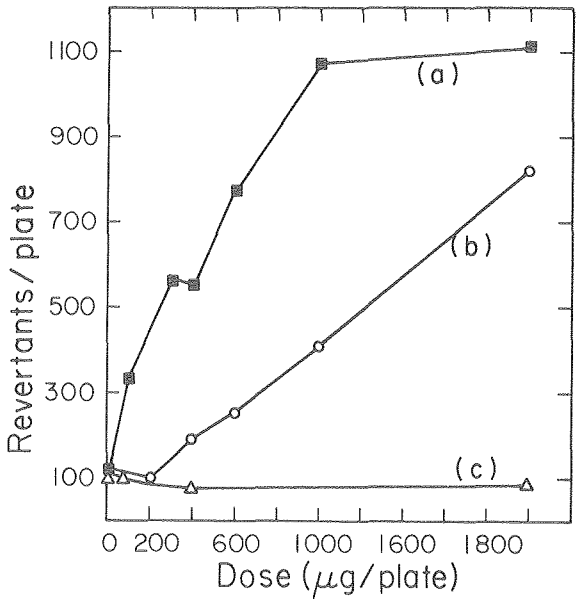

Figure 2. The "standard plate test" of the Salmonella (Ames) assay, in which dose-response curves are generated by incorporating different doses of the test chemical into the entire agar overlay. Shown are recent results (unpublished) for several hydrazine carcinogens: (a) hydralazine, an anti-hypertensive drug; (b) Phenylethylhydrazine, an anti-depressant, and (c) succinic acid-2, 2-dimethylhydrazide, a plant growth retardant. Results shown are for tester strain TA100 in the presence of S-9 Mix from Aroclor-induced rats. Phenylethylhydrazine and hydralazine were also positive in the absence of S-9 Mix. Results shown are the average of two replicate plates. *XBL 809-1924A*

tween (a) results of the same test on different chemicals; (b) results of different tests on a specific chemical; and (c) short-term test results and animal cancer test results.

(a) *Results of same test on different chemicals.* The range of mutagenic potencies among different chemicals in some short-term tests is enormous—well over a million-fold (Table 1). The degree to which this wide potency range is relevant to human risk is one of the most important questions in environmental mutagenesis today (see (c), below). In our laboratory we are extending these results to about 100 carcinogens that have adequate animal cancer test data but that have not previously been tested in the *Salmonella* (Ames) assay (see Ref. 6 for a discussion of the current state of carcinogen testing in the *Salmonella* assay). Some results are shown in Fig. 2. We are including in our data base a potency analysis of these results. We are also calculating potencies from all quantitative results on carcinogens in the published literature for the major short-term tests, including the *Salmonella* (Ames) assay, the major mammalian cell mutagenesis assays, *in vitro* transformation tests, sister chromatid exchange assays, and others.

(b) *Results of different tests on specific chemicals.* An important conclusion from the validation work on short-term tests (reviewed in Ref. 1) is that short-term tests are most effectively used in groups, or batteries. Not only do positive results in different assays reinforce one another, but some short-term tests in a battery may detect classes of chemicals missed by others. See, for example, Fig. 3 which illustrates, for six carcinogens, the consistency and complementarity of short-term test results. Benzo(a)pyrene, aflatoxin B1, and methylmethanesulfonate are positive in the *Salmonella* (Ames) assay, and these results are reinforced by positive results in a wide range of other short-term tests. The remaining three, urethane, DDE (a metabolite of DDT), and natulan are negative in the *Salmonella* (Ames) assay, and may be somewhat less efficiently detected by short-term tests generally. However, the negative results in *Salmonella* are complemented by at least one clearly positive result in another short-term test. The design of test batteries that optimizes both the reinforcing and the complementary aspects of short-term tests has become a primary concern, especially of regulatory agencies that must define general testing guidelines.[3] We are working with EPA's Gene-Tox program, and will use our quantitative data base to aid in the effective and economical design of test batteries.

(c) *Short-term test results and animal cancer test results.* In collaboration with B.N. Ames's group‡ in the Biochemistry Department of UC Berkeley, we are exploring possible quantitative relationships (both positive and negative) between results in short-term tests and animal cancer tests. In some exploratory work, Meselson and Russell[7] calculated carcinogenic potencies for 14 carcinogens and compared these values to results in the *Salmonella* test.[4,8] They found a striking correlation (Fig. 4), although some results (e.g., some nitrosamines) did not correlate well.

Understanding the significance of potency in short-term tests (and for that matter animal cancer tests) is not a simple problem. Many variables in each short-term test can affect the potency of the results (e.g., for the *Salmonella* test, variations in metabolic activation conditions, choice of tester strains, or protocol modifications such as liquid or plate incubations). Using Ames's carcinogenic potency data base as a starting point, we are developing a list of carcinogens that have very different carcinogenic potencies in different species or strains of test animals. We will then compare the mutagenic potencies of chemicals on this list with the potencies

‡The Ames group (in collaboration with R. Peto at Oxford, England and M. Pike at USC on the theoretical aspects) has developed a method for calculating the carcinogenic potencies of chemicals from animal cancer test results. The group has applied the analysis to the world's cancer literature and has created a large computerized data base.

Table 1. Range of mutagenic potencies of carcinogens in the Salmonella (Ames) assay.

Carcinogen	Revertants/nmole	Ratio
1,2-Epoxybutane	0.006	1
Benzyl chloride	0.02	3
Methyl methanesulfonate	0.63	105
2-Naphthylamine	8.5	1,400
2-Acetylaminofluorene	108	18,000
Aflatoxin B_1	7,057	1,200,000
Furylfuramide (AF-2)	20,800	3,500,000

Results are from previous work.[4,5] Potencies (revertants/nmole) were calculated from the linear region of dose-response curves.

	a	b	c	d	e	f	g	h		i	j	k	l	m	n	o	p	q	r	s	t	u	v	w
	AMES	POL A	YEAST	TK	CHO	V79	UDS HUM FIB	UDS RAT	UDS OTHER	ALK ELUT	TRANS BHK	TRANS 10T½	TRANS 3T3	TRANS HE	VIR ENHANC	DROSOPHILA	SPERM AB	DOM LETHAL	MOUSE SPOT	SCE IN VIT	SCE IN VIVO	CHR AB IN VIT	CHR AB IN VIV	MICRONUC
B(A)P	+	[(+	-	+	[+	+	-*	[+	(+	+	[+	+	+	+	[+	(+	+	?	+	+	+	(+	+	-
AFLA B1	+		[+		[+	+	+	[+	+	[+	[+		+	+	(+	[+	-	?		+	[+	[+	[+	+
MMS	+	[+	+	+	+		+	[(+	+	+				+	[+	+	+	+	+	+	+	[+	[+	+
URETHANE	-	-	-						(+		[+	-*		[+	-		-	-		(+		[+	[+	+
DDE	-	-	-*	+		+											-	-				+		
NATULAN	-	[(+	+	+					-			-	-*	[+		[+	[+	[+			+	-	+	+

*Figure 3. Comparison of short-term results in the published literature for six carcinogens: Benzo[a]pyrene, B(A)P; aflatoxin BL, AFLA B1; methylmethanesulfonate, MMS; urethane; DDE (a metabolite of DDT); and natulan. The short-term tests are: (a) the Salmonella (Ames) test; (b) the E. coli pol A DNA repair test; (c) tests for recombination and gene conversion in S. cereviseae D3 and D4; mammalian cell mutagenesis tests in (d) mouse lymphoma L5178Y, (e) CHO/HGPRT, and (f) V79 cells; DNA repair tests in mammalian cells, (g) unscheduled DNA synthesis (UDS) in human fibroblasts, (h) UDS in rat liver cells or in other cells; (i) alkaline elution; in vitro transformation assays using (j) BHK, (k) mouse 10T 1/2, and (1) mouse Balb 3T3 cells and miscellaneous cell lines, (m) hamster embryo (HE) cells, and (n) assays for viral enhancement of transformation; (o) the Drosophila sex-linked recessive lethal assay; in vivo tests (p) sperm abnormality, (q) mouse dominant lethal test, (r) mouse spot test; cytogenetic tests (s) sister-chromatid exchange (SCE) assay in vitro, (t) SCE assays in vivo, (u) chromosome aberration tests in vitro, (v) chromosome aberration tests in vivo, and the (w) micronucleus test. NOTE: + = clearly positive; (+ = quantitative results are weak; [+ = quantitative data are not published or not available. * means an external metabolic activation system was not present. Results are from Table 2 in Ref. 1.* XBL 809-3695

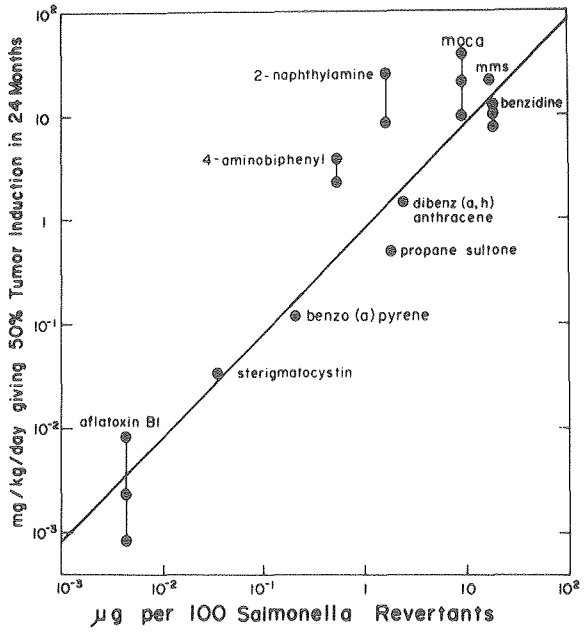

Figure 4. Comparison of the carcinogenic potencies in rodents (Y-axis) with mutagenic potencies in the Salmonella (Ames) assay (X-axis) for 10 chemical carcinogens. Taken from Ref. 7. Copyright 1977 Cold Spring Harbor Laboratory. Reprinted with permission. XBL 8010-12376

measured in the *Salmonella* (Ames) assay for these chemicals, using tissue homogenates from the different species or strains. We are also beginning to develop other lists of carcinogens for which we will develop *in vitro* potency data to compare with potency in the animal cancer tests. For example, we can distill, from Ames's carcinogenic potency data base, a list of all Sprague-Dawley rat liver carcinogens, and then pick pairs of carcinogens from this list that have large differences in potency.

During the first eight months of this project, the primary effort has been to design and implement the data base using the *Salmonella* (Ames) assay as a model system and to set up the new *Salmonella* laboratory.

Design efforts have included the bibliographic and short-term test data components. The design must include permitting flexibility for: (a) ease of input and output; (b) generalized searching of the bibliographic and short-term test data; and (c) ease of adding more short-term tests to the data base.

Progress has been made as follows: (a) The overall data-base system design has been worked out. (b) The bibliographic portion of the data base has been established, complete with data entry and output programs, and bibliographic records have been entered. The *Salmonella* bacterial mutagenesis section of the data base has been designed and implemented. Data entry programs have been written, and data from over 500 experiments have been entered. (c) Work is underway to build a number of searching indexes. The first of these is a Chem-Abstracts Registry number/chemical-name index, which is complete. (d) The development of a summary output program for the *Salmonella* assay is nearing completion. (e) Draft data entry sheets have been designed for mammalian cell mutagenesis assays, *in vitro* transformation assays, and the *Drosophila* sex-linked recessive lethal test.

In the work on statistical packages for short-term data, primary effort has been directed at completing the development of a method for analysis for *Salmonella* (Ames) test data. Most of this work has been done in collaboration with M. Pike. The computer programs for several methods have been written, and these are being coupled to the data base. The methods will be tested on data in our data base from our laboratory and the published literature, and on more detailed data from the NCI's *Salmonella* testing program. We are in the process of obtaining the NCI data on computer tape.

We are also developing a critique of statistical methods currently used for analyzing data from mammalian cell mutagenesis assays. The *Salmonella* (Ames) testing laboratory has begun operation. We are obtaining *Salmonella* test data on carcinogens that have not been tested in the *Salmonella* assay, or that have inadequate test data available.

Almost all equipment has been received; we have set up the *Salmonella* test, prepared standard S-9 Mix, and run a series of standard dose response curves to establish the method in the new laboratory.

For a potency analysis we have developed an initial test list of carcinogens using Ames's carcinogenic potency data-base as a resource. This list includes virtually all carcinogens that have adequate animal cancer test data, but not, as far as an exhaustive literature search could determine, *Salmonella* test data.

We have completed *Salmonella* tests on *hydralazine* (an antihypertensive drug), and *phenylethylhydrazine* (an anti-depressant), which were positive in the standard assay (see Fig. 1B), and on 2,4,5-Trichlorophenoxyacetic acid, trichloroaniline, and succinic acid-2,2-dimethylhydrazide, which were negative in initial tests; trimethylaniline was questionable and is being tested further.

Finally, besides the data base and the testing laboratory, we have recently initiated a short-term project for DOE. This will evaluate existing short-term test data on chemicals and complex mixtures from coal liquefaction processes that may be potential sources of carcinogenic or mutagenic risk.

REFERENCES

1. Hollstein, M., McCann, J., Angelosanto, F.A., and Nichols, W.W. 1979. Short-term tests for carcinogens and mutagens. *Mut. Res.* 65:133–226.
2. McCann, J. and Ames, B.N. 1976. A simple method for detecting environmental carcinogens as mutagens. *Annals of the N.Y. Academy of Sciences* 271:5–13.
3. McCann, J. 1981. Using scientific evidence in public policy: short-term tests and cancer policy. *Adv. in Occup. Hlth.* 1. To be published.
4. McCann, J., Choi, E., Yamasaki, E., and Ames, B.N. 1975. Detection of carcinogens as mutagens in the *Salmonella*/microsome test: Assay of 300 chemicals. *Proc. Nat. Acad. Sci. USA* 72:5135–5139.
5. McCann, J. and Ames, B.N. 1977. The *Salmonella*/microsome mutagenicity test: predictive value for animal carcinogenicity. In *Origins of Human Cancer, Book C,* H. Hiatt, J. Watson, and J. Winsten, eds., pp. 1431–1450. New York: Cold Spring Harbor Laboratory.

6. Ames, B.N. and McCann, J. 1980. Validation of the *Salmonella* test: A reply to Rinkus and Legator. *Can. Res.*, in press.
7. Meselson, M. and Russell, K. 1977. Comparisons of carcinogenic and mutagenic potency. In *Origins* (see Ref. 5), pp. 1473–1481. New York: Cold Spring Harbor Laboratory.
8. McCann, J. and Ames, B.N. 1976. Detection of carcinogens as mutagens in the *Salmonella*/microsome test: Assay of 300 chemicals. *Proc. Nat. Acad. Sci. USA* 73:950–954.

6. RADIATION BIOPHYSICS

The original goal of the Radiation Biophysics Group was to understand the biological effects of ionizing radiations and other selected physical environmental agents at the most fundamental cellular and molecular levels. As the group developed, however, direct pathways from basic biophysics to diagnostic and therapeutic applications in medicine and to environmental science became evident. Consequently, at present we have an interdisciplinary group that extends not only to physicists and cellular biologists but also to a variety of other disciplines, including a group in cancer radiotherapy and radiologic diagnosis.

The Radiation Biophysics Group, led by Dr. Cornelius A. Tobias, is spearheading research on the biomedical applications of accelerated heavy-ion beams, using three accelerators at Lawrence Berkeley Laboratory: the Bevalac, the 184-inch synchrotron, and the 88-inch cyclotron. The Bevalac is a unique national facility that is a center of heavy-ion research involving both American scientists and international collaboration with several countries. Cancer-related research is financed jointly by the National Cancer Institute and the Department of Energy.

Heavy-ion beams show special promise for the treatment of cancer because of their physical and biological characteristics. First, the depth-dose characteristics of heavy ions allow a more effective dose of radiation to be delivered locally to the tumor rather than the skin and normal tissues that surround the tumor. Second, oxygen-deprived cells in cancerous tissue are more resistant to conventional radiation than normally oxygenated cells. Heavy-ion beams eliminate, to a large extent, this oxygen effect.

Controlled clinical studies are being conducted on select groups of cancer patients using carbon, neon, and argon beams accelerated at the Bevalac. These patients are being compared to patients treated with helium-ion beams at the older 184-inch synchrocyclotron. During the current year, the first high-energy silicon beam was accelerated at the Bevalac. Cellular studies with this beam indicate that silicon may be best suited for clinical radiotherapy trials; however, further studies and comparisons need to be made.

Using helium ions, we have begun treating a special group of patients with choroidal melanoma of the eye. When these tumors are found in a growing phase, the patient's eye must be removed surgically. Particle irradiations in a few patients have had remarkable results, effectively controlling this type of tumor for an extended period of time and enabling the patient to retain normal use of the eye.

Intensive developments in diagnostic uses of heavy accelerated ions are taking place. Some of the first tomograms made with neon beams are shown in this report. Heavy-ion beams have greater sensitivity for detecting abnormal densities in the soft tissues of the body than any other method, and the program is now extending its diagnostic studies to such areas of the body as breast, brain and central nervous system and musculoskeletal and cardiovascular areas, as well as to radiotherapy treatment planning. Both active and passive detector systems are being explored.

The group has some of the nation's experts on the effects of low-level radiation. We are developing a new quantitative model for describing the dose-effect relationships of a number of deleterious agents that usually produce molecular lesions in the genetic material, DNA. Living cells attempt to repair these lesions by enzymatic pathways, and the long-term effect depends on whether or not the repair is successful. Where the repair is not successful, we are studying the manner in which variants, mutants, and transformed tumor cells are produced. We are also engaged in testing the joint effects of a variety of physical and chemical agents in an effort to obtain quantitative data on synergism between these agents and different types of radiation.

The group is also developing an entirely new technique called heavy-ion microscopy. This was invented independently, at about the same time, both in our laboratory and at Gesellschaft für Schwerionenforschung (Society for Heavy Ion Research) in Darmstadt, Germany. We are now engaged in collaborative studies that may lead to important advances in the quantitative microscopy of chromosomes.

The Department of Energy has asked our laboratory to become a center of research on the biomedical effects of magnetic fields. There is need for this research because high and sometimes varying magnetic fields will be increasingly used in future energy generation and storage systems. In the current year, studies on magnetic effects on the electrocardiogram have proven to be of special interest.

Another group in the division has also perfected methods of studying mammalian neurons in tissue

culture. The ultimate objective is to understand how networks of neurons communicate, learn, and remember. Meanwhile, these studies are useful for understanding the nature of toxic effects from environmental agents such as carbon monoxide.

The physics of cell membranes is a rapidly developing field. In our laboratories special methods are available to study the viscoelastic properties of cell membranes. Toxic environmental agents, such as mercury ions in miniscule amounts, can cause irreversible alterations in the properties of these membranes.

The members of the group feel that these recent radiation biophysics developments give a strong mandate for continued development of their fundamental and applied aspects. The highlights of achievements during the past year are presented in the articles that follow.

Bevalac Studies

RADIOLOGICAL PHYSICS AND CHEMISTRY

Aloke Chatterjee and John L. Magee

The passage of an accelerated heavy particle in a biological system (such as a cell in suspension) initiates a sequence of processes that are at first purely physical, then chemical, and finally biological. We are interested in all these processes, and particularly in the role of track structure on the biological effects of heavy particle irradiations. It is clear that the track structure is first of all a physical and a chemical problem. We must verify our concepts of track structure by means of physical and chemical criteria (from theory and experiment) before we can have a track model that we can confidently use to interpret biological experiments. Thus our program for developing a track model begins with physical and chemical considerations only.

Track models start with the pattern of energy deposited by the heavy particle, and this can be calculated from a vast store of theoretical and empirical knowledge on stopping power. From stopping power theory we know that heavy particle tracks should be composed of two qualitatively different parts, which we call "core" and "penumbra." Experimental studies in dosimetry have verified that these concepts are correct and that our estimations of initial energy densities in tracks are valid.

The next phase involves chemical phenomena. A chemical model based on the physical energy deposit is under development, in two stages. The first is a study of dilute aqueous solutions so that we can check the model against the many experimental results available in this field, and the second is a study of concentrated solutions so that we have a model system somewhat closer to the biological systems of interest.

Radiation chemical effects in *dilute* aqueous solutions are all similar. Water is decomposed by the initial energy absorption, and subsequent action results from the water radicals. Biological systems, however, are concentrated solutions, and radiation chemical effects in them involve the characteristic effects of such solutions. Here, not only water but solutes also are affected by the direct action of the radiation, and the water radicals are frequently less important than radicals created in the solutes. The most important chemical studies in this program will involve solutes that are themselves materials of biological interest.

In irradiated biological systems, biological effects are initiated by radiation-induced chemical reactions that at first occur in the same way they would in nonliving systems. Biological response to the radiation chemistry stimulus begins on a somewhat longer time scale than the purely chemical response; but once started, it takes over completely. We are attempting to develop a model for cell survival which uses the radical processes in a more explicit way than has been done before. And in such a model, it is important for the pattern of radical reactions to be accurate. Thus, we place great importance on the chemical model of the heavy particle track, and we plan to use all available experimental data to verify it. At present we are still in the first phase of model development, comparing the experimental results of radiation action on dilute solutions. The Fricke dosimeter is the most widely used standard, so it is natural to use it in these comparisons.

Figure 1 shows model calculations of the G values (the number of molecules produced per 100 electron volts) of the Fricke dosimeter in the solid lines for a representative set of six heavy particles over a wide range of energies; all available experi-

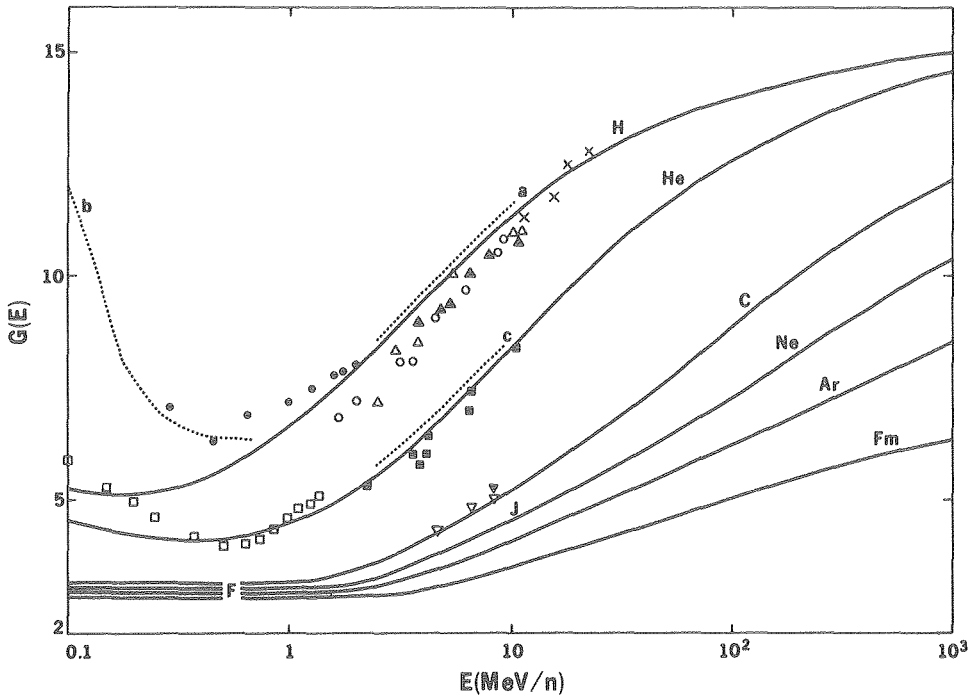

Figure 1. The solid lines give calculated G values of the Fricke dosimeter for the indicated heavy particles; the abscissa is energy per nucleon; the various points and dashed lines give experimental results. XBL 803-8506

mental points are shown. The particles are: H and He, which have been widely used in particle accelerators for years; C, Ne, and Ar, which are currently accelerated in the Bevalac; and Fm (atomic number 100), which is representative of the very heavy particles. The agreement seen in Fig. 1 of the calculated lines with the experimental points must be considered satisfactory in the sense that there is a good overall reproduction of the information obtained from experiment. The rather large scatter of the points arises from serious experimental difficulties, and it would be impossible to improve the calculations at this time.

The principal result of model calculations on dilute solutions is the primary yields for all of the water radicals (hydrated electron, H, OH) and the molecular products (H_2, H_2O_2). It is generally believed that the OH radical has an important role in the biological action of radiation, particularly for cell killing. Figure 2 shows the calculated primary yields of OH radicals for the same particles and energy range as Fig. 1; the calculated primary yields of H_2O_2 are also shown. The G' values shown in Fig. 2 are *differential* on track segment yields, whereas, the G values in Fig. 1 are the traditional G values (integral yields) of radiation chemistry.

Development of the heavy particle track model will continue, and an experimental program is being initiated to verify applications of the model to concentrated solutions.

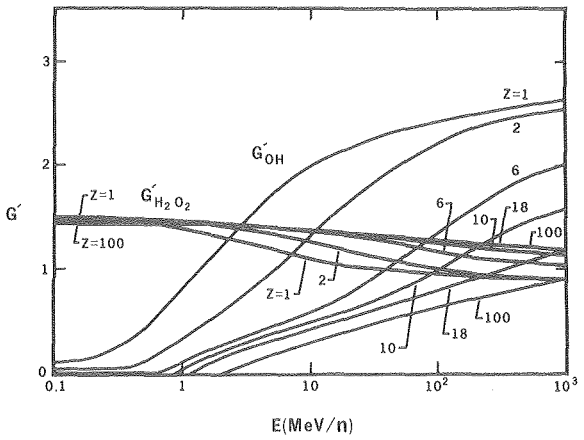

Figure 2. The solid lines give calculated differential G values for the primary yields of OH and H_2O_2 for the same particles and energy range of Fig. 1. The particles are indicated by their atomic numbers: 1 = H; 2 = He; 6 = C; 10 = Ne; 18 = Ar; and 100 = Fm. CBB 807-8444

PHYSICAL CHARACTERIZATION OF ENERGETIC HEAVY-ION BEAMS

Walter Schimmerling, Stanley B. Curtis, T. S. Subramanian, George Gabor,* Selig N. Kaplan,† and Ahren J. Sadoff

The maximum energy deposition of high-energy heavy ion beams used for biomedical research and clinical trials is determined by the amount of material in the target volume (e.g., tissue in radiation therapy) and the amount of various materials required for beam control and modification (water columns, ridge filters, collimators, and beam flattening foils). A significant fraction of the incident heavy ion beam will undergo a nuclear reaction in these materials. The products of these nuclear interactions will, in general, have different biological effectiveness, or "quality," in the target volume. In the case of radiation therapy and the irradiation of animals, these nuclear interaction products constitute the distal dose as well as the dose to nontarget tissues. Our project is concerned with the measurement and prediction of the components of the radiation field, their fluence, and their velocity spectra, all of which are required to predict their biological action.

To identify every particle in the radiation field and measure its velocity, we have designed and built a multidetector particle identification spectrometer consisting of a channel plate time-of-flight telescope, pulse ionization chambers, and a 10-element silicon detector telescope, as well as scintillation counters and multiwire proportional chambers for beam definition.

The complexity of the spectrometer is dictated by the broad energy and mass range of the particles to be detected. Some of these, the lightest and most energetic, will traverse the entire spectrometer without stopping. The heaviest fragments, e.g., stopping argon, will deposit ~ 8000 times more energy per unit length than an energetic proton, but will have a residual range too short to penetrate more than one or two silicon detectors. Therefore, particle identification has to be based on different criteria depending on whether the particle stops in

*Instrument Science and Engineering, Engineering and Technical Services Division.
†Physics, Computer Science and Mathematics Division.

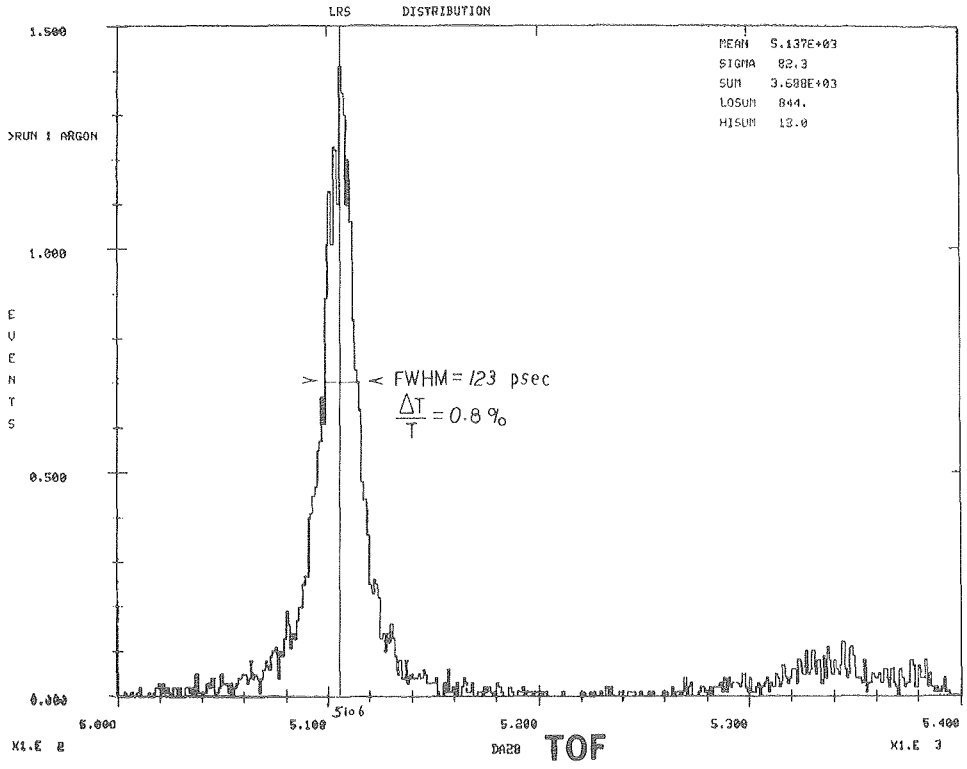

Figure 1. Typical time-of-flight spectrum obtained with an incident argon beam of 509 MeV per nucleon, after traversing 4.24 g/cm² of Lucite. XBL 808-11502

the spectrometer, traverses it without stopping, or stops before reaching the solid state detectors. In this last case, isotopic identification is no longer possible, and charge resolution in the pulse ionization chamber must be used to identify the elements in the radiation field.

The experiments are set up in a heavy-ion beam line of the Lawrence Berkeley Laboratory Bevalac known as Beam 40. This beam line is near the Bevalac Biomedical Facility and allows the use of cell preparation rooms for radiobiological and radiation chemistry experiments planned to compare the beams at both locations. The beam can be shared between these locations, so that the effects of beam geometry on the same incident beam can be evaluated.

Figure 1 is a typical time-of-flight spectrum obtained with an incident argon beam of 509 MeV per nucleon, after traversing 4.24 g/cm^2 of Lucite, showing the contribution of higher velocity secondary fragments. The full width at half-maximum of the argon peak is 123 psec, corresponding to an energy resolution of 2.8%. The energy resolution improves for slower particles, and becomes comparable to that of the solid state detectors at low energies.

The combination of time-of-flight measurements and a solid state detector telescope is particularly powerful for particles that do not stop in the detector. Figure 2 is a plot of data taken with a neon-19 beam at a residual energy of 226 MeV per nucleon. In the figure, each point corresponds to an event with the measured velocity and summed pulse height coordinates. Curves calculated from range-energy relations have been superimposed on the data of Fig. 2. The elements are well separated into distinctive groups that can also be resolved by inspection. This would not be possible using only the information obtained from energy deposition in the

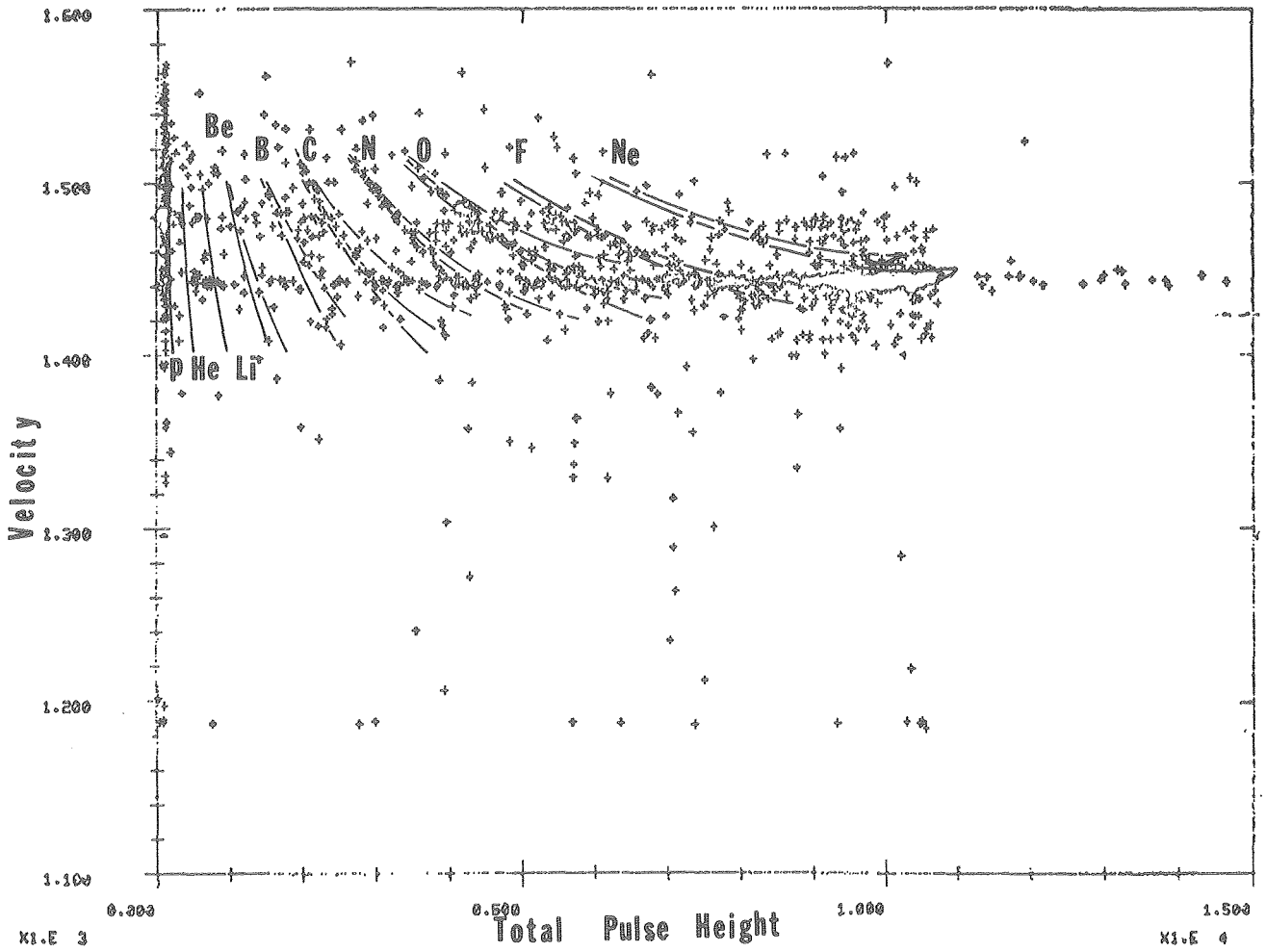

Figure 2. Plot of data taken with a neon-19 beam at a residual energy of 226 MeV per nucleon. Curves calculated from range-energy relations have been superimposed on these data. XBL 806-10521

solid state detector, since the low-velocity component of one element overlaps with the higher velocity component of its neighbors.

Analysis of data shown in Fig. 2 yields the elemental composition of the beam shown in Fig. 3. The dose contributed by secondary particles in this case is 23%.

A data simulation Monte Carlo program was written to test the data analysis programs and to evaluate the efficiency of the detector. This program propagates a heavy ion with a given atomic number Z and atomic weight A through an absorber, evaluates the products of nuclear interactions in successive collisions, and calculates the scattering (beam spreading) of all transported particles due to nuclear and Coulomb interactions. The predictions of this program were compared with experimental velocity distributions and depth dose curves and yielded good agreement. These calculations are being continued with the goal of developing a beam model to predict the physical characteristics of heavy ion beams in arbitrary configurations.

Measurements along the central beam axis will continue, using unmodified beams of carbon, neon, silicon and argon, followed by ridge-filter-modified beams and off-axis measurements to obtain the distributions across the beam spot. Radiobiological and radiation chemistry measurements will be performed in the completely characterized radiation fields, for two important purposes: to establish the factors governing the equivalence between the experimental beam in the Beam 40 area and the beams at the Biomedical Facility, and to obtain an insight into fundamental radiation action mechanisms by exploiting the availability of maximum information in our beam.

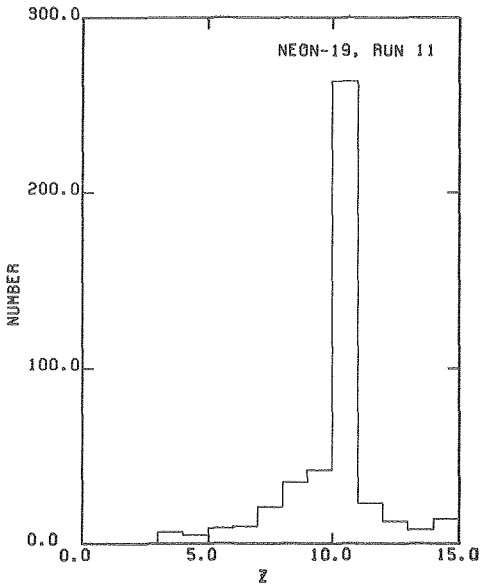

Figure 3. Elemental composition of the neon-19 beam from analysis of data presented in Fig. 2.
XBL 806-10519

NEUTRON PRODUCTION CROSS SECTIONS

Walter Schimmerling, John W. Kast, D. Ortendahl, and T.S. Subramanian

Although the dose contribution of secondary protons and neutrons is small (in most beams, less than 3%), these particles are an important source of background radiation in and around the medical treatment rooms in LBL's accelerator buildings, and quantitative information on these particles is essential. Such information is especially important when sensitive tissues are close to the treatment area, as in choroidal melanoma, a cancer of the eye, treatment for which is currently undergoing clinical trials at the 184-inch synchrocyclotron. Neutrons are also a penetrating component of high-altitude radiation, originating in interactions of cosmic rays with the atmosphere, where they constitute the most important source of exposure for passengers in high-flying aircraft. On a more fundamental level, neutrons are a unique probe of nuclear structure, being insensitive to the Coulomb fields of nuclei.

In a series of experiments performed at the Bevalac in collaboration with R. Madey, B. Anderson, and R. Cecil of Kent State University, we have measured the probability (double differential cross section) of producing neutrons at a given energy and a given angle with respect to an incident heavy ion beam, when nuclei in the beam interact with nuclei in targets of carbon, aluminum, copper, lead and uranium. The energy of the neutrons was obtained from the time of flight (TOF) between the target and each of the neutron detectors, placed at different angles around the target. We also recorded the light output and a position at which each neutron generated the recoil charged particles that gave rise to the detected signal. This resulted in a more accurate assignment of the detector efficiency and angular distribution.

The neutron detector efficiencies were calcu-

lated with a Monte Carlo code developed by our Kent State collaborators and estimated to be accurate to 5% (excluding threshold uncertainties) on the basis of comparisons with available experimental data.

The results for a 337 MeV per nucleon neon beam, incident on a uranium target, are shown in Fig. 1. The curves are the result of a firestreak model calculation by G. Westfall of LBL. Three different energy regions can be distinguished in the neutron spectra: 1) a low-energy "evaporation" region of isotropic neutron emission (Fig. 1 inset); 2) a high-energy exponential tail reflecting the internal momentum distribution of the nucleons; and 3) an intermediate energy region reflecting quasi-free and pre-equilibrium processes. This intermediate energy region becomes less pronounced with increasing angle and is almost nonexistent at 90°.

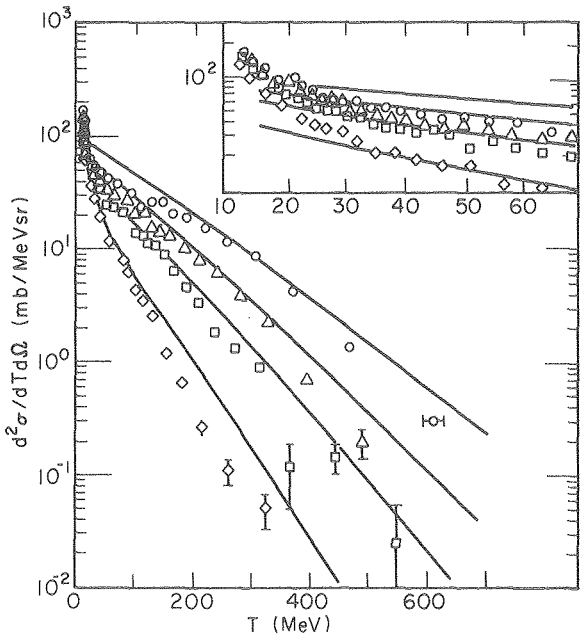

Figure 1. Measured double-differential cross sections for Ne + U → n + X at a mean incident energy of 337 MeV/nucleon, as a function of neutron energy (circles, 30°; triangles, 45°; squares, 60°; diamonds, 90°), and results of a firestreak calculation (solid curves). Inset: Expanded view of the low-energy portion of the spectra. Errors include statistics and small effects of uncertainties in the time calibration. XBL 7910-3833

The cross section, integrated in energy, falls off exponentially with angle. The total cross section for neutron production is proportional to the fifth power of the sum of the radii of the target and projectile. In a geometric interpretation, this is proportional to an overlap area times a multiplicity. This multiplicity is proportional to a geometrical interaction volume.

An insight into the Coulomb effects that modify the spectrum of charged particles is provided by a comparison of neutron-production to proton-production cross sections for identical targets at comparable energies. This ratio is shown in Fig. 2 for our data (open circles) and proton data obtained by other groups at LBL. Different numbers of protons and neutrons contribute to the projectile-target interaction at different impact parameters. An estimate of this difference is provided by firestreak calculations, the results of which are shown as the curves in Fig. 2. The observed ratio of neutron and proton cross sections differs by a factor of approximately 2 from that expected on the basis of the firestreak model calculation.

These unexpected results have indicated the importance of the hitherto neglected Coulomb effects. Preliminary results of some recent calculations by theoretical physicists indicate that the inclusion of Coulomb effects accounts for some of the observed features. Another possible source of the observed discrepancies may be the coalescence into nuclear fragments of the "primordial" neutrons and protons available at the time of interaction, which thus effectively removes them from the observed neutron and proton spectra. Neutron data from our experiments, in conjunction with measured proton distributions, thus provides an excellent constraint on the theory of the formation of light fragments produced in central collisions.

We are currently planning to continue this work, both to understand the physics that apply to particles of interest in biomedical research and space applications and to improve the computer codes used to calculate neutron doses in the Biomedical Facility.

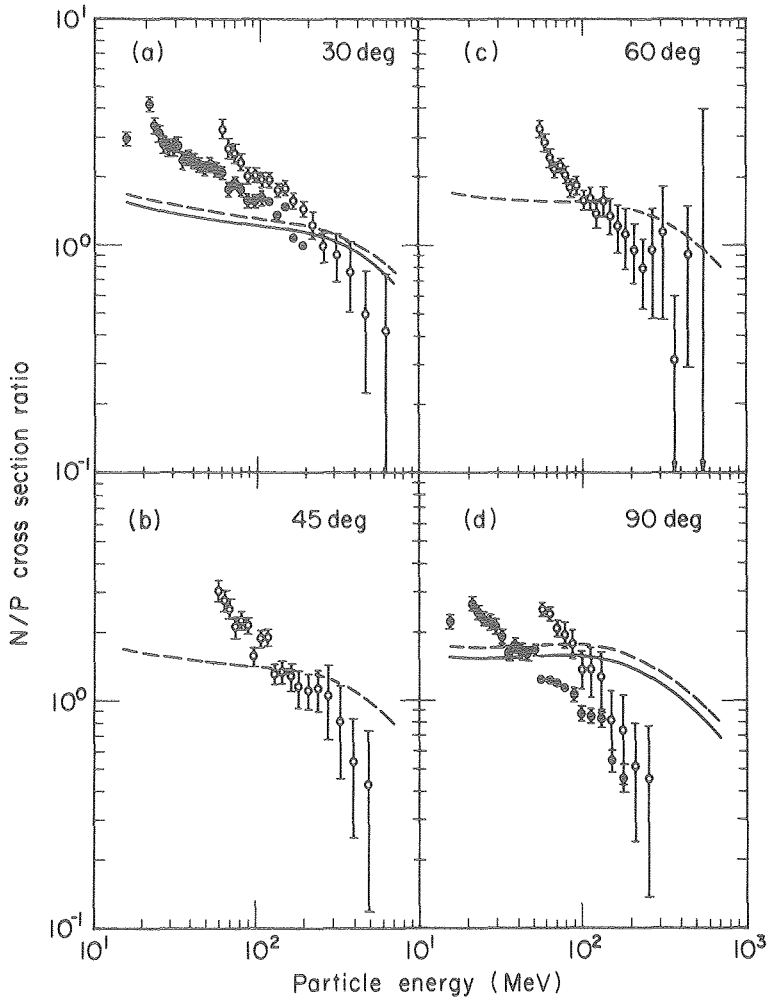

Figure 2. Neutron to proton cross-section ratios as a function of neutron energy at (a) 30 °, (b) 45 °, (c) 60 °, and (d) 90 °. Two sets of ratios are plotted: (I) (Ne + U → n + X at 337 MeV/nucleon)/(Ne + U → p + X at 393 MeV/nucleon); (II) (Ne + U → n + X at 337 MeV/nucleon)/(Ne + Pb → p + X at 385 MeV/nucleon). Full circles: experimental results for I. Open circles: experimental results for II. Solid curve: firestreak calculation for I. Broken curve: firestreak calculation for II. *XBL 7910-3834*

HEAVY-ION MICROSCOPY

Gerhard Kraft, Tracy C. Yang, Todd Richards, Cornelius A. Tobias, and Thomas L. Hayes

Heavy-ion microscopy is a new method to acquire information on the submicroscopic structure of biological cells and other small objects. In light microscopy, the resolution is restricted by the wavelength of the illumination used, and structures smaller than 2500 Å (= 0.25 μm) cannot be resolved. In electron microscopy, smaller structures of about 100 Å are visible, but in its scanning mode (SEM) only the surface of the object is visible, and in its transmission mode (TEM) the angular deflection of the electron beam by the electrons of the target is high so that only thin slices of cellular material can be used if a high resolution is required. In contrast to electrons, charged particle beams, such as protons or heavier ions, exhibit much less multiple scattering on a target, and therefore show less angular deflection across their path through the target.

When penetrating solid material, heavy particles with initial energies above 10 keV/μm interact primarily with the target electrons. Because of the small mass of the electrons compared with the in-

cident heavy ions, many collisons are required to dissipate the projectile energy. The residual energy of the incident ions, therefore, is a smooth function of the electron density of the target, which is mainly given by the product of the atomic number and the density of the target atoms. Small differences in either the chemical composition or the density of the target will be detected as differences in stopping power, and the energy distribution of the incident particles traversing the object will reflect the density distribution of the object.

At present, it is not possible to produce an enlarged image from the energy distribution of the transmitted heavy particles. In heavy-ion microscopy, radiographic methods must be used to convert the energy distribution of the transmitted beam to a range distribution in a nuclear track detector. For this purpose, the object can be directly fixed onto the track detector and irradiated with a monoenergetic ion beam. Where the object is dense, the energy loss will be higher and the range of the particles in the track detector shorter, and vice versa where the object is less dense. The tracks of the particles thus produce a density map of the object inside the detector.

The experimental procedure of heavy-ion microscopy is illustrated in Fig. 1. Mammalian cells are grown on sterile mica plates for one or two days, then fixed with alcohol and dried. The samples are irradiated in a vacuum chamber with a monoenergetic heavy-ion beam with a dose between 10^{12} and 10^{14} particles/cm^2. After irradiation the cells are removed. With the high particle dose used, the tracks produced in the detector overlap, and they can be completely dissolved by an etching procedure that yields a one-to-one replica of the cell in the mica. For use in a SEM, the replica is covered with a thin conducting layer (100 Å Au-Pd), which will not affect the resolution.

In Fig. 2 a replica of a mammalian cell (Chinese hamster V79) is shown, which was obtained with a 1 MeV argon beam. In the lower right part of the image, the cell nucleus (darker region) with the nucleolus is visible. Since the nucleolus is a very dense cell structure, the particle energy was too low to penetrate it, and the image does not show any internal structure. A long fiber stretches to the upper left. The small white grains at the borderline of the cell are replicas of salt crystals, which are remnants of the cell medium. At top left, the mica that was

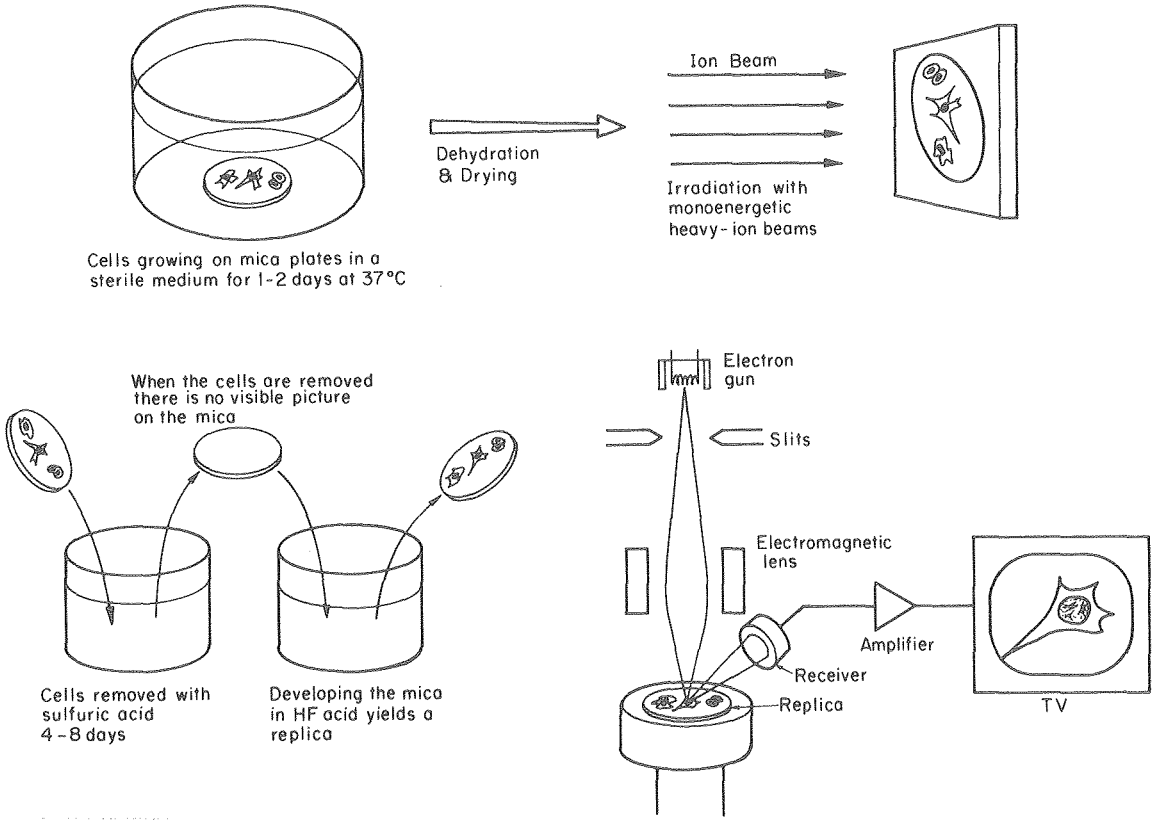

Figure 1. The general experimental procedure for obtaining heavy-ion replicas from biological specimens.

XBL 809-3699

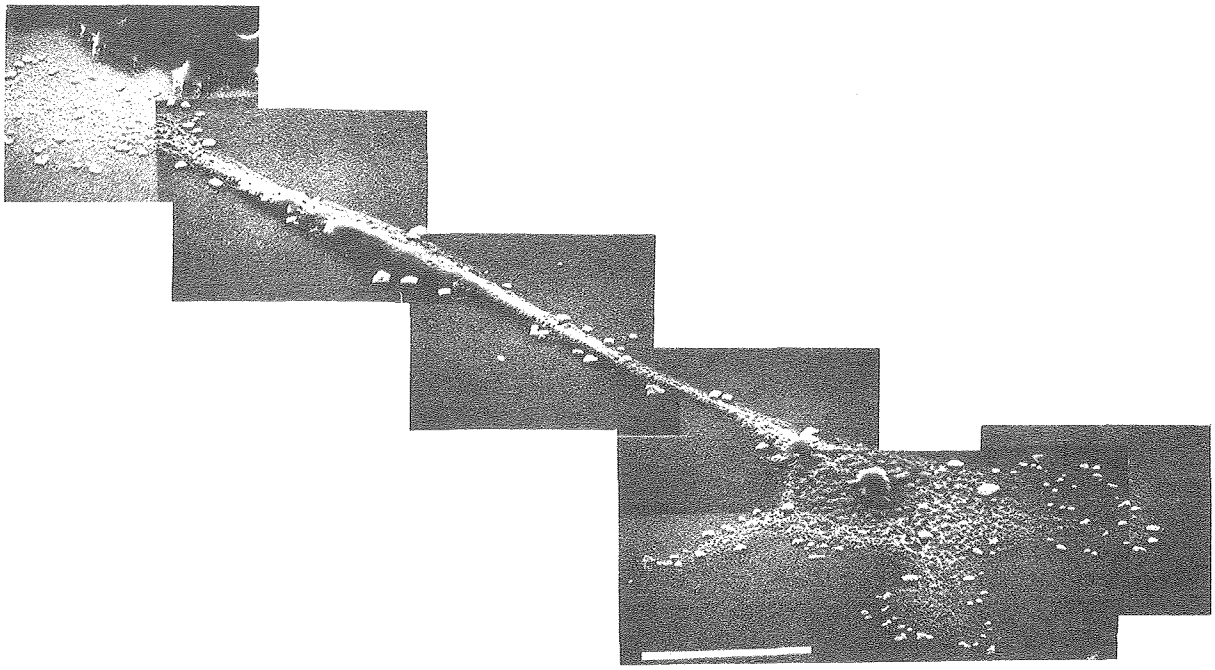

Figure 2. SEM image of a heavy-ion replica of a mammalian cell obtained with a 1 MeV/amu argon beam. At the right side in the nucleus of the cell (dark region) the dense nucleolus is visible. In the upper left, a part of the mica was shadowed from irradiation and the original surface of the mica and the steepness of the etched walls are visible. The marker represents 10 μm. The image was reproduced with a Coates and Welter 50 SEM from the Electron Microscopy Laboratory.

XBB 808-9829

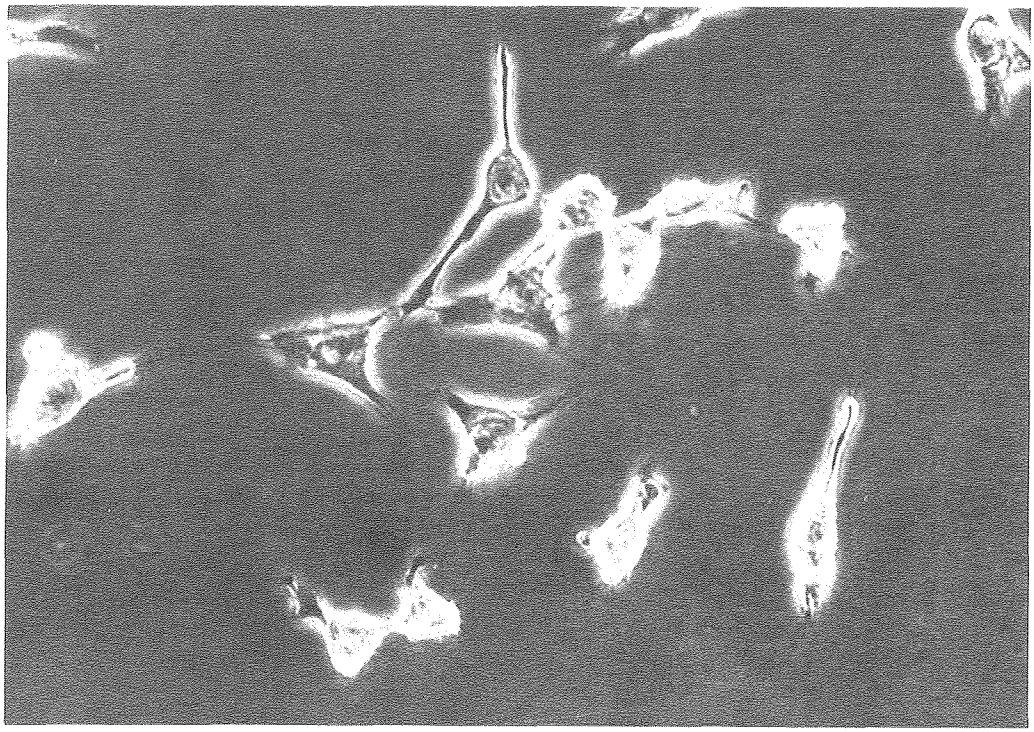

Figure 3. Image of mammalian cells taken with an optical phase contrast microscope having a magnification of about 425 ×.

XBB 8010-11383

not hit by particles is visible, and the steepness of the etching procedure can be seen.

For comparison, Fig. 3 shows an image of a mammalian cell under an optical microscope. The image formed using heavy-ion microscopy exhibits a much better resolution than the optical method. Heavy-ion resolution, however, is restricted by the lateral and longitudinal straggling of the particle beam. Using a theoretical approximation, the calculation of the maximal possible resolution with this technique yields a value of about 300 Å in both lateral and longitudinal resolution for a radiograph of a biological specimen that is 1 μm thick. Compared with this value, the other parameters that influence the total resolution of the heavy-ion technique—such as the energy spread and the lateral divergence of the primary beam or the resolution of the etching process and the resolution of the SEM—are small. Also, the chemical structure of the mica has a lattice constant of about 10 Å, which is negligible.

In the experiment an optimal resolution of about 500 Å was achieved, using 1 MeV/amu argon ions. In further experiments, the influence of the atomic number of the projectiles and the dose effects on the resolution will be studied. It should also be possible to increase the contrast of the image by a "site-specific" incorporation of chemicals containing heavy atoms. For example, with the incorporation of the IUdR or BUdR, DNA precursors, it may be possible to obtain more information concerning DNA conformation between mitoses.

TUMOR RADIOBIOLOGY STUDIES WITH HEAVY CHARGED-PARTICLE BEAMS

Stanley B. Curtis, Tom S. Tenforde, Susan D. Tenforde, Shannon S. Parr, and Marilyn J. Flynn

The response of tumor-cell systems to irradiation with carbon, neon, and argon beams at various positions in the plateau and extended peak regions of the Bragg ionization (dose versus depth) curve is being evaluated from experiments conducted both *in vivo* and *in vitro*. The radiobiological end points being studied include: tumor volume response, cellular survival after tumor irradiation *in situ*, cell-kinetic parameters measured by flow cytofluorometry and time-lapse cinematography, and survival of oxic and hypoxic cells irradiated in suspension. One focus of our research effort during the past year has been on the combined effect of radiosensitizing drugs and charged-particle irradiation. In this article, we present the results of studies on combined drug and radiation treatment of a rat rhabdomyosarcoma tumor and a human melanoma tumor growing in athymic (thymus-less) nude mice.

RADIATION-INDUCED GROWTH DELAY STUDIES

It has been shown by Chapman and his collaborators[1] that electron affinic sensitizers such as misonidazole enhance hypoxic cell killing *in vitro* in the extended peaks of charged particle beams. It is, therefore, of interest to determine whether this effect also occurs in an *in vivo* tumor system. The effect of misonidazole on tumor growth delay induced by peak carbon and neon ions was measured in rhabdomyosarcoma tumors of R1/LBL subline rats for both single and fractionated schedules and compared with that induced by 225 kilovolt peak x rays. In all cases, the sensitizers were administered 30 to 60 minutes prior to irradiation in order to achieve a maximum drug level in the tumor at the time of the irradiation.

The tumors were positioned in the distal 1.5-cm portion of a 4-cm extended-peak ionization region. The initial energy of the carbon-ion beam was either 400 or 474 MeV/u, giving ranges in tissue of 24 or 31 cm, respectively. The neon-ion beams had initial energies of 400 or 557 MeV/u, giving ranges in tissue of 14 or 20 cm, respectively. The absorbed dose rates for both charged-particle radiation modalities ranged from 2 to 10 Gy/min.

Plots of the radiation-induced growth delay as a function of dose are given for the single-dose experiments in Fig. 1, and for the four daily fraction experiments in Fig. 2. The RBE (relative biological effectiveness) values and drug enhancement ratios at the 20-day and 50-day growth delay levels are given in Table 1.

The results of these studies demonstrate that misonidazole has a significant effect on the response of R1/LBL tumors to single doses of x rays, giving enhancement ratios of 1.8–2.1 when the drug was administered intraperitoneally (i.p.) at a 500 mg/kg dose level. For the 4-cm extended-peak regions of carbon and neon beams, misonidazole was found to exert a small potentiating effect on tumor cell killing. The drug enhancement ratios were 1.1 to 1.3 for peak carbon ions and 1.2 to 1.3 for peak neon ions.

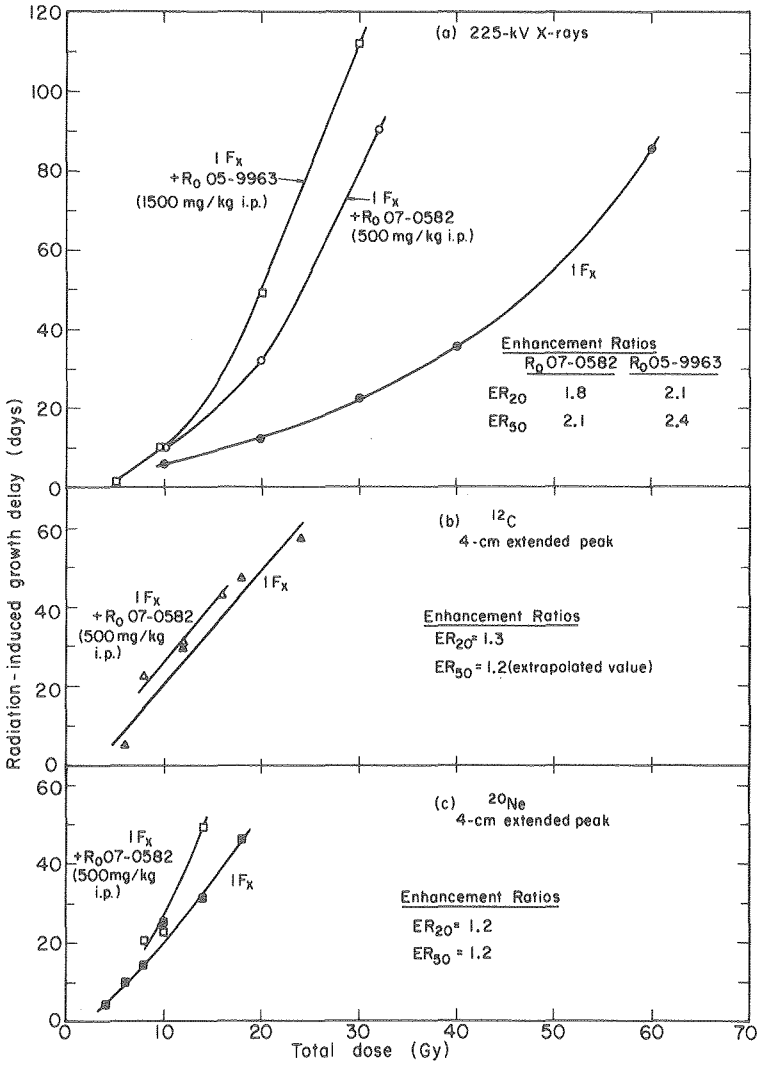

Figure 1. Radiation-induced growth delay curves for R1/LBL tumors receiving combined treatment with (a) single doses of x rays and the hypoxic cell sensitizers Ro 07-0582 (misonidazole) and Ro 05-9963, (b) peak carbon ions and Ro 07-0582 and (c) peak neon ions and Ro 07-0582. To achieve peak drug concentration in tumor at time of irradiation, the sensitizers were administered i.p. at 30–60 min before radiation. Effect of these compounds on tumor radiation response is indicated by enhancement ratios calculated at 20-day (ER_{20}) and 50-day (ER_{50}) growth-delay levels. XBL 805-3285

When misonidazole and x-irradiation were administered in four daily fractions, the drug enhancement ratio decreased significantly. This effect would be expected since reoxygenation of hypoxic R1 tumor cells occurs within the fractionation interval, i.e. 24 hours, and this process reduces the net gain obtained by misonidazole sensitization of hypoxic cells. With carbon and neon beams, dose fractionation had no significant effect on misonidazole enhancement of radiation damage. This finding is not unexpected in view of the reduced dependence on oxygen of cell killing by densely ionizing charged-particle radiation. The reduced oxygen effect would clearly diminish the impact of reoxygenation on tumor radiation response in a fractionated dose schedule, and this could account for the similar effects of misonidazole when used in combination with single and fractionated doses of high-LET (linear energy transfer) radiation.

Preliminary studies have also been undertaken to examine the effect of the O-desmethyl metabolite of misonidazole, Ro 05-9963, on the growth delay

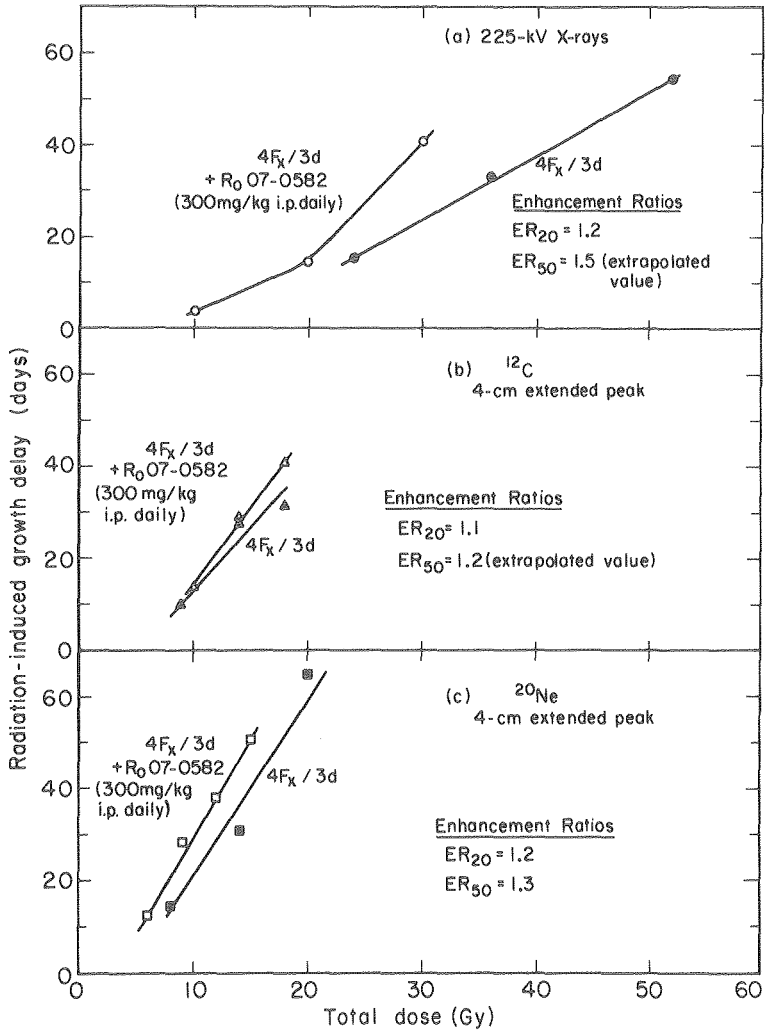

Figure 2. Radiation-induced growth delay curves for R1/LBL tumors receiving fractionated treatments with both misonidazole (Ro 07-0582) and (a) x-ray irradiation, (b) peak carbon ions, and (c) peak neon ions. The sensitizers were administered as four daily fractions with the drug being given i.p. at 30–60 min prior to irradiation. Enhancement ratios show that the sensitizing effect of Ro 07-0582 is reduced in fractionated dose regimens with x rays as compared with single-dose schedules (Fig. 3). In contrast, enhancement ratios with peak carbon ions and peak neon ions are similar for single-dose and fractionated-dose schedules. *XBL 805-3286*

induced in R1/LBL tumors by both low- and high-LET radiation. Initial studies with x rays have yielded single-dose enhancement ratios of 2.1–2.4 for this compound when injected i.p. at a dose level of 1500 mg/kg. These values are slightly greater than the enhancement ratios obtained for misonidazole (1.8–2.1).

REPAIR OF POTENTIALLY LETHAL DAMAGE

Cell survival was assayed *in vitro* following irradiation *in situ* of human Nall melanoma tumors growing subcutaneously in the flanks of athymic nude mice. These studies were carried out in collaboration with M. Guichard and E. Malaise of the Institut Gustave-Roussy, Villejuif, France. Tumors were irradiated with neon ions at the midpoint of a 10-cm extended peak, and cell survival was assayed at 0, 6, and 24 hours postirradiation. Parallel exper-

Table 1. RBE values for radiation-induced growth delay of R1/LBL tumors in vivo following combined treatment with misonidazole (Ro 07-0582) and charged-particle radiation.

Fractionation Schedule*	Radiation Modality†	RBE_{20}‡	RBE_{50}‡	ER_{20}§	ER_{50}§
1 F_x + Ro 07-0582	x rays	—	—	1.8	2.1
1 F_x + Ro 05-9963	x rays	—	—	2.1	2.4
(4 F_x/3d) + Ro 07-0582	x rays	—	—	1.2	1.5‖
1 F_x + Ro 07-0582	^{12}C	2.1	1.4‖	1.3	1.2‖
(4 F_x/3d) + Ro 07-0582	^{12}C	2.0	1.6‖	1.1	1.2‖
1 F_x + Ro 07-0582	^{20}Ne	1.9	1.6	1.2	1.2
(4 F_x/3d) + Ro 07-0582	^{20}Ne	2.9	2.3	1.2	1.3

**For the single fraction schedules, the i.p. dose levels of Ro 07-0582 and Ro 05-9963 were 500 mg/kg and 1500 mg/kg, respectively. For schedules of four fractions in a three-day interval, the daily dose of Ro 07-0582 was 300 mg/kg. In all cases, the i.p. drug injection was given 30 to 60 min prior to irradiation.*

†The peak x-ray energy was 225 kV. Both the carbon-ion and neon-ion beams had an initial energy of 400 MeV/u and the tumors were positioned in the distal 1.5-cm region of a 4-cm extended peak ionization region.

‡The RBE_{20} and RBE_{50} values were calculated from the ratio of the x-ray dose to the charged-particle dose required to produce growth delays of 20 days and 50 days respectively.

§The ER_{20} and ER_{50} values are drug enhancement ratios at the 20-day and 50-day growth delay levels, respectively. Each enhancement ratio was calculated as the ratio of radiation doses without and with administered sensitizer.

‖Extrapolated value.

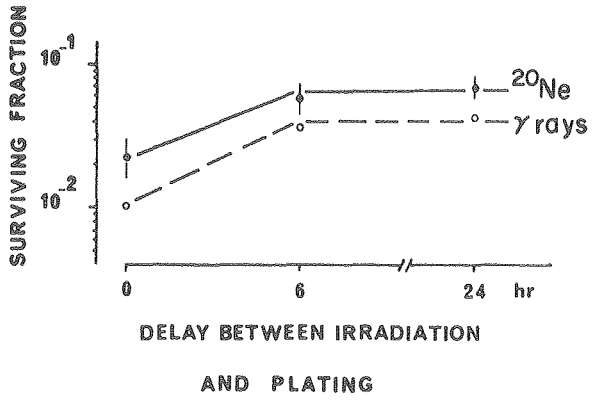

Figure 3. Surviving fractions of human melanoma cells after tumor excision from nude mice are plotted as function of time between irradiation and plating, for peak neon ions (closed circles) and gamma rays (open circles).

XBL 808-10968

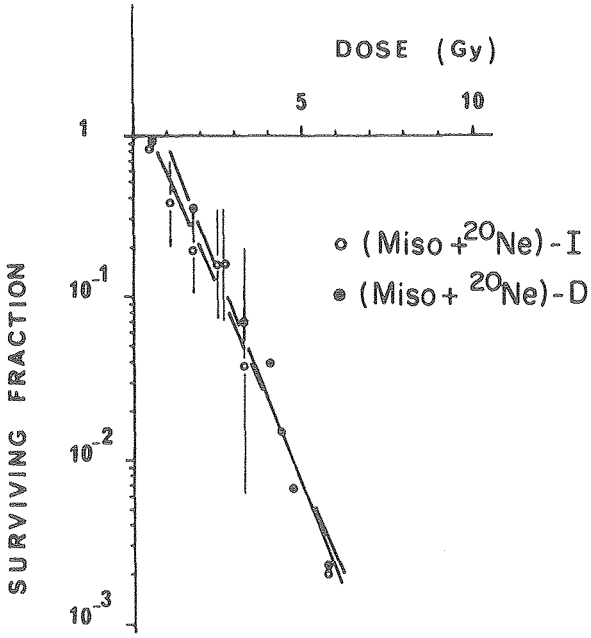

Figure 4. Survival curves for human melanoma tumors receiving combined treatment with misonidazole and peak neon ions. Tumor-bearing nude mice were injected with misonidazole 60 min prior to irradiation. Open circles denote immediate plating; closed circles, plating delayed 24 hours after irradiation.

XBL 808-10969

iments were carried out with tumor-bearing mice that had been administered a 1 mg/g i.p. dose of misonidazole 60 min. prior to irradiation. The principal findings were: (a) At the 10% survival level, the RBE for the peak neon ions relative to ^{60}Co gamma rays was 3.7, which was higher than the RBE of 3.0 previously obtained for 50 MeV neutrons. (b) The repair of potentially lethal damage (PLD) after neon ions was comparable to that observed following ^{60}Co and neutron irradiation. A comparison of the PLD repair kinetics following irradiation with neon ions and gamma rays is shown in Fig. 3. (c) The enhancement ratio for misonidazole with peak neon ions was 1.4, which is similar to the values 1.6 and 1.5 obtained for ^{60}Co and neutron irradiation, respectively. (d) With peak neon ions, as well as with ^{60}Co and neutron irradiation, pre-irradiation injection of misonidazole was found to inhibit PLD repair. Survival data obtained after immediate (I) and 24-hour-delayed (D) plating are shown in Fig. 4 for tumors excised from mice injected with misonidazole. It is clear that little or no PLD repair has occurred.

REFERENCE

1. Chapman, J.D., Urtasun, R.C., Blakely, E.A., Smith, K.C., and Tobias, C.A. 1978. Hypoxic cell sensitizers and heavy charged particle radiation. *Br. J. Cancer* 37 (Suppl. III): 184–188.

CELL SURVIVAL IN SPHEROIDS IRRADIATED WITH HEAVY-ION BEAMS

Adrian Rodriguez and Edward L. Alpen

Biological investigations with accelerated heavy ions have been carried out regularly at the Lawrence Berkeley Laboratory Bevalac for the past four years. Most of the cellular investigations have been conducted on cell monolayer and suspension culture systems. The studies to date suggest that heavy charged particle beams may offer some radiotherapeutic advantages over conventional radiotherapy sources. The advantages are thought to lie primarily in an increased relative biological effectiveness (RBE), a decrease in the oxygen enhancement ratio (OER), and better tissue distribution of dose.

Experiments reported here were conducted with 400 MeV/amu carbon ions and 425 MeV/amu neon ions, using a rat brain gliosarcoma cell line grown as multicellular spheroids.

The tumor-like characteristics of multicellular spheroids were first investigated by Sutherland and coworkers,[1,2] who reported that individual spheroids have many characteristics of solid *in vivo* tumors that are not shared by cells grown in monolayer or suspension culture. They also reported that in this culture format—where nonmonoclonal cells grow in three-dimensional contact—there is variability of cell distribution in the cell cycle, decreasing growth fraction with increasing spheroid size, variation in state of oxygenation in the cells, and some rudimentary forms of intercellular communication. These characteristics have been suggested to be the bases for enhanced survival of cells grown and irradiated in the spheroid condition.

To check these suggestions, studies have been carried out with x-rays and high-energy carbon and neon ion beams. These studies evaluate high-LET (linear energy transfer) cell survival in terms of RBE and the possible contributions of intercellular communication. Comparisons were made of the post-irradiation survival characteristics for cells irradiated as multicellular spheroids (approximately 100 μm and 300 μm diameters) and for cells irradiated in suspension. These comparisons were made between 225-kVp x-rays, 400 MeV/amu carbon ions, and 425 MeV/amu neon ions. Figure 1 shows the placement of samples in the 4-cm-spread Bragg peaks of the ion beams.

X-ray cell survival curves for cells from spheroids had larger D_0's than did the survival curve for cells grown in single-cell suspension (Table 1). (D_0 is the reciprocal of the slope on the exponential portion of the survival curve.) In addition, large spheroids did not have a detectable hypoxic cell fraction that would be evidenced by a radioresistant fraction in the cell survival curve (Fig. 2).

In the plateau region of the carbon beams the survival of cell suspensions and spheroid cells was not significantly different compared to x-rays (Table 1). At 10% survival the RBE's were 1.0 and 0.97, respectively, for cells irradiated in suspension and cells irradiated as spheroids (Table 2). The spheroid cells continued to have larger D_0 values than cells from suspensions for the same radiation modality. Comparison of the effectiveness of the proximal, mid, and distal regions of the spread-out Bragg peak of carbon ions for cell killing in spheroids indicated that cell inactivation increased as a function of increasing LET. The survival dose relationship in the

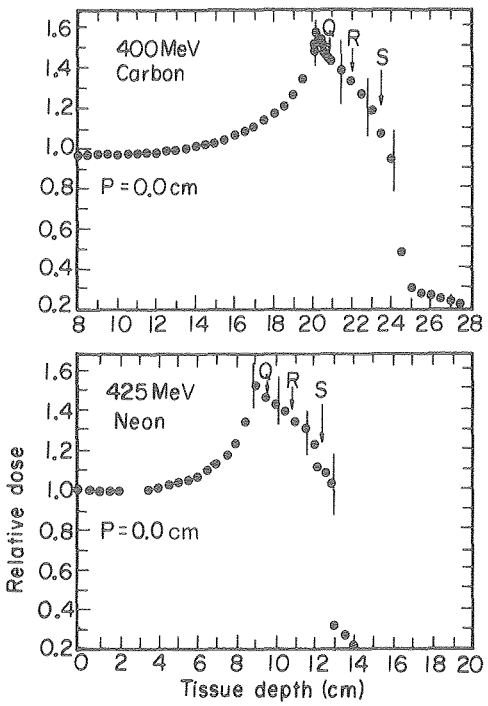

Figure 1. Depth dose distribution of carbon (400 MeV/amu) and neon (425 MeV/amu) beams modified with a brass spiral ridge filter to produce 4-cm-spread Bragg peaks. Irradiated samples were placed in the plateau region (P) with 0.0-cm water absorber and in the proximal (Q), mid (R), and distal (S) segments of the spread peaks.

XBL 793-3219

mid and distal peak regions was exponential (Fig. 3), and the RBE, at 10% survival, was 1.9 and 2.1 compared to 1.5 for the proximal peak (Table 2).

Survival of single cell suspensions and cells from large spheroids irradiated in the plateau region of neon was reduced slightly compared to x-rays. As with plateau carbon ion, the spheroid cells exhibited greater radioresistance compared to the single-cell suspensions (Table 1). Cell survival was the same for cells in suspension and spheroid cells in the neon proximal peak, and inactivation was exponential (Fig. 4A). The RBE values at 10% survival for suspension–grown cells and spheroid cells were 1.6 and 2.1 (Table 2). Examination of survival data for various regions in the spread Bragg peak of neon (Fig. 4B) showed that a maximum RBE at 10% survival of 2.5 was found for the mid-peak, while the lowest RBE value of 1.6 for neon was found for irradiation in the distal-peak (Table 2).

We conclude that the higher average LET (200 keV/μm) in the distal peak region of the neon beam exceeds the maximally effective LET, which for this ion is probably below this value. Consequently there is a significantly reduced cell killing effectiveness observed for irradiation in the neon distal peak for the spheroid cell configuration of 9L cells compared with the positions on the stopping region of the spread out energy peak. In addition the sphe-

Table 1. Summary of survival parameters for 9L cells irradiated as cell suspensions and spheroids with x rays or heavy ions.

	D_0(95% CI*)	D_q(95% CI*)	n†(95% CI*)
225 kVp x rays			
Cells	*190*(185-195)	*250*(245-255)	*3.7*(3.3-4.2)
Spheroids	*260*(235-285)	*310*(280-340)	*3.3*(2.1-5.0)
Carbon 400 MeV/amu			
Plateau—cells	*180*(160-200)	*280*(250-310)	*4.7*(2.8-7.8)
spheroids	*260*(232-279)	*340*(305-370)	*3.7*(2.7-5.1)
4-cm Spread Bragg Peak			
Proximal—cells	*180*(172-186)	*0*	*1.0*
spheroids	*240*(220-255)	*70*(63-72)	*1.3*(1.0-1.7)
Mid—spheroids	*210*(200-220)	*0*	*1.0*
Distal—spheroids	*190*(181-200)	*0*	*1.0*
Neon 425 MeV/amu			
Plateau—cells	*165*(155-175)	*260*(250-280)	*4.8*(3.8-6.2)
spheroids	*220*(190-250)	*275*(240-320)	*3.5*(1.9-6.1)
4-cm Spread Bragg Peak			
Proximal			
cells & spheroids	*190*(185-200)	*0*	*1.0*
Mid—spheroids	*160*(150-170)	*0*	*1.0*
Distal—spheroids	*245*(230-260)	*0*	*1.0*

**CI = confidence interval—the number ranges in parentheses.*

†n = intercept of the ordinate. Its values tend to be assymetrical at these extreme regions.

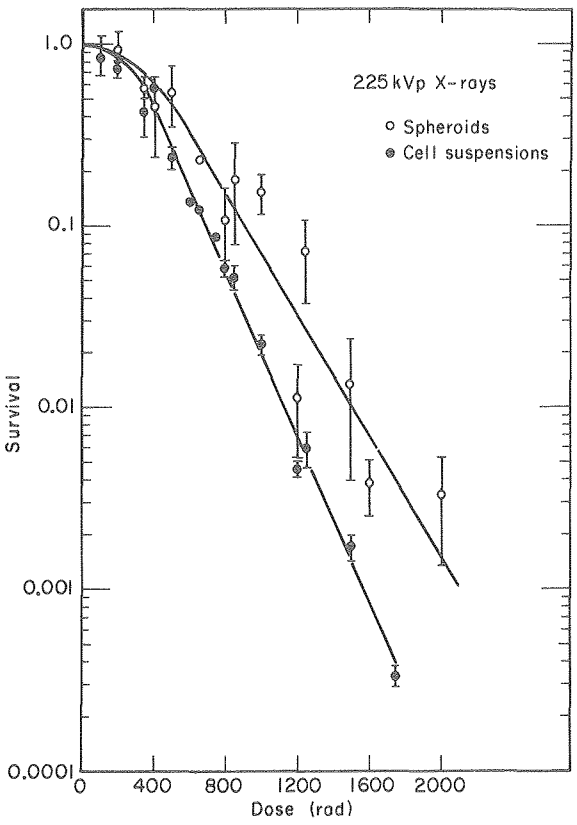

Figure 2. Survival curves for cells irradiated with x rays as spheroids (○) and as cell suspensions (●). The curve for spheroid cells represents the pooled results for small (100μm) and large (300μm) diameter spheroids. Standard deviations are indicated by bars. *XBL 7911-3908*

roid survival enhancement effect appears to be abolished in the spread Bragg peaks where the LET is above 60 KeV/μm.

REFERENCES

1. Sutherland, R.M., McCredie, J.A., Inch, W.R. 1971. Growth of multicell spheroids in tissue culture as a model of nodular carcinomas. *J. Natl. Cancer Inst.* 41:113–120.
2. Inch, W.R., McCredie, J.A., Sutherland, R.M. 1971. Growth of multicell nodular carcinomas in rodents compared with multicell spheroids in tissue culture. *Growth* 34:271–281.

Table 2. RBE values for 9L cells and spheroids irradiated with heavy ions relative to 225 kVp x rays.

	RBE for Survival of 50%	RBE for Survival of 10%
Carbon 400 MeV/amu		
Plateau—Cells	0.94	1.0
Spheroids	0.94	0.97
4-cm Spread Bragg peak		
Proximal—Cells	3.0	1.7
Spheroids	2.1	1.5
Mid—Spheroids	3.4	1.9
Distal—Spheroids	3.7	2.1
Neon 425 MeV/amu		
Plateau—Cells	1.0	1.1
Spheroids		1.2
4-cm Spread Bragg peak		
Proximal—Cells	2.9	1.6
Spheroids	4.0	2.1
Mid—Spheroids	4.4	2.5
Distal—Spheroids	2.9	1.6

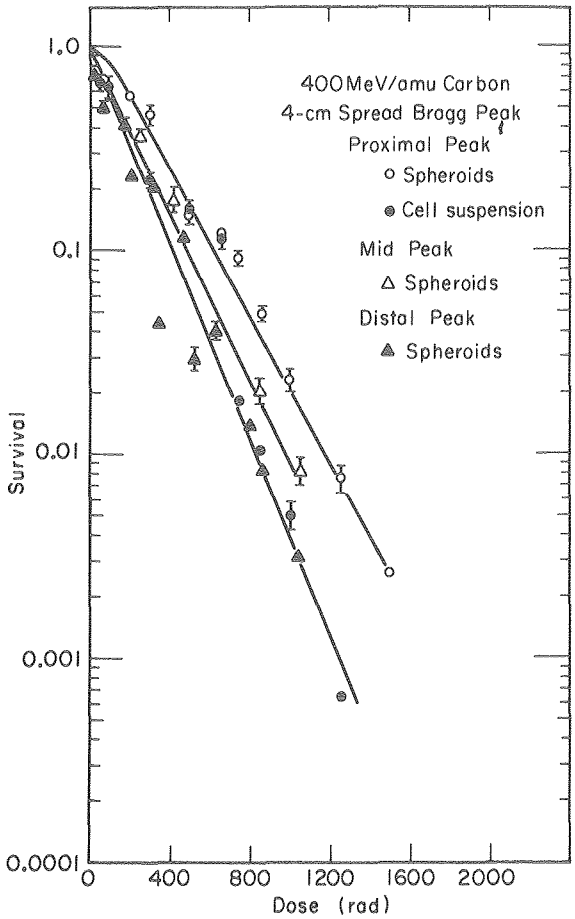

Figure 3. Survival curves for cells irradiated as spheroids in 4-cm-spread Bragg peak of 400 MeV/amu carbon ions. Positions are proximal (○), position Q; mid (Δ), position R; and distal (▲), position S. (Q, R, S refer to Fig. 1.) Survival curve is also shown for cells irradiated in suspension in the proximal peak (●). XBL 7911-3906

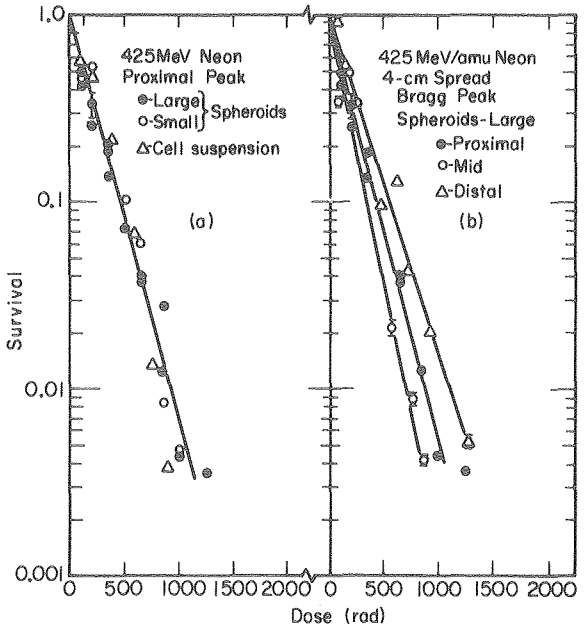

Figure 4. (a) Survival curve for cells irradiated as large (300 μm) spheroids (●), small (100 μm) spheroids (○), and cell suspensions (Δ) in proximal portion of 4-cm-spread Bragg peak of a 425 MeV/amu neon ion beam (position Q of Fig. 1). (b) Survival curves for cells irradiated as large (300 μm) spheroids in the proximal (●), mid (○), and distal (Δ) portions (positions Q, R and S, respectively, Fig. 1) of a 425 MeV/amu neon ion beam. XBL 7911-3904

HIGH-ENERGY BEAMS OF RADIOACTIVE NUCLEI AND THEIR BIOMEDICAL APPLICATIONS

Edward L. Alpen, Aloke Chatterjee, Jorge Llacer*

Energetic charged particles heavier than electrons are now being used in radiation therapy. The various charged-particle radiation modalities include: pions at Los Alamos, helium through argon at LBL, and protons at Harvard. All have one thing in common: they exhibit a favorable depth-dose characteristic where localized tumor volume is concerned. They can deliver a high dose to the treatment volume while minimizing the dose to surrounding normal tissues.[1] This preferential deposition of dose is attributable to the Bragg ionization phenomenon of heavy charged particles. Figure 1 shows a typical Bragg ionization (depth versus dose) curve for a 425 MeV/amu neon beam as measured with a variable thickness water phantom and ionization chamber.[2]

Because the Bragg peak (the point of maximum dose) of monoenergetic heavy particles is quite sharp, and because the degree of ionization in the peak region is several times higher than in the pla-

*Engineering and Technical Services Division.

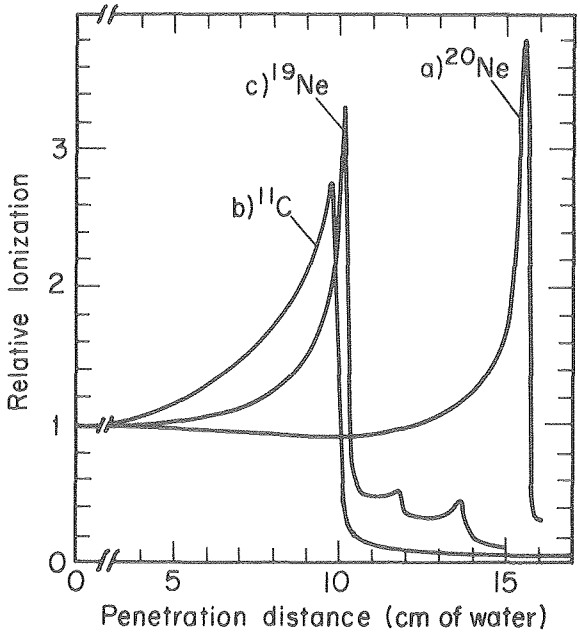

Figure 1. Experimentally measured Bragg ionization curves for high-energy, heavy particle beams.[11] (a) 425 MeV/n ^{20}Ne beam, range in water is 15.8 cm, and peak in ionization occurs at 15.6 cm; these are primary beam particles accelerated in the Bevalac.[12] (b) Measurements made with secondary beam of ^{11}C nuclei produced from primary beam of ^{12}C particles; Bragg peak occurs at 9.7 cm. (c) Data for secondary beam of ^{19}Ne particles; Bragg peak occurs at 10.25 cm. Small amount of contamination is present as indicated by two small peaks of ^{17}F and ^{15}O. XBL 798-3750A

teau region, extreme care must be exercised in locating the peak within the tumor volume. Not being able to treat with the Bragg peak because of this difficulty has been a severe limitation of the heavy-particle therapy program.[3] Although the location of a tumor can be reasonably well defined through conventional diagnostic techniques, placing the peak on the tumor depends on knowing the density and composition of intervening substances—bone, tissue, sinus, air, blood, etc.—through which the beam must pass. We know from experience with heavy-particle therapy that the precise localization of the Bragg peak is important for proper evaluation of this treatment modality.

In many cases, Bragg-peak treatment is not only desirable but essential for deriving maximum benefit from energetic charged particles. But so far, accurate procedures have not easily been achievable because precise information on the effective stopping power of normal tissue between entry port and target tumor was lacking. Exact calculation of beam stopping point is impossible because of the unknown composition of intervening tissue in patients.

The average linear energy tranfer (LET) of a heavy charged particle is given by the Bethe stopping power formula[4]:

$$-dE/dx = \frac{4\pi z^2 e^4}{mc^2\beta^2} NZ\left[\ln\frac{2mc^2\beta^2}{I(1-\beta^2)} - \beta^2 + \text{correction terms}\right] \quad (1)$$

where z is the charge on the incident particle,
NZ is the number of electrons/volume in the medium,
β is the velocity of the incident particle in units of the velocity of light, c,
I is the mean excitation potential of the medium,
e is the electronic charge,
mc^2 is the rest energy of an electron.

Correspondingly, the range R can be calculated as:

$$R = A\int_0^E \frac{dE'}{|dE'/dx|} \quad (2)$$

where E is the energy per nucleon of the incident heavy particle, and A is its mass number.

For a homogeneous medium, applications of equations (1) and (2) are straightforward, and positioning the Bragg peak at a specified depth is simple. But if the medium is nonhomogeneous (as in a patient), and if we do not know the explicit path length for specific tissues, then equations (1) and (2) are not useful. The electron density and the composition of each volume element that a beam penetrates are essential for calculating the depth of penetration of a charged particle for a given energy. One solution is to estimate electron density from x-ray computerized tomography information.[5] Error in this procedure can be as high as 8 mm over a pathlength of 20 cm due to several effects: x-ray beam hardening, reconstruction artifacts, calibration errors, and possible inaccuracies in separating Compton from photoelectric effects (G.T.Y. Chen, private communication). Of course, for shorter pathlengths, the error will be smaller.

RADIOACTIVE BEAMS

The availability of high-energy beams of radioactive species is the most recent advance in the field of accelerator physics. These beams will also have important applications in therapeutic and diagnostic radiology and in nuclear medicine.

One of the primary interactions experienced by relativistic heavy ions is the peripheral nuclear collision.[6,7] The main characteristic of this type of reaction is that only a small amount of excitation energy is imparted to the projectile—enough to cause a breakup of the nucleus, but not enough to produce significant changes in the projectile's velocity or trajectory.[8] Thus, radioactive nuclei are produced as secondary particles from peripheral nuclear fragmentation reactions. These nuclei have trajectories and energies differing little from that of the parent particle. Various radioactive beams produced as a result of these reactions, now regularly available with sufficient intensity (about 10^7 particles/pulse) from the Bevalac, are: ^{11}C, ^{13}N, ^{15}O, and ^{19}Ne.

Since the charge-to-mass ratio of the radioactive product nuclei is quite different from most of the other fragments (which are also produced in peripheral nuclear collisions) and from the parent nucleus, isolation of a given radioactive beam has been achieved quite effectively by magnetic deflection.[9] Figure 1 shows a Bragg ionization curve measured for the ^{11}C beam, a positron emitter, with a half-life of 20 min. In this type of measurement, made with a variable thickness water absorber,[10] each ion species present in the beam exhibits an identifiable signature: a sharp peak at the end of its range. All the fragments produced in a peripheral nuclear collision have the same energy per nucleon, but because of their different charge and/or mass, they exhibit different depths of penetration, as can be deduced from equations (1) and (2).

The measured Bragg peak of the ^{11}C beam produced from 240 MeV/n ^{12}C occurred at a depth of 9.7 cm of water; the unreacted ^{12}C beam emerging from the target had earlier been found to have the Bragg peak at a depth of 10.6 cm. The absence of any ^{11}C peak at 10.6 cm depth confirmed the near 100% purity of the separated ^{11}C beam, and decay measurements confirmed the ^{11}C half-life of 20 min. The beam flux monitored at the experimental area was typically 2×10^7 of ^{11}C particles/pulse compared to the flux of 1.5×10^{10} particles of ^{12}C beam—a yield of about one part in 750.

Results comparing the physical characteristics of ^{20}Ne (the parent beam) and ^{19}Ne (the radioactive beam) are also shown in Fig. 1. Data have been plotted in Fig. 1 to show the Bragg ionization phenomenon for a pure ^{20}Ne beam from the Bevalac. The peak of ionization occurs at 15.6 cm of water, which corresponds to about 425 MeV/n. The separation between the maximum range of the particles and the position of the Bragg peak is only about 2 mm.

In order to produce ^{19}Ne, we put 3 cm of beryllium in the parent beam path so that ^{20}Ne can undergo nuclear fragmentation. A fraction of the parent beam loses one neutron and is converted into ^{19}Ne nuclei. Figure 1 shows the data for ^{19}Ne when this particular beam was tuned into the experimental area. The Bragg peak of ^{19}Ne occurs at 10.25 cm, about 0.95 (= 19/20) times the residual range of ^{20}Ne beam. The residual range of ^{20}Ne after it went through 3 cm of beryllium was 10.8 cm. Beyond the range of ^{19}Ne, there are a few more small peaks, indicating a small contamination with such products as ^{17}F (half-life ~60 sec) and ^{15}O (half-life ~2 min). All these species have approximately the same charge-to-mass ratio and hence could not be separated. Nevertheless, the amount of contamination is very small, and their half-lives and ranges are so different that the electron density measurements done with ^{19}Ne beam are not affected.

SUITABLE RADIOACTIVE BEAMS AND A DETECTOR DEVICE (PEBA)

Positron emission (the decay mode of ^{11}C and ^{19}Ne) allows one to easily pinpoint the location of the nuclear disintegrations that occur where the beam particles stopped. The emitted decay positron stops within a short distance (typically less than 2 mm) and annihilates. Radioactive beams that decay by positron emission have special advantages over other radioactive beams for increased efficiency in detection. The two detectable gamma rays (511 keV) are generate with an angle of 180° between them, and also in time coincidence. In such a situation, collimation is not needed, and the effective solid angle or collection is increased.

In spite of these fine advantages of radioactive beams, much of the success of the technique depends upon the availability of a proper detection device. Such a device—called a positron-emitting-beam analyzer (PEBA)—has been constructed in our laboratory[11] and is shown schematically in Fig. 2.

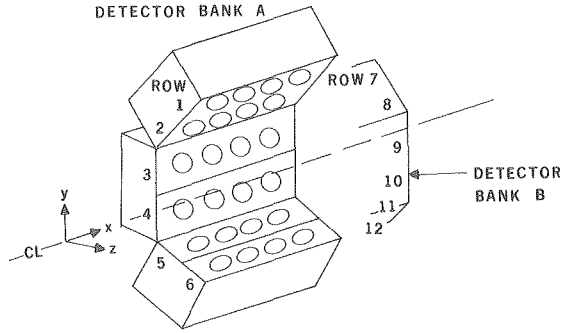

Figure 2. Conceptual design of detector device (PEBA) showing two banks of 24 detectors, defining a volume along path of heavy-ion beam. XBL 772-7742

BRAGG PEAK LOCALIZATION

Several exploratory measurements have been conducted with radioactive beams to test the feasibility of using these beams to measure effective stopping power of heterogeneous media for heavy charged particles. Such measurements will provide direct information on the average electron density and average stopping number (see equation (1)) of a target with an unknown heterogeneous beam path. This information, once obtained with a suitable radioactive beam, can be used in equations (1) and (2) to calculate the energy of any heavy particle of therapeutic choice so that the Bragg peak of the therapeutic beam can be placed on the tumor volume. Figure 3 is a representation of the general geometry used in experiments. A beam of high-energy heavy ions was collimated to a diameter of 1.58 cm (PEBA has a good positional accuracy as long as the beam diameter is less than 2 cm), and made to enter target materials (mixed or homogeneous) positioned between the detector banks and centered along the beam axis.

We have made measurements with ^{11}C and ^{19}Ne beams, but the short half-life of ^{19}Ne (~19 sec) allows prompt repeated measurements, making that nucleus very interesting for our purposes. We will report only the results obtained with it.

Prior to the data collection with the ^{19}Ne beam, a ^{22}Na point source embedded in plastic was used to establish the x = zero reference point on the detector. The activity of the point source was seen by PEBA as a nearly Gaussian distribution with a full width at half maximum of about 1 cm. The centroid of the distribution was established as x = zero. Centroid position was found to be reproducible with ±0.5 mm accuracy, if at least 150 counts were accepted to form an image.

The initial energy of the ^{20}Ne parent beam was 425 MeV/n, and that of the product ^{19}Ne beam was 302 MeV/n. In the experiment reported here, ten pulses from the Bevalac (with a period of approximately 4 sec) were injected into a solid Lucite cylinder 25 cm long and 7.62 cm in diameter. The purpose was to compare the measured beam-path length with the calculated value for a material of well-known composition. The total number of particles injected was 5.94×10^5, yielding approximately 8.95×10^4 disintegrations in the first 10-sec measurement interval starting 4 sec after the end of the irradiation. The Lucite cylinder was placed axially in the beam path, as in Fig. 3. The separation between the two banks of crystals was 20 cm, and all the crystals were focused on the beam axis. The zero of the PEBA device was at 10.1 cm from the leading end (direction of the beam) of the Lucite bar.

Figure 4 shows the data display of the PEBA analysis program. A peak centroid at x = 1.57 cm (PEBA coordinates) is shown. The average activity detected uncorrected for absorption was 59 nCi, with a total of 173 counts collected. The efficiency was found to be 0.26% for the configuration used, consistent with data obtained with fixed radiation sources. Expected error in the measurement was σ = 0.05 cm. The fluctuation depth of the ^{19}Ne beam in repeated measurements was 8.53 cm ± 0.05 cm.

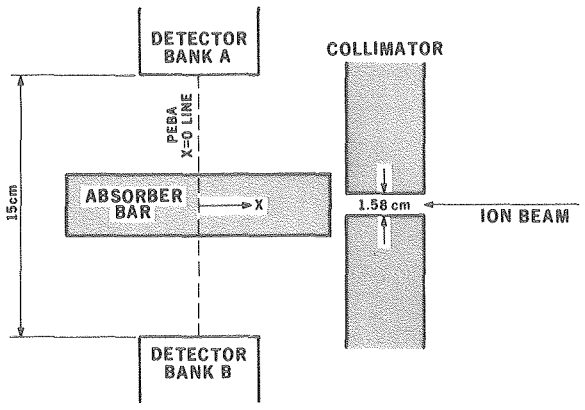

Figure 3. General geometrical setup for experiments with PEBA in irradiation chamber. The x = zero line is placed in center of detector banks. Distance between banks (shown as 15 cm) can be varied so that maximum efficiency can be obtained with irradiation subjects of various dimensions. XBL 788-9963

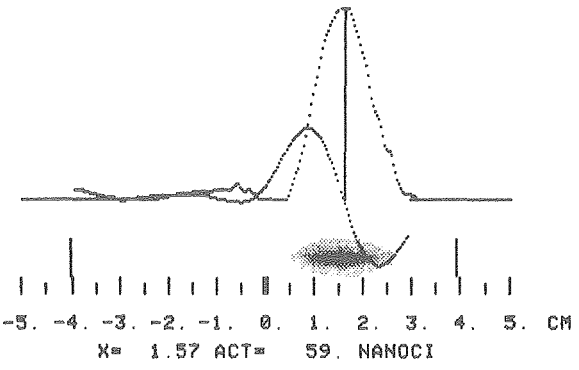

Figure 4. One-dimensional image of end-of-range peak of ^{19}Ne beam of Fig. 1 in an absorber of Lucite. Centroid of peak is measured by convolution of the image with an antisymmetric function selected for insensitivity to statistical fluctuations. This centroid is obtained at the zero crossing of the results of the convolution, also shown (sinusoidal curve). Activity detected was 59 nCi (uncorrected for absorption), the result of 10 sec of counting (4 sec after the end of a 10-pulse irradiation lasting 40 sec). XBL 7912-13606

Since the theoretical mass penetration depth of ^{19}Ne in Lucite is within 1% that of water, and since the density of the plastic had been measured to be 1.186, the theoretical penetration can be calculated as (penetration in water/1.186). From the original data of Fig. 1, we estimate the maximum penetration in water to be 10.3 ± 0.1 cm; the corresponding penetration in Lucite would then be 8.68 ± 0.1 cm. This result agrees well with the PEBA measurements within the expected errors.

Similarly, accurate results were obtained when ranges of ^{19}Ne were measured in pure paraffin (fat-like) and pure $CaSO_4$ (bone-like) materials, establishing the technique with appropriate precision. In another experiment, various thin slices of different materials were interposed between the beam and the solid Lucite cylinder. Progressively, from the beam entry port, the materials were a 3-mm thick $CaSO_4$ plate, a 1-mm Lucite plate, a 9-mm paraffin plate, and the long Lucite column. As in Fig. 4, we examined the video display of the beam-stopping region in the reference material Lucite rod. The residual range in the rod was 7.54 cm, while calculation from the stopping-power formula for the complex heterogeneous column shows the range should be 7.60 cm, a reasonably close agreement.

In the future these measurements will be made with suitable phantoms, with animals, and ultimately with patients. The goal is to demonstrate that the radioactive-beam technique and the PEBA device can provide information useful for planning treatments using heavy particle beams in the Bragg peak region.

POTENTIAL APPLICATIONS OF RADIOACTIVE BEAMS

Irrespective of the choice of therapeutic beam, ^{19}Ne or ^{15}O can always be used to obtain information that will ensure placement of the Bragg peak of the beam at the desired location in a short time. For example, if ^{12}C particles have been selected to treat a tumor volume, ^{19}Ne then can be used to determine the average electron density along the beam path. This information will permit determination of the required energy for ^{12}C particles to stop at the same place where ^{19}Ne stopped. We will verify the correctness of this procedure experimentally by using phantoms and animals. The radioactive-beam technique has the potential of being highly useful, and will not be limited by the choice of a particular therapy beam. Also, the Bevalac will soon have the capability of quickly switching from one beam to another.

Bragg-peak localization will not be the only use of radioactive beams. Its application in nuclear medicine may give rise to new diagnostic techniques that are not possible at present. Because they are instant tracers, radioactive beams can be implanted quickly into the body without invasive methods—even in a single beam pulse of 1 msec duration. In the next instant, their transport can be traced with the help of a suitable detection device. Neon-19, with its 19-second half-life, may be a good candidate for these applications. Radioactive-beam techniques may thus prove to have special advantages over conventional nuclear medicine, which has used surgery or injection to deposit doses of radionuclides. Use of beams as tracers may also yield possible applications for stroke therapy in detecting microcirculation rates in various parts of the brain.

REFERENCES

1. Tobias, C.A., Anger, H.O., and Lawrence, J.H. 1952. Radiobiological use of high energy deuterons and alpha particles. *Am. J. Roentgenol. Radium Ther. Nucl. Med.* 67:1–27.
2. Lyman, J.T. and Howard, J. 1977. Dosimetry and instrumentation for helium and heavy ions. *Int. J. Radiat. Oncol. Biol. Phys.* 3:81–86.
3. Lawrence, J.H., Tobias, C.A., and Linfoot, J.A. 1971. Heavy particles in the treatment of acromegaly and Cushing's disease and their potential value in other neoplastic diseases. In *Nuclear Medicine* (2nd edition), W.H. Bladh, ed., pp. 806–820. New York: McGraw-Hill.
4. Bethe, H.A. 1930. Zur Theorie des Durchgangs schneller Korpuskularstrahlen durch Materie. *Ann. Physik* 5:325–400.
5. Chen, G.T.Y., Singh, R.P., Castro, J.R., Lyman, J.T., and Quivey, J.M. 1979. Treatment planning for charged particle radiotherapy. *Int. J. Radiat. Oncol. Biol. Phys.* 5:1809–1819.
6. Greiner, D.E., Lindstrom, P.J., Heckman, H.H., Cork, B., and Bieser, F.S. 1975. Momentum distributions of isotopes produced by fragmentation of relativistic C-12 and O-16 projectiles. *Phys. Rev. Lett.* 35:152–154.
7. Heckman, H.H., Greiner, D.E., Lindstrom, P.J., and Bieser, F.S. 1971. Fragmentation of nitrogen-14 nuclei at 2.1 GeV per nucleon. *Science* 174:1130–1132.
8. Chatterjee, A., Tobias, C.A., and Lyman, J.T. 1976. Nuclear fragmentation in therapeutic and diagnostic studies with heavy ions. In *Spallation Nuclear Reactions and Their Applications,* B.P.

Shen and M. Kerker, eds., pp. 169–191. Dordrecht-Holland: D. Reidel Publishing Co.
9. Alonso, J.R., Chatterjee, A., and Tobias, C.A. 1979. High purity radioactive beams at the Bevalac. *IEEE Trans. Nucl. Sci.* NS-26(1):3003–3005.
10. Tobias, C.A., Lyman, J.T., Chatterjee, A., Howard, J., Maccabee, H.D., Raju, M.R., Smith, A.R., Sperinde, J.M., and Welch, G.P. 1971. Radiological physics characteristics of the extracted heavy-ion beams of the Bevatron. *Science* 174:1131–1134.
11. Llacer, J., Chatterjee, A., Jackson, B., Lin, J. and Zunzunegi, V. 1979. An imaging instrument for positron emitting heavy ion beam injection. *IEEE Trans. Nucl. Sci.* NA-26(1):634–647.
12. Ghiorso, A., Grunder, H., Hartsough, W., Lamberston, G., Lofgren, E.F., Lou, K., Mair, R.M., Mobley, R., Morgado, R., Salsig, W. and Selph, F. 1973. The Bevalac—an economical facility for very high energetic heavy particle research. *IEEE Trans. Nucl. Sci.* NS-20(3):155–158.

RESPONSE OF MOUSE BONE MARROW AND SKIN TO HEAVY CHARGED PARTICLES

E. John Ainsworth, John C. Schooley, Lynn J. Mahlmann and John C. Prioleau

The studies reported here have two objectives. The first is to explore fundamental radiobiological issues such as relationships between relative biological effectiveness (RBE) and physical parameters of charged particle beams such as linear energy transfer (LET), charge, or velocity. The second is to contribute data on biological responses *in vivo* to charged particles that could be relevant to the use of charged particles for various medical applications. Pursuant to these objectives, we have used two well-known model systems: survival of colony-forming unit in the spleen (CFU-S), as assayed by the Till and McCullough technique, and the early radiation-induced reaction in the flank skin of the mouse. Data have been collected previously by others on the responses of various normal tissues to charged particles, e.g. the gut, testis, esophagus, lung, and spinal cord, but the response of CFU-S has not been described. Our studies in progress on mouse skin response involve a greater number of fractions, and lower doses per fraction, than used in earlier studies by others. It is important to establish clearly any consistent differences between "normal tissues" and cell cultures irradiated *in vitro* with respect to RBE-LET relationships. Additionally, because different normal tissues will vary in radiation sensitivity, repair, and repopulation potential, our knowledge of the spectrum of normal tissue response will be increased by the present studies.

Survival curves for CFU-S are shown in Fig. 1. LAF_1 or CB_6F_1 mice were given graded doses of radiation, their femoral bone marrow was harvested at 2 hours and injected into supralethally irradiated recipients, and the number of spleen colonies present at 8 or 10 days was determined using a low-power microscope. Because there are many points for each survival curve, only the regression lines (computed with a program developed by E.L. Alpen) are presented. The gamma radiation survival curve conforms generally to expectations with an extrapolation number (N) of approximately 1.2 and a D_o of 136 rad. (D_o is the reciprocal of the slope on the exponential portion of the survival curve.) The survival curves for heavy charged particles appear to be adequately fitted by a single exponential, the

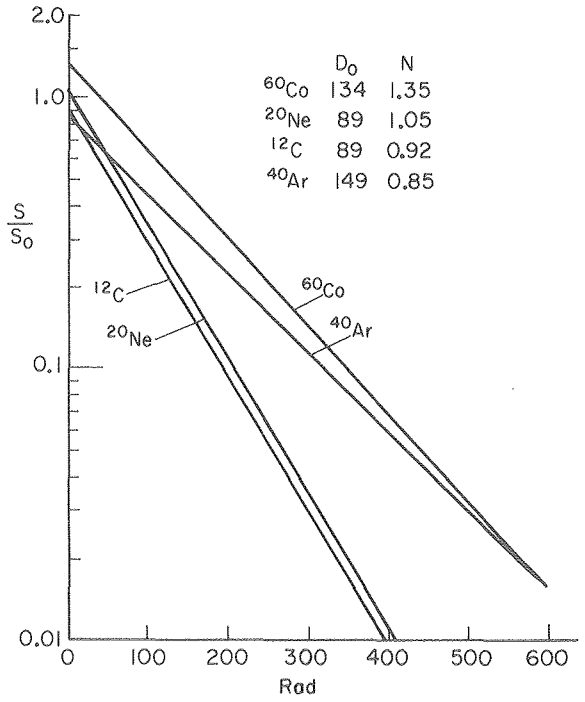

Figure 1. Survival curves for hematopoietic stem cells (CFU-S) irradiated in vivo. Mice exposed to heavy charged particles were positioned at the center of a 4-cm-spread Bragg peak. *XBL 807-3511*

extrapolation numbers are 1 or less, as would be expected for responses to densely ionizing radiations, and the D_o values for neon and carbon ions are identical.

Based on D_o, argon ions appear less effective than carbon and neon ions, as it indicates that "overkill" or "saturation" occurred with ^{40}Ar ions where the dose-averaged LET_∞ is estimated to be 400–500 keV/μm. Interestingly, carbon ions characterized by an LET_∞ of 70 to 80 keV/μm are equally as effective for killing CFU-S as are neon ions characterized by LET_∞ of ~150 keV/μm. Either the maximum killing efficiency occurs at an intermediate LET_∞ where no data are available, e.g. 100–120 keV/μm, or the RBE-LET curve is flat over the range of ~80–150 keV/μm. Over the dimension of a mouse, estimated LET varies greatly, and the most appropriate descriptor for average LET in this exposure geometry remains under study. New information from microdosimetric studies will be important in this regard.

In terms of RBE at the 50% survival level, the RBE for carbon, 2.2, is somewhat higher than the RBE for neon, 1.8. At the 10% survival level, the RBE's for carbon and neon are similar, 1.6 and 1.7 respectively. Lower RBE values, 1.5 and 1.0, are inferred at the 50% and 10% survival levels for argon ions. Extrapolation numbers of less than 1 for carbon and argon ions could be an artifact, but a similar situation has been observed previously for fission spectrum neutrons.

It is of interest that the N value is lowest for ^{40}Ar ions, because this ion is estimated to produce the greatest reduction in the shoulder of survival curve for clonogenic crypt cells in the mouse intestine. Although no data are available at 100–120 keV/μm and a "peak" RBE may have been missed, the results available are consistent with the hypothesis that either the peak RBE for killing CFU-S occurs at an estimated LET value below ~150 keV/μm or the RBE is essentially independent of LET over the range of ~80–150 keV/μm. Since the killing of clonogenic cells in mouse intestine is influenced by particle mass or charge, under conditions where dose-averaged LET is estimated to be quite similar, the use of LET as an independent variable is open to serious question.

Other studies in progress using CFU-S as a model system explore the late effects of irradiation on the size of the CFU-S population in animals in which a portion of only one femur and the tibia/fibula were irradiated. Sustained perturbations in the population kinetics of CFU-S could be related to altered control systems and leukemogenesis. These studies have only recently been initiated and the data are not sufficient to justify further comments here.

Previous studies conducted on mouse skin response at this laboratory by Leith and by Raju at Los Alamos Scientific Laboratory defined the response of the flank and foot respectively after a single dose or only a few fractions of heavy charged particles. Because RBE is related inversely to dose, and because at the doses per fraction used in previous studies extrapolations must be made to predict RBE at doses in the radiotherapeutic range, further mouse skin studies were initiated. Estimates are being made of the amount of repair/recovery that occurs between eight 300-rad fractions of carbon or neon ions or 220 kVp (kilovolt peak) x rays.

The method used was to challenge animals with graded doses of "homologous" radiation at the time of the eighth fraction and at subsequent intervals. (Some were irradiated with heavy charged particles and then challenged with x rays.) The results are still being evaluated and aspects of the dosimetry re-explored, so no firm conclusions are yet appropriate. Using the skin scoring procedures described previously by Leith, the response of animals was tallied 3 times per week between 7 and 35 days after irradiation, and scores over the entire observation period were averaged and are presented in relation to carbon-ion dose in Fig. 2. The dose-response

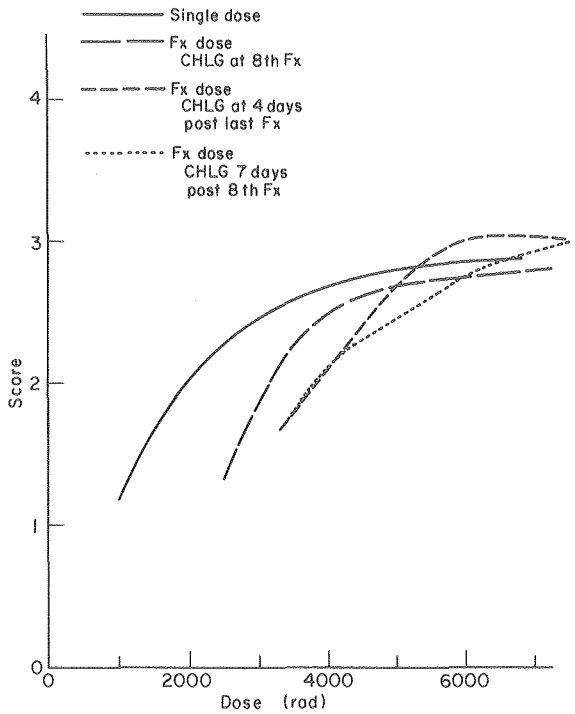

Figure 2. Mouse flank skin response as a function of plateau carbon-ion dose. Responses were evaluated 3 times per week and averaged over 7 to 35 days. XBL 809-3673

curves were eye-fitted and are presented without points for clarity. For illustrative purposes, the figure shows the kinds of results obtained for all irradiations studied. Results for repair/recovery between radiation fractions indicates that a higher total dose must be given to achieve the same reaction level as was produced by a single dose. Likewise, some additional incremental dose was necessary to achieve a given reaction level when animals were challenged at either 4 or 7 days after the eighth radiation fraction. The most probable explanation is that cell proliferation occurred following completion of the eight fractionated doses, thereby increasing the skin tolerance to an additional dose of radiation. When full assessment is completed of radiation dosimetry and the average or peak responses of the skin following the other radiations studied, it is expected that RBE estimates can be provided for the skin response after single doses, and estimates of repair/recovery and proliferation before each irradiation quality can be made.

The technical assistance of Colleen Cogorno, Andy Shih, and Para Lee is gratefully acknowledged.

LIFE-SPAN STUDIES ON MICE EXPOSED TO HEAVY CHARGED PARTICLES OR PHOTONS

E. John Ainsworth, John C. Prioleau and Lynn J. Mahlmann

The carcinogenic risk associated with heavy charged (HZE) particles is currently undefined. Precise relationships have been established for relative biological effectiveness (RBE) and linear energy transfer (LET) for the killing of cells *in vitro* and for other short-term (acute) biological responses to charged particles, but comparable information is lacking on carcinogenic response. Experiments are in progress to study induction/promotion of Harderian gland tumors, and the present life-span studies should provide complementary information because it is inferred that over the dose range explored in the present experiments, most of the life shortening is attributable to induction/promotion of neoplastic diseases. The information sought is important both for understanding fundamental mechanisms of radiation carcinogenesis and for assessing the risk of the space radiation environment and of radiation therapy or other medical applications of heavy charged particles in young patients whose life expectancy could permit expression of a tumor.

The hypothesis tested in the core experiment that we have designated SKYHOOK is that LET_∞-dependence for life shortening and excess mortality rates observed after mice are exposed to heavy charged particles (HZE) will conform to existing theory and observations based on other endpoints; namely, a peak RBE at a dose-averaged LET_∞ value of approximately 100 keV/μm, with RBE diminishing at lesser and greater values of LET_∞. Because results on cell killing obtained by E.L. Alpen in this laboratory show different RBE values, at the same approximate LET_∞, for different charged particles, the possibility exists that LET_∞ by itself is not a fully adequate descriptor for biological response, and physical characteristics such as mass, charge, or velocity may also be of great importance.

The experimental design for SKYHOOK is shown in Table 1. The HZE particle and gamma radiation doses selected are the same as those used previously in similar studies that compared life shortening and carcinogenic effects of fission-spectrum neutrons and gamma radiation. One fundamental question addressed by this pilot experiment is the extent to which at least certain charged particles serve as a surrogate for fission spectrum neutrons or simulate the neutron response. In the practical matter of risk assessment, should charged particles prove to be less hazardous than fission spectrum neutrons, then any quality factors chosen for neutrons should be conservative, and appropriate, where the risk of charged particles is projected. If any charged particles are more carcinogenic than neutrons, that fact must be revealed.

At dose-averaged LET_∞ values that range from <1 to ~ 500 keV/μm, the effects of stopping and nonstopping particles or gamma radiation are compared specifically to address the question of the adequacy of LET_∞ as a descriptor for biological response and RBE. The principal endpoint in the SKYHOOK experiment is excess mortality rate, days of life-span loss, and percent life shortening in relation to dose and other physical properties of the radiations studied. Some autopsies are being performed, but staffing is not adequate at present to provide for complete studies of carcinogenesis responses in these animals. It is hoped that such efforts can be expanded in the future, and collaborative arrangements are being explored with personnel at the NASA Ames Research Center.

Table 1. Particle and dose conditions administered to 2640 B6CF$_1$ Male Mice (Revised SKYHOOK I protocol).

Radiations		Single dose (rad)		Fractionated doses (rad)		
5 HZE Particle conditions		Dose	N	Total	Dose/ Fraction	N
^{12}C-SOBP*.†	~80 keV/μm	0	50	50	0.0	50
		40	80	40	1.6	80
^{20}Ne-plateau	~32 keV/μm	80	50	80	3.3	50
^{20}Ne-SOBP	~150 keV/μm	120	50	120	5.0	50
^{40}Ar-plateau	~100 keV/μm	160	50	160	6.6	50
^{40}Ar-SOBP	~500 keV/μm	240	50	240	10.0	50
		320	50	320	13.3	50
^{60}Co Gamma	<1 keV/μm	0	50	0	0.0	50
		143	80	417	17.3	80
		268	50	569	23.7	50
		417	50	845	35.0	50
		569	50	1416	60.0	50
		788	50	1889	79.0	50

** SOBP = spread-out Bragg peak.*

† In addition to administration of regular fractionated doses of ^{12}C ions, total-dose dependence is assessed by exposing groups of 50 mice to single doses of 40, 80 or 160 rad of stopping carbon ions, and within 1–2 hours thereafter, administering a single dose of 268 gamma rad.

Most of the animals in the SKYHOOK project have received the single doses of charged particles or photons indicated in Fig. 1 so that dose-response relationships can be determined. Results from this single-dose study must be in hand before any additional studies can be planned to address response at lower radiation doses, should they be deemed necessary.

To test the hypothesis that photon and HZE particle-induced damage is independent and that no interaction exists when doses are separated by 30 minutes to 2 hours, groups of 50 animals were given graded doses of carbon ions followed, as soon as feasible, by a single gamma radiation dose. Because all computations of rem (Roentgen equivalent in man) dose assume independence where high and low LET radiations are present in a complex radiation environment, it seems appropriate to test the hypothesis that no interactions occur.

Approximately 320 animals have received 24 weekly doses of carbon ions or gamma radiation (Fig. 1) to establish the extent to which life-shortening responses are either reduced or increased as a consequence of dose fractionation. Previous results have shown that fractionation of the gamma radiation dose markedly diminished the life-shortening effect per rad, whereas fractionation of the fission neutron dose increases life shortening and excess mortality even at a total dose of 20 rad. When

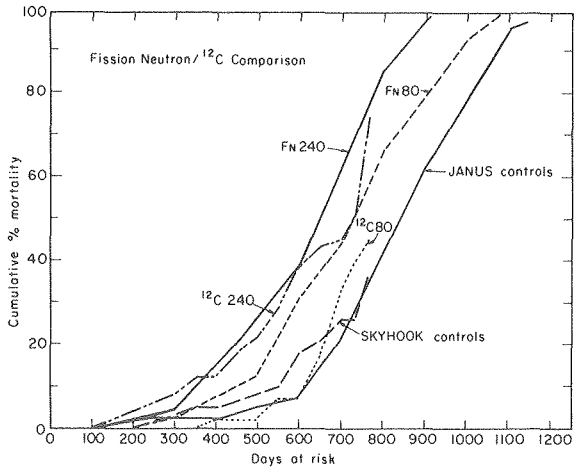

Figure 1. Cumulative mortality among animals that received 240 or 80 rad of either carbon ions or fission spectrum neutrons (Fn). *XBL 8010-3769*

the single-dose results are in hand, the appropriateness of extending the fractionation studies to other heavy charged particles will be evaluated.

Mortality from the SKYHOOK experiment is insufficient at this time for even preliminary conclusions to be drawn, but results are available from another experiment, designated SKYHOOK-P, that was initiated prior to SKYHOOK. The original intention was to use the same strain of mouse, the B$_6$CF$_1$,

in SKYHOOK as was used previously in neutron/gamma ray studies at Argonne National Laboratory. This proved to be impossible because of unavailability of this hybrid, but approximately 180 of those mice were available from Argonne. These, in groups of 40–45, were given single carbon ion doses of 80 or 240 rad, or a single gamma radiation dose of 788 rad, and approximately 40 served as unirradiated controls. Unfortunately, the mice were not all of uniform age at the time of irradiation, and this may complicate interpretation of the results. Figure 1 compares cumulative mortality among animals that received 240 or 80 rad of either carbon ions or fission spectrum neutrons. At 240 rad the pattern of mortality is similar for carbon ions and neutrons, but at the total dose of 80 rad, earlier mortality was observed among neutron-irradiated animals than among animals irradiated with carbon ions. We infer from these results that carbon ions pose no greater hazard level than fission neutrons, and based on the results at 80 rads, carbon ions could be less hazardous where life shortening is the endpoint.

The technical assistance of Colleen Cogorno, Andy Shih, and Para Lee is gratefully acknowledged.

CATARACTOGENIC EFFECTS OF HEAVY CHARGED PARTICLES

E. John Ainsworth, J.G. Jose, Mary E. Barker, and Vivian V. Yang

Manned space flights may increase in the future in connection with the use of advanced technologies such as Satellite Power Systems (SPS) to generate electricity. Many of the risks associated with extended habitation and work in a space environment remain undetermined; of particular concern are the hazards of high-energy, heavy charged particles (HZE) to which space workers will be exposed. One important tissue at risk is the eye, especially the cornea, lens, and retina. The cataractogenic effects of other densely ionizing radiations, or high linear energy transfer radiations (high LET), such as neutrons, have been studied previously by others, but no data are available on the cataractogenic effects of HZE particles. This project evaluates the cataractogenic effects of non-stopping and stopping HZE particles on the crystalline lens of the CB_6F_1 mouse. (Other projects in the Biology and Medicine Division are exploring effects on cornea and retina.) The principal effort has been directed toward semiquantitative assessment of radiation-induced cataracts by slit-lamp biomicroscopy; more recently morphologic changes have been evaluated by both light and electron microscopy. If relationships between early morphologic changes and the probability of subsequent cataract formation can be established, especially over a range of low doses, the time and effort expended in sequential cataract assessment by slit-lamp biomicroscopy could be decreased.

Mice 80–110 days old were given graded doses of 220 kVp x rays, or non-stopping (plateau) ^{12}C, ^{20}Ne, or ^{40}Ar ions from the Bevalac to the upper body only. Thus, a dose-weighted LET range from a few keV/μm to approximately 100 keV/μm is being evaluated and the findings will permit inferences to be drawn concerning LET-RBE relationships. Commencing at approximately 6 months, when cataracts first began to develop after the highest doses used, the mice have been evaluated every 2 to 3 months. The severity of cataracts, or the fraction of the lens affected, has been scored on a 1.0 to 4.0 basis: a value of 0.5 indicates an abnormal lens where 1.5% of the posterior lens is involved; a score of 4.0 indicates 50% or greater involvement. The results available at 13 months after irradiation from our first replicate are shown in the Fig. 1. The sample sizes are 15 to 18 per dose-group, and the x-ray doses are 10 times those shown on the abscissa, as indicated in the figure legend. The results show the expected LET_∞-dependence with ^{40}Ar ions being the most cataractogenic and 220 kVp x rays being the least; within the charged particle realm alone, there is some indication that neon ions characterized by an LET_∞ of approximately 32 keV/μm are more effective than are carbon ions where the estimated LET_∞ is approximately 12 keV/μm. The experiment was designed and the doses selected such as to exclude an RBE of 10 or greater over a HZE particle dose range of 30–90 rad. The results available at this time indicate that the RBE for the most effective heavy charged particle, namely ^{40}Ar ions, characterized by an LET_∞ of approximately 100 keV/μm, is less than 10. A replication was planned at the outset to increase sample sizes and the reliability of the data collected, and when the early results became available, it was clear that dose selection for the second x-ray replicate should concentrate at doses between 15 and 300 rad so that accurate estimates of RBE could be made within the "low dose" realm. All of our irradiations are now completed for Replicate II. Additional animals have also been irradiated and are

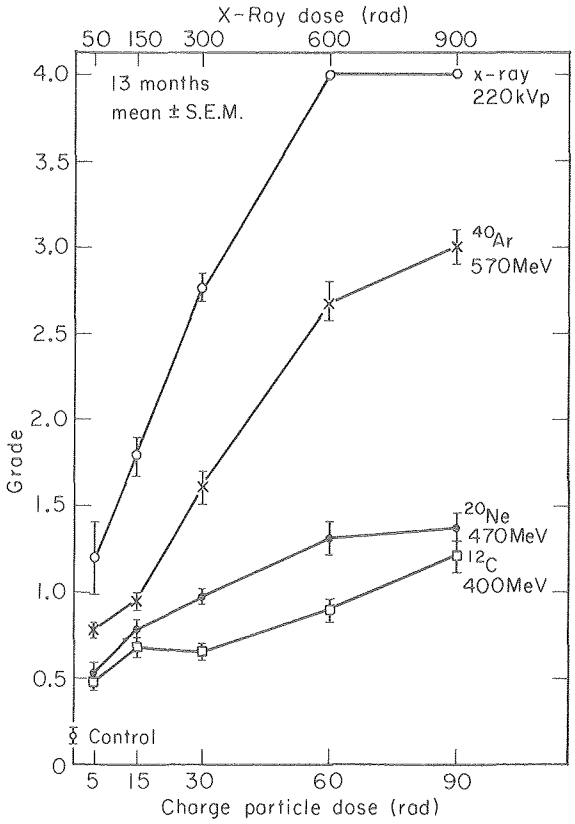

Figure 1. Average cataract score in groups of 16–18 CB_6F_1 mice at 13 months after irradiation. *XBL 809-3671*

programmed for serial sacrifice to provide critical morphological data. The current plan is to continue biomicroscopic examinations on these animals until we are convinced that we have accurate average severity score plateaus. This appears essential since any estimate of RBE could be influenced by the time at which the assessment was made, if indeed, the cataractogenic process is progressive. Preliminary results, not presented here, from animals exposed to stopping ^{20}Ne particles indicates that the cataractogenic process is progressive to at least 24 months after irradiation.

Slit-lamp evaluations have also been done on animals dedicated to other experiments and some useful data have been collected. A few examinations have been completed on animals exposed to stopping (4-cm-spread Bragg peak) ^{12}C ions in connection with ongoing studies on life shortening and carcinogenesis. The results show that when doses of 40, 80 or 120 ^{12}C rad were administered in 24 equal fractions over 24 weeks rather than as a single dose, there is no reduction in the cataractogenic effects; this contrasts markedly with the effects of fractionation of a cobalt-60 gamma radiation dose of 417 rad because a large degree of sparing was observed. Although the sample sizes are quite small (5–20), we have been able to evaluate animals exposed to ^{56}Fe ions in connection with a study of Harderian gland carcinogenesis. At approximately one year after irradiation, significant corneal and lens lesions were observed in 10% to 40% of the animals.

Preliminary morphologic studies show that at 15 months after 5 or 30 ^{20}Ne rad the bow region of the mouse lens was quite similar to the control group. However, the epithelial nuclei at the bow region showed abnormality after 90 ^{20}Ne rad. At this dose, the anterior and posterior fibers of the lens also demonstrated irregularity in shape and size. The degenerative changes were more severe in the animals that were exposed to ^{40}Ar particles. The lens fibers at the bow region were only slightly disrupted after 5 rad. After 30 rad, the fibers at the bow area and anterior superficial region contained areas of advanced swelling and vacuolation (Fig. 2). The degenerative changes of the anterior fibers in mice that received 90 ^{40}Ar rad appeared in the deeper midcortical regions compared to the ^{20}Ne irradiated mice. In general, the morphology of cataract damage to the lens by HZE particles are similar to those caused by photons. We also found that a much higher dose of x-ray irradiation, 300 rad, was required to induce comparable degenerative changes in the bow region as seen at doses as low as 5–30 rad range in the HZE-treated animals. Additional data are needed before meaningful RBE estimates

Figure 2. Electron micrograph of anterior cortical region adjacent to the bow area of lens at 15 months after 30 rad of 570 MeV ^{40}Ar. Note the swelling and apparent vacuolation of the fibers. *XBB 808-10087*

for bow disruption can be made. Early morphological changes to the lens should be evaluated at various early times after irradiation to determine the initial site of HZE damage and mechanisms of HZE-induced lens opacification. We also are undertaking a preliminary examination of the cornea of these animals.

The contributions of Dan Judd, Bennett McAllister, and Steven Dentone to these studies are gratefully acknowledged. We also acknowledge the technical assistance of Colleen Cogorno, Andy Shih, and Para Lee.

LATE CARDIOVASCULATURAL EFFECTS OF CHARGED PARTICLE IRRADIATION

Vivian V. Yang, Mary E. Barker, and E. John Ainsworth

Vascular damage results from exposures to ionizing radiation and other environmental insults and from normal aging. The use of a slowly dividing tissue such as the coronary vasculature to study these effects provides a direct method of evaluating late morbidity and mortality and the long-term risks associated with nuclear technologies.

It has been demonstrated that injuries to blood vessels as well as the heart musculature can result from exposures to x rays, gamma rays, and fission neutrons. However, the risk to the cardiovasculature for charged particles is unknown for both human and animal species. Based on clinical observation, we know that late radiation damage to the cardiovascular system is a contributing factor to degenerative changes in all tissues and can be a significant factor in the patient response to radiotherapy. In fact, even when a tumor has been successfully treated, the vascular damage caused by radiotherapy can later endanger the patient. For example, heart failure many years after treatment of breast or lung tumors with cobalt-60 gamma rays is recognized as a potential hazard.

Although charged particles are now being used for the treatment of cancer patients, there has been no systematic investigation of their biological effects on the vasculature. This study is designed to evaluate the ultrastructural changes in the hearts and cardiac vessels of mice after exposure to charged particles. The quantitative morphological analysis of coronary damage will provide baseline information on dose-response relationships and relative biological effectiveness (RBE) for various charged particles characterized by different ionization densities.

The most predominant ultrastructural changes in the hearts of mice after exposure to charged particles were found in the larger coronary arteries. The preliminary data reported here are based on the examination of mice in experiments on Harderian gland carcinogenesis. The mice had been sacrificed at 15 months after receiving charged-particle radiation (160 rad of ^{40}Ar; 20, 40, or 80 rad of ^{20}Ne; 80 or 160 rad of ^{2}He) and compared with age-matched controls. In the control animals (Fig. 1) the coronary artery endothelium was continuous; the subjacent intimal region contained a variable amount of basal lamina material and was separated from the media by the internal elastica. Collagen and elastic fibers were present between smooth muscle cells in the media; collagen predominated in the adventitial layers. Minute areas of degeneration in smooth muscle cells were also noted. Irradiation produced various degenerative changes in the larger coronary arteries at 20 rad ^{20}Ne (Fig. 2), and these changes were more severe at 80 rad ^{20}Ne and 160 rad ^{40}Ar (Fig. 3). In the control group, about 11% of the smooth muscle areas examined showed deterioration (Table 1). In the irradiated groups, this percentage increased significantly, ranging between 20 and 40%.

The patterns of morphological damage in the mice hearts were quite similar to those found after cobalt-60 gamma rays and fission neutron radiation described by Yang et al.[1] Accumulation of matrix material that stains positively with Schiff periodic

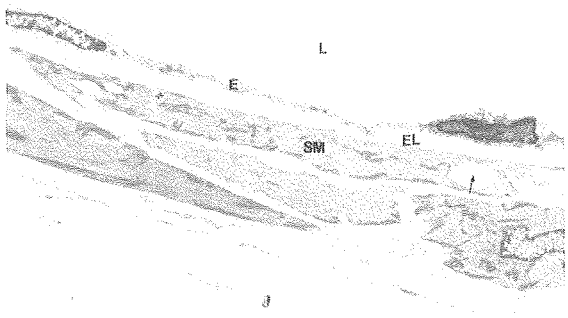

Figure 1. Electron micrograph of coronary artery from control animal. Continuous endothelium (E) lining the lumen (L), smooth muscle (SM), elastic lamina (EL) and small area of smooth muscle degeneration (arrow) are noted. Magnification: 2900×. *XBB 809-10515*

Figure 2. Electron micrograph of coronary artery after 20 rad Ne dose. There is fragmentation of smooth muscle cells (SM) with accumulation of matrix material (arrow) and fibrosis (F). Magnification: 2800×. XBB 809-10516

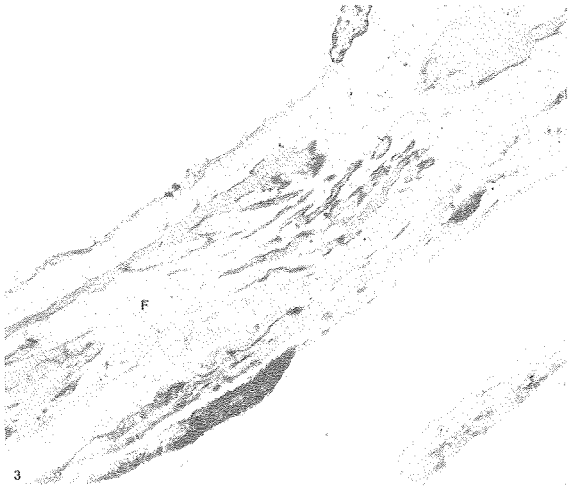

Figure 3. Electron micrograph of coronary artery after 160 rad Ar dose. There is marked loss of medial smooth muscle with extensive fibrosis (F). Magnification: 3350×. XBB 809-10514

*Table 1. Mean fractional volume (V_v) of degenerated smooth muscle cells in coronary arteries.**

No. of Mice	Radiation Parameters	Dose (rad)	V_v
3	570 MeV ^{40}Ar-4 cm SOBP	160	$0.43 \pm 0.05^{\dagger}$ n = 10‡
3	470 MeV ^{20}Ne-4 cm SOBP	80	$0.31 \pm 0.04^{\dagger}$ n = 9
3	470 MeV ^{20}Ne-4 cm SOBP	40	$0.29 \pm 0.03^{\dagger}$ n = 7
3	470 MeV ^{20}Ne-4 cm SOBP	20	$0.20 \pm 0.04^{\S}$ n = 7
3	920 MeV ^{2}He-10 cm SOBP	160	$0.22 \pm 0.01^{\dagger}$ n = 9
3	920 MeV ^{2}He-10 cm SOBP	80	$0.22 \pm 0.01^{\dagger}$ n = 9
3	Control	0	0.11 ± 0.02 n = 9

Mean ± SEM
**These values are for non-nuclear cytoplasm*
$^{\dagger}p<0.001$
‡*n = numbers of coronary arteries examined*
$^{\S}p<0.005$

acid, indicating the presence of mucopolysaccharides, was shown to be one of the earliest changes in atherosclerosis. The loss of integrity of smooth muscle cells in larger arteries after exposures to charged particles may influence long-term cardiovascular functional capacity. One of the significant findings in this study was the appearance of plaques in the coronary arteries of animals exposed to 80 rad ^{20}Ne and 160 rad ^{40}Ar (Fig. 4). These plaques appear to involve smooth muscle proliferation and resembled lesions associated with human cardiovascular disease.

In order to determine comprehensively the RBE and linear energy transfer (LET) relationships for vascular injury, we hope to evaluate additional animals given an array of doses of various charged particles and photons. We are also planning to study the morphological changes that occur at 4 days, 1 month, 6 months, and 12 months after irradiation in order to elucidate the mechanisms of damage to the coronary vasculature caused by charged particles.

Figure 4. Electron micrograph of coronary artery after 160 rad Ar dose. Arrows mark an intimal plaque. There is fragmentation of the internal elastic lamina (IE), and plaque contains smooth muscle cells (SM), debris, and fibrosis. Magnification: 4100×. *XBB 809-10513*

REFERENCE

1. Yang, V.V., Stearner, S.P. and Ainsworth, E.J. 1978. Late ultrastructural changes in the mouse coronary arteries and aorta after fission neutron or ^{60}Co γ irradiation. *Rad. Res.* 74:436–456.

CELLULAR RADIOBIOLOGY OF HEAVY-ION BEAMS

Cornelius A. Tobias, Eleanor A. Blakely, Frank Q.H. Ngo, Ruth J. Roots, and Tracy C. Yang

RBE AND OER MEASUREMENTS OF SILICON ION BEAMS

The relative biological effectiveness (RBE) and the oxygen enhancement ratio (OER) have been used to evaluate the radiobiological properties of accelerated charged particles for potential use in cancer radiotherapy. Track segment survival experiments have been performed with carbon, neon and argon beams with initial energies of several hundred MeV/amu. Carbon and neon beams have a greater advantage than argon in the ratio of depth to entrance biological effectiveness; however, argon has the lowest OER among the three beams studied.[1] These observations led to the proposal by Tobias et al.[2] that an ion with an atomic number between neon and argon would retain an effective depth dose profile, while maintaining a low OER. Consequently, a silicon beam has been used to test this hypothesis.

Two experiments have been completed with human T-1 cells using silicon beams with two initial energies (530 MeV/amu and 670 MeV/amu). Some representative results are illustrated in Fig. 1. In brief, the silicon data are consistent with the proposed hypothesis, and with expectations based on previous measurements from neon and argon beams of comparable range. The OER profile is very similar to argon, but the RBE profile is more like that of neon. Cell survival measurements for the 4-cm extended peak indicate that silicon may be of significant therapeutic usefulness for deep-seated tumors.

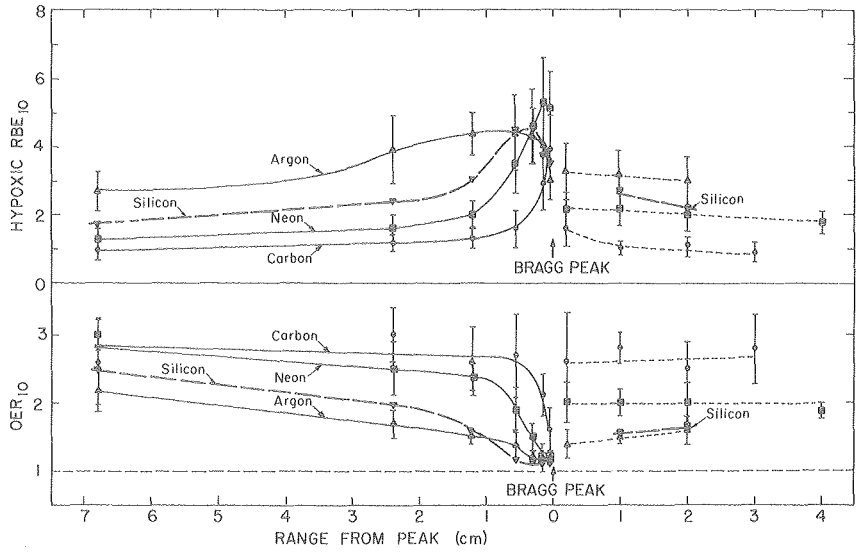

Figure 1. OER and hypoxic RBE at 10% survival as a function of beam range for carbon, neon, silicon and argon. Error bars represent 95% confidence interval. *XBL 808-3603*

HEAVY-ION CELL CYCLE PROGRESSION EFFECTS

There have been studies of division delay, and/or G_2-block, induced by several high-LET (linear energy transfer) radiation modalities, including neutrons, pions, alpha particles and heavy ion beams. Lücke-Hühle et al. (1979) quantitatively measured cell cycle progression effects induced by high energy heavy ions at the Bevalac, using Chinese hamster V-79 monolayers in track segment experiments with monoenergetic heavy ion beams. They observed a profound G_2-block which had an LET dependence similar to the cell killing endpoint, but with a greater biological effectiveness. In contrast to results from γ-rays and x-rays, they found with flow-microfluorometry (FMF) techniques that heavy ions did not affect cell traversal through the G_1 and S phases.

We have extended this investigation by measuring percent labelled mitoses (PLM), mitotic index and cell numbers and survival after exposure to the same Bevalac beams. The PLM techniques have been discussed elsewhere,[3] as have the cell- and colony-count methods.[4,5] A major goal of this project was to study perturbations in the progression of cells through the division cycle, using several experimental techniques. The FMF and the PLM techniques do not distinguish between cell kinetics for surviving cells versus the kinetics of cells that will eventually die from radiation damage. The colony-count assay, however, can be used to measure the delayed growth kinetics due only to surviving cells at times post-irradiation. Hence, we were interested in correlating results from these different techniques in order to evaluate whether the potentially surviving and non-surviving cells undergo similar delayed kinetics.

We have completed the initial phase of this study, which used the PLM technique on asynchronous cell populations. A second phase, which is in progress, includes the study of synchronous cells with the colony assay. As an example of our preliminary asynchronous results, the PLM curves following neon peak irradiation are depicted in Fig. 2.

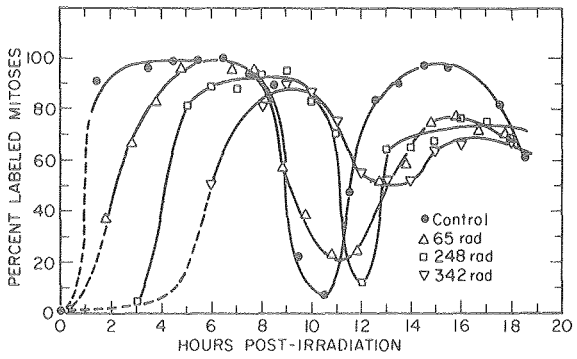

Figure 2. PLM results from a single neon-peak experiment. The doses causing the more dramatic shifts of curves to the right are lower than those of the x-ray (control) experiment. Also, for the high dose the second wave of labeled mitoses is probably perturbed by cells that are blocked in M, or that were at G_1 at the time of irradiation but have moved to mitosis. Both factors complicate interpretation of these curves at this postirradiation time. *XBL 805-3356*

Based on the resolution afforded by this technique, the following tentative conclusions may be drawn:

(1) High-LET radiations induced delay in G_2 and M phases at a rate greater than that induced by similar killing doses of x rays. This is consistent with results from the previous FMF analysis of Lücke-Hühle.

(2) The magnitude of delay in G_2 + M increases linearly with dose, at least up to the dose region corresponding to 2% survival. The linear dose-effect relationship applies to all radiation qualities. This is consistent with previous FMF measurements of Lücke-Hühle, and similar to division delay observed by Elkind et al.,[5] and Ngo et al.,[6] but is different from the exponential dose dependency for mitotic delay described by Schneider and Whitmore[7] and by Skarsgard et al.[8] The latter authors used much higher doses, however.

(3) The PLM techniques presently employed for asynchronous populations do not allow an unequivocal determination of the prolongation of S phase. Work is in progress to study differences in the mechanism of the G_2 block and division delay for low- and high-LET radiations.

POTENTIATION OF LETHAL EFFECT FOLLOWING FRACTIONATED EXPOSURES

We have shown previously for Chinese hamster V79 cells that two doses of high-LET heavy-ion radiations separated by 2 to 3 hours are more effective in cell killing than when the two doses are administered at once.[9] We called this unconventional phenomenon a potentiation effect. Potentiation was not observed with low-LET or intermediate-LET irradiations, such as occurs with Bragg plateau exposures for the high-energy carbon or neon ion beams. In these cases, the two-dose repair was measured.

One possible explanation of the potentiation effect is radiation-induced cell synchronization. That is, following the first exposure, the population undergoes a redistribution of the density distribution of cell-stages, such that a few hours later an inherently more sensitive population is irradiated by the second dose. Experiments have been designed to test this hypothesis.

At room temperatures (~22°C), a majority of V79 cells previously in exponential growth phase would be halted from progression. Hence, if synchrony were the only mechanism involved in the potentiation effect, one would expect that no potentiation would be observed when cells were incubated at room temperature (RT) during fractionation. Two types of experiments have been conducted with the same cell line and a neon-ion beam at the Bragg peak (F position). The dose-average mean LET_∞, as estimated by Tobias, was 183 keV/μm. The data are shown in Fig. 3. In the left panel, synchronized mid-S (5.5 h after mitosis)

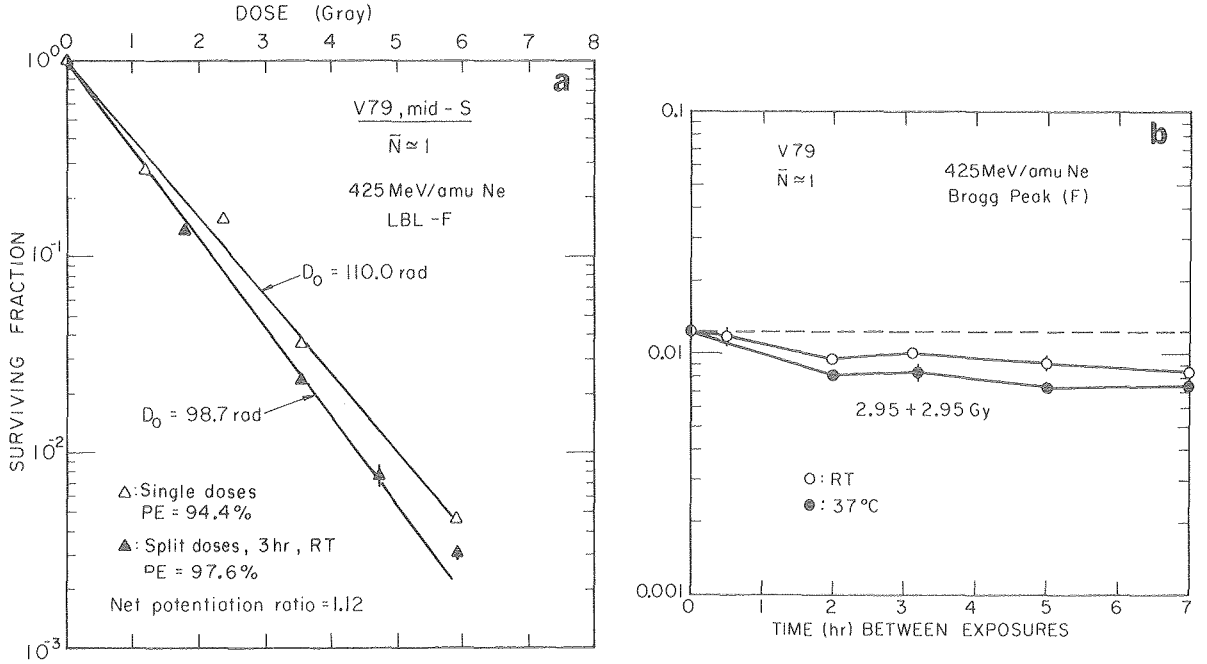

Figure 3. Further studies of dose-fractionation effects on V79 cells with $^{20}_{10}Ne$ at position F: (a) survival data for synchronized V79 cells in mid-S stage following single and split-dose irradiations; (b) survival data of asynchronous V79 cells irradiated with two doses separated by various incubation times, at either RT or 37°C. XBL 806-3389A

phase cells were irradiated with single graded doses of high-LET neon ions, or with a pair of doses, between which the samples were incubated at RT for 3 h in a humidified air incubator containing 5% CO_2 to maintain the pH control of the growth medium. According to the cell-age response curve we have measured, mid-S phase cells are less resistant to the neon beam than late-S phase cells (8 h after mitosis).[10] (1980a). Hence, even if the synchronized population after the first doses continued its progression into a later S phase, one would expect that the two-dose survival curve should lie above the single-dose curve. In contrast, the data show the opposite.

In the right panel, an asynchronous population was irradiated with two equal doses of neon with the fractionation interval varying from 0 up to 7 h. During the two-dose intervals, the samples were kept at either RT or 37°C. The dashed line represents the survival due to the sum of the two doses given at once. It is seen that two-dose potentiation occurs with either temperature used for incubation, but quantitatively less effect was associated with RT incubation throughout the 7 h period. These observations imply that at least two mechanisms are involved in the effect of potentiation, only one of which is due to radiation-induced cell synchronization. Further quantitative biochemistry is needed to clarify the mechanisms and LET dependence of the potentiation effect.

POTENTIALLY LETHAL DAMAGE

Potentially lethal damage in actively growing cells

The lethal expression of potentially lethal damage (PLD) may be modified by alterations in postirradiation conditions.[11] It has been reported that treatment of cells with hypo- or hypertonic solutions prepared by varying the concentration of NaCl in phosphate buffer solution (PBS) can enhance the lethal expression of PLD after x- or neutron-irradiation.[6]

Using hypo- and hypertonic NaCl/PBS treatments, we have addressed these questions: (1) Is there any difference in the mechanism of radiosensitization by hypotonicity compared to hypertonicity? (2) How do the PLD repair kinetics in question change with radiation quality? We have completed a series of experiments using Chinese hamster V79 cells in culture and energetic heavy-ion charged particles produced at the Bevalac.[12] Cells in exponential-growth phase were treated with 0.04 M NaCl/PBS (hypotonic) or 0.5 M NaCl/PBS (hypertonic) for 20 minutes during or immediately after heavy-ion irradiations. Cells treated with 0.14 M NaCl/PBS (isotonicity) postirradiation for the same period of time were used as controls. Results were quantified by colony-forming assay and by analysis of survival-curve shapes. The hypo-, hyper- or isotonic treatments alone were non-toxic to the V79 cells. The heavy ions used were 400 MeV/n carbon and 425 MeV/n neon; they cover a range of dose-average mean LET_∞:16,38,85, and 183 keV/μm.

Results indicated that: first, anisotonic treatments given postirradiation were always more effective in enhancing radiosensitization than the same treatment given during irradiation. Second, computer-fitting analysis of the survival curves indicate that for a given radiation, both the hypo- and the hypertonic treatments postirradiation increased the final slope ($1/D_o$) of the curve to approximately the same degree, the extent of which, however, decreased as LET increased (Fig. 4). Third, within experimental uncertainty, only the hypertonic treatment caused a significant increase of the initial slope (low-dose region); the hypotonicity treatment did not increase the slope. The change in initial slope with hypertonicity also appears to decrease with increased LET (Fig. 4). We notice, however, for the highest LET radiation (~183 keV/μm) used in this study, the amount of PLD produced is still significant (Fig. 4). Fourth, the repair kinetics of this type of PLD were rather rapid, with a half time of about 15 minutes, and appear to be LET-independent.

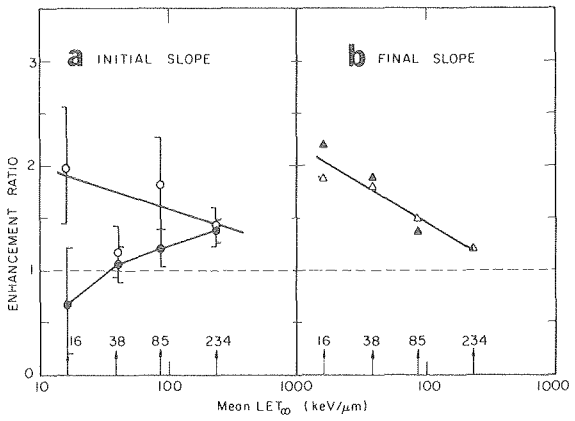

Figure 4. The effects of postirradiation treatments with hypertonicity (0.5 M NaCl, closed symbols) or hypotonicity (0.04 M NaCl, open symbols) on (a) initial slope and (b) final slope of survival curves as a function of LET values. Error bars represent 95% confidence limits. XBL 805-3363A

We may conclude from these observations:

1. The mechanism responsible for the sensitization effect by anisotonicity is primarily a suppression of repair, or an enhancement of misrepair of PLD induced by radiation.

2. This PLD is not entirely similar to sublethal radiation damage.

3. The hypo- and the hypertonicity treatments may each affect the single-track inactivation rate differently.

4. The amount of PLD decreases with increased LET, but at an LET of 183 keV/μm a significant magnitude is still present.

Potentially lethal damage in plateau-growth cells

Repair of PLD inflicted by heavy ions or x rays has been investigated in plateau-growth cells by T. Yang using the delayed plating technique. Mouse embryo cells, C3H10T1/2, which are widely used in chemical- and radiation-induced transformation studies, were grown to a confluent phase at which cell proliferation stopped because of contact-inhibition. Survival levels were compared between confluent cells that were trypsinized immediately after irradiation and cells that were kept in confluent phase for various lengths of time before plating. Prolonged incubation of these cells, up to two days, showed no appreciable effect on plating efficiency.

Interestingly, we found that repair of PLD was almost completed within 6 hours after x-irradiation, while it could take as long as 24 hours to reach completion after an exposure to argon particles. This LET-dependent phenomenon, compared to the LET-independent observations made by anisotonic assays, suggests that at least two types of PLD may be induced by radiation. Experiments are in progress to study possible differences in repair of PLD due to cell lines or cell growth conditions.

RADIATION INDUCED MACROMOLECULAR LESIONS AND CELLULAR RADIATION CHEMISTRY

Our studies of the interaction of densely ionizing particles with macromolecules in the living cell may be divided into four parts: characterization of lesions to cellular DNA in the unmodified Bragg ionization curve;[13] characterization of lesions to cellular DNA in the spread Bragg curve as used in radiation therapy; and elucidation of the cellular radiation chemistry characteristic of high vs. low LET radiation qualities. A report on the first two parts of these studies was made in last year's annual report, while the third is presently under investigation in the collaboration with A. Chatterjee.

The radiation chemistry that is important in radiation-induced cell killing changes as the ionization density (radiation quality) changes. For low-LET radiations, such as x rays, slightly more than 50% of the total radiation induced lethality is caused by the hydroxyl radical (OH•) as reflected by the fact that the D_o dose more than doubles when cells are protected maximally against OH-radical attack. However, as the ionization density in a particle track increases, the importance of OH-radical action diminishes, partly because of radical recombination reactions. Cell monolayers, grown in glass vessels, were irradiated in Dulbecco's phosphate buffered saline (PBS) or PBS containing the hydroxyl radical scavenger ethylene glycol, under aerobic conditions. The decreased cell sensitivity achieved after maximal scavenging of the hydroxyl radical is a measure of the extent of the cell lethality mediated by this free radical species.

In Fig. 5, the radiation sensitivities of mammalian cells protected maximally against OH• action, expressed as the inverse of the radiation dose sufficient to kill 90% of the cell population, have been plotted against the radiation quality (LET_∞) for sev-

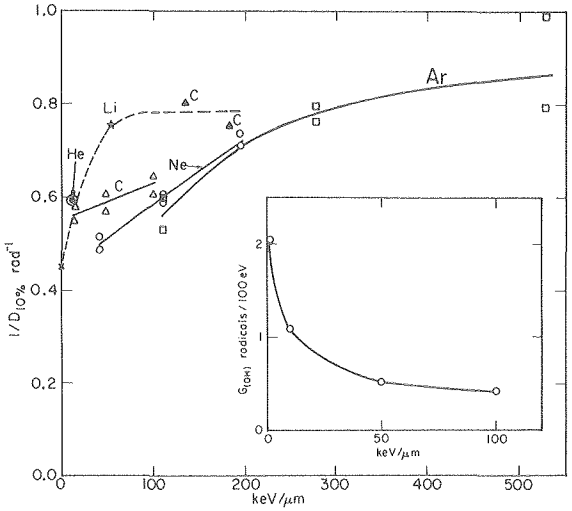

Figure 5. Radiosensitivity ($1/D_{10\%}$ rad^{-1}) of Chinese hamster ovary cells protected maximally against OH-induced lethality as a function of track segment mean LET (keV/μm). Accelerated particle beams used were: 11.4 MeV/n Li^{3+} (*), 15.6 MeV/n C^{6+} (▲) 228 MeV/n He^{2+} (●), 308 MeV/n C^{6+} (Δ), 425 MeV/n Ne^{10+} (○), and 570 MeV/n Ar^{18+} (□). Inset shows dependence of $G_{(OH)}$ on the value of LET (neutral pH). Data redrawn from figure published by I.V. Vereschinksii and A.K. Pikaev in Introduction to Radiation Chemistry, Israel Program for Scientific Translations (1964).

XBL 805-3313

eral different particle beams, including He, Li, C, Ne, and Ar of initial energies from 11.4 to 570 MeV/amu. It is seen that the fraction of the total radiation sensitivity mediated by OH-radicals diminishes as the LET increases; however, the extent of hydroxyl-radical-dependent lesions is governed by particle velocity and Z number, and LET is not suitable for correlation. In the case of the low-energy particle beams (11.4 MeV/n Li^{2+} and 15.6 MeV/n C^{6+}) and the low Z-beams (228 MeV/n He^{2+}), where the dose contributions from low-LET delta rays and fragmentation are minimal, the decrease in the extent of OH-radical induced cell lethality with respect to LET corresponds to the decrease in $G_{(OH)}$ as a function of LET, as depicted in the Fig. 5 insert. This close relationship is not found with the high energy particle beams, where delta-rays and fragmentation become important. Our data indicate that OH-radical-mediated damage becomes small at high LET values where radical-radical recombination is high. Further experiments are planned to obtain more information for higher-LET particle beams with regard to the direct versus indirect actions of radiation damage.

LETHAL EFFECTS OF DUAL RADIATIONS

We have demonstrated with asynchronous cells that low- and high-LET radiations do not act *independently* in cell killing, but cause a synergistic interaction.[14] The magnitude of interaction appeared to be dose dependent. Based on these previous studies, we proposed three basically different mechanisms to account for the interaction: (1) direct physical interactions of lesions caused by the low and high-LET beams; (2) saturation of lesions—the cell dies because at some critical time after the exposures too many lesions remain unrepaired; or (3) one radiation deleteriously affects repair capacity for the lesions caused by the other radiation.

We have attempted to clarify which of these mechanisms is a better description of the interaction effect by quantitative measurements of the effect as a function of the cell-cycle stages.

Chinese hamster V79 cells were synchronized by mitotic selection methods with no further chemical treatments. The selected mitotic population was plated into plastic dishes and grown in a humidified air incubator containing 5% CO_2 at 37°C. The cell-cycle parameters (G_1, S, G_2, and M phases) were estimated by ^{3}HTdR-label techniques. At various times of incubation, corresponding to different stages of the cell cycle, the cells were irradiated with x rays or neon ions, either alone or combined, with little delay between the two radiations. The irradiated cells were then trypsinized for assay of single-cell survival. Results of a typical experiment are shown in Fig. 6.

Panel A shows the age-response curves for cells irradiated with the following doses: 5.5 Gy x rays, 3.3 Gy neon, or 3.3 Gy neon plus 5.5 Gy x rays. The dashed curve was constructed by assuming that neon and x rays act independently. (It traces the products of x-ray and neon surviving fractions at various cell stages.) Hence, at each point in the cell cycle time the difference in survival between the observed curve and the dashed curve is a measure of the magnitude of damage interaction. It is seen that the magnitude of interaction varies throughout the cell cycle. The interaction effect was small at G_1 and G_1/S phases and probably for G_2 and M phases, but was comparatively large during the time of DNA synthesis. This property is more quantitatively demonstrated in Figs. 6B, 6C, and 6D for cells at the G_1/S border (2.5 h after mitosis), early S (5 h after mitosis), and late S (7 h after mitosis), respectively. Each of these synchronized populations was irradiated with 3.3 Gy of neon immediately followed by several graded doses of x rays. By comparing and fitting the survival data of the combined irradiations to the appropriate portion of the x-ray survival curve, we have estimated that in terms of damage interaction, 3.3 Gy of neon irradiation is equivalent to 1.4 Gy, 3.1 Gy and 4.1 Gy of x rays for cells at these respective stages (2.5 h, 5.5 h, and 7 h after mitosis). The ratio of 3.3 Gy to the equivalent x-ray doses yields the effectiveness of neon particles relative to x rays in causing interaction with x rays at each of these cell stages. These ratios are given at the lower left corner in each panel. Results indicate that among the selected cell stages studied in this experiment, late S phase shows the greatest interaction between neon and x-irradiation, and G_1/S shows the least.

Early work of Sinclair led to the conclusion that V79 cells in their late S stage have the largest capacity for repair.[15] This repair property is probably true to some extent for the high-LET particles, as judged by the similarity of the cell-age response curves derived from x-ray and neon ions (panel A). Since the greatest synergistic interaction occurs in late S phase, we may tentatively conclude that the third mechanism, i.e., inhibition of repair, most probably accounts for the interaction effect.

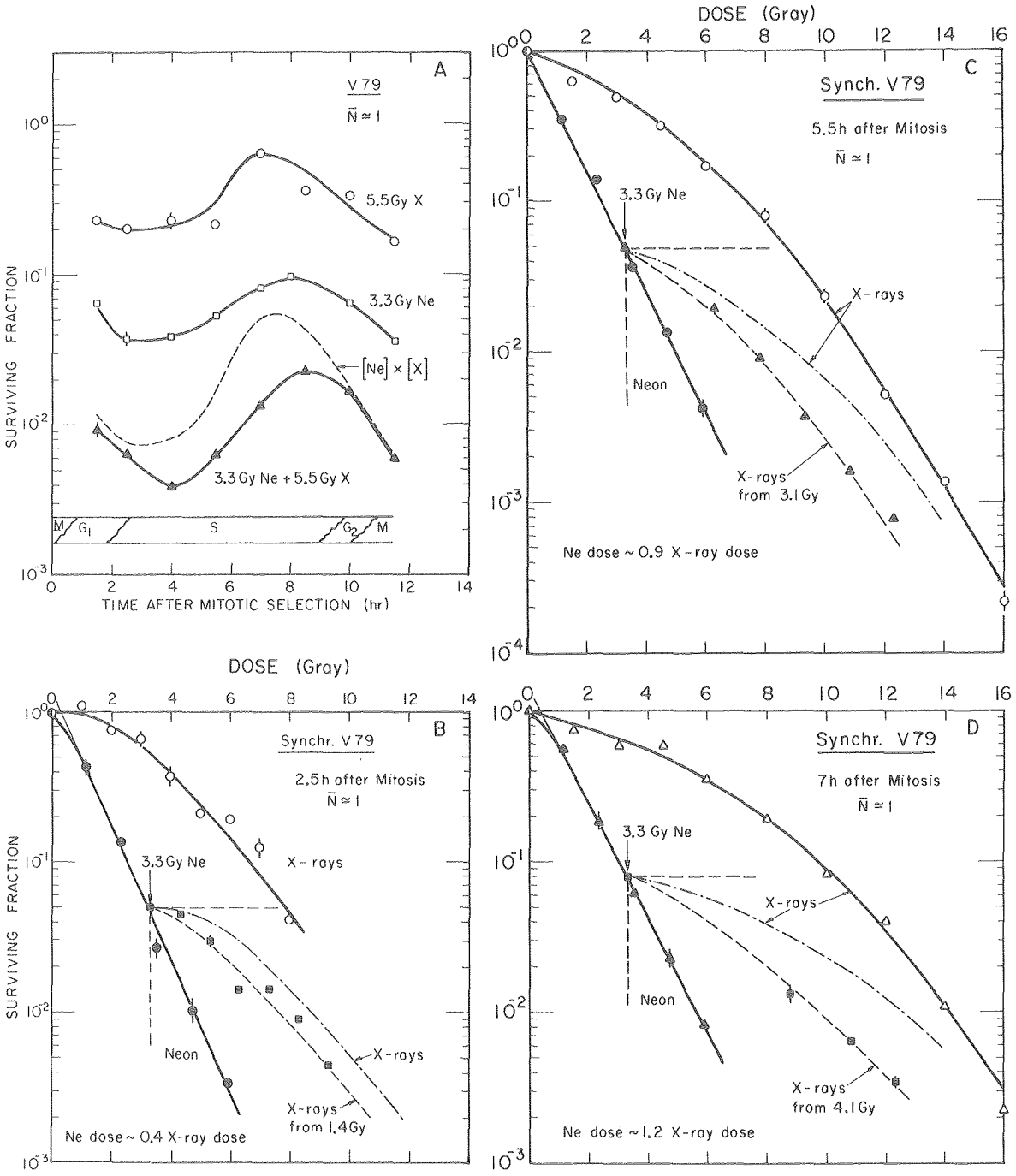

Figure 6. (A): Upper two curves demonstrate measured variation in radioresponse of V79 cells with cell-cycle stages following single x-ray or single neon-ion dose. Lowest curve measures survival from same doses of both neon ions and x-rays given in rapid sequence at various cell stages. Dashed curve was constructed from upper two survival curves on the basis of no interaction between x rays and neon ions. Cell-cycle stages at various times after mitosis were estimated in lower portion. (B), (C), (D): Interactive effects of a primary dose of neon ions on x-ray survival for cells in (B) G_1/S, (C) mid-S, and (D) late S stages. Survival curves of each synchronized population for x- or neon-ion irradiation alone are shown as references. Combined radiation treatments were 330 rad neon ions plus graded x-ray doses. *XBL 794-3421A*

THE REPAIR-MISREPAIR MODEL

We have developed a biophysical model, the repair-misrepair model (RMR), for interpretation of cellular effects caused by heavy charged particles. The principal assumption of the RMR states that the cellular expression of radiation damage results from competition between eurepair (true or perfect repair) and misrepair processes of molecular lesions, which are established in about 10^{-4} seconds following irradiation. The fate of the initial lesions depends on the repair processes. Eurepair will lead to survival, whereas misrepair may bring about cell death, or the appearance of variants—mutation, for example, or malignant transformation. The new model is different from most other existing models because of its explicit treatment of the enzymatic repair processes.[16]

The RME model is currently being expanded to describe the biological effects of combined or multiple modalities that act as deleterious agents. A variety of environmental agents are considered, such as ionizing radiations of different qualities, UV light, hypo- or hyperthermia, radiomimetic chemicals, anisotonic solutions, and mutagens. Classifications of the interaction between two noxious agents are being defined in mathematical terms in the framework of RMR. Details of the theory are treated elsewhere.[17]

We shall describe here an application of the model for the study of low-dose effects, a problem of great interest to many researchers and environmentalists. The traditional method of studying low-dose effects was to study the dose-effect relationship at "high" doses and to extrapolate the results to very low-dose levels by statistical means. However, the accuracy of such a procedure is always a problem, primarily because of the "biological uncertainties" of the measurable data. For example, it is debatable whether or not the dose-effect relationships for mutation or cell transformation are a linear or a higher-order function of dose.

This problem has been the subject of international debate and there is no complete agreement among the experts on the "linearity" problem. The importance of solving this problem is reflected in recent publications by the United Nations Select Committee on the Effects of Atomic Radiations[18] and the BEIR-III Committee of the National Academy of Sciences.[19]

The repair-misrepair model introduces into the consideration of low-dose radiation effects an element that has been consistently neglected or ignored in the past. According to the model, the effects of a low dose of radiation strongly depends on the nature and quantity of lesions present in the genetic apparatus of living cells at the time the radiation is administered. The model also indicates that various environmental effects can produce molecular lesions similar to radiation-induced lesions, and that it is even possible such lesions occur in the course of normal activity of living cells. We know that normal oxidation-reduction processes involve the production of free radicals, and that the cell has enzymes that are capable of injuring DNA. The deleterious lesions produced are usually not permanent, but rather have a finite lifetime because repair processes attempt to eliminate them. The lesions that persist until a critical time in the cell's cycle are named "remnant" lesions.

The magnitude of effects expected from a small dose of radiation would then depend on the number and type of remnant lesions present at the time of exposure. The new lesions produced by the radiation add to the existing remnant lesions. The slope of the dose-effect curve then depends on this interaction, and on the efficiency of the repair systems present at the time the radiation acts. Thus, the response of a given living system to a given dose of radiation might be different from one time to another. The cellular response depends on the totality of deleterious lesions accumulated, from both radiation and other causes.

When living systems are continuously exposed to radiations, it is important, therefore, to consider that a balance exists between the rate of production of new lesions and the rate of their repair. When the repair is misrepair, then this may lead to either a lethal effect or the formation of a variant. Nonlethal variants that survive exposure to ionizing radiation may accumulate with time even in the absence of classical recombination processes, which may be advantageous or disadvantageous to the individual cell. If variants exist that improve the time rate of repair, and the efficiency of eurepair, then such variants may have a selective advantage over other cells. The aspects of the model that deal with radiation-induced variants in the repair system lend plausibility to some of the processes that must have been operating during the course of evolution to produce the degree of resistance to radiation and other agents that exists among highly differentiated organisms today. The gene-controlled repair systems might not have formed in the course of evolution if the population of the Earth had not been constantly bombarded by space radiations and ionizing radiations from radioactive elements in the crust and mantle of the Earth.

To further understand the effects of low-level deleterious agents, the RMR model prescribes that we should understand the chemical nature of the lesions produced in the genetic apparatus by each agent, and the magnitude of the effect these agents may have on the various cellular repair systems. Some quantitative aspects of the model are described elsewhere.[17]

REFERENCES

1. Blakely, E.A., Tobias, C.A., Yang, T.C.H., Smith, K.C., and Lyman, J.T., 1979. Inactivation of human kidney cells by high-energy monoenergetic heavy-ion beams. *Radiat. Res.* 80:122–160.
2. Tobias, C.A., Alpen, E.A., Blakely, E.A., Castro, J.R., Chatterjee, A., Chen, G.T.Y., Curtis, S.B., Howard, J., Lyman, J.T., and Ngo, F.Q.H. 1979. Radiobiological basis for heavy-ion therapy. In *Treatment of Radioresistant Cancers,* M. Abe, K. Sakamoto, and T.L. Phillips, eds., Elsevier/North-Holland Biomedical Press, pp. 159–183.
3. Lücke-Hühle, C., Blakely, E.A., Chang, P.Y., and Tobias, C.A., 1979. Drastic G_2 arrest in mammalian cells after irradiation with heavy-ion beams. *Radiat. Res.* 79:97–112.
4. Blakely, E.A., Ngo, F.Q.H., Chang, P.Y., Lommel, L., Kraft-Weyrather, W., Kraft, G., and Tobias, C.A. 1980. Heavy-ion cell cycle response and progression effects. In *Biological and Medical Research with Accelerated Heavy Ions at the Bevalac, 1977–1980,* C. Tobias, ed., pp. 125–135, LBL-11220.
5. Elkind, M.M., Han, A., and Volz, K.W. 1963. Radiation response of mammalian cells grown in culture. IV. Dose dependence of division delay and postirradiation growth of surviving and nonsurviving Chinese hamster cells. *J. Nat. Cancer Ins.* 30:705–721.
6. Ngo, F.Q.H., Han, A., Utsumi, H., and Elkind, M.M. 1977. Comparative radiobiology of fast neutrons: relevance to radiotherapy and basic studies. *Int. J. Radiat. Onc. Biol. Phys.* 3:187–193.
7. Schneider, D.O., and Whitmore, G.F. 1965. Comparative effects of neutrons and x-rays on mammalian cells. *Radiat. Res.* 18:286–306.
8. Skarsgard, L.D. 1964. Survival and mitotic delay in Chinese hamster cells after heavy ion and x-irradiation. *Radiat. Res.* 22:235 (Abstract).
9. Ngo, F.Q.H., Blakely, E.A., Tobias, C.A., Chang, P.Y., and Smith, K.C. 1978. Fractionation gain factor from therapeutic heavy-ion beams. *Int. J. Radiat. Oncol. Biol. Phys.* 4: Suppl. 2, 92 (Abstract).
10. Ngo, F.Q.H., Blakely, E.A., and Tobias, C.A. 1980a. Effects of combined low-and high-LET radiations. In LBL-11220 (Ref. 4).
11. ICRU (International Commission on Radiation Units and Measurement) Report #30, 1979.
12. Ngo, F.Q.H., Tobias, C.A., Blakely, E.A., Chang, P.Y., Oleszko, O. and Lommel, L. 1980b. Radiation quality, damage repair, and anisotonicity. *Radiat. Res.* 83:402–403 (Abstract).
13. Roots, R., Yang, T.C.H., Craise, L., Blakely, E.A., and Tobias, C.A. 1979. Impaired repair capacity of DNA breaks induced in mammalian cellular DNA by accelerated heavy ions. *Radiat. Res.* 78:38–49.
14. Ngo, F.Q.H., Blakely, E.A., and Tobias, C.A. 1980c. Sequential exposures of mammalian cells to low- and high-LET irradiations. I. Lethal effects following x-ray and neon-ion irradiation. *Radiat. Res.* (In Press).
15. Elkind, M.M. and Sinclair, W.K. 1965. Recovery in X-irradiated mammalian cells. In *Current Topics In Radiation Research* Vol. 1, pp. 165–220.
16. Tobias, C.A., Blakely, E.A., Ngo, F.Q.H., and Yang, T.C.H. 1980a. The repair-misrepair model of cell survival. In *Radiation Biology in Cancer Research,* R.E. Meyn and H.R. Withers, eds. New York, Raven Press, pp. 195–230.
17. Tobias, C.A., Blakely, E.A., and Ngo, F.Q.H. 1980b. The repair-misrepair model of cell survival. In LBL-11220, (Ref. 4).
18. United Nations Scientific Committee on the Effects of Atomic Radiations 1977. "Sources and Effects of Ionizing Radiation" 1977 report to the General Assembly. New York, United Nations, 1977.
19. The BEIR-III Committee of the U.S. National Academy of Sciences 1980. Committee on the Biological Effects of Ionizing Radiation (BEIR). The Effects on Populations of Exposure to Low Levels of Ionizing Radiation. National Academy of Sciences, Washington, D.C., 1980.

CELL TRANSFORMATION AND MUTAGENESIS STUDIES WITH HEAVY-ION RADIATION

Tracy C. Yang, Cornelius A. Tobias, Laurie M. Craise and Doris S. Tse

The main effort of this research project, supported by NASA, NCI and DOE, is to collect quantitative data useful for estimating and understanding the potential risks—such as late effects in normal tissues from mutation and cell transformation—of space flight and heavy-ion cancer therapy. The primary goal of this research, however, is to elucidate the fundamental mechanisms of mutagenesis, DNA repair, and carcinogenesis. Mechanistic studies on mutagenesis and cell transformation with heavy-ion radiation will help to provide a firm base for a scientific theory that can be used to evaluate the potential mutagenic and tumorigenic effects of low doses and of low-dose rates of both low- and high-LET radiations.

It is generally observed and well documented that radiation can cause mutation and increase the frequency of tumor formation in animals. In recent years, experimental results from various major laboratories have shown that radiation can directly induce mutation and transform normal mammalian cells into malignant ones. Most mutation and cell transformation work reported in the literature were done with x rays, gamma rays, and neutrons, and there is very little information on the effect of heavy ions on mutation and cell transformation of mammalian cells.

We initiated studies on mutation and cell transformation with energetic heavy ions about a year ago, and some interesting preliminary results have been obtained.

When cultured mouse embryo cells (C3H1OT1/2) were irradiated with carbon particles, a small fraction of all the cells that survived the radiation treatment showed a property characteristic of tumor cells, i.e., loss of density-inhibited growth. The frequency of transformation appears to be dose dependent, increasing exponentially at low doses and reaching a plateau at high doses (Fig. 1). The effectiveness of 470 MeV/n carbon ions in transforming mammalian cells is about the same as x rays for a given dose. The relative biological effectiveness (RBE) for 470 MeV/n ($LET_\infty \sim 10$ keV/μm) carbon ions is thus about one. Carbon particles with a residual range in water about 1.4 cm (~70 MeV/n; $LET_\infty \sim 34$ keV/μm), however, consistently gave a higher frequency of transformation per viable cell than x rays. Our data suggest that the frequency of transformation depends on both the radiation dose and LET (linear energy transfer). At present the precise relationship between RBE and LET for cell transformation is not known and is under investigation.

Using two different genetic markers (ouabain-resistant mutation and 6-thioguanine resistant) and two mammalian cell lines (C3H1OT1/2 and CHO), we have performed some studies on the mutagenic effects of heavy ions. The induction of ouabain-resistant mutation in C3H1OT1/2 cells by ultraviolet (UV) light, x rays, 10.2 MeV/n lithium ions, 8.5 MeV/n argon ions, and alpha particles of Am^{241} were examined; no mutant was found in cells treated with radiation, except UV light. Results showed that ionizing radiation, including high-LET heavy ions, cannot effectively induce ouabain-resistant mutation. This finding is not totally unexpected, since other investigators have obtained negative results in V79 cells treated with gamma rays and accelerated helium ions.

There were some positive results on the induction of 6-thioguanine resistant mutant with heavy ion radiation. Asynchronous Chinese hamster ovary (CHO) cells in the exponential-growth phase were irradiated with x rays or neon ions (425 MeV/n; LET_∞

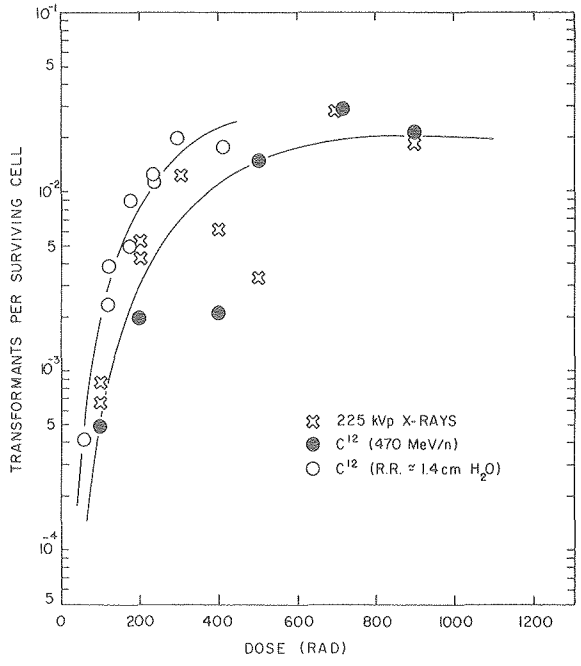

Figure 1. Dose-response curves for x rays and carbon ions in inducing oncogenic transformation of mouse embryo cells (C3H10T1/2). XBL 807-10658

~ 30 keV/μm). Respread method was used to obtain the mutation frequency, and results are given in Fig. 2. Both neon ions and x rays increased the number of mutants per viable cell curvilinearly with an increase of dose. Neon particles appear to be highly effective in producing mutation, as compared to x rays. A comparison between the RBE for mutation induction (~3.6) and for cell killing (~1.4) at 10% survival level indicates that neon ions can produce more mutation lesions than lethal injuries, as compared to x rays.

Among many theories, the somatic cell mutation theory of cancer has been attractive, and many carcinogens have been found to be effective mutagens. If the cell transformation is a result of mutation, a very interesting question will be: "Which type of mutation lesions is directly involved in the alteration of growth properties of mammalian cells?" We have shown that high-LET radiation can cause cell transformation directly and effectively and that no ouabain-resistant mutant can be found with heavy ions. Results of our mutation and cell transformation studies with heavy ion radiation, therefore, suggest that the ouabain-resistant-related "point mutation" may not be the type of mutation lesions involved in the malignant cell transformation.

Many of the mutations induced by ionizing radiation appear to be macrolesions that arise from chromosome breaks, and deletion may be involved in the 6-thioguanine resistant mutation. The importance of the deletion mutation in malignant cell transformation is not clear at present. Some investigators have proposed that double DNA strand breaks may be the cause of cell transformation, and the sister chromatide exchange has also been suggested as a possible mechanism for carcinogenesis. Cell transformation, however, can be a result of misrepair of certain primary lesions induced by radiation, and these primary lesions may include more than one type of molecular lesions.

Because heavy-ion radiation can provide a wide spectrum of LET and because various biological effects, e.g., cell killing, recovery kinetics, DNA breaks, etc., have shown a strong LET dependency, a systematic study of the mutagenesis and oncogenesis of heavy particles can yield quantitative information that can be analyzed and compared with results of other biological effects of heavy ions to shed light on the interrelation between mutation, malignant cell transformation, cell killing, repair, and DNA lesions. More insights on the mechanisms of carcinogenesis may thus be obtained. Work is in progress to collect such quantitative information.

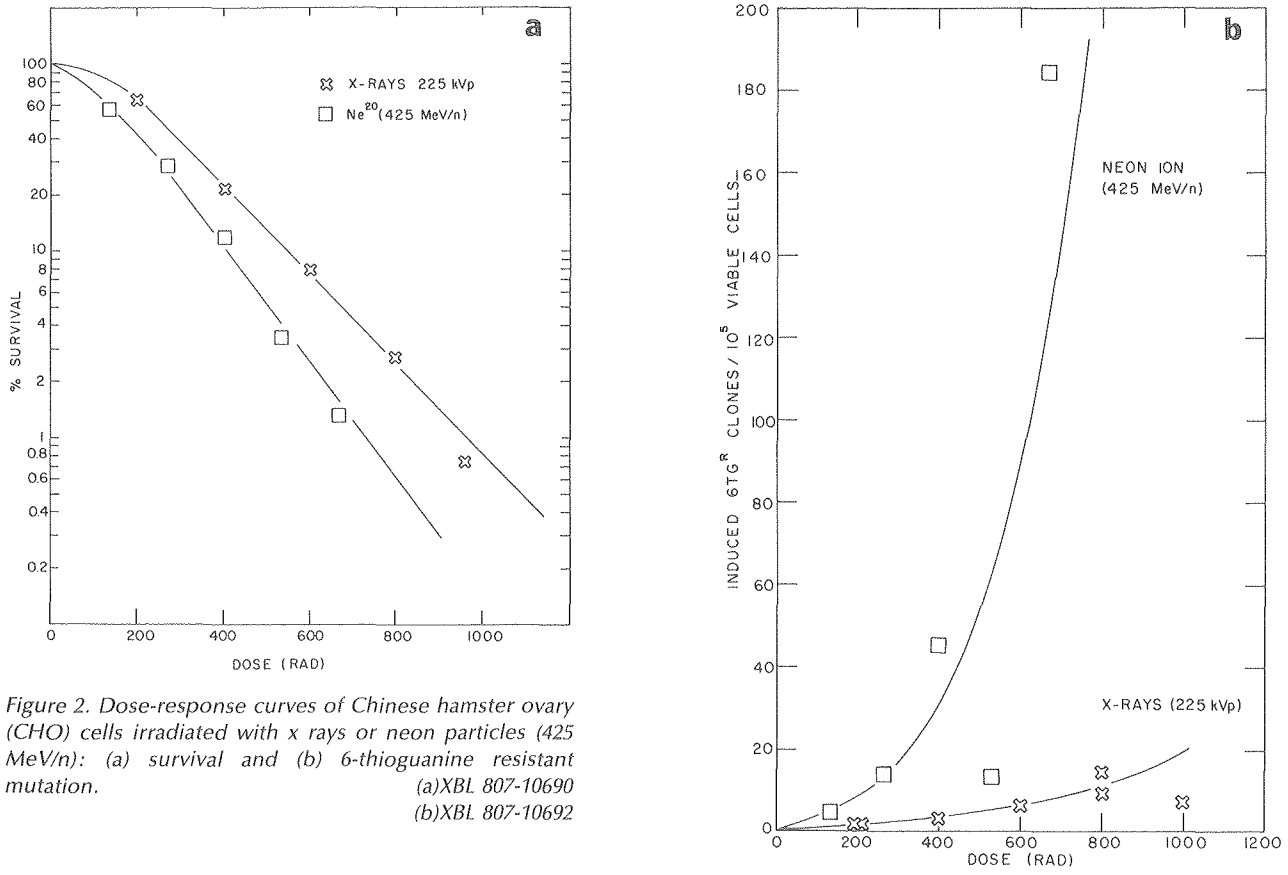

Figure 2. Dose-response curves of Chinese hamster ovary (CHO) cells irradiated with x rays or neon particles (425 MeV/n): (a) survival and (b) 6-thioguanine resistant mutation. *(a)XBL 807-10690* *(b)XBL 807-10692*

HEAVY-ION RADIOGRAPHY

Jacob I. Fabrikant, Cornelius A. Tobias, William R. Holley, and Eugene V. Benton*

Heavy-particle radiography has clinical potential as a newly developed noninvasive low-dose imaging procedure that provides increased resolution of minute density differences in soft tissues of the body. The method utilizes accelerated high-energy ions, primarily carbon and neon, at the Bevalac accelerator at the Lawrence Berkeley Laboratory. The research program for medicine utilizes heavy-ion radiography for low-dose mammography, for treatment planning for cancer patients, and for imaging and accurate densitometry of skeletal structures, brain and spinal neoplasms, and the heart. The potential of heavy-ion imaging, and particularly reconstruction tomography, is now proving to be an adjunct to existing diagnostic imaging procedures in medicine, both for applications to the diagnosis, management and treatment of clinical cancer in man, and for the early detection of small soft-tissue tumors at low radiation dose.

*University of San Francisco, San Francisco.

PHYSICS RESEARCH APPLIED TO HEAVY-ION IMAGING

The physics research, which forms the scientific basis of the imaging method, is progressing along two important lines—imaging with passive detectors, and imaging with active, "on-line" detector systems. At present, to make a radiograph of a clinical patient, heavy-particle beams of carbon or neon ions are passed through the body structures, and the beam stops in a stack of plastic foils. These passive detectors are special nuclear track detectors originally developed for space research. Each heavy particle causes a minute lesion in the plastic foil that can be developed by the application of sodium hydroxide. The beam pulse produces patterns of small holes that are transferred by an optical scanning method to a computer for further quantitation and image processing and eventual display (Fig. 1). The final image formed by heavy ions, such as carbon, compared to conventional x rays, provides much improved and higher contrast with significantly lower radiation doses.

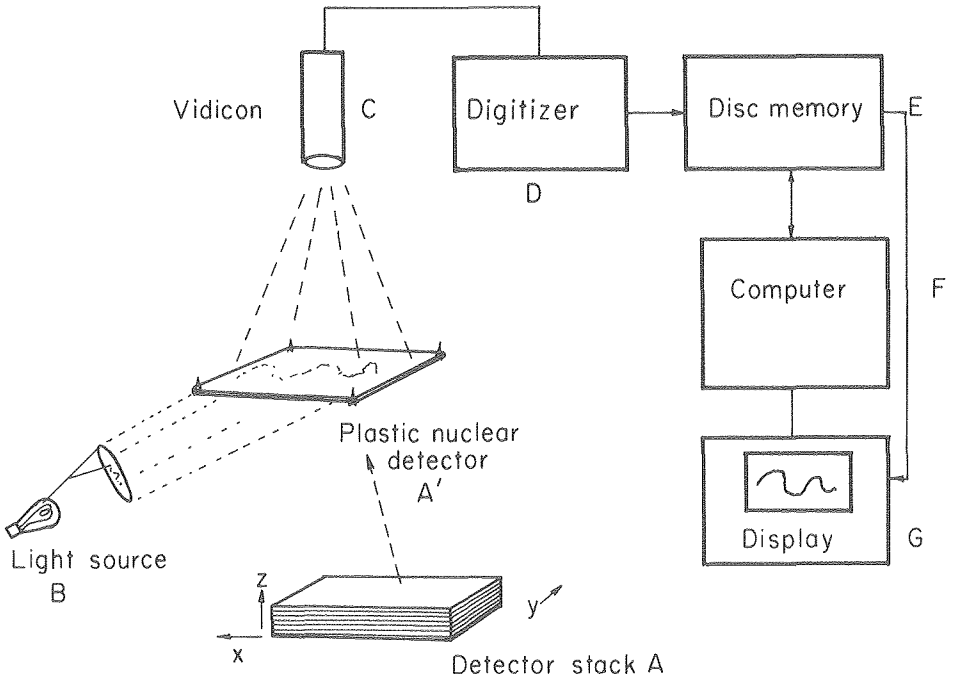

Figure 1. Heavy-ion radiography using passive nuclear track detectors is performed by placing a stack of nuclear detectors behind the subject. The charged particles come to rest in the foil of the stack. Each stopping particle produces a lesion, or track, in the detector sheet, which is later developed in an etching solution. The lesions form an image on each plastic sheet. The information on the sheets is later processed for quantitative radiography and image display.

XBL 7610-9382

An important development has been the production of active "on-line" computerized tomography (CT) of tissue-equivalent phantoms using solid-state detectors of germanium and silicon and neon beams. J. Llacer in our laboratory has succeeded in achieving the first heavy-ion (neon ions, 425 MeV/amu) CT reconstruction using the quantitative information on the residual range distribution of the neon particles in the solid-state detectors. This information is transferred directly to the computer, which immediately reconstructs the image. Figure 2 is the neon-ion CT image reconstruction of a resolution phantom showing the position of 1-mm diameter copper pins in a plastic material; the bright points represent the location of the small pins, while the dark round spots represent small holes containing water.

APPLICATIONS TO MEDICINE

The research program of heavy-ion radiography applied to clinical disease in man is directed toward tissue densitometry of neoplasms compared with normal tissues, imaging of tumors for charged particle radiotherapy planning, low-dose mammography, radiography of the brain and spinal cord, and musculoskeletal radiography. An important development has been imaging of the heart with fast-pulse heavy-ion CT scanning.

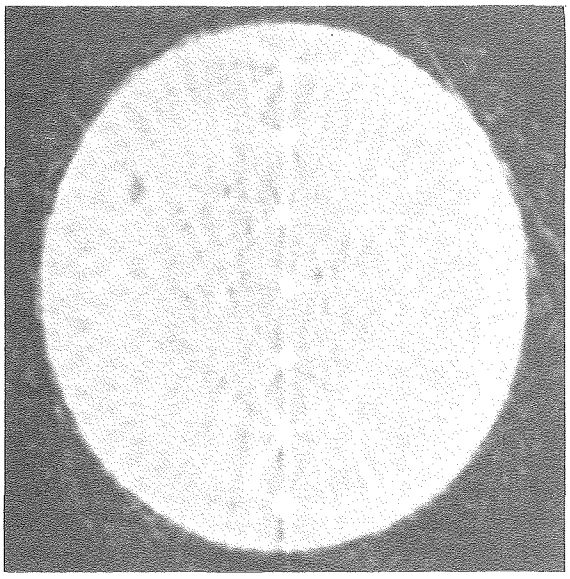

Figure 2. Active "on-line" neon-ion (425 MeV/amu) CT image reconstruction of a resolution phantom using the quantitative information on the residual range distribution of the neon particles in solid state germanium and silicon detectors. *XBB 809-10938*

Tissue densitometry

Highly accurate measurements of the stopping power distribution in human tissues can be obtained with heavy-ions; the stopping power relates to electron density. This provides a unique potential for acquiring a great deal of new information on the electron densities of normal and diseased tissue, information that has not been available in the past with such a degree of accuracy. In our laboratory, the stopping powers of a variety of human tissues have been measured with heavy-ion beams, such as carbon ions. The stopping-power measurements were achieved with better than 0.1% accuracy. Different neoplasms are compared to the normal tissues in which they arose or to which they metastasized. In most instances, the tumor density is significantly higher than normal tissue density, and in almost every instance, the tumor-tissue contrast with heavy ions is better than with x rays.

Heavy-ion radiotherapy treatment planning

Initial studies of heavy-ion radiography applied to charged particle radiotherapy treatment planning were carried out in patients with cancer of the pancreas. Figure 3 is a computer-synthesized gray-level carbon-ion (400 MeV/amu) linear radiograph of the abdomen of a patient undergoing heavy-ion radiotherapy. Here, 150 nuclear plastic detector sheets were used. The integrated stopping-power values are used for computer synthesis and image display. The soft tissues, lumbar spine, ribs, liver, spleen, head of the pancreas (cursor), colon and small intestine are clearly defined. Such computerized-synthesized images and isodensity plots provide valuable quantitative data for improved charged particle beam delivery, treatment planning for charged-particle radiotherapy, and, ultimately, the development of heavy-ion CT reconstruction applied to charged-particle radiotherapy. Heavy-ion imaging has the potential for determining the precise stopping power distribution at each point with the application of heavy-ion CT scanning, thereby making unnecessary the assumptions and corrections that now must be applied to x-ray procedures for heavy-charged-particle treatment planning. Furthermore, our current research has demonstrated that heavy-ion radiography detects smaller tissue densities than do x rays, and this provides the opportunity for detecting normal and abnormal tissue densities within the tumor site and in the normal and abnormal tissues and structures surrounding the neoplasm. This affords valuable additional information for treatment planning and provides a quantitative measure of tumor

and normal tissue response during and following charged-particle radiotherapy in each clinical cancer patient.

Mammography

The heavy-ion radiographs of breast cancer patients display density resolution superior to x rays, and this is particularly valuable in patients with dense breasts and with fibrocystic disease of the breast. Satisfactory diagnostic mammograms are now obtained with very low radiation doses, in the range of only 20 mrad. This is substantially lower than the radiation dose given with conventional x rays of the breast presently in use and significantly reduces the potential risks of radiation exposure.

The research observations on 37 patients examined with low-dose heavy-ion mammography indicate that small breast cancers as well as cysts, abscesses, mammary dysplasia, and benign breast tumors are clearly imaged with this unique radiographic procedure. In three patients, breast cancer was not diagnosed by conventional x-ray mammograms, but was demonstrated on carbon-ion mammograms. Figure 4 is a computer-synthesized carbon-ion (250 MeV/amu) mammogram of the left and right breasts of one such patient. A nonpalpable breast density lying just beneath the nipple in the left breast was seen on the heavy-ion image, but not on the x-ray mammogram. The breast lesion was an abscess containing a small carcinoma *in situ*. No neoplasm was demonstrated in the right breast. Both breasts have dense fibrocystic disease, surrounded by a large amount of fatty tissue.

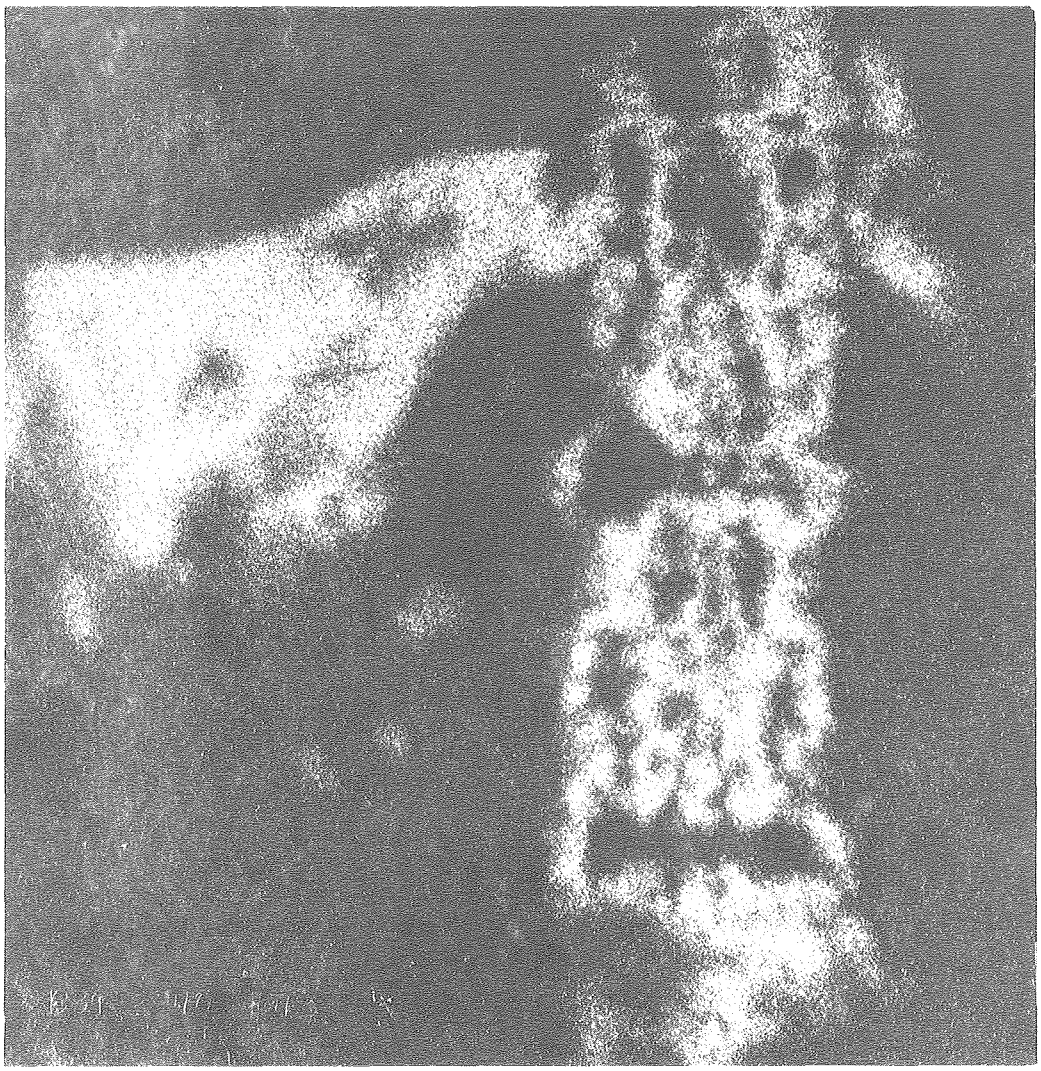

Figure 3. Computer-synthesized gray-level carbon-ion (400 MeV/amu) linear radiography of the abdomen of a patient undergoing heavy-ion radiotherapy for carcinoma of the head of the pancreas. XBB 782-1165

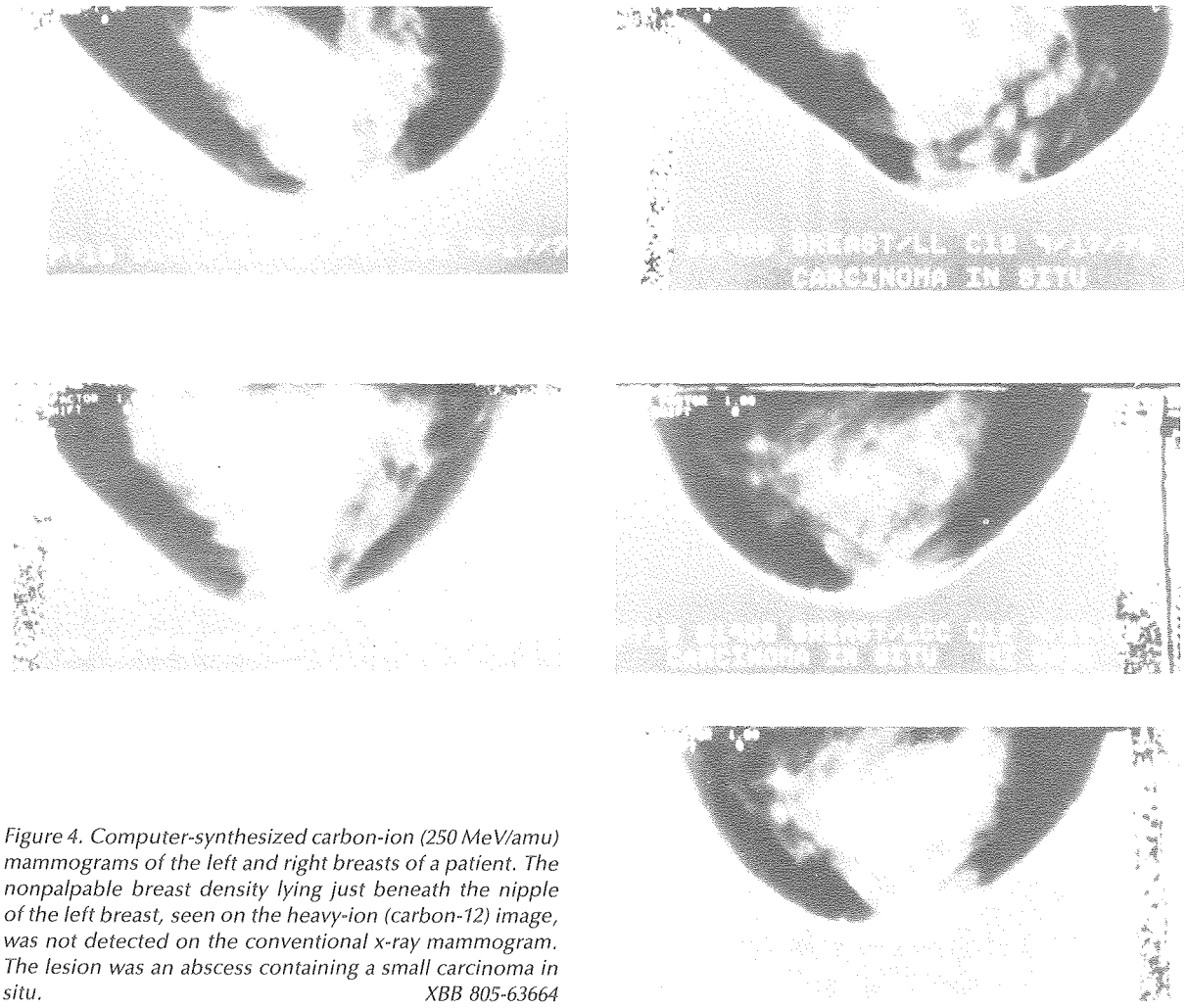

Figure 4. Computer-synthesized carbon-ion (250 MeV/amu) mammograms of the left and right breasts of a patient. The nonpalpable breast density lying just beneath the nipple of the left breast, seen on the heavy-ion (carbon-12) image, was not detected on the conventional x-ray mammogram. The lesion was an abscess containing a small carcinoma in situ. *XBB 805-63664*

The stopping power density distributions determined as a consequence of range distributions can be employed is a variety of visual display forms to derive valuable diagnostic information; our investigations on breast density patterns demonstrate one potentially valuable approach. Figure 5 is a statistical analysis of the density distribution patterns of the breast tissue structure derived from carbon-ion mammograms of both breasts in the same patient. The density histogram of the frequency of pixels plotted against residual range is bimodal; the low-density portions are fatty tissue, the large peak is due to water, and the high density region represents breast cancer. Comparison of both breasts identifies differences or structural asymmetry, which permits identification of the relatively high density distribution of the cancer in the affected breast.

Radiography of the brain

We have achieved the first heavy-ion computerized tomography reconstruction of the human brain, and have made comparisons with x-ray CT scans. In this image, the neon-ion beam (425 MeV/amu) passed through a 1.5 mm slit in a 3 cm brass block, and 97 projections are obtained at two-degree intervals in a plastic nuclear detector stack of 120 foils. The carbon-ion CT reconstruction of the brain illustrated in Fig. 6 demonstrates high resolution of the soft-tissue structures; the density resolution appears better than in the x-ray CT scan, and differences in density are readily determined between the regions of the white and gray matter of the cerebral cortex and the structures of the midbrain, the corpus callosum, the anterior commissure, the ventricles of the brain, and the optic chiasm. Study of the inner structure of the brain, including the detection of small tumors, has now come within reach of heavy-ion tissue densitometry and computerized tomography.

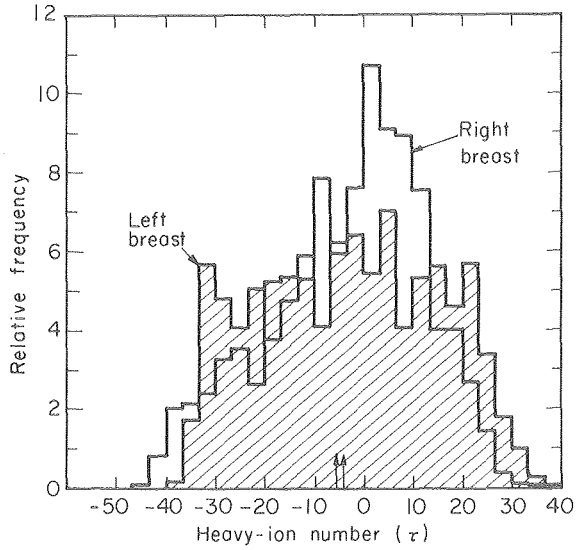

Figure 5. Statistical analyses of the density distribution patterns of the normal and abnormal breast tissue structure derived from carbon-ion (250 MeV/amu) mammograms of both breasts in the same patient. Data are displayed as density histogram of pixel frequency plotted against residual range. *XBL 8010-3718*

Musculoskeletal radiography

Our investigations are demonstrating the potential usefulness of heavy-ion imaging of the musculoskeletal system for the diagnosis and therapy of primary cancer and metastatic neoplasms. Because of the high x-ray absorption coefficient in bone, x-ray radiography of the bones and joints for detecting even small abnormalities is extremely useful. However, this is not the case for soft-tissue radiography, and particularly for the diagnosis of soft-tissue tumors. We have been investigating the applications of heavy-ion imaging for examination of bone structure detail, and also for associated soft-tissue detail, such as muscles, tendons, supporting connective tissues, and cancers.

CARDIAC RADIOGRAPHY

The imaging of the moving heart—the normal and abnormal myocardial structure and the cardiac chambers—in man, can be potentially achieved as a noninvasive procedure with two-dimensional and three-dimensional heavy-ion CT reconstruction.

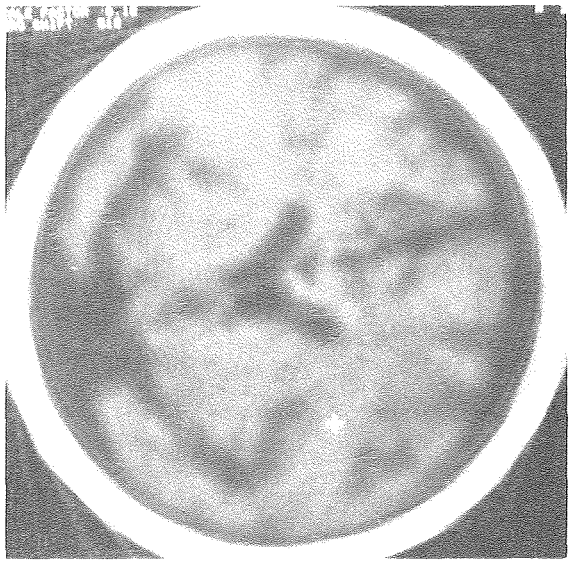

Figure 6. Neon-ion (425 MeV/amu) CT reconstruction of the human brain; coronal scan is through the middle third of cerebral cortex and midbrain. *XBB 809-10848*

Measurable differences in stopping power values by the normal, ischemic, and infarcted myocardium, and the cardiac chamber blood pool, would be required. It is now feasible to evaluate differing myocardial tissue compositions by means of quantitative density distribution values.

Figure 7 is a neon-ion (425 MeV/amu) CT reconstruction of the dog heart following surgically-induced myocardial infarction two months previously. On the neon-ion CT image, the thick left wall and interventricular septum are clearly seen; the prominent papillary muscles protrude into the large left ventricular chamber. The large, thin right ventricular wall is noted, with some changes in density present on the anterior wall (at 1 o'clock) which is in the region of the infarct. The flat, narrow right ventricular chamber is readily visualized. Such imaging capabilities, potentially achievable with heavy-ion radiography in man, would provide a valuable, noninvasive imaging method for the experimental and clinical study of myocardial tissue ischemia, infarction and necrosis, for the detection and sizing of myocardial infarctions, for evaluation of effectiveness of methods designed to limit myocardial infarct size, and possibly for evaluation of the functional anatomy of the normal and ischemic myocardium.

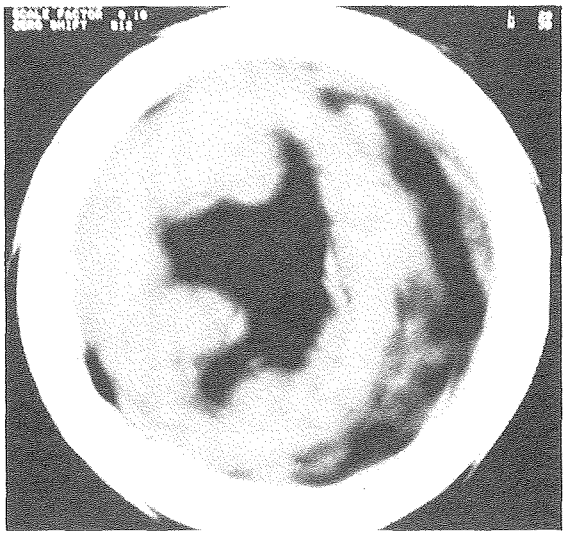

Figure 7. Neon-ion (425 MeV/amu) CT reconstruction of the dog heart; transverse scan is through the myocardium of left and right ventricles, interventricular septum, and chambers. Reconstruction was obtained by D. Feinberg, Ph.D. student in biophysics. *XBB 809-10852*

CLINICAL PHYSICS FOR CHARGED PARTICLE TREATMENT PLANNING

George T.Y. Chen, Samuel Pitluck, and John T. Lyman

CT SCANNER INSTALLATION

Tumor position relative to adjacent critical structures and inhomogeneities must be precisely known for accurate charged particle dose delivery. Most cancer patients treated at LBL have been positioned upright, which is a natural isocentric orientation for a fixed horizontal therapy beam. Up to this time, computerized tomography (CT) scans at community hospitals (which are performed with the patient recumbant) have been of limited value in determining the exact tumor location in treatment position. With the installation of a CT scanner specially modified for scanning patients in the upright position, this shortcoming will be resolved. The scanner has been delivered to Building 55 (Research Medicine) and is expected to be operational in early 1981.

The unit chosen is an EMI-7070, which has a stationary detector ring and a scan speed of 3 seconds. The scanner is equipped with a trunion that allows the detector ring to be rotated from vertical to horizontal. When the detector plane is vertical, the scanner may be used in the conventional manner, with the patient lying on the scanner couch. When the detector plane is horizontal (Fig. 1), the patient may be either seated or standing. In this mode, the gantry is translated up or down to cover the area of interest. The scanner is capable of taking 2 mm slices every 15 seconds for 100 consecutive slices. A normal reconstruction is performed within 35 seconds of scan completion. A two-pass bone correction algorithm, which is specified to generate quantitative CT data to 2% of its true value (independent of object shape, size or presence of inhomogeneities) may be obtained within an additional 100 sec. The scanner can also generate with plain view reconstructions, which are produced by translating the patient past the detectors without x-ray

tube rotation. This provides an image useful for interpreting axial views and their positional relationship to conventional radiographs.

TREATMENT PLANNING—CURRENT STATUS

Pixel-by-pixel treatment planning programs have been developed at LBL to calculate the dose distribution from multi-port charged particle beams. The process begins by taking a sequential set of CT scans through the region of interest. These scans are then viewed by a team of radiotherapists and physicists on a graphics unit. An interactive graphics program has been developed to facilitate localization of the tumor and entry of target volumes into the computer treatment planning system. Options available in this program include: 1) standard window and leveling capability to adjust the CT image for optimal tumor delineation; 2) contouring routines that allow the radiotherapist to define the target volume to be treated; 3) ability to recall and display previous contours and to modify them if needed; 4) entry on the transaxial view of reference points that later assist in the placement of a computer-generated treatment portal; 5) measurement of geometric and water-equivalent pathlengths between arbitrary points; and 6) determination of the mean CT number and standard deviation in an irregular region of interest. These features allow the radiotherapist and physicist team to define the target volume, make measurements of the lesion size and CT characteristics, and determine the water-equivalent depth of structures of interest.

The CT data are then prepared for treatment planning. Pixel-by-pixel treatment calculations generally require some data manipulation beforehand.

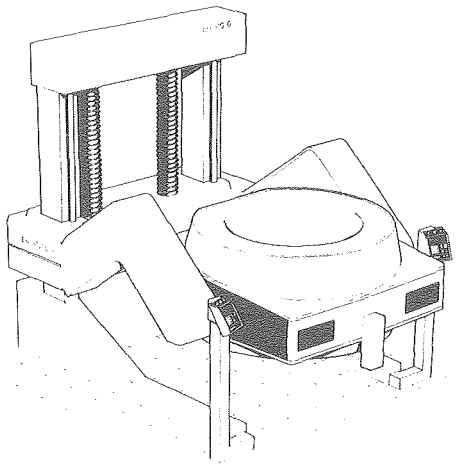

Figure 1. Upright CT scanner. *XBL 7912-13720*

These operations include removing extraneous apparatus (head holders, scan table, bolus) from the image. In addition, air in the gastrointestinal tract must be edited for proper compensation. An automatic threshold edge detection algorithm has been developed to detect the body air boundary and set all pixel values outside to air density. The algorithm utilizes the raster graphics memory, since a 320 × 320 matrix cannot be contained in the computer core.

Next, a series of treatment planning programs is run to generate: 1) a port design based on the projected tumor volume; 2) the design of a three-dimensional compensator required to stop the beam at the distal edge of the contour; and 3) both physical and isoeffect isodose distributions. The objective in charged particle dose delivery is to shape a three-dimensional high-dose region around the defined target volume. This is done on each slice by calculating the appropriate compensation to stop the primary beam at the distal end of the target contour. The core of the treatment planning algorithm is a subroutine modified to calculate the water-equivalent distance from the distal end of the target contour to the body air interface along the specified beam direction. Given this water-equivalent range and the maximum range of the heavy-ion beam, the amount of external absorber along that ray is well defined. The calculation is done in a matrix of water-equivalent densities per pixel, derived using a calibration curve. By examining the target contours in all CT slices, the planning program automatically determines the appropriate spread Bragg peak beam to be consistent with the tumor volume, and calculates the required water column setting for the treatment.

Examples of the program output are shown in Figs. 2 and 3. Figure 2 shows the treatment portal as designed from a series of target contours delineated on 14 sequential CT scans. The port shape is overlaid on an anterior-posterior projection of multiple CT slices.

The isodose distributions are calculated in an 80 × 80 matrix by a range-shifting algorithm. Beam models used in the calculation of isodose distributions are discussed elsewhere. Either cobalt rad equivalent units (CoRE) or physical depth dose distributions may be used in planning. Figure 3a is a treatment plan for a two-field irradiation of a pancreatic carcinoma, where the broad light line delineates the target volume. Isoeffect lines in 10% increments show that the high-dose region is confined to the target volume. Critical organs such as the kidneys and spinal cord are largely spared. In ad-

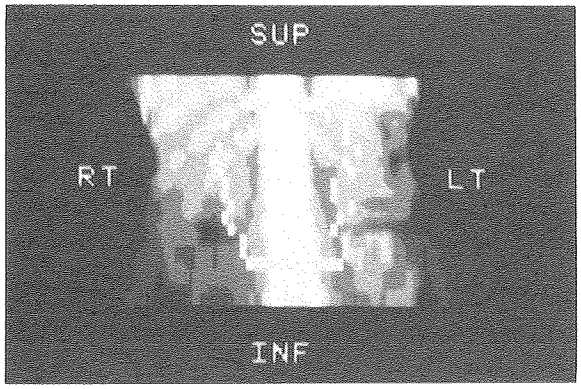

Figure 2. CT-derived portal template overlaid on generated coronal image. *XBB 807-8635*

dition, the dose to the gastrointestinal tract from the entering carbon beams is less than 40%. A comparison of the integral dose for the irradiation of this volume as compared with a four-field 25 MeV box irradiation of the same target (Fig. 3b) shows a reduction in the integral dose of the normal tissue by about 50%.

In three dimensions, target volumes may be rather irregular in shape. With fixed ridge filter beam delivery, a spread Bragg peak must be chosen to correspond to the maximum target dimension over all slices. This insures biological dose uniformity over the tumor volume, but results in overdosing normal tissues in other areas.

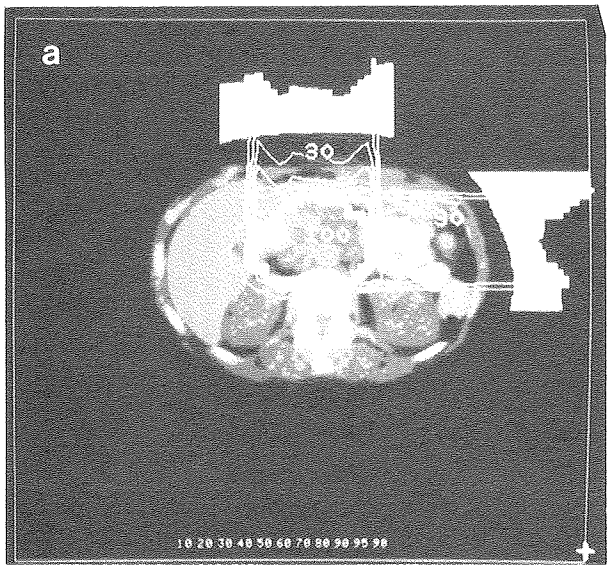

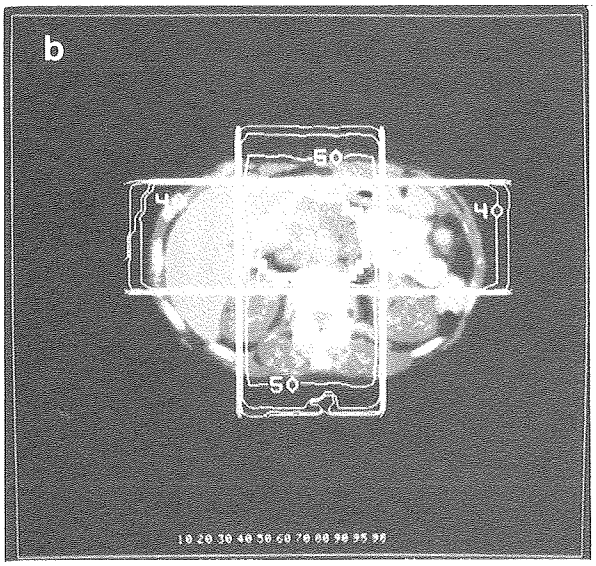

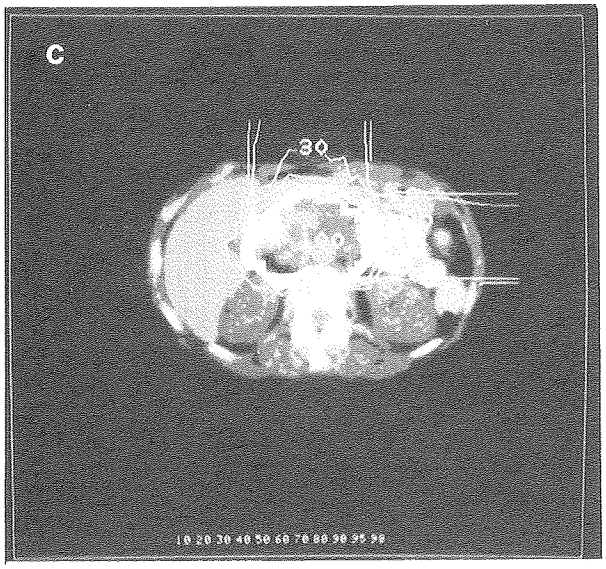

Figure 3. (a) Treatment plan for pancreatic lesion (fixed ridge filters) with isoeffect lines. (b) 25 MeV-photon four-field plan, equally weighted. (c) Beam-scanned carbon two-field treatment plan with isoeffect lines.

(a) XBB 807-8631
(b) XBB 807-8634
(c) XBB 807-8633

Beam scanning may be used to overcome this disadvantage. In beam scanning, a charged particle pencil beam is scanned across the field by magnetic lenses. At each raster point, the depth of penetration, spread Bragg peak dimension, and dose may be delivered to a precalculated value. In this section, we limit the discussion to the quantitative gain provided by such techniques in sparing normal tissues over conventional fixed-ridge-filter delivery methods, omitting radiobiologic considerations in the implicit use of very high dose rates for faster beam scanning.

The figure of merit used to evaluate the goodness of a plan is the ratio of the normal tissue integral dose (NTID) as delivered by beam scanning (BS) versus fixed ridge filter (FRF) methods. A low figure of merit indicates a more favorable condition for beam scanning. Variables influencing the normal tissue integral dose include the three-dimensional target shape, size, and depth, and field arrangement.

In simulating beam scanning, an appropriate ridge filter for each ray is chosen from a family of ridge filters quantized in 1 cm units. The spread Bragg peak selected is at least as large as the target size along the ray. The pancreatic tumor consisted of contours outlined on fourteen distinct CT slices. Anterior and one or two lateral fields are used in the planning. The output of the treatment planning program included the total integral dose summed over all slices, the integral dose within the tumor volume, and the normal tissue integral dose (NTID).

A representative treatment plan from fixed ridge filter therapy was shown earlier in Fig. 3a. Conformation of the stopping region at the distal edge of the contour with fixed ridge filters and compensators necessarily results in a higher proximal-region dose. In elliptical target volumes, as seen in Fig. 3a, the wedge-shaped 40% dose regions located near the beam edges are due to the use of fixed ridge filters. Use of a fixed ridge filter consistent with the maximum target dimension also implies that this ridge filter will not be appropriate for CT levels where the tumor is smaller. Also note that there is a small region outside the target volume treated to 100%. The beam scanned treatment plan (isoeffect isodose) is shown in Fig. 3c. Both the intermediate (50%) and high isodose (100%) lines conform much more closely to the target volume. The conformation of the high-dose region in other CT planes would be comparable. The fragmentation dose is also reduced since it is dependent upon ridge filter size.

The figure-of-merit analysis was used on the identical target volume for helium, carbon, and neon ions. The results show that beam scanning with carbon reduces the normal tissue integral dose the greatest, with neon second and helium third. The NTID is a function of the spread-peak-to-plateau ratio and the size of the fragmentation dose of different ions. From the CoRE depth dose currently in use, carbon exhibits the most favorable spread-peak-to-plateau ratio, with a moderate fragmentation component. Results are summarized in Table 1.

In comparison to photon therapy, both fixed ridge filter and beam scanning substantially reduce the normal tissue integral dose. Again, using the same pancreatic target volume for comparative purposes, the NTID (for fixed ridge filters) is reduced by about 35% using fixed ridge filters and 55% by beam scanning. In each case, the target volume received close to 100% dose uniformly.

Normal tissue integral dose is not a strong function of field arrangement for centrally located lesions, as would be expected from finite range beams. Comparisons of the NTID for two field right-angle pairs, two field opposed and three field treatment plans all resulted in the same normal tissue integral dose within 2%. See Table 1.

TREATMENT PLANNING COMPUTER

A VAX 11/780 computer will be installed in the Building 55 Therapy Physics area in late 1980. This

Table 1. Normal tissue integral dose (NTID)—summary of results.

Treatment Plan	NTID	NTID/NTID (25MeV)
25 MeV photons; 4 fields; equal weights	11394	1.00
Carbon; fixed ridge filters; 2 fields; equal weights	7093	0.62
Carbon; 2 beam-scanned fields; equal weights	5278	0.46

NTID ratios—various charged particles

Helium	$\frac{\text{NTID (beam scanning)}}{\text{NTID (fixed ridge filters)}}$	=	0.86
Carbon	$\frac{\text{NTID (beam scanning)}}{\text{NTID (fixed ridge filters)}}$	=	0.75
Neon	$\frac{\text{NTID (beam scanning)}}{\text{NTID (fixed ridge filters)}}$	=	0.83

NTID as function of field arrangement for slice 5 only (carbon ions)

Field Arrangement	NTID
2 fields, right angle pair	1.0
2 fields, opposed pair	1.02
3 fields, AP and 2 laterals	1.01

computer will provide the increased computational power required to handle a number of large matrices. With this computer, it is feasible to perform dose calculations on 320 × 320 CT density matrices, thereby increasing calculation accuracy. Calculation of isodose surfaces in saggital or coronal planes will also be possible. A hard-wired data link between the VAX and the EMI 7070 CT scanner will be installed to facilitate data transfer between the two devices. The VAX will be used for Monte Carlo simulations of beam transport on CT density matrices to evaluate the need for incorporation of multiple Coulomb scattering algorithms in treatment planning. This computer facility is shared with the charged particle radiography group and other Biomed users.

CHOROIDAL MELANOMA TREATMENT PLANNING

Treatment planning for the irradiation of ocular melanomas is currently done via telephone link to the Massachusetts General Hospital computer. Use of a code developed by M. Goitein of MGH and a graphics terminal allows the visualization of tumor relative to critical structures of the eye (Fig. 4a). Interactive adjustment of the position of the eye is an elegant method of optimizing the proper beam entry angle to spare critical structures. At LBL, recent interest in the visualization of ocular tumors with high-precision CT (available at UCSF) has led to a study to evaluate this means to assist in treatment planning. A particular advantage of CT is its ability to define the relative position of soft tissues surrounding the eye (Fig. 4b).

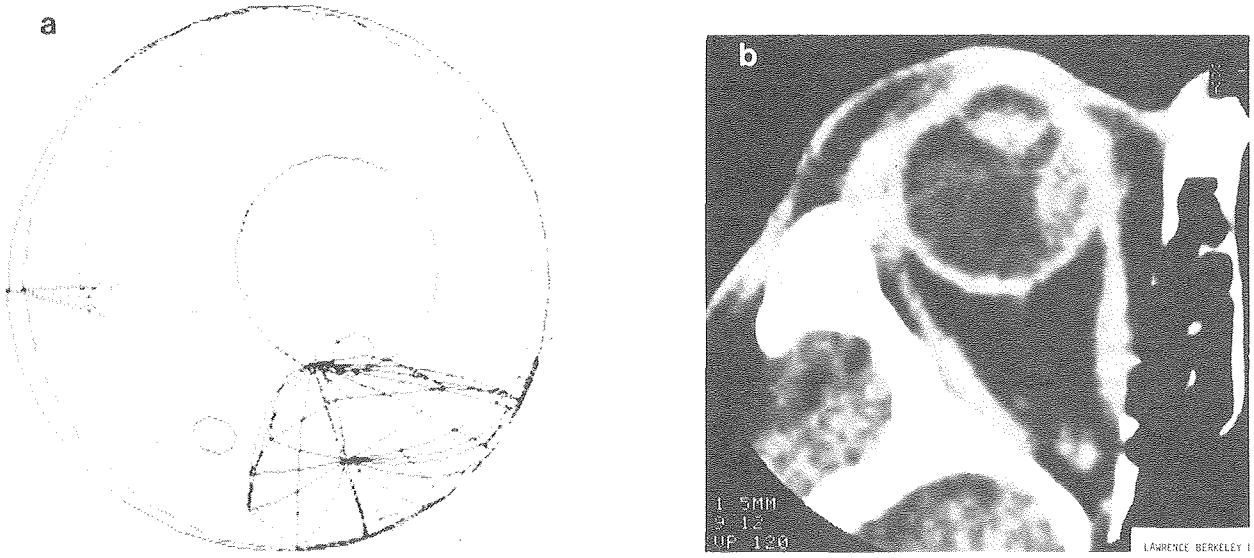

Figure 4. (a) Beam's eye view of eye tumor with internal structures. Cross marks the macula; optic disc and nerve are seen to its left, and tumor is inferior to lens. (b) CT scan, 1.5 mm slice thickness, showing choroidal melanoma tumor in eye.
(a) XBB 805-6637
(b) XBB 807-8581

TREATMENT OF CANCER WITH HEAVY CHARGED PARTICLES

Joseph R. Castro

The project, "Treatment of Cancer with Heavy Charged Particles," has been ongoing since 1975. Continued patient accrual during FY 80 has included irradiation with helium ions at the 184-inch cyclotron (56 patients) and irradiation with carbon, neon and argon ions at the Bevalac (29 patients). A CT (computerized tomography) scanner able to scan patients in both the upright and horizontal positions has been installed; thus improved treatment planning will soon be available.

The clinical radiotherapy trial has accrued 243 patients irradiated with particles and 13 patients irradiated as controls in randomized studies (Table 1). Of the 243 particle patients, 194 have been treated with helium ions, either solely or in combination with photon irradiation, and 49 have received all or part of their irradiation with one of the heavier particles, either carbon, neon, or argon ions.

The project thus can be divided into two general phases:

1) Evaluation of improved dose distribution *without* significant biologic advantage by use of helium ion irradiation; and

2) Evaluation of improved dose distribution *and* enhanced biologic effect by irradiation with heavy charged particles such as carbon, neon, and argon ions.

The aim of the helium ion radiation therapy program has been to test the potential clinical advantage of improved dose localization. No significant enhancing of biological effect in terms of tumor regression has been observed with helium ions. Observation of skin, intestinal, and mucosal reactions with helium ions has confirmed the clinical RBE (relative biological effectiveness) of 1.2 (proximal peak) to 1.4 (distal peak). This correlates well with RBE estimates based on *in vivo* and *in vitro* pretherapeutic studies.

Dose fraction sizes of 200 CoRE per fraction, 4 fractions per week to total doses of 6000 to 7000 equivalent rad have been used to keep dose prescriptions of helium ion irradiation comparable to low-LET (linear energy transfer) photon irradiation. In some instances, helium ions have been used after a portion of the total irradiation course has been given with photon irradiation, that is, as a "boost" at the end of therapy.

With helium ion irradiation, the highest number of patients treated have had localized, unresectable carcinoma of the pancreas. Fifty-four patients have been irradiated with helium ions as of September 1, 1980, receiving a minimum of 5000 equivalent rad, with most patients receiving 6000 equivalent rad in 7.5 weeks. Of these, 30 patients have been entered in a randomized trial contrasting helium irradiation plus 5-Fluorouracil chemotherapy against low-LET photon irradiation plus the same chemotherapy in the treatment of carcinoma of the pancreas. This clinical cooperative trial is coordinated by the Northern California Oncology Group and the Radiation Therapy Oncology Group, which provide the required statistical backup, quality control, and an-

Table 1. Heavy particle clinical trial patients (7/75–7/80).

Anatomic Region	Helium	Heavy Particle
Head/Neck	11	11
Intracranial	15	9
Eye	22	—
Thoracic	30	6
Abdomen/Retroperitoneal	97	18
Pelvis	15	—
Other	4	5
	194	49
Low-LET-photon control patients (randomized pancreas trial)	13	
Consultation only, not accepted for particle radiation therapy	57	
TOTAL ALL PATIENTS REFERRED: 313		

cillary services. To date, 15 patients have been irradiated with helium ions and 15 have been treated with low-LET photons, with no significant difference as yet in survival between the study and control arms. Nine patients with advanced carcinoma of the pancreas have been irradiated with heavier particles such as carbon or neon ions, in order to evaluate both improved dose distribution and enhanced biologic effect.

Helium ions have been used in a variety of other target sites where improved dose localization has appeared to be a possible advantage. These have included: (1) selected head and neck tumors around the base of the skull and cervical spine, as well as in the paranasal sinuses; (2) localized soft tissue sarcomata; (3) carcinoma of the stomach (localized); (4) carcinoma of the esophagus; and (5) a variety of locally advanced and/or recurrent neoplasms in the abdomen and pelvis. In particular, a group of 22 patients with localized ocular melanoma has been irradiated with helium ions using a modified Bragg peak of 14–23 mm, delivering 7000–8000 equivalent rad in 5 fractions over 7 to 9 days. Extremely sharp lateral edges and distal fall-off of the beam have permitted precise dose localization while sparing the critical structures of the eye, in most patients. Thus for nearly all patients in this group, vision has been preserved and the tumor in the eye has been controlled. The direction of the gaze, angulation of the beam, and shape of the treatment aperture, as well as the beam penetration depth and range modulation, are established in a planning session using a computerized treatment planning program developed by M. Goitein at Harvard. The tumor is precisely localized by surgical placement of radioopaque tantalum rings about its base. Coordinates of the rings are obtained from orthogonal x-ray films. These data and measurements of the tumor height and the anterior-posterior diameter of the globe as determined from an ultrasound study are used to locate the tumor relative to the structures of the eye. The dose and fractionation have been chosen to facilitate intercomparison of results with the proton-treated patients.

The helium trial will continue to accrue patients to study the influence of improved dose localization on: (1) selected head and neck tumors; (2) ocular melanoma; (3) carcinoma of the pancreas (randomized study); and (4) carcinoma of the esophagus.

For pancreatic, esophageal, and gastric tumors, treatment with heavier particles is contemplated when the required beams become available.

The goals of the Phase I-II heavy particle (C, Ne, and Ar) study are: (1) evaluation of acute and subacute response of normal tissues such as mucosa, skin, and intestine; (2) initial evaluation of tumor response; (3) development of effective treatment techniques using carbon, neon, and argon ions based on experience obtained with helium ions; and (4) clinical evaluation of the physical and biological dose distributions available with neon, carbon, and argon ions. To date, 49 patients have been irradiated at the Bevalac. Forty-seven of these have been irradiated with either the neon or the carbon ion beam, as access to the argon ion beam has been limited. Our initial clinical efforts have been to confirm the RBE estimates for various tissues provided by pretherapeutic investigation (Table 2). To this end, we have irradiated several patients with metastatic advanced tumors, paying careful attention to skin, mucosal, and pulmonary reactions. Carbon and neon ions have also been utilized to treat patients with carcinomas of the pancreas too advanced for the randomized helium clinical trial; primary or metastatic malignancies of the brain; localized, unresectable abdominal or pelvic tumors such as recurrent colonic carcinoma; advanced cancer of the head and neck; and a few patients with carcinoma of the lung.

The Phase I-II study of heavy particles is planned to accrue an additional 50 patients during FY 81. Data accumulated in this pilot study will be utilized to design Phase III prospective studies with heavy particle(s) and to provide input for the medical accelerator design study.

Table 2. Phases I and II preliminary heavy-ion Bragg peak patient data.

Beam and initial energy (MeV/amu)	Patient diagnosis	Radiation end point	Dose/fraction (physical rad)	Fractionation time (days)	RBE estimate (relating to Co^{60})	Reference radiation
Carbon 308	Kaposi's sarcoma	Skin reaction	100 rad/fx × 10fx = 1000 rad 140 rad/fx × 10fx = 1400 rad 170 rad/fx × 10fx = 1700 rad	11	2.7 (at 120 rad/fx)	10 MeV electrons 250 rad/fx × 10fx = 2500 rad 300 rad/fx × 10fx = 3000 rad 350 rad/fx × 10fx = 3500 rad
400	Left lung metastic nodules from carcinoma of uterine cervix	Tumor regression	185 rad/fx × 8fx = 1480 rad	11	2.5	8 MeV x-rays 500 rad/fx × 8fx = 4000 rad
Neon 425	Metastatic subcutaneous leiomyosarcoma	Skin reaction	120 rad/fx × 8fx = 960 rad	10	3.3	15 MeV electrons 400 rad/fx × 8fx = 3200 rad
557	Multiple metastatic lung nodules	Tumor regression	350 rad/fx × 4fx = 1400 rad 175 rad/fx × 8fx = 1400 rad 117 rad/fx × 12fx = 1400 rad 85 rad/fx × 16fx = 1400 rad	28 30 30 31	2.4 2.9 3.2 3.5	none
670	Metastatic melanoma, skin	Skin reaction	85 rad/fx × 18fx = 1530 rad 100 rad/fx × 16fx = 1600 rad	34 24	3.5 ~3.2	Helium (232 MeV/amu) 4248 rad/18fx/30d 4 MeV x-ray 6350 rad/20fx/30d
Argon 570	Metastic sarcoma, right supraclavicular fossa	Skin reaction and tumor regression	143 rad/fx × 4fx = 572 rad	4	~2.7	none
570	Metastatic melanoma, skin	Skin reaction	139 rad/fx × 4fx = 556 rad 217 rad/fx × 4fx = 868 rad	2	2.7 (at 139 rad/fx) 2.3 (at 217 rad/fx)	none

Magnetic Field Studies

BIOLOGICAL EFFECTS OF MAGNETIC FIELDS

Tom S. Tenforde, Cornelius T. Gaffey, Michael S. Raybourn, Ruth J. Roots, Lynette Levy and James D. Dixon

Magnetic field interactions, and their underlying mechanisms, are being studied in experimental animals and in selected tissue, cellular, and molecular systems that are potentially sensitive to this form of non-ionizing radiation. A major programmatic objective is to obtain baseline data to establish magnetic field exposure guidelines for industrial and research facilities and, in particular, for newly developing energy technologies, including fusion reactors, magnetohydrodynamic systems and magnetic energy-storage rings. A brief summary is given below of results obtained during the past year in several selected research areas within the magnetic field bioeffects program.

The effects of exposure to DC magnetic fields up to 20 kG strength on the physiological performance of experimental animals is being evaluated from functional measurements on the cardiac, neural, visual and hematopoietic systems. Other measurements on test animals exposed to DC fields include the monitoring of activity and neurobehavioral parameters, and the automated recording of several circadian parameters including deep-body temperature and respiration. The only significant

magnetic effect that has been observed to date is a marked change in the electrocardiogram (ECG), which exhibits a series of new signals in the presence of a DC magnetic field. These magnetically-induced signals have been observed in rodents, dogs and baboons used as test subjects, and have the properties of being: (1) field strength dependent; (2) detectable in the larger animals (dogs and baboons) at a threshold field level of approximately 1 kG; (3) immediately and completely reversible upon cessation of the field exposure; (4) dependent upon the orientation of the animal relative to the lines of magnetic induction. Our observations to date indicate that these ECG signals are induced potentials associated with intracardiac, aortic and post-aortic blood flows in the presence of a magnetic field. Available evidence also indicates that there is no significant effect of magnetic field interactions on the polarization properties of heart muscle or on heart rate.

Studies of nerve electrical excitability have been given emphasis because of the potential electrodynamic coupling between an imposed magnetic field and the ionic flows involved in impulse conduction. Using frog sciatic nerve preparations, electrophysiological recordings have been made of the amplitude and conduction velocity of evoked action potentials. As demonstrated in Fig. 1, neither of these properties of maximal action potentials is affected by the application of a 20 kG magnetic field. Electrical recordings from sciatic nerves have also shown that a 20 kG field has no influence on the latency period (the time interval between a stimulus and the appearance of an evoked action potential) or on the relative refractory period (the recovery time required before a nerve can exhibit a second full action potential following an initial evoked action potential).

Another area of investigation involves the measurement of structural and functional alterations in

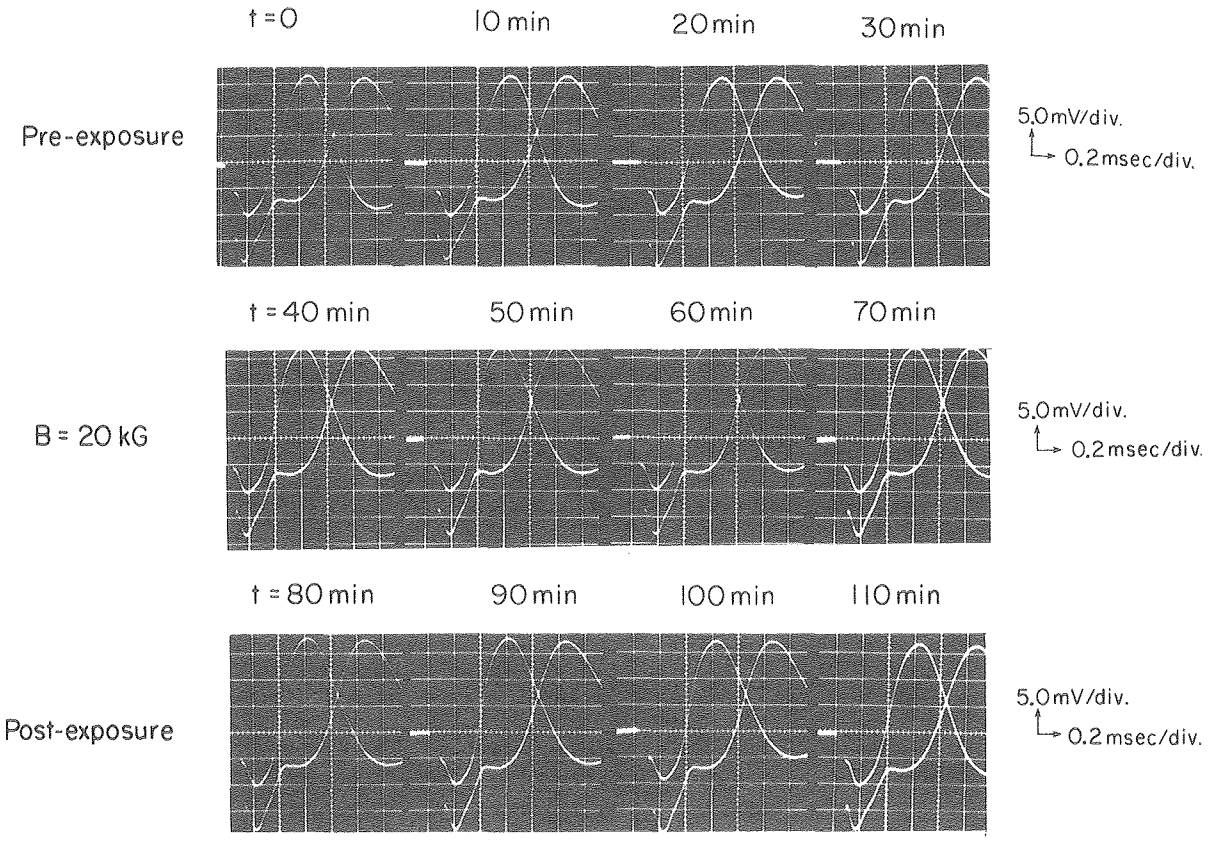

Figure 1. Measurements of the action potential conduction velocity along a frog sciatic nerve during (1) a 30-min pre-exposure control interval, (2) 30-min exposure to a 20 kG DC magnetic field (with the lines of magnetic induction parallel to the long axis of the nerve), and (3) 30-min post-exposure interval. The pair of evoked action potentials was recorded by electrodes positioned 1 cm apart along the length of the nerve fiber. The conduction velocity, 28 m/sec, was unaffected by the magnetic field exposure, and there was also no effect on the action potential amplitude. A total of 8 sciatic nerves exposed parallel to the field, and 8 exposed perpendicularly, have yielded identical results. *XBB 809-9996A*

macromolecular systems exposed to high DC magnetic fields. Of particular interest are diamagnetic macromolecules that have differing magnetic susceptibilities along orthogonal symmetry axes, and which consequently exhibit orientation in a DC magnetic field. Examples of macromolecules with this property are retinal photopigments, DNA in solution, and chloroplasts. Experimental efforts in our laboratory have been focused on the use of physicochemical techniques to evaluate potential magnetic effect on the conformation of superhelical double-stranded DNA from the bacteriophage ϕX-174 (collaborative studies with G. Kraft). As shown in Fig. 2, both the agarose gel electrophoresis profile and the relaxation time for ϕX-174 DNA aligned by a pulsed electric field (the electro-optical birefringence technique) have demonstrated the absence of any persistent structural change following exposure of the DNA to a 21.5 kG field. It has not been possible, for technical reasons, to examine magnetically-induced conformational changes with these techniques during exposure of the DNA sample to an applied field. Consequently, structural alterations may not have been detected because of their rapid "relaxation" following termination of the magnetic field exposure. A second series of experiments was therefore undertaken in which an intercalating agent, AMT (4'-aminomethyltrioxsalen), was bound to ϕX-174 DNA during magnetic field exposure, and physicochemical techniques were then used to determine whether a magnetically-induced conformational change in the DNA had altered the AMT binding characteristics. As shown in Fig. 2, both the gel electrophoresis profile and the electro-optical relaxation time measurements were identical when ϕX-174 samples were subjected to AMT crosslinking in the presence or absence of a DC magnetic field. Consistent with the negative results of these physiochemical measurements, assays for the infectivity of ϕX-174 DNA in bacterial hosts have also demonstrated that no effect results from exposure to a 21.5 kG magnetic field.

Because recent reports from a number of laboratories have indicated that measurable biological effects accompany exposure to weak 60 Hz electric and magnetic fields in the vicinity of high-voltage power lines, pilot studies were initiated during the past year to examine the influence of a low-intensity 60 Hz magnetic field on selected experimental test systems (collaborative studies with S. Kronenberg, H. Davis and E. Bennett). In contrast to results obtained by other investigators, chronic exposure to a 25 G (peak), 60 Hz magnetic field was found to have no demonstrable effect on cellular growth properties. In other studies with 60 Hz magnetic fields, no significant changes were observed in several neurobehavioral parameters of exposed rodent populations, including activity patterns and the retention of memory in a passive avoidance training task.

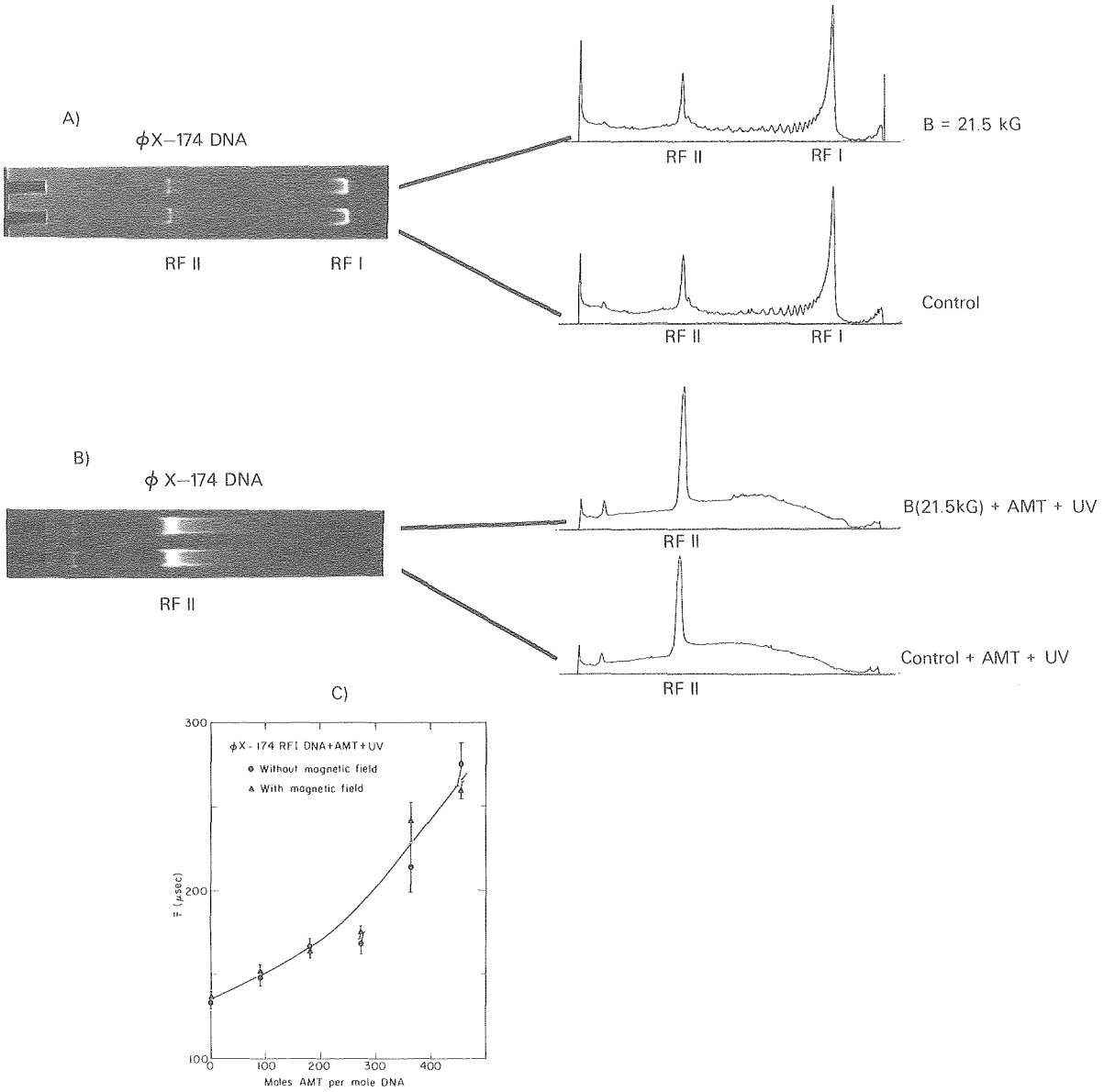

Figure 2. Gel electrophoresis profiles and electro-optical birefringence measurements for ϕX-174 DNA samples exposed to a 21.5 kG magnetic field for 1 hr, and controls. (A) Agarose gel electrophoresis profiles of native ϕX-174 DNA; the predominant peak (RF I) arises from superhelical DNA molecules, and the minor peak (RF II) from a small proportion of DNA molecules with a circular conformation. (B) Exposed and control samples crosslinked with AMT (375 moles AMT per mole DNA). The crosslinking, activated by illumination with an intense 360 nm UV light, converts ϕX-174 DNA to predominantly the RF II form. Accompanying densitometer scans of the gel profiles show that the DNA conformation was unaffected by the magnetic field, and that AMT crosslinking of the DNA was identical in the presence and absence of the field. (C) Plot of the relaxation time ($\bar{\tau}$) ± 1 S.D. for control and exposed (21.5 kG, 1 hr) ϕX-174 DNA samples as a function of AMT concentration. DNA was aligned by applying a 9.25 kV/cm electric field pulsed for 200 μsec, and the relaxation time was then determined optically. Relaxation time measured by the electro-optical method is inversely proportional to the rotational diffusion coefficient of the DNA, and is thus a sensitive measure of its molecular size and conformation. For both exposed and control samples, relaxation time increased similarly with AMT concentration, reflecting the conversion of ϕX-174 DNA from a superhelical RF I conformation to a circular RF II form. The electrooptical data, with and without AMT cross-linking, indicate that the magnetic field had no measurable effect on ϕX-174 DNA conformation. *XBB 809-10617*

Biophysical Studies

IN VITRO ELECTROPHYSIOLOGY OF CNS NEUROTOXICITY TO ENVIRONMENTAL POLLUTANTS

Michael S. Raybourn, Julia A. Twitchell, and Walter Schimmerling

This project has been developing the techniques and procedures necessary to provide a quantitative *in vitro* bioassay of the functional neurotoxicity of environmental agents to central nervous system (CNS) tissues for both acute and chronic exposures. Our focus has been on hypoxia and carbon monoxide (CO). In the upcoming year, methyl mercury insults will also be addressed.

We have nearly finished our control studies on the acute effects of the basic variables of temperature and pH on cerebellar Purkinje cell (PC) spontaneous electrical activity. The rationale here is to provide a quantitative context wherein the relative effects of hypoxia and presumed electron transport chain perturbations (via CO) could be assessed in terms of the underlying cellular mechanisms. We have attempted to separate synaptic (i.e. intercellular) from intracellular contributions by use of divalent cations ($Co^{++}Cl$) to pharmacologically block synaptic transmission and, thus, isolate Purkinje cells from their normal afferent inputs. We have not found any marked or consistent effects on PC activity with changes in the pH of the superfusing media over the range that our experimental gas exposures—O_2 at low partial pressure (pO_2) and CO—induce. Moreover, we do not see any clear effects until pH values drop to around 4.0–4.5. We can conclude, then, that the media pH changes that we do see during tissue hypoxia (−0.5 pH unit) do not significantly contribute to altered cellular activity.

Our thermal kinetics studies have demonstrated the expected coupling between elevated temperatures and increased firing rates of Purkinje cells. The mean temperature sensitivity (Q_{10}) for this was 3.9 (S.D. = ± 2.8) when sampling with normal synaptic input present. However, synaptically-isolated "pacemaker" PC's possessed markedly lower Q_{10}'s (X = 1.9, S.D. = ± 0.4). This suggests that the two modes of spike electrogenesis (synaptic, endogenous) utilize different enzymatic reactions. The pacemaker (endogenous) Q_{10} value is quite comparable to the Q_{10} values of the glycolytic and Krebs cycle enzymes while the higher values for synaptically-mediated activity almost certainly reflect complex, multicellular processes.

Our initial acute hypoxia studies have concentrated on relatively small changes in ambient pO_2 (down to 11%) for two reasons. Adequate dose response functions are needed for known local tissue pO_2 levels in this range since most previous *in vitro* studies employed quite low oxygen levels (0 to 5% pO_2) in order to cause CNS damage detectable by their methodologies (usually morphological). Also, the sensitivity of our bioassay should allow us to detect functional changes in CNS behavior at more clinically-relevant levels of hypoxia (10 to 15% pO_2).

We have completed the hypoxic dose-response characterization for synaptically active preparations at room temperature. Our hypoxic data show that:

1. Any decrease in local pO_2 (down to 13.5%) results in an initial *increase* in firing rate. This is followed, in an approximately dose-dependent fashion, by a gradual decrease back to control firing levels. Smaller pO_2 drops (to 18%) often result in a prolonged facilitation of firing that only gradually approaches control levels. Larger pO_2 decrements (18% to 13.5%) usually result in briefer periods of facilitated firing and final rates fall correspondingly below control levels.
2. Hypoxic insults of 13.5%, or lower, often do not show this initial facilitation, but, instead, result in a dose-dependent reduction in firing rates. The duration of these hypoxic insults greatly determines whether a return-to-control can be achieved. So far, 5 minutes of 11 to 13.5% pO_2 seems to be tolerated by the cells, whereas 15 minutes or longer at these levels almost invariably results in cell loss.
3. The cell-to-cell variability of these findings probably stems, in part, from the combination of intercellular (i.e. synaptic) and intracellular mechanisms being perturbated. Our current work is addressing these questions, using the pharmacologically-isolated PC. This will allow us to study the "pure" intracellular response to hypoxic insult.

Based on our current data on acute CO exposures (N = 52 cells), we can tentatively sum up by

stating that short duration exposures (4 to 15 min.) of gas phase CO at concentrations of 500 to 1000 ppm result in threshold perturbations in spontaneous PC activity. These effects are seen both in mean firing rate and in the fine structure of interspike-interval histograms. Development of the more rigorously quantitative (and sensitive) dose response functions based on changes in membrane excitability thresholds are under way (see Fig. 1).

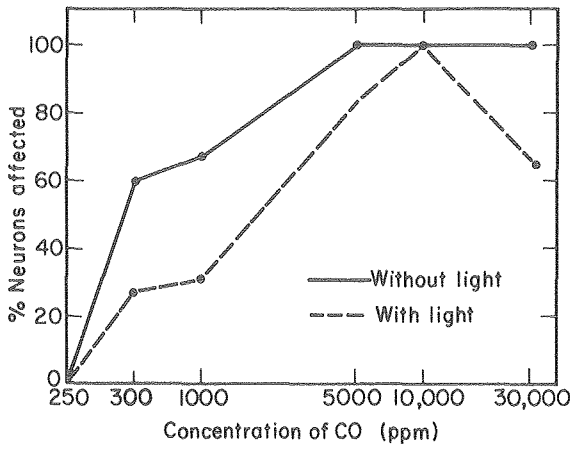

Figure 1. Dose response of neurons to CO (gas phase). The difference in the two curves represents the extent of disinhibition produced by light via photodisassociation of CO from intracellular building sites (cytochrome aa_3 oxidase). *XBL 784-3022*

Our chronic incubation studies have initially concentrated on determining the upper limit of CO concentration times duration of exposure that will allow normal culture development. To date we have reduced our exposures to thirty minutes of 500 ppm CO as the upper limit. Above this level, we do not get any appreciable culture growth and/or electrophysiological activity.

The initial transient increase/decrease in cellular activity in response to hypoxia is also seen with CO exposures. However, as in hypoxia, this is a highly dose-dependent phenomenon with 500 ppm to 1000 ppm CO being the only range over which this biphasic sequence occurs. Greater CO concentrations always result in inhibition only. The biphasic nature of neurone response to hypoxia has been attributed to an activation of glycolysis (via hexo- and pyruvate kinase) with the subsequent inhibition (Crabtree effect) due to changing cytoplasmic levels of ATP/ADP•Pi.

We are currently addressing the question of whether or not our electrophysiological signals represent a cell membrane manifestation of these bioenergetic processes. In doing so, we hope to quantitatively determine the relative contributions of glycolysis and oxidative phosphorylation to neuronal membrane function.

CELL-MEMBRANE BIOPHYSICS AND ENVIRONMENTAL AGENTS

Howard C. Mel

The biophysical and biorheological (flow) properties of whole-cell and cell-membrane systems have been under concerted investigation to learn more about normal cell-membrane physiology and about alterations in abnormal states. Understanding the meaning of "abnormality" in this context, whether arising from disease or from the action of external chemical or physical agents, can lead to more detailed, earlier, and more sensitive identification of changes, as in clinical diagnosis, and aid in developing countermeasures when the changes reflect hazards to human health. The human red blood cell is a prime object of study in this work because of its widespread distribution throughout the body, its ready availability for sampling, and its sensitive and multifaceted response characteristics.

In recent times, research laboratories around the world have been paying increasing attention to the so-called rheological properties of blood cells. This refers to their behavior under conditions of flow, and to flow-like responses (within the cell and/or membrane) to cell-membrane alterations. In this sense, certain dynamic responses of the overall cell-membrane system, such as deformability and mechanical and osmotic fragility, can be viewed as analogues of such molecular properties as flexibility or conformational change, chemical bond disruption, and the like. Furthermore, during its normal functional life the red cell is in constant motion and undergoing continually changing states of form and deformability, without which it could not circulate properly and carry out its appointed biological functions. It is also constantly subjected to disrupting forces, forces that eventually lead to the cell's destruction. Thus, the traditional static view of the cell, as usually pictured in books and research articles, is incomplete if not highly misleading.

The experimental technique that we call "resis-

tive pulse spectroscopy" (RPS), developed in our laboratory, continues to play a leading role in these investigations, since it provides a rapid, coordinated, automatic methodology that can yield static and dynamic information on cell size, form, deformability, fragility and membrane recovery processes. Furthermore, all these properties can be measured with only a single, very small sample of blood—from a finger prick, for example, or from the residual of samples taken for other purposes—which is important because they are interactively interrelated. An outgrowth of the electronic particle counting and sizing technique known as Coulter counting, RPS employs controlled conditions of fluid flow rate, medium composition, cell rigidification procedures, electrical orifice conditions, and on-line computer processing to extract a good deal more (and more reliable) information from the spectra of resistive particles than was previously possible. To complement and enlarge upon the capabilities of RPS, a number of other biophysical and cytological techniques are also brought to bear in the studies.

Two findings will serve to illustrate the principal, fundamental RPS measurements. Fig. 1 is an automatic spectral sequence showing red cells undergoing a systematic loss of deformability in response to the important chemical fixative agent glutaraldehyde (GA). It has previously been shown that the "shoulder" or "bimodality" on the RPS apparent size curves, for cells undergoing a change in deformability, provides a new kind of measure of the cells' deformability.[1] Such a "disappearing shoulder" is clearly seen in the kinetic sequence of Fig. 1. To quantitate and scale this bimodality-deformability parameter, a dimensionless RPS index has been developed.[2] The time sequence values of the index for four times in this sequence are shown in Table 1.

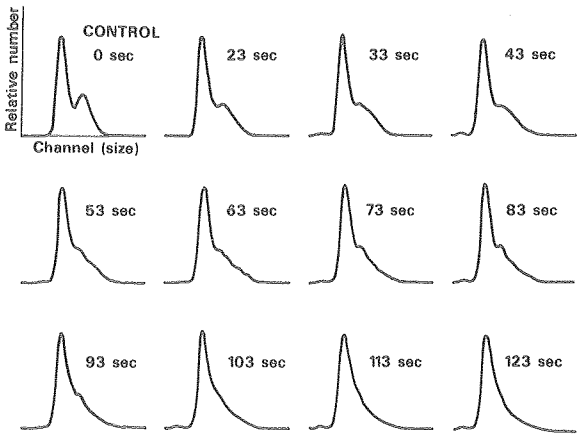

Figure 1. Glutaraldehyde-fixation kinetics spectral sequence. RPS spectra of red blood cells mixed at time t = 0 seconds into solution containing 0.25% glutaraldehyde. Note gradual loss of deformability shoulder.

DBL 745-4792A

The principal-mode (or mean) sizes can also be automatically determined from such curves, and the complex kinetics of size change for a sequence such as Fig. 1 has been presented elsewhere.[3]

A different set of properties is obtainable from the RPS technique called "dynamic osmotic hemolysis" or DOH. When the small blood sample is quickly added to a hemolytic medium of low osmotic pressure, the kinetics of formation of "ghosts" can be followed and depicted as in Fig. 2. On each spectrum the leftmost, that is, the "smaller-sized" peak represents the ghosts (the closed RBC-membranes that have lost their hemoglobin); the rightmost peak represents the still intact cells. This kind of experiment thus provides a new measure of osmotic fragility—much faster and simpler than the conventional laboratory or clinical measures. In addition, it is possible from the information in Fig. 2 to follow the "mechanical recovery" of the membrane following the hemolytic act, from plots of the apparent size of the ghosts (ghost peak position vs. time, at both normal and reduced flow rates). An example of this is given in Fig. 3.

MERCURY EFFECTS ON THE RED CELL–MEMBRANE SYSTEM

With the above background, we present here some recent results from a study of the effects of very low concentrations of mercury.[4] Effects are seen on all of the properties discussed above (size, form, deformability, fragility, recovery). With respect to fragility, the smallest amounts of mercury are seen first to "protect" cells against hemolysis while the higher concentrations lead to enhanced hemolysis (Fig. 4). If cells were preincubated in the mercury the hemolytic effect is exaggerated (Fig. 5).

Size and deformability effects are shown in Fig. 6. Another curious protection effect is seen here, whereby the low concentrations of mercury are able to counteract the usual cell-swelling resulting from low osmotic pressure, and thereby "restore" a more

Table 1. Loss of RBC deformability during glutaraldehyde (GA) fixation.

Time lapse following GA exposure (seconds)	0	20	70	120
"Deformability index"	1.58	0.95	0.72	0.34

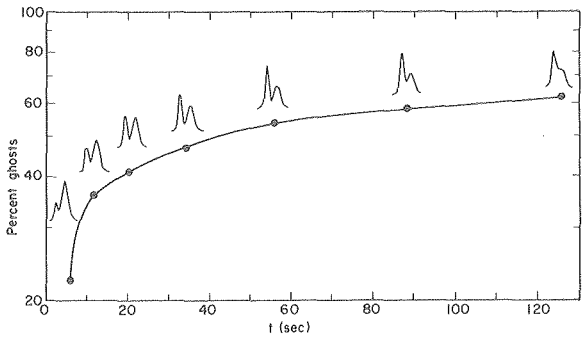

Figure 2. Osmotic fragility of red blood cells by dynamic osmotic hemolysis (DOH). The continuous curve represents the cumulative percentage of ghosts (left peaks) versus time following exposure to hemolytic medium (123 m0sm PBS). RPS spectra are shown above each experimental point. *XBL 792-3184A*

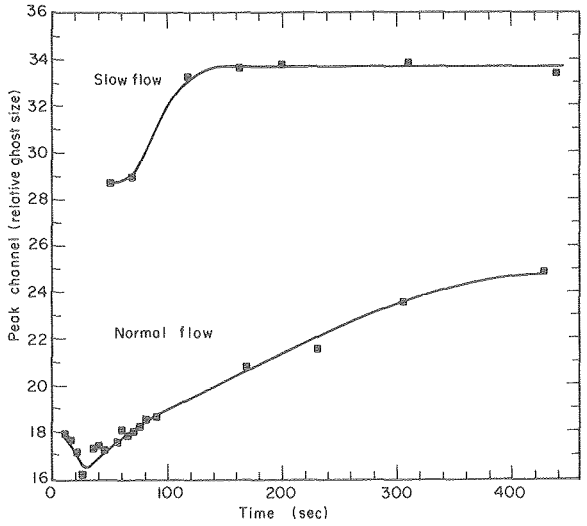

Figure 3. Kinetics of ghost repair. RPS size (modal channel) of ghost subpopulation is plotted versus time, for normal and slow sample flow rates (lower and upper curves, respectively). Note that at the slow flow rate, the reduced mechanical shear is insufficient to re-rupture the recovering membrane and expel ghost contents after about 120 seconds, while at fast flow the shear is large enough to reopen ghosts all the way out to 300+ seconds.
XBL 782-2870A

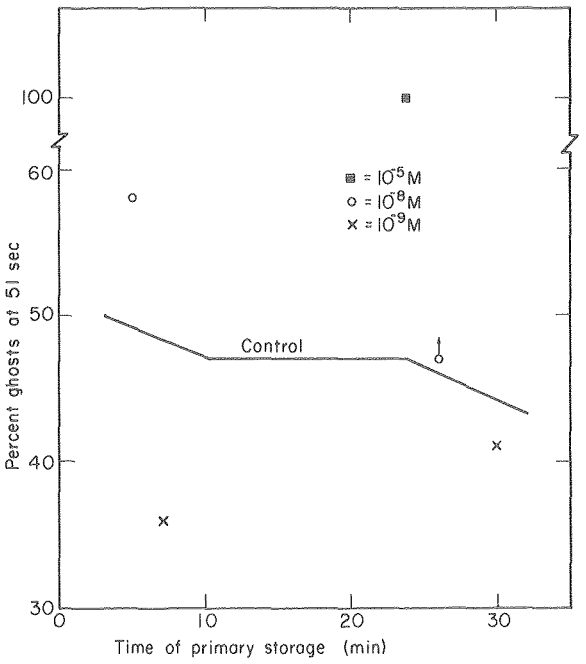

Figure 4. Hemolytic and protective effects of $HgCl_2$. Data are taken from the 51-second spectra of DOH sequences. Conditions: "instantaneous" exposure; storage temperature 37 °C; 3.5 × 10^5 cells/ml. *XBL 792-3181B*

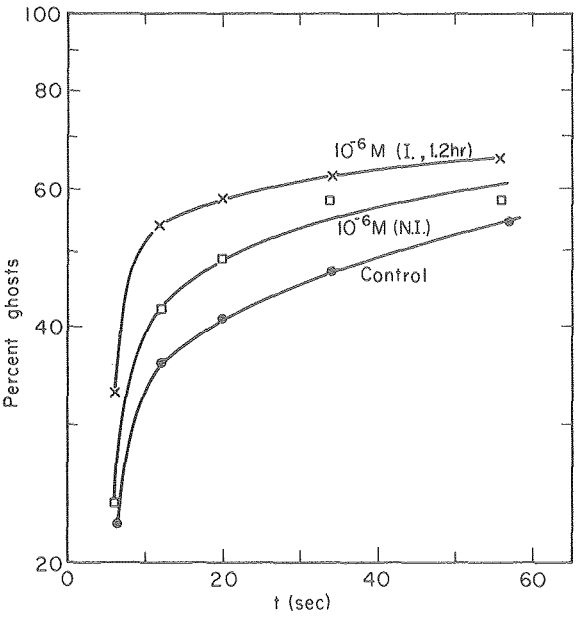

Figure 5. Osmotic fragility of red blood cells exposed to 10^{-6}M $HgCl_2$. DOH sequence in 123 m0sm PBS, for control cells, cells incubated 1.2 hours, and "instantaneously" exposed (non-incubated) cells. Conditions: room temperature; 1.0 × 10^6 cells/ml. *XBL 792-3180B*

normal size and deformability for such cells (which by all odds should be approaching a spherical state and therefore also be undeformable). The apparent explanation for these variously protective and damaging effects of this toxic heavy metal is that they proceed by first introducing a very selective kind of membrane damage, causing loss of potassium from the cell. Later, or with larger concentrations of mercury, more massive damage occurs to the entire ion regulation system, and the excess osmotic pressure of the hemoglobin is able to drive the cell to its hemolytic fate.

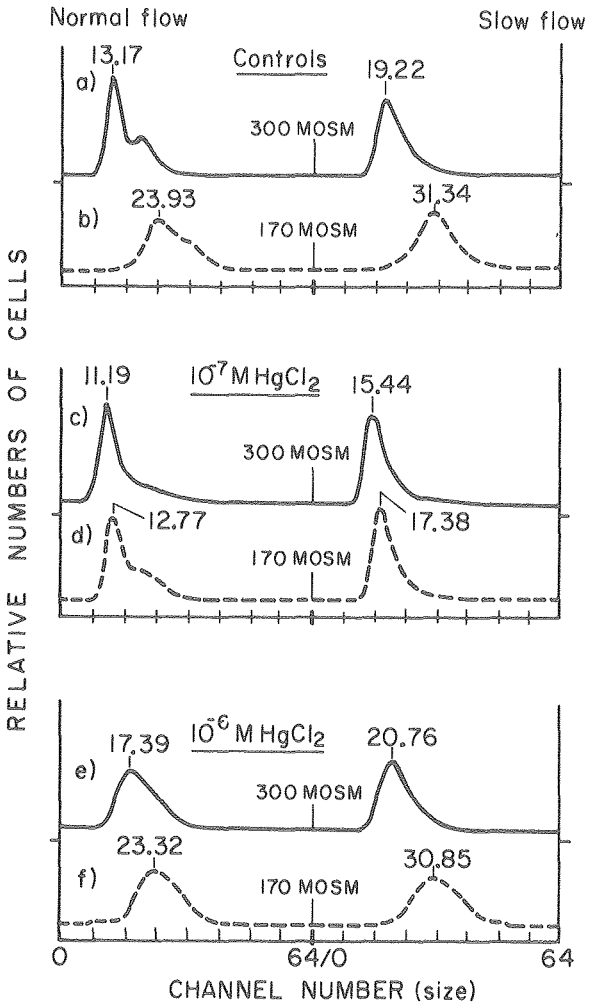

Figure 6. Effects of mercury on red blood cell size and deformability after 90-minutes exposure, as a function of mercury concentration and osmolarity. At 10^{-7}M, $HgCl_2$ counteracts the effect of 170 mOsm, reducing the volume and increasing the deformability (d versus b).

XBL 806-3390B

TIME AND TEMPERATURE EFFECTS

A recent and surprising discovery was that, when fresh blood was diluted in an isotonic medium to prepare stock samples for further study, mature red cell–membrane properties underwent extensive and rapid changes. An example is given in Fig. 7. This behavior, which is not yet common knowledge, must be considered when carrying out virtually any studies of red cell properties, in order to avoid gross misinterpretations of data.

ELECTRICAL EFFECTS

Additional new information has been discovered during the past year on the electrical conductive properties of the cell-membrane, as indicated in Fig. 8. These curves point up an intriguing property of the red cell membrane—its voltage-dependent conductance. (Is the red cell thus a kind of "nerve cell" in disguise?)

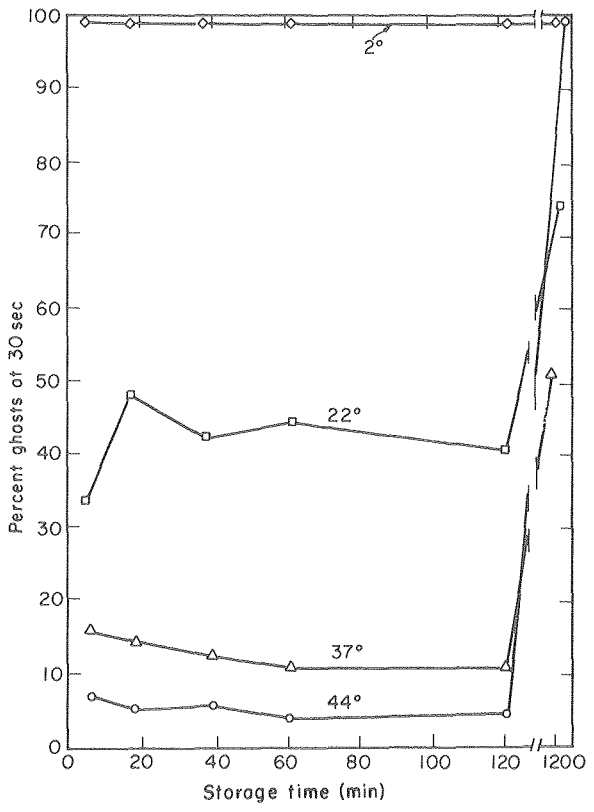

Figure 7. Ghost formation in 30 seconds at 128 mOsm versus primary sample storage time: effects of temperature. As shown, not only do different temperatures produce widely differing degrees of hemolysis, but the effects of in vitro aging on osmotic fragility are temperature dependent as well.

XBL 792-3187B

RED CELL PATHOLOGY

As a final example we present some results from a current study on alcoholic liver disease. Fig. 9 indicates how such patholgoical cells are larger and more osmotically resistant. That they form larger ghosts, which recover more quickly than normal cells, is indicated in Fig. 10.

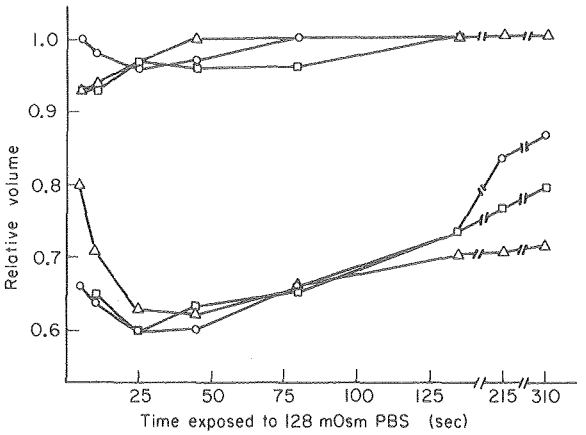

Figure 8. Electrical differences in late post-hemolytic recovery: ghost and critically swollen spherocyte volumes relative to the maximum spherocyte volume during the course of hypotonic lysis. At less than 135 sec after exposure to hypotonic medium, there is no apparent current leakage. Later time points reveal a systematic differential ionic leakage for ghosts. (Critically swollen intact cells remain constant in number through the course of the experiment.) Measurements were made at three electric field strengths. Assuming that 50% of the potential drop occurs across 100 microns, the curves correspond to: ○ = 0.82 kV/cm; □ = 1.03 kV/cm; Δ = 1.30 kV/cm. XBL 8011-3819

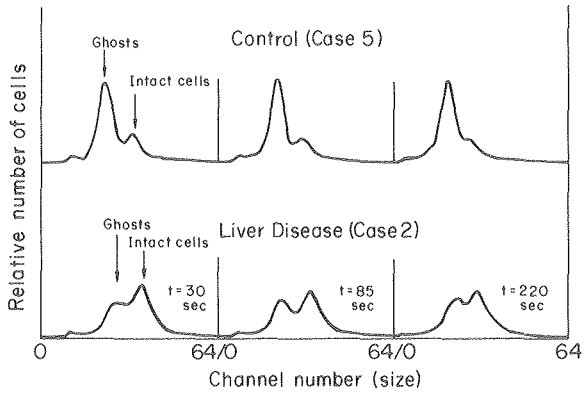

Figure 9. Comparison of rate and extent of hypotonic lysis in normal versus alcoholic liver disease blood. Each spectrum represents mixed populations of ghosts and critically swollen intact red blood cells at successive time intervals. The spectra were collected 30, 85, and 220 sec after initial dilution into hypotonic media. Not only are the liver disease cells more resistant, they also form larger ghosts that recover more quickly than controls (see Fig. 10).

XBL 809-3713

Besides Howard C. Mel, Professor of Biophysics, members of this group include Steve Akeson, Tom Reed, James Yee, Anne Poley, Gary Richieri, Rick Renslo, Sara Rabinovicci, Dennis Kumata and Jon White.

REFERENCES

1. Mel, H.C., and Yee, J.P. 1975. Erythrocyte size and deformability studies by resistive pulse spectroscopy. *Blood Cells* 1:391–399.
2. Yee, J.P. 1979. Development and application of resistive pulse spectroscopy studies on the size, form and deformability of red blood cells. Ph.D. Thesis, University of California, Berkeley, California 94720, 1979. Lawrence Berkeley Laboratory report LBL-8840.
3. Yee, J.P., and Mel, H.C. 1978. Cell membrane and rheological mechanisms: dynamic osmotic hemolysis of human erythrocytes and repair of ghosts as studied by resistive pulse spectroscopy. *Biorheology* 15:321–339.
4. Mel, H.C., and Reed, R.A. 1980. Red cell-membrane biophysical responses to very low concentrations of inorganic mercury. Submitted to *Cell Biophysics*.
5. Kachel, Volker. 1979. Electrical resistance pulse sizing. In *Flow Cytometry and Sorting;* M.R. Melamed, P.F. Mullaney, and M.L. Mendelsohn, eds., New York: John Wiley & Sons, Inc.

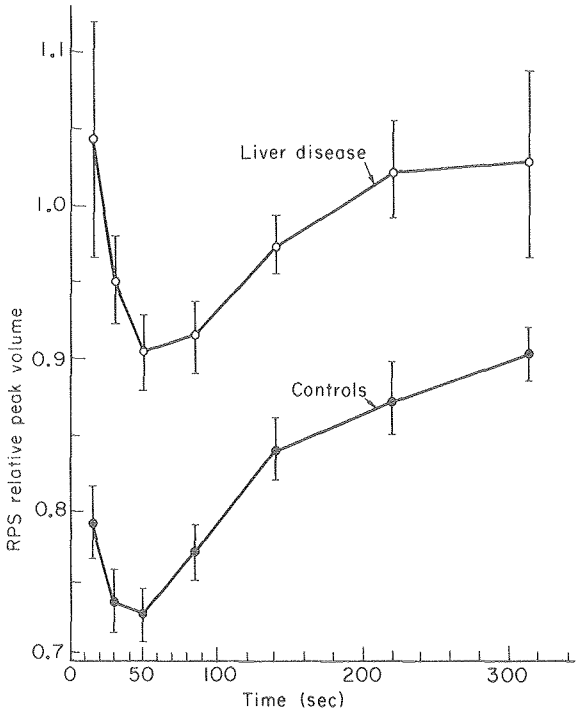

Figure 10. Kinetics of ghost volume changes after initial hypotonic dilution for red blood cells from alcoholic liver disease compared to normal healthy controls.

XBL 809-3714

7. STRUCTURAL BIOPHYSICS

Complex biological problems may often be solved by using biophysical approaches, applying the methods of physics to an appropriate biological system. In this way, fundamental aspects of biological structure and function may be elucidated. The Structural Biophysics Group, under John Burki, is currently engaged in fundamental research in three general areas: the application of scanning and transmission electron microscopy to elucidate structural aspects of biological material; studies of DNA, eucaryotic genetics and mutagenesis; and the use of advanced lipoprotein techniques in studies of atherosclerosis. This year's annual report gives the results of 19 studies within the Structural Biophysics Group. Subjects range from properties of fly ash taken from Mount St. Helens to studies of the serum proteins of baboons. Five of these diverse projects illustrate the range and approaches of the Structural Biophysics Group.

In applying scanning electron microscopy (SEM) to the study of progressive pulmonary edema, investigators have begun a successful application of an alternative sample preparation system. Lungs are fixed by rapid freezing with liquid nitrogen and freeze-fractured at low temperature and high vacuum, then gold-coated and transferred *in vacuo* to a special low-temperature SEM stage for observation. This new technique has permitted a more authentic examination of hydrated (wet) lung samples and offers many advantages over "dry" systems in determining three-dimensional structure of alveolar sacs *in vivo*.

The yeast genetics group has successfully introduced recombinant DNA procedures to study of the yeast gene system by cloning the RAD52 gene, one of the genes involved in recombination and repair in yeast. Its cloning will facilitate many new studies on the genetic recombination mechanism in yeast. In addition, the cloning method can be applied to almost any gene on the yeast genetic map.

Investigations of mutagenesis in highly synchronous Chinese hamster cells have shown that the mutagenic effects of various environmental agents are different at different times in the cell life cycle, complicating the results of earlier studies. In certain cases these effects are very pronounced; for example, x-rays induce many more mutations in the early period of the cell cycle than at other times.

The discovery of new multiple subclasses of low-density lipoproteins (LDL) from human sera has opened new research areas. Investigators in the lipoprotein group have used several methods to characterize these LDL peaks, including isopycnic banding, polyacrylamide gel electrophoresis, and lipid staining. They have established conditions for examining 10 distinct bands in normal human subjects. Preliminary results suggest an association between one or more of the smaller LDL subspecies and human atherosclerotic risk.

It has been established that *new* plasma lipoproteins exist in baboons on a cholesterol diet. These baboon studies have an advantage over human studies in that selective breeding has resulted in baboon progeny which have either elevated or low concentrations of plasma cholesterol in response to an atherogenic diet. Preliminary studies suggest that certain lipoprotein variants may be due to single-gene inheritance. This work opens the way for sorting out a possible genetic factor in atherosclerotic disease.

The highlights of achievements during the past year in these and other areas of investigational interest are presented in the articles that follow.

Electron Microscopic Studies

HUMAN LUNG STUDIES: POSITIONAL MORPHOLOGY

S. Jacob Bastacky, L. Michael Sprague, Barbara Von Schmidt,* Gregory R. Hook, Gregory L. Finch, and Thomas L. Hayes

Pulmonary medicine presents us with significant health problems. The nation is experiencing an epidemic of lung cancer with 100,000 new cases expected in 1980. In premature infants, the major cause of hospitalization and death is the immaturity of their lungs and our difficulties in supporting their respiratory function. Gaseous and particulate air pollutants attack the lung both acutely and chronically. Asthma, chronic bronchitis and emphysema are chronic and unfortunately common diseases which cause structural change and considerable disability. Pulmonary edema complicates a significant number of hospitalizations for heart, lung, and other diseases.

An adequate understanding of the structure and function of the human lung is basic to advances in pulmonary medicine. We have developed unique tools and are applying them to fundamental problems of lung architecture, physiology, and disease.

Gas exchange between an oxygen-rich atmosphere and a carbon-dioxide-rich bloodstream is the principal but not exclusive function of the lung. A passive-diffusion gas-exchange membrane such as exists in the lung is most efficient when it is maximal in surface area and minimal in thickness. The air-blood barrier in the human lung is about half a micrometer thick (less than one-tenth the width of a red blood cell) and has a surface area of 70 to 160 square meters (the singles play area of a tennis court is 190 square meters). This membrane is folded into the chest in the form of a branching system of tubes with distal outpouchings; its form is analogous to that of a tree. This bronchial tree develops as an elaborate branching structure in three-dimensional space, a structure that has been difficult to study with conventional two-dimensional light and electron microscopy.

The abundant depth of focus and the broad, continuously variable magnification range of the scanning electron microscope (SEM) make it well-suited to studying the lung's convoluted and highly organized surface. Practically attainable magnifications ranging from 10 times to 20,000 times with resolution down to 100 Å allow us to image subcellular elements, single cells, neighborhoods of cells, or large airways.

Since the information content of the image produced by the microscope depends on the sample surface, preparative procedures, and the microscope's optics, the usefulness of scanning electron microscopy can be increased by presenting to the microscope a prepared sample whose surface is native (not an artifact of sectioning) and is presented in its original context. Such a sample preserves its topological property of connectedness. For our lung studies, we image the air/tissue interface of an unsevered airway such that all zones of the airway are present in their intrinsic order. This is accomplished by microdissecting an airway in the lung, following it over its full length, and studying the morphologic features of the lung that appear along its wall. We have developed microdissection techniques and SEM photomontage techniques that allow evaluation of structural detail along the airway as part of the information about any given point. This permits rigorous comparison of data within and between samples.

The microdissection techniques generate unit-airway samples that are mapped with the scanning electron microscope at low magnification (10×, 100×). The maps are used to choose specific features for surface analysis at higher magnification in the SEM. Subsurface structure can be correlated with surface structure by choosing loci from the maps for excision and subsequent section analysis in the light microscope or transmission electron microscope. Further dissection can be carried out by hand or in the electron beam. A prime contribution of this approach is that information can be maintained in context and the position of analytic data within the lung can be reported. Figure 1 demonstrates such a stepwise examination of ciliated epithelium.

We are using this technique to study several structural features of the human lung, such as its air sacs, the alveoli. We find that the configuration of alveoli changes with respect to their shape, as does the thickness of their walls with progress along the airway. The proximal alveoli have thick walls, tend to be rounder, smaller, and more irregular in size

*Children's Hospital Medical Center of Northern California.

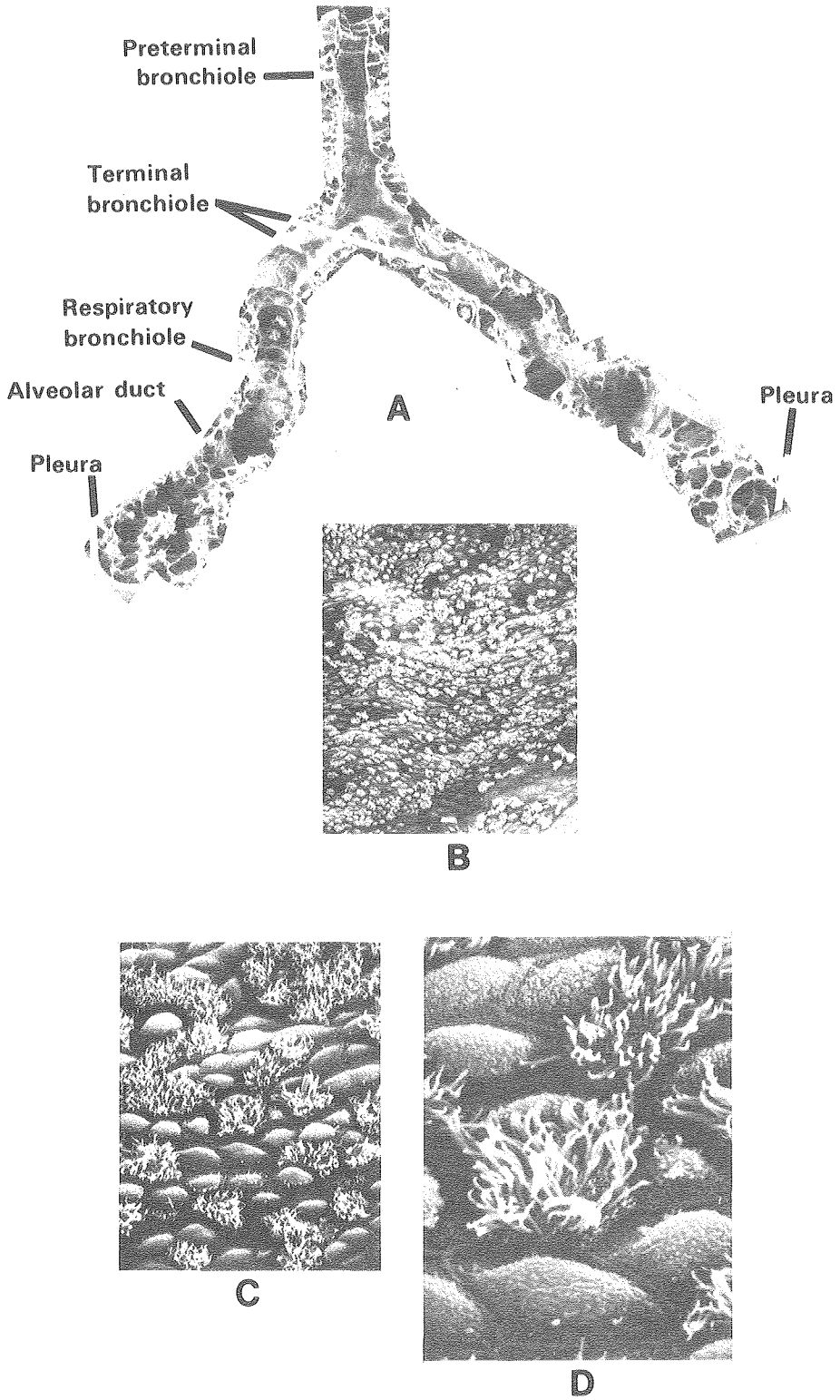

Figure 1. (A) SEM map of the last centimeter of the human airway. Two branches are dissected open, magnified, and displayed here. The terminal bronchiole becomes two respiratory bronchioles as alveoli begin to appear along the wall. This map is used to choose areas for higher-magnification SEM analysis (magnification ~10×). (B) Lining of the right-hand terminal bronchiole (~200×). The surface of the ciliated epithelium begins to appear discontinuous. (C) Center of the field in (B) (~800×). Individual cells can be seen, some covered with fingerlike cilia and some without cilia. Cells are demarcated by a raised border. (D) Ciliated cell in the center of (C) (~3,200×). The cell is covered with about 200 cilia that move back and forth about 20 times per second in life, moving a layer of liquid and trapped particles. *XBB 8010-11560*

than the more distal alveoli. This most likely represents changes in the composition of the wall of the mouth of the alveolus. To determine this, we are developing a technique of correlative transmission electron microscopy (TEM). Alveolar walls at each point along the airway are microdissected out after SEM examination and embedded for sectioning at a given orientation. TEM determination of the internal structure of precisely located septa, i.e., quantitative analysis of smooth muscle, collagen, elastin, capillary volume, and cell type, can thus be performed. This information can be correlated with the SEM-determined surface features of the identical septa. This sort of structural information suggests that alveoli in different positions along the airway have differing mechanical properties, which would cause them to behave differently under disease conditions such as atelectasis, edema, noxious insult, and bronchoconstriction. This knowledge is significant for our understanding of the mechanics of both physiological and artificial ventilation.

We are also studying the distribution of secretory glands along the conducting airway. Preliminary evidence suggests that glandular elements may persist as primitive shallow diverticula more distally than has been generally appreciated. These secretory pockets could be significant in hypersecretory states such as asthma and in pathologic secretory states such as cystic fibrosis.

Since 30% to 40% of adult Americans smoke, according to the Surgeon General, a subpopulation of humans exposed to environmental air pollutants are smokers. Ciliated epithelium in the airways of smokers undergoes metaplastic change under the influence of continuous irritation. Our preliminary comparison of smokers and nonsmokers as studied by positional morphology techniques indicates that changes are not uniform; rather, microenvironments differ in type and extent of cell change so that islands of one cell type appear. These islands may represent stages in the development of lung cancer.

For some years there has been interest in studying the liquid surface lining material in the distal lung. This is a highly hydrated layer that suffers considerable deformation and shrinkage with fixation and drying during conventional preparation for electron microscopy. With a new method, we have avoided these problems and can study the surface lining material of the alveolus *in situ*. The lung is frozen and a portion examined in the frozen-hydrated state in a specially constructed SEM with cold stage and attached cryo-chamber.

We are studying the accumulation of pulmonary edema in the lung with the cold stage microscope. At the cellular level we have been studying the interaction of the lung macrophage with particulate pollutants and have developed a quantitative evaluation for surface characteristics of the pulmonary alveolar macrophage. We are interested in the interactions of volcanic ash as well as fly ash with the lung. More detailed descriptions of these projects are to be found elsewhere in this report.

We are developing a pool of lung samples and scanning electron microscope montage maps that can be used as a data base for evaluation of these and other variables. We collaborate in this effort with surgeons, pathologists, pulmonary physicians, lung scientists, and hospitals in the San Francisco Bay Area, and other parts of the country.

SCANNING ELECTRON MICROSCOPY OF CULTURED HUMAN ALVEOLAR MACROPHAGES

Gregory L. Finch, Thomas L. Hayes, Gerald L. Fisher,* and David W. Golde**

The pulmonary alveolar macrophage (AM), by virtue of its phagocytic properties, is an important factor in defending the lung against bacterial and pollutant insult. The complex shapes and surface features of human AM have been qualitatively described by many researchers using the scanning electron microscope (SEM). We have extended previous observations by describing a scheme for quantification of not only AM size but the incidence of various surface features and shapes as well. This permits rigorous statistical testing of differences noted between AM populations. Correlation of AM morphology with function may provide insights into mechanisms of AM functional alterations in disease states and in response to cellular insult.

Our morphological classification scheme was used to explore possible differences between cultured AM obtained from human cigarette smokers and nonsmokers. The cells were obtained by bronchopulmonary lavage and allowed to attach to glass coverslips in a medium containing 20% fetal calf serum. After culturing for 1, 2, or 25 hours, glass

* Battelle Memorial Laboratories, Columbus, Ohio.
**Department of Medicine, University of California, Los Angeles.

adherent AM were prepared for the SEM by glutaraldehyde fixation, osmium tetroxide postfixation, and critical-point drying. Fifty cells per sample were randomly selected for detailed morphological analysis using a predetermined sampling grid. Area, form, degree of cell spreading, and the relative abundances of surface features, including ruffles, filopodia, blebs, microvilli, multiple features, and featureless cells were quantified. Cell projected area was determined from micrographs taken at 0° tilt.

Three shape classifications were employed to characterize AM; rounded, spread, and intermediate. Rounded cells (Fig. 1) had a highly rounded central region with little or no membrane spread along the coverslip, whereas spread cells (Fig. 2) exhibited no distinct rounding and generally had membrane spread thinly along the coverslip. Intermediate cells (Fig. 3) usually had a "fried egg" appearance, with a rounded central region and spreading along the substrate.

The rich diversity of cell surface features were also examined and classified. The ruffled type (Fig. 3) was a common morphology and consisted of membranous ruffles, folds, ridges, veils, or lamellipodia. The filopodial type (Figs. 1, 3) was characterized by thread-like filopodia extending outward along the substrate. The microvillous type (Fig. 1) displayed finger-like microvilli projected outward usually from the rounded central area. Blebs, rounded membrane outcroppings, were observed infrequently. Craters (Fig. 2) were often observed in the periphery of spread cells, and may represent the remnants of lysosomal vacuoles ruptured during SEM preparation.

If a cell exhibited none of the above surface features, it was classified as having no significant surface features. In these cells, most of the cell surface appeared essentially smooth, with no distinguishing characteristics. If a cell had more than one of the surface features, it was also classified as having multiple features.

The classification data obtained were used to examine differences between smoker and nonsmoker AM populations and between culture times. Smoker AM had a greater incidence of ruffles, filopodia, multiple features, and rounded cells; nonsmoker AM had greater incidences of featureless and spread cells. Microvilli and blebs were observed infrequently and displayed no trends with respect to differences between smokers and nonsmokers. The incidence of filopodia, multiple features, and intermediate shapes generally increased with increasing culture time, and a decreasing incidence with in-

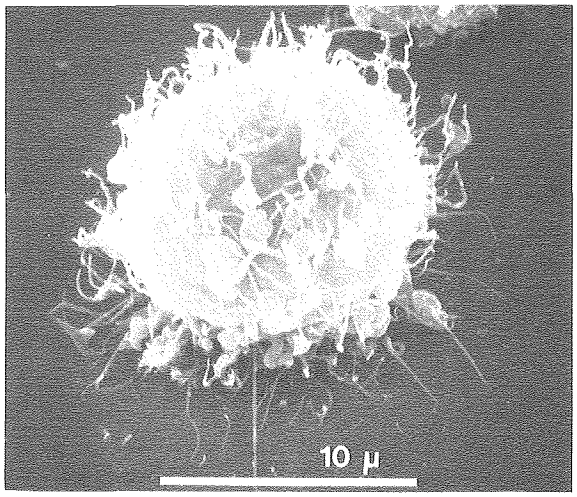

Figure 1. Smoker alveolar macrophage of the rounded type displaying long microvilli over the surface. (2-hour incubation; bar = 10 μ; original magnification 4300×.)
XBB 809-10954

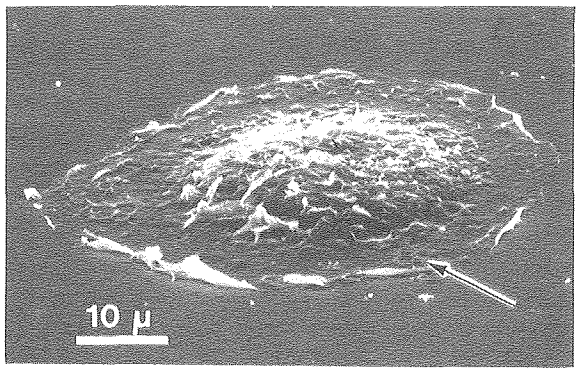

Figure 2. Smoker alveolar macrophage of the spread type displaying peripheral craters (arrow). (1-hour incubation; bar = 10 μm; original magnification 1400×.)
XBB 809-10953

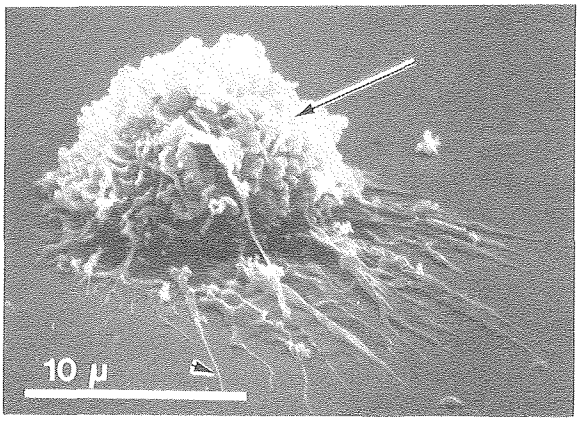

Figure 3. Smoker alveolar macrophage of the intermediate type exhibiting ruffles (arrow) and filopodia (arrowhead). (1-hour incubation; bar= 10 μm; original magnification 3400×.)
XBB 809-10952

creasing time in culture was observed for featureless and spread cells. Figure 4 illustrates the data obtained for the incidence of filopodia. For the 1- and 2-hour culture periods, slightly greater sizes and size variances were observed for smoker AM; however, after 25 hours in culture, nonsmoker AM populations possessed these characteristics. Projected area for both groups, however, was observed to decrease after 25 hours in culture (Fig. 5). Area frequency distributions appeared to be logarithmically normal in distribution (Fig. 6) as has been generally reported by other researchers. Statistical analyses indicated that, for projected area in general, the greatest variance was due to variations among the individuals lavaged rather than those due to smoking or nonsmoking.

Our work extends previous work by many researchers because quantitation of various parameters is achieved. Also, data obtained using this morphological scheme will be correlated with AM functional data such as glass adherence, viability, and phagocytosis to illuminate, it is hoped, the significance of the morphological alterations observed. Moreover, this study shows that rigorous statistical testing can be applied to features observed using the SEM to more accurately describe alterations in AM populations. This is of value not only in assessing the effects of cigarette smoking on AM morphology; efforts are continuing to characterize AM as sensitive indicators of exposure to inhaled environmental pollutants.

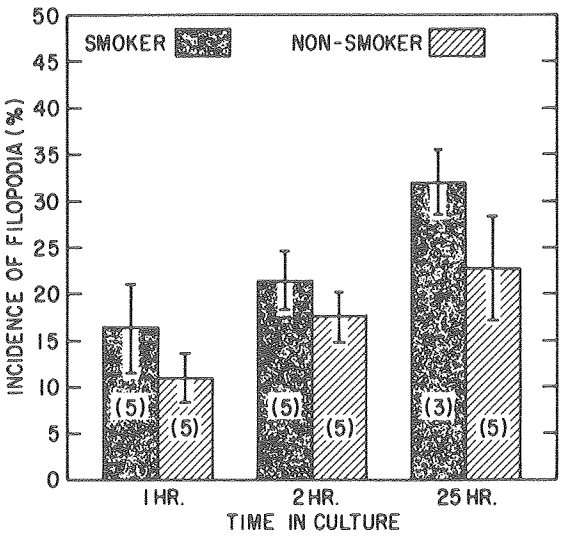

Figure 4. Smoker and nonsmoker incidence of filopodia for 1, 2 and 25 hours in culture. Numbers in parentheses indicate number of samples in statistical pool. Error bars indicate standard error of mean. (Reproduced courtesy of Scanning Electron Microscopy, Inc.) *XBL 809-11929*

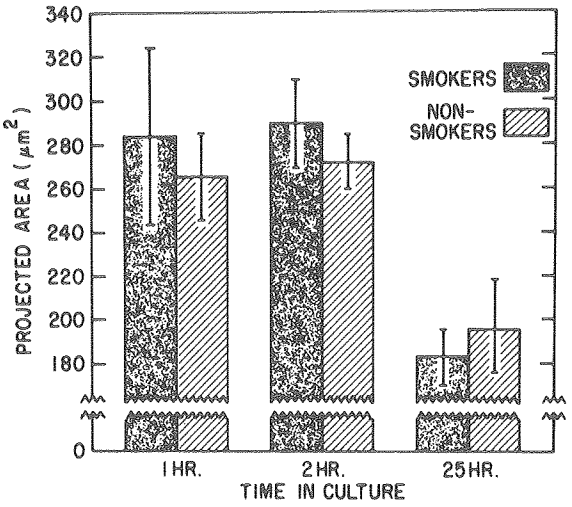

Figure 5. Smoker and nonsmoker alveolar macrophage mean projected areas for 1, 2, and 25 hours in culture. Error bars indicate SE. (Reproduced courtesy of Scanning Electron Microscopy, Inc.) *XBL 809-11928*

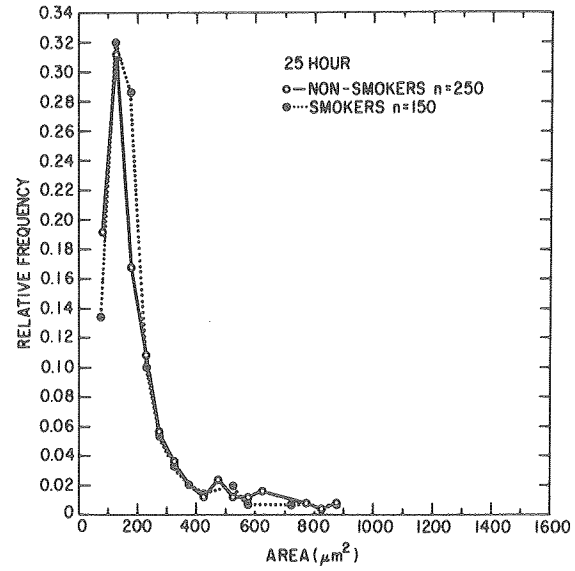

Figure 6. Distribution of projected areas for smoker and nonsmoker alveolar macropage at 25-hour culture time. *XBL 809-11927*

LOW-TEMPERATURE SCANNING ELECTRON MICROSCOPY OF PROGRESSIVE PULMONARY EDEMA

Gregory R. Hook, S. Jacob Bastacky, and Thomas L. Hayes

Pulmonary edema is a common disorder in medicine. The high incidence is due chiefly to the prevalence of left ventricular failure, causing pulmonary venous hypertension, which in turn results in hemodynamic pulmonary edema. A less common but clinically important form of pulmonary edema results from the inhalation of noxious gas, such as ozone. Rarer are the edemas resulting from exposure to high altitude or drug overdose. All forms of pulmonary edema result in fluid accumulation in the lung. In the advanced stages, fluid fills alveolar spaces, the sites of gas exchange, which results in loss of respiratory function.

Lung structure is particularly well suited to investigation by scanning electron microscopy (SEM) because the lung contains an enormous surface area arranged into millions of small (approximately 0.25 mm diameter) alveolar sacs. The SEM, operated in the secondary electron mode, can provide three-dimensional surface structure information at high magnification and large depth of field to focus on the convoluted topography of the lung. However, the vacuum environment of the standard SEM prohibits examination of wet lungs. Conventional SEM sample preparation requires chemical fixation, dehydration, and drying prior to observation, a procedure that causes loss of all water, sample shrinkage, positional rearrangement, and lipid extraction. This loss of water precludes direct investigation of fluid distribution in pulmonary edema.

An alternative sample preparation system developed in our laboratory permits observation of the sample in the frozen-hydrated state at low temperature. In this system the lungs are fixed by rapid freezing with liquid nitrogen, freeze-fractured at low temperature and high vacuum, gold-coated, and transferred *in vacuo* to the low-temperature SEM stage for observation. This preserves water in the frozen state and minimizes sample shrinkage, positional rearrangement, and lipid extraction, although ice crystal damage does occur. Preservation of fluids is essential in ultrastructural investigation of pulmonary edema because this disorder represents an imbalance in fluid homeostasis.

Currently our laboratory is using low-temperature SEM to study the fluid distribution in the alveolar septum during progressive hemodynamic pulmonary edema in collaboration with N. Staub of the Cardiovascular Research Institute at the University of California, San Francisco. Edema is induced by vascular saline loading of dogs while monitoring the physiological parameters of airway inflation pressure, pulmonary artery pressure, left ventricular end diastolic pressure, blood gas content, blood protein content, and blood hematocrit. The chest is opened and the lungs frozen at known inflation and vascular pressures. Specific areas of the lung are selected for low-temperature SEM observation. Qualitative information on alveolar shape and texture and quantitative information on alveolar septum thickness are obtained by applying stereological techniques to SEM stereomicrographs of frozen-hydrated, edematous dog lung. Low-temperature SEM minimizes the large error in biological dimensional analysis introduced by sample shrinkage during sample preparation. Freezing is also useful for rapid fixing of a dynamic pleomorphic structure such as the lung.

Shown in Fig. 1 are cross-fractured, gold-coated, frozen-hydrated alveoli from a normal dog lung. Open alveoli with straight, thin, smooth walls are present. A sample from a dog loaded with fluid to 10% body weight is shown in Fig. 2. The alveolar septum thickness has increased and nonuniform surface texture is evident. With 30% fluid loading, as in Fig. 3, the septum has further increased in thickness and appears irregular in form. These observations extend our understanding of fluid distribution to the level of alveolar septum. Previously, fluid accumulation was visualized only by light microscopy, which did not permit accurate assessment of the alveolar septum in progressive pulmonary edema. Initial low-temperature SEM data indicate a progressive thickening of alveolar septa with increasing pulmonary edema.

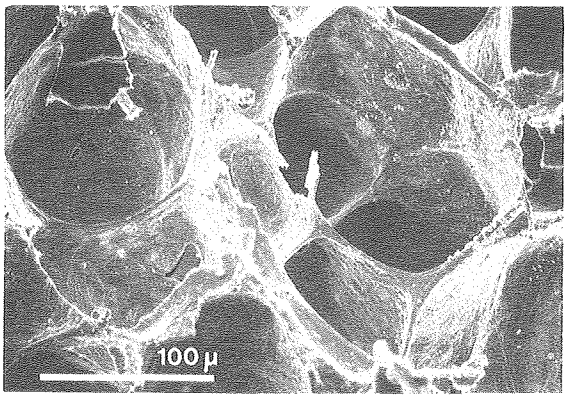

Figure 1. Low-temperature SEM micrograph of frozen-hydrated normal dog lung.Lung was frozen at an inflation pressure of 20 cm H_20. XBB 809-10955

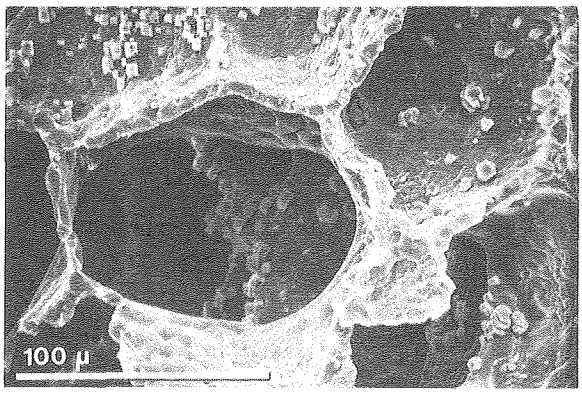

Figure 2. Low-temperature SEM micrograph of the frozen-hydrated lung of a dog fluid-loaded to 10% body weight. The lung was frozen at an inflation pressure of 20 cm H_20. XBB 809-10956

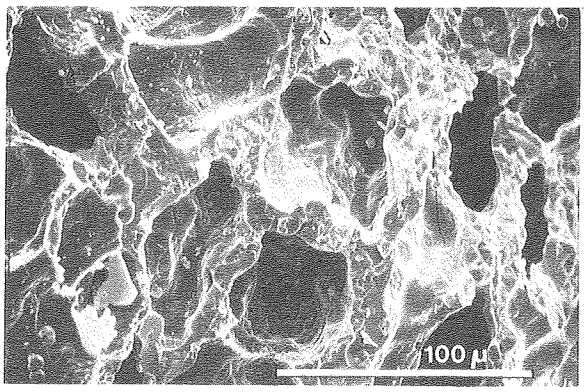

Figure 3. Low-temperature SEM micrograph of the frozen-hydrated lung of a dog fluid-loaded to 30% body weight. The lung was frozen at an inflation pressure of 20 cm H_20. XBB 809-10957

VOLCANIC ASH: ANALYSIS OF HUMAN LUNG SPECIMENS

Thomas L. Hayes, S. Jacob Bastacky, Gregory L. Finch, and Gregory R. Hook

As tissue samples become available from autopsy and surgical procedures on the large human population exposed to volcanic ash from Mount St. Helens, accurate methods for the measurement of lung exposure at the cellular level become increasingly important. Although tissue blocks from the lungs can be analyzed by sensitive bulk techniques such as neutron activation or atomic absorption, such analyses will not provide data on the extent of alteration in the individual cell environment that has resulted from the chronic inhalation of the volcanic ash particles. It has been shown that such data are often considerably different from the bulk measurements in cases where a high degree of heterogeneity exists among individual ash particles,[1] and that individual cell exposure to ash chemical elements can be several times as great as that predicted from the bulk analysis results.

Biological effects of particulate contaminants can be initiated at the cellular level and while certain of these effects are important only when large numbers of cells are affected, other biological consequences (e.g., mutagenesis, carcinogenesis) are probably initiated by changes in a single cell or a small group of cells.

Cellular contact with the pollutant particle can be due to absorption at the cell surface, phagocytosis of the particle to the interior of the cell, or

sequestering of the particle in interstitial tissue spaces. In general, each cell interacts with only a small number of particles. Thus, differences in chemical elemental composition among particles are not averaged out on the basis of large numbers of particles per cell, and individual particle chemistry becomes important in evaluating individual cell exposure. The multiparticle analytical procedures often used to determine pollutant particle chemistry yield elemental concentrations averaged over many particles and cannot predict completely the exposure potential at the individual cell level where small numbers of unique particles of varying composition are involved. If pronounced particle heterogeneity exists, the elemental and chemical concentrations to which single cells are exposed could be markedly different than the averaged elemental concentrations obtained from multiparticle methods. Recently published analyses,[2,3] and our own preliminary results suggest that a very high degree of particle heterogeneity does exist for samples of the ash from Mount St. Helens.

Microbeam techniques—the scanning electron microscope (SEM) with characteristic x-ray and electron microprobe—have been used for mineralogical identification of individual particles and have been considered more reliable for silica than methods using x-ray diffraction of bulk samples.[2] The microbeam techniques also can localize the analysis to very small volumes equivalent to single particles or even component phases of the particle. Applying these electron microbeam techniques to the problem of lung exposure allows individual cell environments to be evaluated with respect to major chemical element composition, particle number and location, and position of the cell along the unit airway.

In the past, small blocks of lung tissue were often cut or sectioned and the planar face examined by electron microscopy. Usually, only small segments of airways and obliquely sectioned structures could be seen, and exposed surfaces from varying levels of the airway were present in each planar block surface. A given airway segment could not be located precisely with respect to position along the bronchial tree. Microdissection preparative techniques have been developed that open individual airways of human lung specimens from the lobar bronchus to the termination point at the pleural surface.[4] The continuous luminal surface of the airway is thus exposed and available for analysis. Features can be precisely located along the branching airway. A single feature, such as an interalveolar system, can be examined with the SEM, then excised under the dissecting microscope, embedded, sectioned, and viewed in cross-section in the light microscope or transmission electron microscope. It is possible to analyze both the surface and interior of a single precisely located structure.

The frozen-hydrated and freeze-drying techniques applied in this program significantly reduce the ash particle and macrophage translocation that can occur if standard fixative procedures alone are employed. Also, in high-water-content surface layers the frozen-hydrated technique offers perhaps the only method with the capability to preserve structural integrity. Analysis of the mucous layer in the frozen-hydrated state is used to establish the position of ash particles within the layer and maintain the relative positions of particles and underlying cells.

An accurate measurement of lung cell dose is important to the assessment of the role of volcanic ash in any future public health problems in the large human population affected by the Mount St. Helens eruption. The measurement techniques developed in this laboratory, when applied to autopsy and surgical specimens from the exposed population, provide a data base on lung exposure at the cellular level. Such data would be an important addition to the parameters of dose-response relationship of this ash.

METHODS

1. Frozen-hydrated analyses

Lung specimens, obtained at surgery under procedures in operation over the past two years, are analyzed in the frozen-hydrated state. The specimen is inflated with air, clamped, resected, and frozen in liquid nitrogen, all within 15 minutes. The frozen specimen under liquid nitrogen (LN_2) is transferred to a dry nitrogen box, and controlled cryofracture with a cold knife is used to expose the luminal surface of the airways. The specimen, mounted on a pre-cooled holder, is transferred to the low-temperature preparation chamber (AMRay Biochamber) attached to the SEM.[5]

Frozen samples may be inserted into this chamber through an airlock using a holder that prevents condensation of atmospheric water vapor onto the sample. This airlock is also used to attach carbon or metal evaporating devices to the system, and permits them to be removed to recharge their evaporants at any time. During evaporation, the sample and the source can be viewed through windows and the sample can be tilted (0–90°) and rotated while

mounted on a shuttle attached to a copper block. The shuttle can be moved by an insulated push rod between stations for coating/insertions, fracturing, and SEM examination. In the fracturing position atop the LN_2 reservoir, a cold knife, whose height can be adjusted in 5 μm increments, moves horizontally across the sample surface. Its action can be viewed with a 10–100× stereo microscope.

The SEM cold stage, which constitutes the examination position, has X (+12, −25 mm), Y (± 6 mm) and Z (8 to 45 mm working distance) motion, rotation (±175°) and single-axis eucentric tilt (−5, +90°). It is cooled by a Joule-Thomson refrigerator that permits high-pressure (1500 psi) nitrogen gas to expand in a counter-current heat exchanger. The temperature of the shuttle can be measured and controlled (using ohmic heating) in the fracturing and examination positions. The temperature of the cooling block is also monitored, and an alarm sounds when any selected reading exceeds a preset limit. Sample temperatures need not rise above −170°C during the entire preparation of a freeze fracture sample and temperatures as low as −196°C can be attained in the SEM. The present system incorporates an ion-pumped LaB_6 electron gun that has demonstrated 5 nm resolution. Analytic x-ray procedures are identical to those described in the previous reports.[6–8]

2. Analysis of airway and alveolar surfaces exposed by preparative microdissection

Specimens of human lung from autopsy and/or surgical procedures under existing, approved Human Use protocols (see below) will be analyzed for volcanic ash content at the cellular level. Distribution and major element composition of particulates will be evaluated by scanning electron microscopy[9] and energy dispersive characteristic x-ray analysis of the bulk material. Peak to background spectra analysis previously reported in frozen-hydrated studies[6] will be used to reduce dependence of specimen geometry. Microdissection is performed to expose the airway surface of specimens which are fixed and critical-point dried according to previously reported methods.[4]

3. Source and characterization of calibration particles and reference samples of Mount St. Helens volcanic ash

The peak-to-background ratios for each of 12 elements is converted to weight percent by calibration to standard glass spheres and chips (National Bureau of Standards, glass composition K961, K308) and to frozen standard salt solutions.[7] Reference samples of Mount St. Helens volcanic ash were collected from five ground sites (Portland, Spokane, and three rural areas) and size fractionated samples will be used to establish particle classes and frequency on the basis of major element composition. These composition classes serve as reference compositions for the identification of any ash particles that may be located *in situ* in the lung specimens under study. Enhancement ratios (ratio of concentration in selected volcanic ash particles to average ash concentration from bulk analysis) were used to adjust bulk analysis values to a value more appropriate for single-particle identification.

4. Exposure of isolated preliminary macrophage cells

Bovine pulmonary macrophage cells were obtained by lavage and exposed to volcanic ash particles suspended in standard media.[10] Elemental analysis of elemental composition of ash particles associated with individual cells was carried out by SEM x-ray analysis utilizing the peak-to-background methods developed for single particle electron probe microanalysis.[8,11]

RESULTS

The analyses of individual volcanic ash particles and subunits of particles indicated that a high degree of chemical heterogeneity exists in the specimens of ash collected to date (Fig. 1). Also, in lavaged pulmonary macrophage cells exposed *in vitro* to volcanic ash, individual particles exhibited more than a tenfold range in elemental concentration (Fig. 2). Single-particle concentrations of twelve chemical elements in selected ash particles were compared to the bulk analysis obtained by x-ray fluorescence analysis. The large enhancement ratios indicated substantial element segregation into specific particles (Table 1).

DISCUSSION

In testing for the toxic effects of volcanic ash, individual cell exposures must be taken into account since mutagenic and carcinogenic possibilities may exist. It would seem wise to investigate, in the cases of individual cells, the full range of exposure made possible by the very nonuniform distribution of chemical elements among individual particles. Test exposures based upon average concentrations (obtained by multiparticle analysis techniques) would not reveal damage that might occur in those few

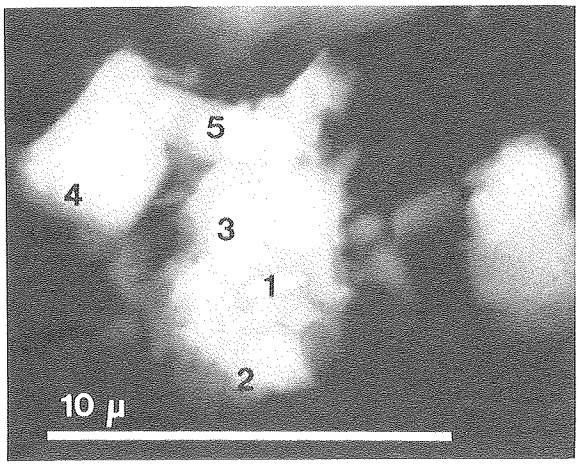

Figure 1. Heterogeneity among sub-units of volcanic ash particles. The elemental analysis for each indicated location is as follows:

Location	Elemental Analysis (%)			
	Si	S	Ca	Fe
1	38	8	13	2
2	19	1	3	3
3	18	4	7	8
4	29	1	3	1
5	15	18	12	1

XBB 800-12027

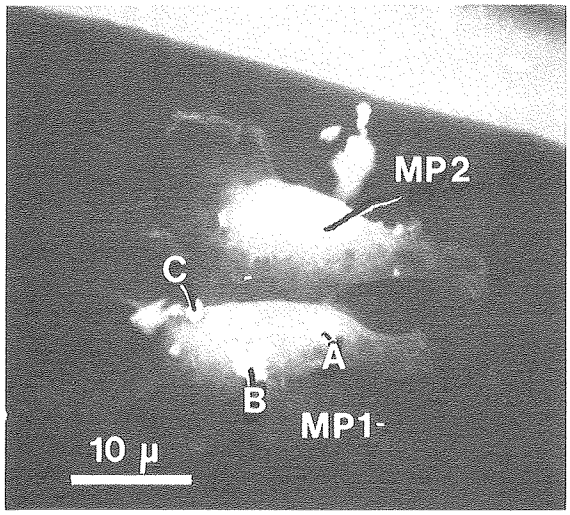

Figure 2. Heterogeneity among volcanic ash particles in individual pulmonary macrophage cells. Elemental analysis of each of four locations (three on one macrophage cell) is as follows:

Location	Elemental Analysis (%)			
	Si	S	Ti	Fe
MP1 - A	1	6	7	1
MP1 - B	37	1	1	3
MP1 - C	4	1	3	42
MP2 -	25	1	0	2

XBB 800-12028

Table 1. Enhancement ratios of 12 chemical elements in individual ash particles from Mount St. Helens.

Element	Ratio*	Element	Ratio*
Mg	9	Ca	4.6
Al	2.3	Ti	6
Si	2.3	V	4.5
P	1.2	Cr	25
S	370	Mn	10
K	3	Fe	120

**Ratio of concentration in selected particles to average concentration from bulk analysis.*

cells which come in contact with the concentrated form of the element found in the occasional particle.

Since the chemical components of volcanic ash are spatially distributed in the form of nonuniform particles and since the biological system with which they interact is also spatially compartmentalized into the basic biological functional unit of the cell, each cell exposure probability becomes a function of the specific particles ingested by or associated with the surface of that cell. Continued applications of techniques which evaluate the microenvironment of individual cells are a useful adjunct to the bulk multiparticle analyses and can help to identify any uniquely toxic particles that might not be recognized in studies that assume a more uniform cell exposure model.

The authors wish to acknowledge the contribution of J. Jaklevic and R. Giauque of Lawrence Berkeley Laboratory who performed the bulk analyses using x-ray fluorescence techniques.

REFERENCES

1. Hayes, T.L., Pawley, J.B., Fisher, G.L., and Goldman, M. 1980. A model for the exposure of individual lung cells to the foreign elements contained in fly ash. *Environ. Res.* 22:499–509.
2. Fruchter, J.S. et al. 1980. Mount St. Helens ash from the 18 May 1980 eruption: Chemical, physical, mineralogical, and biological properties. *Science* 209:1116–1125.
3. Hooper, P.R., Herrick, I.W., Laskowski, E.R., and Knowles, C.R. 1980. Composition of the Mount St. Helens ashfall in the Moscow-Pullman area on 18 May 1980. *Science* 209:1125–1126.

4. Bastacky, J., Sprague, L.M., and Hayes, T.L. 1980. Positional microstructure of the human lung: Microdissection and correlative microscopy techniques (LM, SEM, TEM). Thirty-eighth Ann. Proc. Electron Microscopy Soc. Amer., San Francisco, G.W. Bailey, ed.
5. Pawley, J.B., and Hayes, T.L. 1977. A freeze fracture preparation chamber attached to the SEM. Thirty-fifth Ann. Proc. Electron Microscopy Soc. Amer., Boston, G.W. Bailey, ed., pp. 588–589.
6. Echlin, P., Lai, C.E., Hayes, T.L., and Hook, G. 1980. Elemental analysis of frozen-hydrated differentiating phloem parenchyma in roots of *Lemna Minor L. Scanning Electron Microscopy/1980/II,* pp. 383–394. Chicago: SEM, Inc.
7. Lai, C.E., and Hayes, T.L. 1980. Calibration of SEM frozen-hydrated analyses using standard salt solutions and peak to background measurements. Thirty-eighth Ann. Proc. Electron Microscopy Soc. Amer., San Francisco, G.W. Bailey, ed., pp. 800–801.
8. Statham, P.J., and Pawley, J.B. 1978. A new method for particle x-ray microanalysis based on peak to background measurements. *SEM/1978/I,* pp. 469–478. Chicago: SEM, Inc.
9. Hayes, T.L., Lai, C.E., Fisher, G.L., and Prentice, B.A. 1980. Coordinated scanning electron microscopy and light microscopy for the evaluation of chemical element heterogeneity among individual fly ash particles. Thirty-eighth Ann. Proc. Electron Microscopy Soc. Amer., San Francisco, G.W. Bailey, ed., pp. 254–255.
10. Finch, G.L., Fisher, G.L. Hayes, T.L., and Golde, D.W. 1980. Morphological studies of cultured human pulmonary macrophages. *Scanning Electron Microscopy/1980/III,* pp. 315–326. Chicago: SEM, Inc.
11. Small, J.A., Heinrich, K.F.J., Newbury, D.E., and Mykelebust, R.L. 1979. Progress in the development of the peak to background method for the quantitative analysis of single particles with the electron probe. *SEM/1979/II,* pp. 807–816. Chicago: SEM, Inc.

PROGRESS ON THE HIGH-RESOLUTION MAP OF BACTERIORHODOPSIN OBTAINED BY ELECTRON CRYSTALLOGRAPHY

Steven B. Hayward

A method of treating errors in electron imaging of crystalline objects has been developed. This method is analogous to the treatment of errors used by x-ray crystallographers in solving protein structures by the multiple isomorphous replacement method. The method allows data from several images to be combined to give the structure with the least square error averaged over the unit cell. Application of the method to low-dose images of the purple membrane (bacteriorhodopsin) of *Halobacterium halobium* has produced a tentative map at 3.7 Å resolution.

Although low-dose electron microscopy of crystalline biological specimens has been shown to be a remarkably accurate method of structure determination at moderate (~ 7–9 Å) resolution, attempts to achieve resolution commensurate with the microscope capabilities have so far been unsuccessful. The chief reason has been that large, coherent images of crystals are impossible to obtain, because of distortions introduced by the projector lenses, lack of specimen flatness, and gradients in focus due to slight specimen tilt.

We set out to overcome these difficulties by looking for a way to combine data from small image areas in such a way as to minimize the errors in the resulting map. This problem is similar to that faced by protein crystallographers, whose data from isomorphous derivatives can be subject to significant errors. Blow and Crick solved this problem in 1959 by considering phase probability distributions for every reflection, based on the changes in intensity of those reflections occurring on binding heavy atoms at known locations.[1] The centroid of each probability distribution is calculated, and a Fourier synthesis is performed using the centroid phase and the structure factor amplitude weighted by the centroid amplitude (the so-called "figure of merit"). Reflections with well-determined phases have figures of merit close to one and contribute more to the synthesis than do those with ill-determined phases. Blow and Crick proved that the synthesis done in this way has the least square error when compared to the "true" synthesis.

We have applied the concepts of phase probability distributions and figures of merit to the analysis of low-dose images of crystalline specimens. In order to develop phase probability distributions, we have analyzed the statistics of the background noise in image Fourier transforms. The background prob-

ability distributions were found empirically to obey a simple analytical relationship. This analytical relationship could then be used to generate phase probability distributions for all reflections based simply on the ratio of the amplitude at the reflection to the average background around the reflection in the Fourier transform. Image areas were combined simply by multiplying their respective phase probability distributions.

This procedure was applied to 12 small (1000 unit-cell) image areas of purple membrane. The resulting phase probability distributions were used to calculate centroid phases and figures of merit. The average figure of merit is plotted as a function of resolution to 3.7 Å in Fig. 1. The fact that the figures of merit fall off slowly with resolution means that, even at high resolution, the phase probability distributions are relatively peaked.

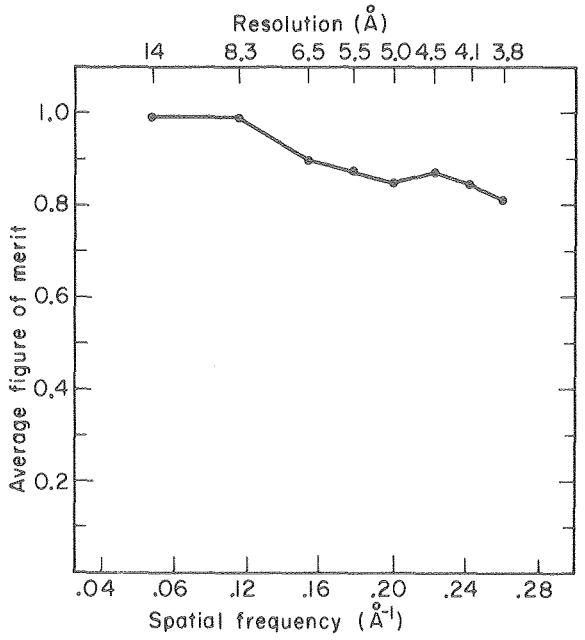

Figure 1. Plot of the average figure of merit versus resolution. *XBL 8010-3716*

A Fourier synthesis was performed using these figures of merit to weight the amplitudes determined by electron diffraction. The phases used were the centroid phases. The resulting 3.7 Å map is shown in Fig. 2. This map must be considered tentative, since work is currently underway to use more information to develop the phase probability distributions. Nonetheless, this method of treatment of errors has been shown to extract previously inaccessible data from electron microscope images, and will probably find widespread use in the future.

REFERENCE

1. Blow, D.M. and Crick, F.H.C. 1959. *Acta Cryst.* 12:794–802.

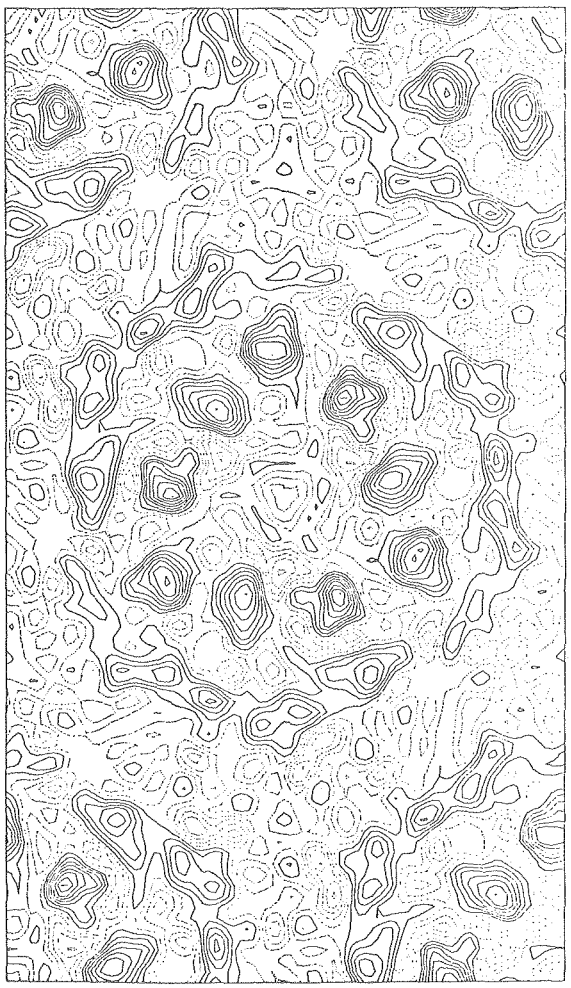

Figure 2. Projected potential of H. halobium purple membrane to 3.7 A° resolution. All reflections are included, with an average figure of merit of 0.89. *XBL 8010-3717*

DNA and Genetic Studies

CIRCULAR INTENSITY DIFFERENTIAL SCATTERING OF LIGHT BY HELICAL STRUCTURES—THEORY

Carlos Bustamante,* Marcos F. Maestre and Ignacio Tinoco, Jr.*

We have obtained general expressions for the fields and intensities of scattered electromagnetic radiation by helical structures whose optical properties are described by a uniaxial polarizability along the tangent to the helix. We have also derived analytical expressions for the circular intensity differential of scattering (CIDS) as a function of the helix parameters and the wavelength of light. Finally, we have shown that a sufficient condition for the existence of differential scattering for right and left circularly polarized light is the existence of an asymmetric polarizability. The choice of a uniaxial polarizability is found to give rise to *form* CIDS. (For a discussion of the differences between *form* CIDS and intrinsic circular dichroism, see Ref. 1.)

For incident plane-polarized light, the scattered fields were found to be generally elliptically polarized. The Stokes parameters describing the state of polarization of the scattered radiation were derived. These results, it is expected, will make it possible both to characterize chiral regions in macromolecular structures and to describe the light-scattering properties of cholesteric and twisted nematic liquid crystals. The theory can also describe the radiation modes of helical antennas. Analysis and numerical calculations were made of the total scattering and differential scattering of circularly polarized light by helices as models of chiral structures. The differential scattering patterns are much more sensitive than the total scattering to helical parameters. For large helices the angular dependence of these patterns show lobes that alternate in sign. The number of lobes and the positions of the zeros directly measure the ratios of radius and pitch to wavelength. The signs depend on the sense of the helix. The results are compared with measured circular intensity differential scattering of membranes from the bacterium *Spirillum serpens*. Good qualitative agreement is obtained (see Fig. 1). The development of scattering theory of circular dichroism (CD) has opened the way for interpretation of differential scattering patterns of single oriented scatterers, such as intact nucleus of mammalian cells, individual sperm heads, condensed chromosomes *in situ*, etc., in terms of their large-order organization.

To study individual samples of such microscopic organization, a technique has to be developed to allow the measurement of the CD scattering of such objects in the region of their absorbance bands. A CD microscope has therefore been developed in our laboratory (Fig. 2) which allows the measurement of a single cell or nucleus in wavelength regions ranging from 350 nm down to 200 nm. This is the wavelength region in which both nucleic acids and proteins have their main rotational bands. Figure 3 shows the measurement of intact red cells and of intact lymphocyte nuclei in the stage of the CD microscope. This signal includes both the forward scattering component and the CD intrinsic spectrum. The data, preliminary in nature, show that CD spectrum of nucleohistones can be obtained *in situ* down to 200 nm (Fig. 3). Recent measurements have shown that the CD of a single lymphocyte gives enough signal to allow the measurement of the CD spectrum of its nucleic acids *in situ*. Variations of the instrument will allow the measurement of the CD back scattering and CD side scattering as function of wavelength in the 350 to 200 nm wavelength region.

*Department of Chemistry, University of California at Berkeley, and Chemical Biodynamics Division

REFERENCE

1. Tinoco, I., Bustamante, C., and Maestre, M.F. 1980. The optical activity of nucleic acids and their aggregates. *Ann. Rev. Biophys. Bioeng.* 9:107–141.

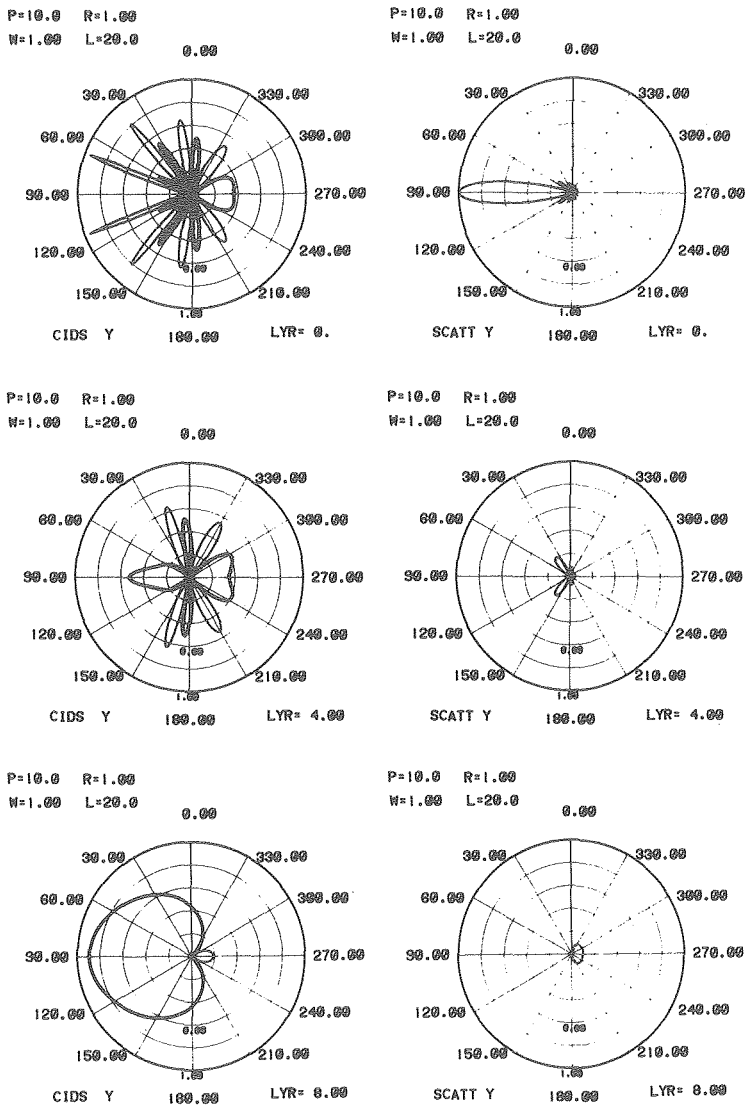

Figure 1. Computed CD scattering patterns (left column) versus total scattering (right column) for a helix of period 10 × wavelength and diameter of 1 × wavelength. These are polar plots of intensity versus scattering angle at various layer lines in the scattering space. Layer lines = 0, 4, and 8. *XBL 806-10526*

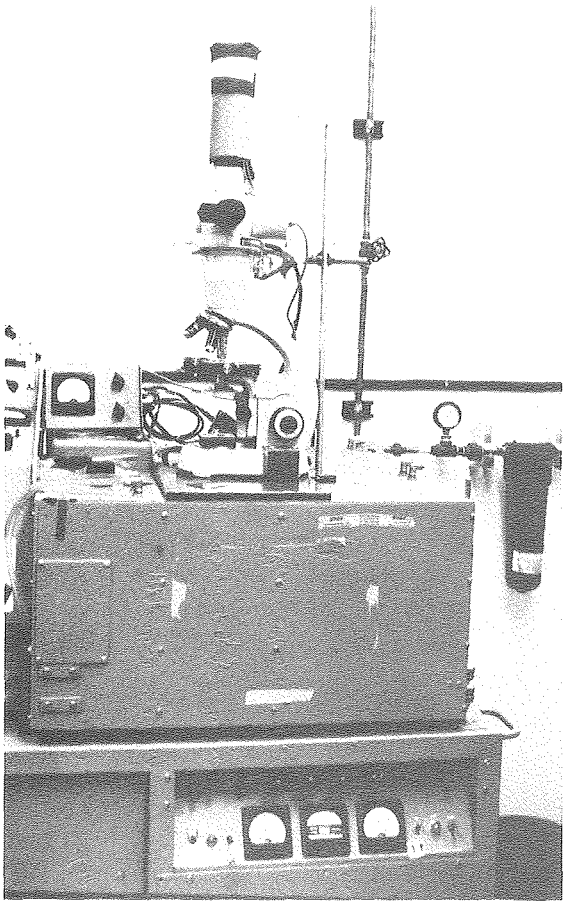

Figure 2. The CD microscope as presently mounted on a Cary 60 CD dichrograph. Recording and data analysis is done by the standard instrument. *CBB 808-9131*

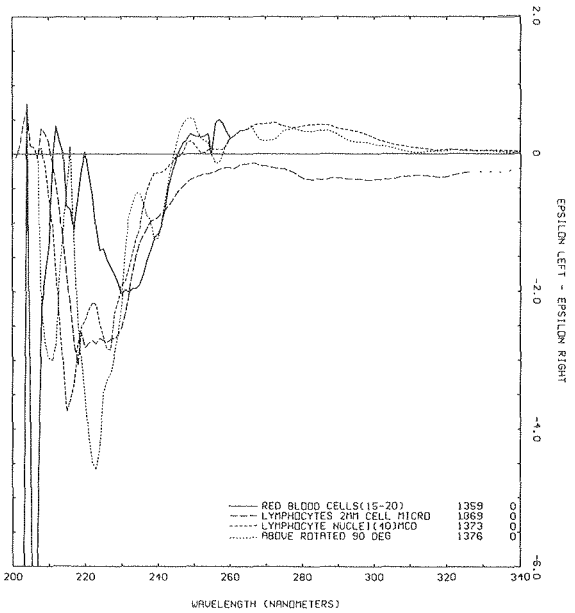

Figure 3. Preliminary data obtained from intact red cells (human) and lymphocyte nuclei in the CD microscope. *XBL 808-3653*

INTERACTION OF GENE 32 PROTEIN AND GENE 32*III WITH SYNTHETIC POLYNUCLEOTIDES

Marcos F. Maestre and Kathleen B. Hall

Phage T4 gene 32 protein (gp32) was allowed to interact with poly(dI)·poly(dC), poly(I)·poly(C), and the corresponding single strands. The resulting complexes were examined by circular dichroism (CD) spectropolarimetry as a function of temperature. It was found that the melting temperature of the polynucleotides was lowered by approximately 20° C for the ribopolymer and 25° C for the deoxy analog. It was seen from the spectra that while the protein destroyed the interstrand interactions, it maintained the intrastrand ones. The spectra of these melted polymers imply that gp32 allows the nucleic acid to retain much the same structure in the complex as in the original conformation, a result demanding a certain amount of flexibility on the part of the protein. (See Fig. 1a and 1b.)

These experiments were repeated using gp32*III, obtained by tryptic digestion of gp32. This non-cooperative protein disrupted the polynucleotide structure so that its CD was reduced to less than that of the melted strands. This result is further evidence that gp32, which binds cooperatively to the DNA, acts to stabilize the structure of the strands. Such a stabilizing role may be important for the T4 replication complex, of which gp32 is a part. (See Fig. 1c.)

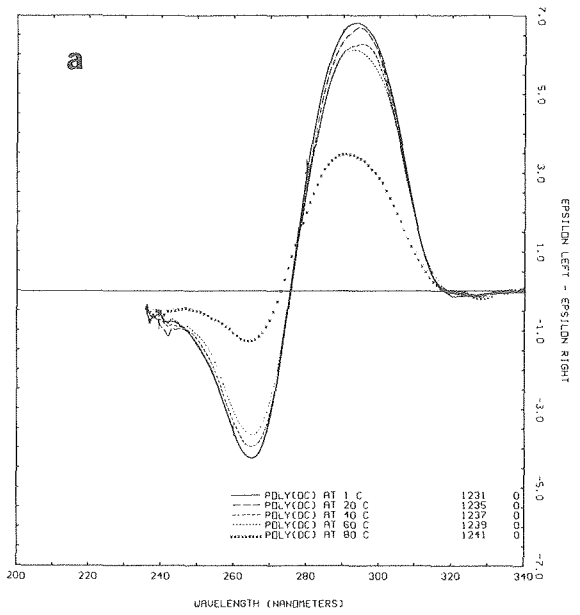

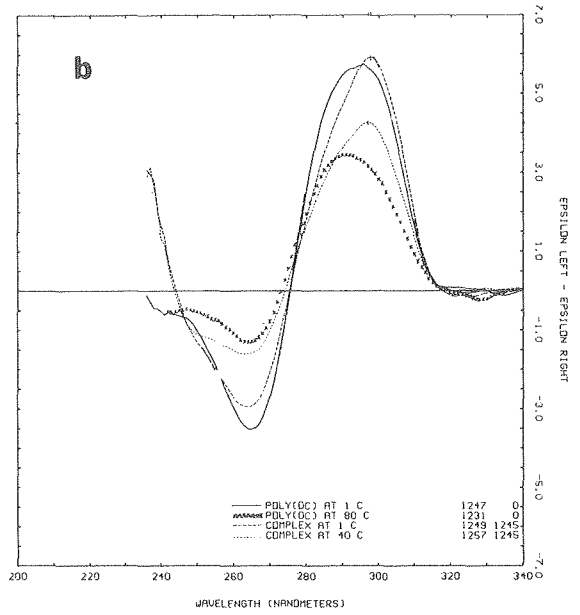

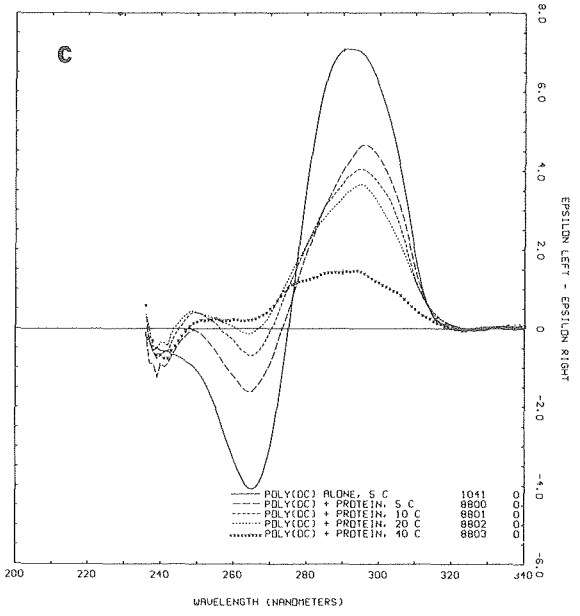

*Figure 1. (a) Circular dichroism (CD) spectra of poly(dC) as a function of temperature. (b) CD spectra of poly(dC) and gp32 complex as a function of temperature as compared to the poly(dC) melting behavior. The gp32 complex shows the CD spectrum at 40°C, which is similar to the CD spectrum of the polymer alone at 80°C. (c) The CD spectra of the poly(dC)-gp32*III complex shows a progressive destabilization of the stacking interactions as the temperature is increased so that at 40°C the CD magnitudes are more reduced than that of the poly(dC)-gp32 complex.*

(a) XBL 809-11603
(b) XBL 809-11605
(c) XBL 809-11604

DNA REPAIR MECHANISM

Junko Hosoda

DNA replication, some steps of recombination, and the repair process are done by multiprotein complexes. The interactions among the component proteins are the most important factor determining the overall activities of the complex. Gene 32 protein (gp32) of bacteriophage T4 binds tightly, cooperatively, and selectively to single-stranded DNAs. DNA coated with gp32 serves as the foundation of the assembly of the replication-recombination-repair complexes.

It has been suggested that gp32 has two protruding regions—domain A at the carboxyl terminus and domain B at the amino terminus—which are involved in gp32 interactions with itself and with other replication proteins.[1-3] These interactions may control the overall activities of the complexes.

We prepared three types of proteins and examined their interactions and activities; 32*I protein is produced by the proteolytic cleavage of the A domain (51 amino acid residues), 32*II protein by cleavage of approximately half of the B domain (9 residues) and 32*III protein by cleavage of *both* the entire A and B domains (21 residues).

We show here one of the gp32 interactions altered by the A domain cleavage and another by the B domain cleavage.

The A-domain cleavage reduces the affinity of gp32 for the T4 DNA polymerase. It has been shown that gp32 stimulates T4 DNA polymerase. Moreover, a direct association of the gp32 with the polymerase has been shown by cosedimentation of the two proteins through sucrose gradients.[4]

To test whether the removal of the A domain from gp32 alters its intrinsic affinity for the polymerase, a mixture of the DNA polymerase and either intact gene-32 protein or 32*I protein was sedimented through sucrose gradients.

The T4 DNA polymerase alone sediments as a sharp peak that moves more slowly than an alkaline phosphatase marker (Fig. 1a), while both the intact gp32 (Fig. 1c) and the gp32*I (Fig. 1b) self-associate and therefore sediment heterogenously across a broad region of the gradient. The sedimentation rate of the DNA polymerase is increased dramatically in the presence of gp32, and it now cosediments with the bulk of the gp32 oligomeric complex (Fig. 1c). However, when cosedimented with 32*I protein, the DNA polymerase sediments at a rate indistinguishable from the rate measured in the absence of gp32 (Fig. 1b). Thus the removal of the A domain from 32 protein has reduced its affinity for the T4 polymerase to less than 10^4 M^{-1}, the limit of detection by this assay.

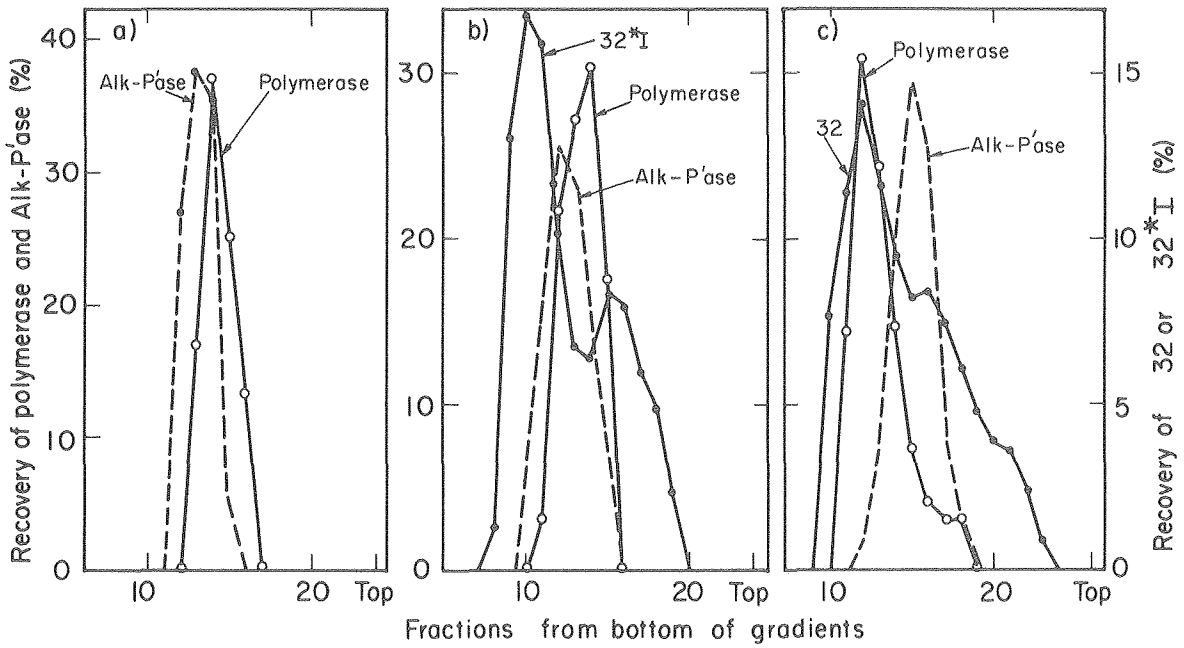

*Figure 1. Sucrose gradient sedimentation analysis of T4 DNA (a) by itself, (b) mixed with 32*I (minus A domain), no binding, and (c) bound to gp32.* XBL 785-3101

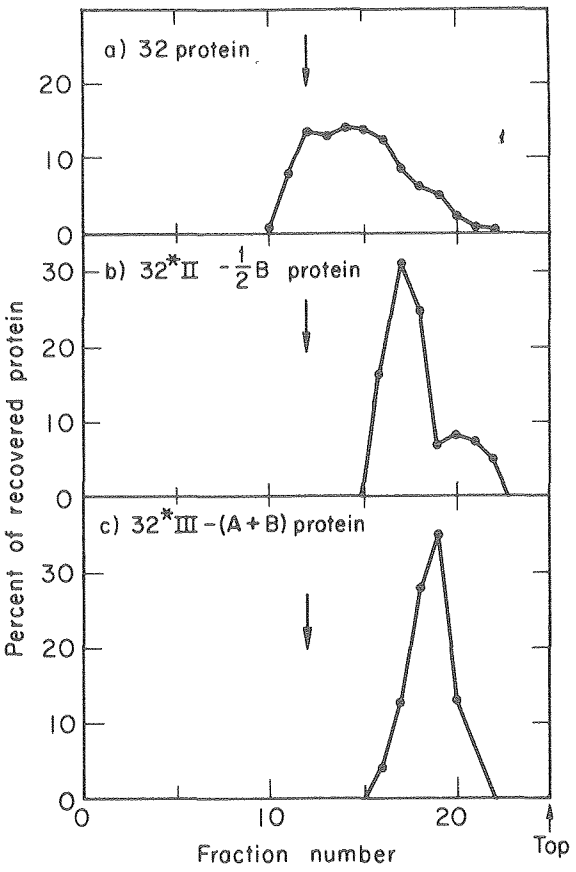

*Figure 2. Self-association analysis of sucrose gradient sedimentation; (a) gene 32 protein (gp 32); (b) gp32*II minus half of B domain; (c) gp32*III minus A and B domains. The arrow in the gradient indicates position of alkaline phosphatase marker.* XBL 809-3668

The B domain cleavage alters the gp32 interaction with itself. Figure 2 compares the sedimentation of 32, 32*II and 32*III proteins in sucrose gradients. In contrast to intact gp32 protein (Figs. 1c and 2a) and the 32*I protein (Fig. 1b), both gp32*II that has lost the distal half of the B domain (Fig. 2b) and gp32*III that has lost both the A and B domains (Fig. 2c) no longer self-associate and sediment slowly through the sucrose gradients.

We have substituted 32*I protein for the intact protein in a variety of *in vitro* DNA replication reactions to probe the roles of the A domain in DNA replication.[5] The results, complemented by previous physical studies of the protein, suggest that an intact A domain is essential for the control of the helix-destabilization potency of gp32 in the complexes. Roles of the B domain in replication-recombination-repair actions are under investigation.

REFERENCES

1. Moise, H. and Hosoda, J. 1976. *Nature* 259:455–458.
2. Hosoda, J. and Moise, H. 1978. *J. Biol. Chem.* 253:7547–7555.
3. Williams, K.R. and Konigsberg, W.H. 1978. *J. Biol. Chem.* 253:2463–2470.
4. Huberman, J.A., Kornberg, A., and Alberts, B.M. 1971. *J. Mol. Biol.* 62:39–52.
5. Burke, R.L., Alberts, B., and Hosoda, J. In press. *J. Biol. Chem.*

GENETIC STUDY ON YEAST

Robert K. Mortimer

Our research during the past year has moved ahead on several fronts. We have completed a major compilation of all the genetic mapping data for the yeast *Saccharomyces cerevisiae*. The map describes the location of over 300 genes on 17 chromosomes (Fig. 1). A report on this work will appear in *Microbiological Reviews* in December 1980.

We have introduced recombinant DNA procedures into our experiments and have successfully cloned *RAD52*, one of the genes involved in recom-

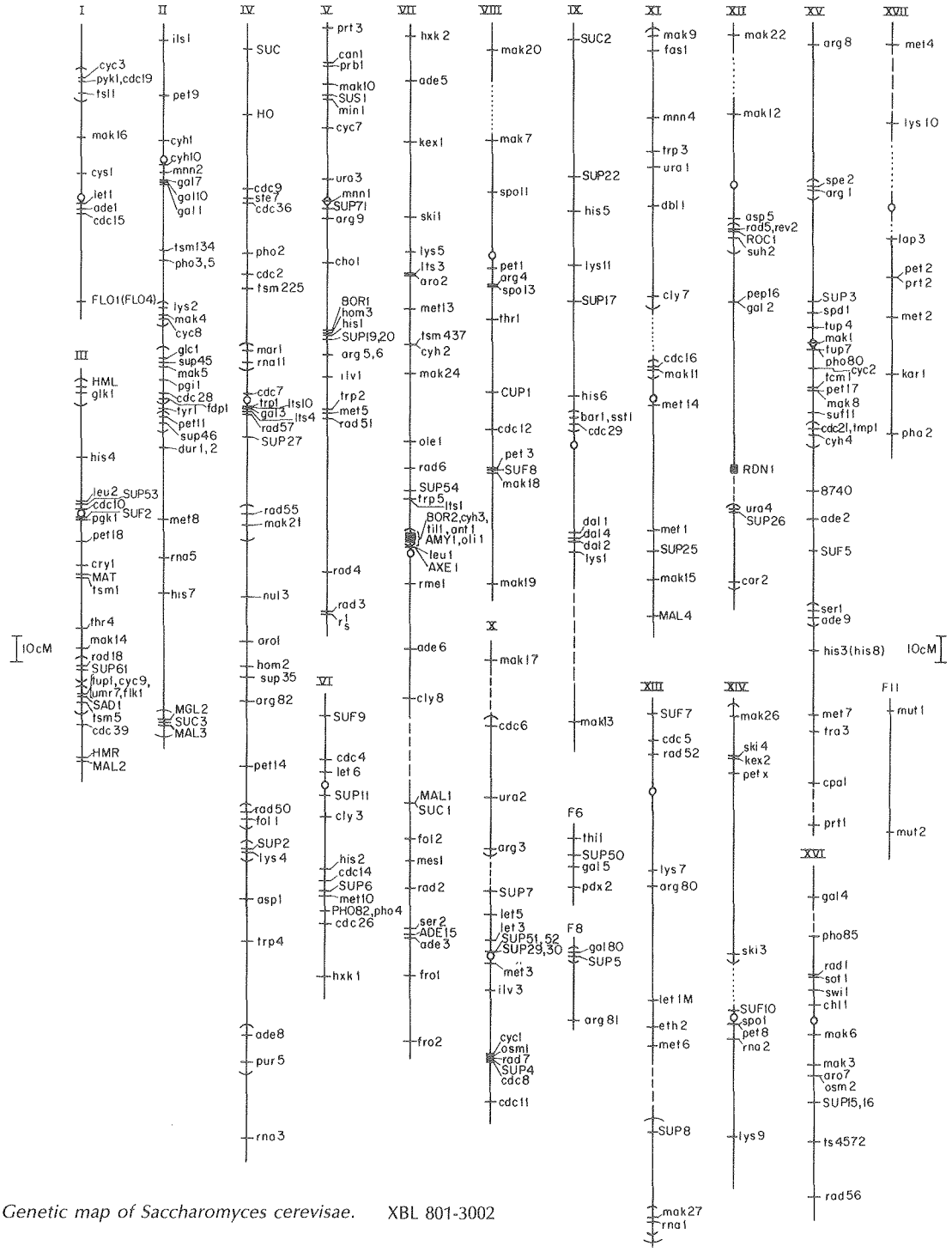

Figure 1. Genetic map of Saccharomyces cerevisiae. XBL 801-3002

bination and repair of radiation damage. We plan to use this clone to determine the gene product. We have also found that diploid cells homozygous for *RAD52* have exceptionally high frequencies of mitotic loss of chromosomes. This loss is stimulated by ionizing radiation.

We consider this effect to be a very significant finding and are now following it up. The effect has also been seen with certain other *RAD* mutants.

MUTAGENESIS IN MAMMALIAN CELLS

H. John Burki

The induction of mutation by environmental agents is important because it is now known that most mutagens are carcinogens. Much work on yeast systems has demonstrated that the process of mutagenesis in eucaryotic cells is a complex process involving damage and repair of DNA. The next step is to study these mutagenic processes in simple mammalian cell systems such as Chinese hamster cells in culture. Simple mammalian (including human) cell cultures provide an intermediate zone of research between work on microbial systems and studies of whole animals and man himself. Our approach to elucidating the mechanisms of mutagenesis in mammalian cells is to experiment with highly synchronized cell populations. These synchronous populations should enable us to examine the *biochemistry* of mutagenesis under the advantage of "biological resonance" since all cells in the population are performing similar functions at the same time during the experiment. This is not the case when experiments are performed on asynchronous mammalian cell culture.

SOLAR AND UV INDUCED DAMAGE

Mutagenesis in synchronous cells

There is a very large difference in the induction of mutants resistant to diphtheria toxin by ultraviolet (UV) light during the cell cycle. There appears to be a sensitive period in the middle of the G1 stage of the cell cycle.[1] This result strongly suggests that some mechanism or characteristic of the G1 stage is important for mutagenesis in mammalian cells. The sensitivity could be due either to some particular biochemistry occurring at that time in the cell cycle or to the absence of error-free repair at this stage. We cannot yet rule out the importance of recombination processes or of possible G1-dependent error-prone repair processes.

There appears to be a different response for the induction of resistance to ouabain (OUA) or 6-thioguanine (6TG) during the cell cycle. Ouabain resistance is more easily induced during DNA synthesis, while 6TG resistance is induced throughout the cycle with small peaks in G1 and S.[1] These results, demonstrating that the life cycle patterns for induced mutation vary with the endpoint used, suggest that mutation induction is a function of the specific endpoint chosen. It also suggests that different mutagenic mechanisms induce these three types of mutations.

It is clear that the results for mutation induction during the cell cycle are also mutagen-specific because the results after exposure to ethyl nitrosourea (ENU) in the same system are completely different. Although the mutation induction curves in *asynchronous* cells are the same for ENU and UV, in synchronous populations the ENU results are *not* a function of the time in the cell cycle.[2] This flat response in the cell cycle (Fig. 1) is most likely related to the absence of the repair of damage by alkylating agents of the 06 alkyl guanine type[3] in Chinese hamster ovary (CHO) cells. On the other side of the coin it suggests that repair may very well be important in the characteristic age response found for mutation in the cell cycle after UV.

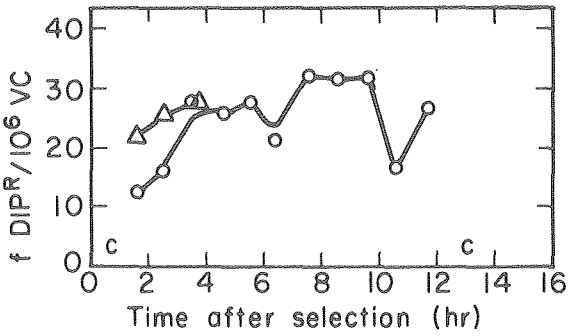

Figure 1. Induced resistance to diphtheria toxin (DIP^R) in CHO Clone 9 (wild type) during the cell cycle after treatment with ethylnitrosourea (ENU), 200 μgm/ml for 30 minutes. 7-day expression, "○"; 9-day expression, "Δ"; controls "c." *XBL 8010-3721*

Isolation and characterization of mutants ultra-sensitive to UV light

We have been able to develop a replica plating technique in our laboratory for the isolation of CHO clones sensitive to various environmental mutagens. We have used this technique to isolate two clones of CHO, clones 27-1 and 43-3B, which are vastly more sensitive to UV-induced reproductive death than the wild-type clones we have been using, i.e., clones KK, 9 and 10. The fluence response curves of the KK and 43-3B clones for UV-induced cell killing are shown in Fig. 2(a). Clone 27-1 shows similar results to those seen in Fig. 2(a) for clone 43-3B. Except for their ultrasensitivity to UV, both appear to be quite similar to the wild type in growth rate and plating efficiency; they also appear to be synchronizable, like the wild-type clone. Future work will determine the response in the cell cycle of these UV-sensitive mutants.

But the most interesting result thus far with these mutants is that they are also hypermutable by UV light. The fluence response curves for the induction of diphtheria toxin resistance in wild-type clone KK and in clone 43-3B are compared in Fig. 2(b). The enormous difference in results shows that an efficient, error-free repair process exists for the repair of UV-induced damage in the DNA of CHO cells. When this DNA repair system is inactivated, mutations are formed with a much higher frequency in surviving cells after UV exposure. It will be important in future studies to determine whether the increased mutations are due to lack of repair or to the use of an error-prone pathway of mutagenesis after removal of the error-free pathway, as in the case of diploid yeast.

Future studies with synchronous cells will enable us to tell whether this hypermutability is cell-cycle-dependent or related to cell cycle biochemistry, or whether it is related to repair processes independent of the cell cycle.

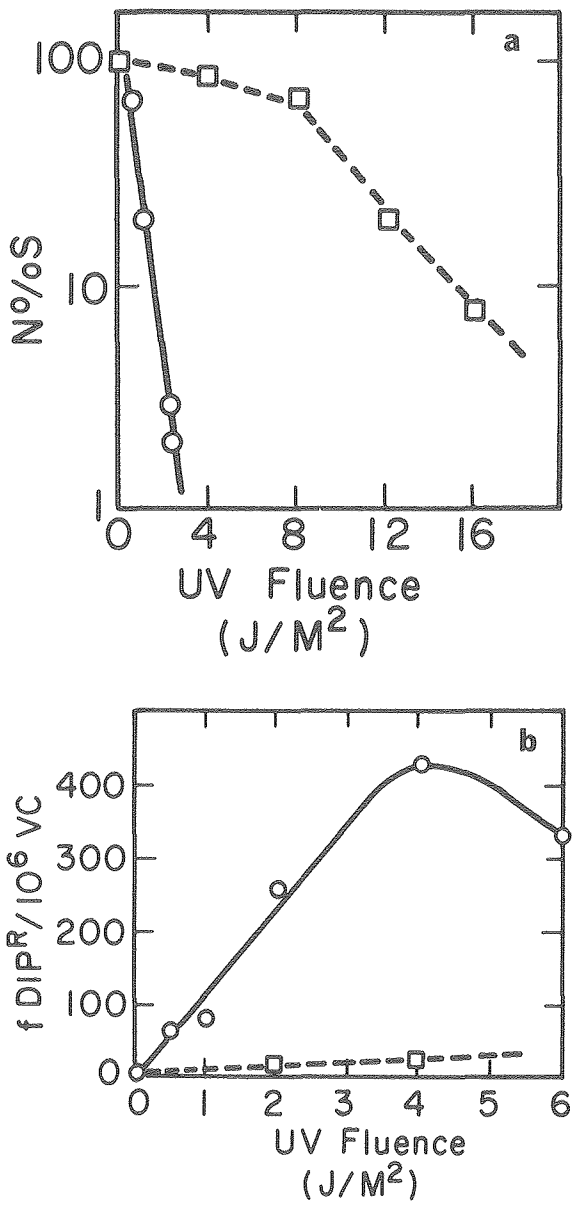

Figure 2. (a) Survival curves for clone KK (□) and clone 43-3B (○) after acute exposure to germicidal UV light. Fluence rate was 0.5 J/M²/sec. (b) Induced resistance to diphtheria toxin (DIP^R) as a function of UV fluence for wild-type clone KK (□), and for clone 43-3B (○). (a) XBL 8010-3722 (b) XBL 8010-3723

TRITIUM AND BROMODEOXYURIDINE (BUdR) INDUCED DAMAGE

BUdR studies in synchronous cells

In synchronous cells the order of DNA replication is very specific. There are early, middle, and late replicating segments. There are at most times in the DNA synthesis period many replicating regions and replication clusters. Bromodeoxyuridine is incorporated into replicating DNA instead of thymidine and can be used to put the BUdR into certain replicating regions in synchronous cells. When BUdR is incorporated into certain regions, it causes mutations in those regions of the DNA. We have shown that BUdR induces mutations to 6TG and OUA resistance in the DNA replication period at distinct times during the replication of early-replicating DNA.[4] It is not clear why the mutations are induced, but there are two competing ideas at this

time: 1) the BUdR is mutagenic because it enters the DNA and is repaired by error-making repair enzymes; or 2) the BUdR induces the DNA polymerase to make errors during the normal DNA replication process. Both hypotheses recognize that the damage to the DNA is extremely local—that is, where the BUdR enters the DNA. Therefore BUdR continues to be useful for studies of the order of replication of genes in CHO cells. We have recently completed BUdR mutagenesis studies with a third marker, resistance to diphtheria toxin. We have found that the gene or genes associated with resistance to this toxin are replicated in time between the genes for 6TG and OUA resistance. The order of replication is 6TG at 5 hours, diphtheria toxin resistance at 5.5 hours, and resistance to ouabain at 6.0 hours. These are all times in the early replicating DNA part of the DNA synthesis period. We have repeated these experiments with three wild-type clones of CHO cells, i.e. clone KK, clone 9 and clone 10. The results are all the same, suggesting that the order of replication of the DNA is similar in all clones of CHO cells.

Ionizing radiation induced mutation in the cell cycle

When cultured CHO cells are exposed to acute doses of 50-kV x rays at different times during the cell division cycle, there is a characteristic cell cycle response for radiation-induced reproductive death and induced resistance to 6TG. For cell killing the sensitive times in the cycle are the G1, G2, and M stages and the early S period, as others have reported. For mutation induction the sensitive period is the G1 period with a maximum sensitivity near the boundary between the G1 and the S period. Cells appear to be quite resistant to the induction of mutations for 6TG resistance at other times in the life cycle.[5] This result for mutation induction could be due to a variety of causes, such as shortness of time for repair before the replication of the region of DNA associated with 6TG resistance, recombination mechanisms in the G1 period, or a possible error-prone repair process. It is not yet clear which is correct. The result for mutation induction also raises questions about the mutability of cells *in vivo* in the GO stage. Are cells in this stage like cells in the G1 stage, i.e., hypermutable? This result will affect estimates of the impact of environmental mutagens drawn from studies of log growth of asynchronous mammalian cell systems.

These results will also affect the design of future experiments with tritium and tritiated precursors since the effects of tritium are due in large part to the beta particle produced in tritium decay. This beta particle causes radiation effects similar to the effects of the soft x rays used in our control experiments discussed above.

Mutants sensitive to ionizing radiation

We have found that our UV-ultrasensitive mutants are hypermutable by ionizing radiation. The mutant CHO cells appear in preliminary experiments to have lost some of the "shoulder" characteristic of the survival curve of wild type CHO cells. These mutants will be very useful in the future for analysis of the mechanisms of mammalian cell killing and mutagenesis induced by ionizing radiation.

REFERENCES

1. Burki, H.J., Lam, C.K. and Wood, R.D. *Mut. Res.* 69:347–356 (1980).
2. Goth-Goldstein, R. and Burki, H.J. *Mut Res.* 69:127–137 (1980).
3. Goth-Goldstein, R. *Can. Res.* 40:2623–2624 (1980).
4. Burki, H.J. and Aebersold, P.M. *Genetics* 90:311–321 (1978).
5. Burki, H.J. *Rad Res.* 81:76–84 (1980).

Lipoprotein Studies

LIPOPROTEIN METHODOLOGY AND ITS BIOLOGICAL APPLICATIONS

Frank T. Lindgren

Our methodological efforts are focused on improving the analytic ultracentrifuge as a fundamental standard for lipoprotein characterization, measurement, and calibration of other simplified methods. Further, we have compared several simplified methods for lipoprotein quantification that may be used in clinical laboratories. Our simplified automated agarose electrophoresis system has been proven in two pilot studies, now completed. Such a system will be directly applied to a diet/HDL study now under way and to a genetic/environmental study in Portugal. The fundamental physical-chemical studies are currently aimed at understanding the nature and extent of lipoprotein degradation in both the preparative and analytical ultracentrifuge. Our computerized schlieren film reading should help to quantify, in particular, the LDL and HDL subfractions. We may thus define the nature of atherogenicity within the LDL class as well as antiatherogenic features of the HDL spectrum. Such information may ultimately provide understanding of atherosclerosis on the macromolecular level.

COMPUTERIZED ANALYSIS

During the past year we have made the computerized film-reading procedure operational for ultracentrifugal analysis of both low and high density lipoproteins. Since we do not have a large-capacity computer, we still have to send the edited input from our large analytic ultracentrifuge program to the LBL CDC-7600 computer. We currently send this input by punched paper tape via a telephone line. A more efficient, higher speed data transmission process, however, is currently being worked on. We are also beginning to apply our computerized system to subfraction analysis of both high density lipoprotein (HDL) and low density lipoprotein (LDL). This would be an improvement for HDL work and an innovation for LDL because of the greatly increased accuracy of the digitized schlieren patterns. Instead of a fixed, limited number of points defining each schlieren curve, a flexible and indefinite number are obtained automatically without human effort and tedious manual measurement. These (x, y) data points are automatically recorded and processed by our small computer, yielding final input data to the big computer without transcription error.

We have expanded the use of our computer densitometer–sonic digitizer system to the point of saturation. It is used on the schlieren programs, agarose electrophoresis, the newer LDL and HDL gradient gel electrophoresis, polyacrylamide gel electrophoresis, and electron microscope particle sizing. Much time has also been spent in systems development of these major applications. However, increased efficiency and smoother functioning will require an improved computer system. We need greater functional memory as well as a multiplex capability to accommodate at least three simultaneous on-line users. Work now is delayed, with unfortunate results in data acquisition and processing. For example, gradient gel analysis optimally must be processed after staining on a demanding time-related basis, but such time is not always available because of other urgent demands on the computer.

COMPARISON OF LIPOPROTEIN ANALYSIS PROCEDURES

In collaboration with R. Krauss, several simplified lipoprotein procedures were compared using analytic ultracentrifugation as a standard. Such a comparison of techniques will help to decide how they may eventually be used or adapted to practical clinical tests for early evaluation of cardiovascular disease risk and for observing the progress of treatments that attempt to reduce such risk. These included the Lipid Research Clinics procedure, the Freiderwald heparin-$MnCl_2$ technique, the commercial Helena Laboratories electrophoresis procedure, and our own micro-agarose automated electrophoresis. Except for the Helena method, all others have roughly comparable quantitative results, with various advantages and limitations found for each. A study with H. Eder successfully calibrated a graded dextran sulfate precipitation technique that yields both the HDL_2 and HDL_3 subfractions.

OTHER STUDIES

Work continues on resolving the question of whether centrifugation may lead to lipoprotein distortion. This issue, which arose from earlier studies,

is of great importance because most current work in the field is based on centrifugal fractionation and measurement. We have conclusively shown flotation rate (S_f) dependence of LDL and its subfractions on g-force in the analytic ultracentrifuge. When S_f rates are extrapolated to 1 × g, these rates, in flotation units, are approximately 2 F rate units higher at 1.20 g/ml and 1 F rate unit higher at 1.063 g/ml. One interpretation of these findings is that the lipoprotein molecules distort significantly higher under high g-force stress with potentially some field alignment giving a frictional ration $f/f_o \approx 1.15$, which could correspond to an oblate spheroid with an axial ratio of about 3/1 or 4/1. Such a situation could explain the very low molecular weights and spherical sizes obtained by traditional ηF_o versus ρ analytic ultracentrifugation. In collaboration with T. Forte and V. Shore, significantly higher molecular weights were obtained by electron microscopy and by low-speed sedimentation equilibrium. Such data would be reasonably consistent with the flotation velocity studies if the proposed shape distortion is assumed.

We have completed a pilot study using our automated agarose system on samples from some 2,500 LBL employees. This population is continuing to serve as a source of blood for experiments in which specific types of lipoprotein distributions are needed. Another pilot study, done in collaboration with D. Goldring and R. Burton of St. Louis Children's Hospital, St. Louis, Missouri, involved a multiracial school population of 12-to-16-year-olds. This project was a test of techniques to be used in our Oporto, Portugal, studies.

The Portugal project duplicates LBL equipment and methods of simplified lipid and lipoprotein analysis for a genetics versus environment study. Technician J. Adamson and I spent some three weeks in Oporto, assisting our Portuguese collaborators, F. Guerro and F. Sena-Esteves of the University of Porto, to get operational results on triglyceride and total cholesterol measurements by autoanalyzer, density by refractometry, preparative ultracentrifugation, and lipoprotein separation and quantification by agarose electrophoresis. All equipment was provided by the Gulbenkian Foundation with financial support by NATO and the Portuguese government.

PLASMA LIPOPROTEINS IN THE HUMAN NEONATE

Paul A. Davis and Trudy M. Forte

The connection between plasma lipoproteins and coronary heart disease has stimulated intense scientific interest in the elucidation of lipoprotein metabolism. As part of this effort, the study of the lipoprotein classes, the apolipoproteins within these classes, and their metabolism in the neonate has been undertaken in our laboratory. The various neonatal lipoprotein classes and their associated apolipoproteins are isolated, examined, and compared to the adult.

Neonatal blood is collected from the umbilical cord vein of the placenta, and the red blood cells, lymphocytes, and other constituents are removed by low-speed centrifugation. The levels of triglyceride and total cholesterol are determined and the plasma pooled according to sex. The levels of triglyceride and total cholesterol for neonatal plasma are much lower than those for adult plasma—about 47 and 64 mg/dl, respectively, as compared to average adult levels of 121 mg/dl triglyceride and 197 mg/dl total cholesterol. Neonatal plasma is then fractionated into the various density classes—very low density lipoproteins (VLDL), $d \leq 1.006$ g/ml; low density lipoproteins (LDL), $d \leq 1.063$; and high density lipoproteins (HDL), $d \leq 1.21$—by sequential ultracentrifugation.

The size distribution of the particles within each density class is analyzed by electron microscopy and by polyacrylamide gradient gel electrophoresis; the latter permits a more detailed determination of lipoprotein subspecies. The results of the electrophoresis of HDL (Fig. 1a) on a 4–30% polyacrylamide gel show that fetal HDL has a broad particle size distribution with four discernible peaks having diameters of 11.7, 10.2, 9.4, and 8.5 nm. Low density lipoproteins on 2–16% gel (Fig. 2a) show a tighter particle size distribution with three discernible peaks (31.6, 30.1 and 26.1 nm). The HDL and LDL classes are then subjected to further subfractionation by ultracentrifugation. The LDL was separated into intermediate density lipoproteins (IDL), $d \leq 1.019$, and LDL, $d \leq 1.019$, and these were then subjected to gradient gel electrophoresis. The results (Figs. 2b and c) show that the larger and smaller peaks fractionate as LDL while the intermediate peak fractionates as IDL. The subfractionation of HDL results in the two

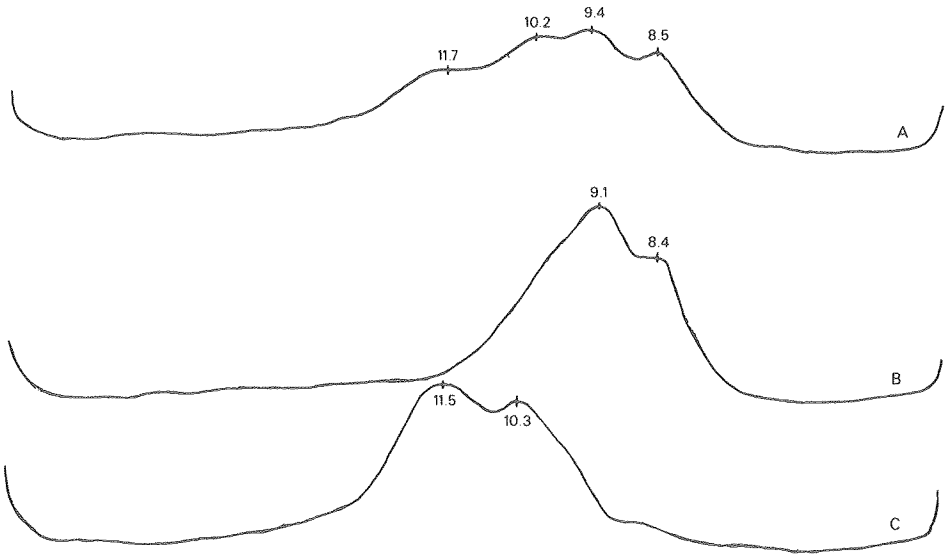

Figure 1. Densitometric scan of cord-blood HDL fractions after Electrophoresis on a 4–30% polyacrylamide gradient slab gel and staining with Coomassie Brilliant Blue G-250. The numbers indicate particle sizes in nanometers. *XBL 809-11801*

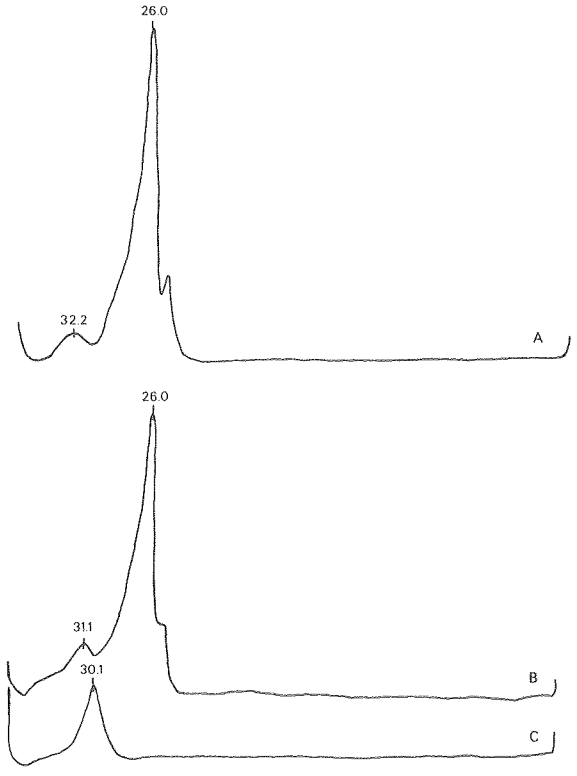

Figure 2. Densitometric scan of cord-blood LDL fractions after electrophoresis on a 2–16% polyacrylamide gradient slab gel and staining with Coomassie Brilliant Blue G-250. The numbers indicate particle sizes in nanometers.
XBL 809-11802

larger peaks fractionating as HDL_2 ($d \leq 1.125$) and the two smaller peaks fractionating as HDL_3 ($d \geq 1.125$) (Figs. 1b and c).

The apolipoprotein composition of each class of lipoprotein particle are examined by sodium dodecyl sulfate (SDS) gel electrophoresis (3 and 10% gels) and gel electrophoresis of the tetramethyl urea (TMU) solubilized apolipoproteins in the presence of 7 M urea. The TMU-soluble apolipoproteins in 7 M urea show a pattern of apolipoproteins similar to that of the adult (Fig. 3). SDS gel electrophoresis carried out in the presence or absence of the reducing agent, mercaptoethanol, also shows a pattern similar to the adult, except for the presence of a reducible band with a molecular weight of approximately 45,000. Upon reduction, this band disappears with a resulting increase in the intensity of the apo E and A-II bands (Fig. 4). The behavior of this ~45,000 MW apolipoprotein suggests that it may be a mixed dimer of apo E and A-II. The use of 3% gels for SDS gel electrophoresis shows the presence of the large molecular weight form of apo B (MW $\geq$ 560,000) in VLDL and LDL, with the LDL fraction containing additional lower molecular weight forms of apo B (MW $\geq$ 450,000, $\geq$ 170,000) (Fig. 5). When the LDL is subfractionated, the IDL contains the large molecular weight form of apo B, while LDL with a density $\geq$ 1.019 has all three forms (Fig. 5).

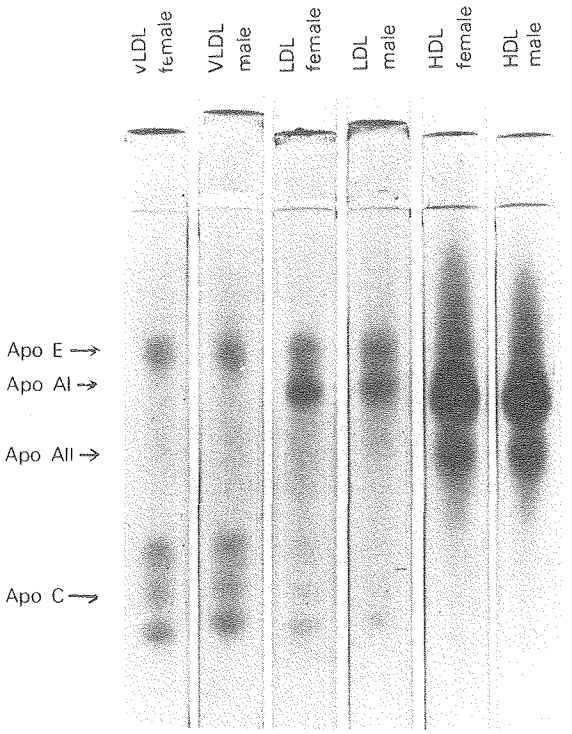

Figure 3. Urea-polyacrylamide gel electrophoresis of tetramethyl-urea-soluble apoproteins from cord blood lipoprotein fractions, stained with Coomassie Brilliant Blue R-250. *XBB 809-10600*

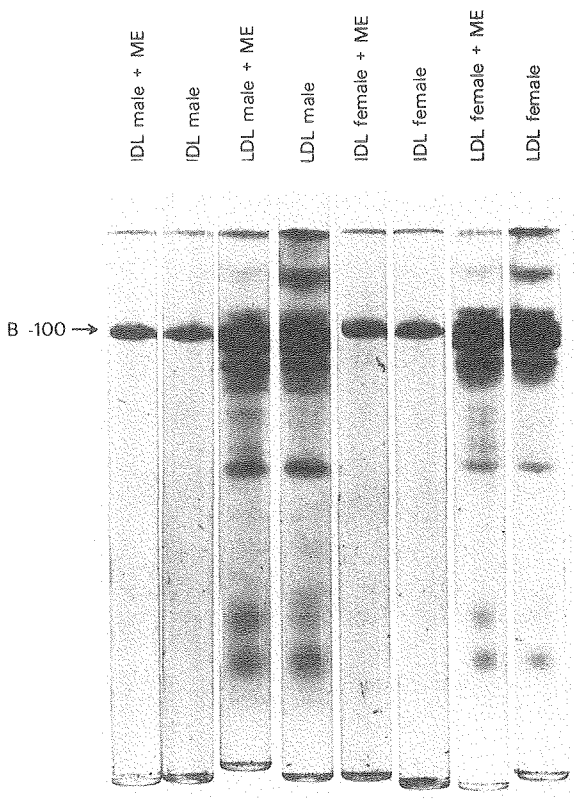

Figure 5. SDS-polyacrylamide gel electrophoresis (3% gel) of cord blood lipoprotein fractions, stained with Coomassie Brilliant Blue R-250. *XBB 809-10599*

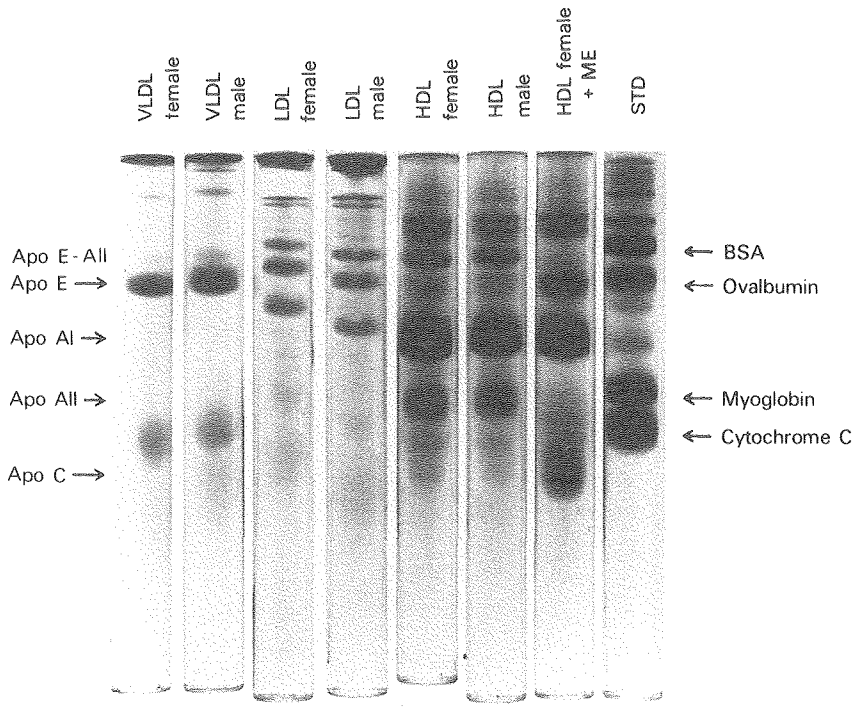

Figure 4. SDS-polycrylamide gel electrophoresis (10% gel) of cord blood lipoprotein fractions, stained with Coomassie Brilliant Blue R-250. *XBB 809-10601*

The results so far obtained show that fetal blood contains all the major classes of lipoproteins, albeit in different proportions, with little discernible sex difference. All the major apolipoproteins are present and are, in general, distributed similarly to the adult throughout the density classes. There are some differences in that the apo-B forms distribute differently upon subfractionation, with the adult IDL containing the three forms and LDL containing only one, while the fetal blood shows the reverse pattern. Additionally the fetal HDL contains a higher relative amount of E-AII, a protein complex present only in trace amounts in the adult. Further differences may be apparent when apolipoproteins and the lipoprotein classes are examined by isoelectric focusing and other more sensitive techniques.

The characterization of the lipoproteins present in umbilical-cord blood should give further insight into lipoprotein metabolism in general and identify those features which are specific for the fetal condition. In addition, these studies should allow the detection of lipoprotein metabolism dysfunctions at an early stage, allowing for prompt treatment with a resulting decline in the incidence and/or severity of coronary heart disease.

SUBCLASSES OF SERUM LOW DENSITY LIPOPROTEINS

Ronald M. Krauss, Mason M.S. Shen, Frank T. Lindgren and David J. Burke

Low density lipoproteins (LDL) are the major vehicles for transport of cholesterol in human serum and are primary determinants of the atherosclerotic process. We have provided evidence for the existence of multiple subclasses of LDL that differ in their physico-chemical and biological properties.

Analytical ultracentrifugation of LDL in normal humans revealed polydispersity, and in certain cases multiple peaks were observed (Fig. 1). A density gradient ultracentrifugation procedure was developed that resolved LDL into as many as four isopycnic bands, (of defined density), corresponding to the analytic ultracentrifuge schlieren peaks. Molecular weight, lipid:protein ratio, and triglyceride content declined progressively with increasing density of fractions withdrawn from the gradient, except

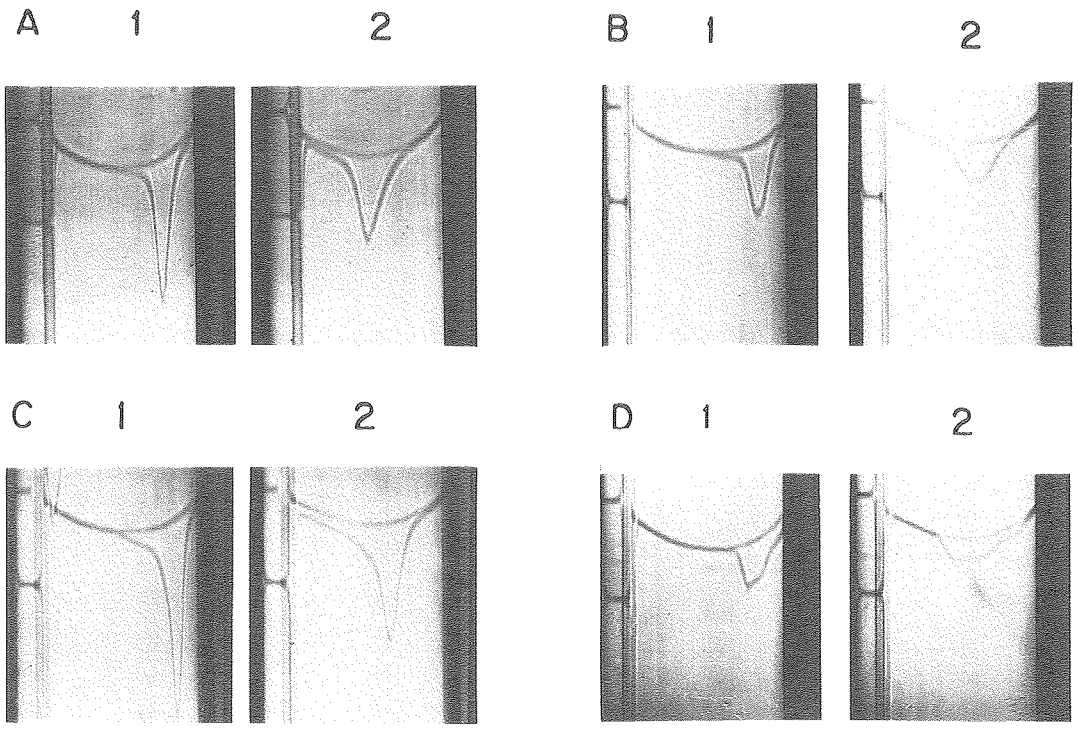

Figure 1. Schlieren patterns during analytical ultracentrifugation of LDL from four normal subjects. Centrifugation speed was 52,640 rpm at 26°C with NaBr solution of density 1.061 g/ml. Pairs (A) and (B) are from men and pairs (C) and (D) are from women. Photograph 1 of each pair was taken at 30 min and photograph 2 at 64 min after the centrifuge reached the designated speed. *XBB 808-10084*

for an absolute increase in triglyceride content in the fractions containing the most dense band. Differences in thermal transitions of cholesteryl esters were observed which paralleled the ratio of cholesteryl ester to triglyceride and indicated that the cholesteryl esters were most highly ordered in the middle bands.

Further heterogeneity within LDL was detected using polyacrylamide gradient gel electrophoresis, which achieves separation of LDL particles on the basis of size and/or shape. This procedure revealed up to 10 distinct bands in LDL from normal subjects (Fig. 2). Application of this technique to fractions separated by the density gradient ultracentrifugation procedure confirmed the electron microscopic finding that LDL particle size decreased with increasing density, and also showed that each of the isopycnic bands could be resolved into multiple subspecies. These subspecies could also be detected after electrophoresis of whole plasma (without ultracentrifugation), using a lipid stain. This technique provides an extremely sensitive and precise means for measurement of the newly defined LDL subspecies and is now being applied in several metabolic and clinical studies.

Results of these studies to date indicate major differences in metabolic relationships among individual LDL subspecies. Levels of the larger LDL subspecies are higher in women than men, increased by estrogen use, slightly increased in highly trained runners, and strongly correlated with levels of "anti-atherogenic" HDL (HDL_2). In contrast, levels of LDL subspecies that are smaller and denser are higher in men than women, reduced in runners, increased in patients with hypertriglyceridemia, and strongly inversely correlated with levels of HDL_2. This information suggests that one or more of these smaller LDL subspecies may have a preferential role in determining atherosclerotic risk.

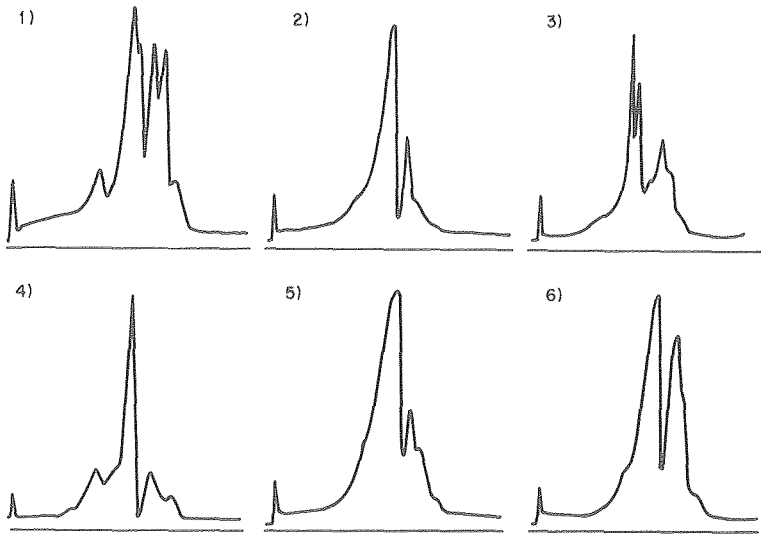

Figure 2. Densitometric scans of LDL electrophoresed in 2–16% polyacrylamide gels and stained for protein. The results are from six normal subjects and show multiple distinct peaks, reflecting varying concentrations among the individuals. *XBL 809-3663*

HORMONAL INFLUENCES ON SERUM HIGH DENSITY LIPOPROTEINS

Ronald M. Krauss

Studies of gonadal hormone effects on serum lipoproteins have been undertaken to elucidate the basis for sex differences in lipoprotein distribution, which in turn are likely to contribute to the well-known "protection" of menstruating women from coronary artery disease.

Effects of conjugated estrogens on high density lipoproteins (HDL) were examined using analytic ultracentrifuge measurements of HDL in groups of postmenopausal estrogen users and non-user controls. Two separate populations were studied—one retrospectively at Modesto and one recently in col-

laboration with S. Lewis at the Naval Medical Research Center, Oakland. In both, HDL_2 ($F^{\circ}_{1.20} \geq 2.0$ or HDL_{2a+2b}) was higher in hormone users; when the HDL were examined using a three-component schlieren analysis, the significant increase was confined to the HDL_{2a} region. Also in parallel with the male-female differences in HDL was a slightly lower level of HDL_3 in the users. In the second study, measurements of serum estrogens and gonadotropins (FSH and LH) were also carried out in the users ($n=14$) and controls ($n=17$). Highly significant correlations of total HDL and HDL_{2a} with FSH, and to a lesser extent with LH, were found in both groups. In the combined groups, and in hormone users alone when the variable of relative body weight was controlled for, a positive correlation emerged between levels of HDL_{2a} and estrone; there was also a significant multiple regression of estrone and FSH or LH on total HDL. These results suggest that in postmenopausal women HDL levels may be dependent on FSH (and/or on LH) and that the serum estrone level may exert a weaker effect on HDL that is probably additive and independent of the gonadotropin effect.

In a third study, measurements of HDL and gonadal and pituitary hormones in four healthy menstruating young females were carried out at weekly intervals during two complete menstrual cycles for each subject. In most of the individual cycles, increases were observed in HDL_{2b} and in some cases in HDL_{2a}, these increases occurring at or after the ovulatory surges in LH. While there was not sufficient data to establish a significant association of HDL and hormonal changes in these subjects, these results were consistent with a possible gonadotropin effect on HDL.

Studies of combined estrogen-progestin effects on HDL were undertaken in collaboration with the Walnut Creek Contraceptive Drug Study which was sponsored by the National Institute of Child Health and Human Development. Analytic ultracentrifuge measurements showed that the levels of total HDL in a group of 19 users of various combinations of oral contraceptives were significantly higher than in 18 controls, but that the increase was confined to lipoproteins of $F^{\circ}_{1.20} < 3.5$, primarily HDL_3. Furthermore, HDL cholesterol levels were not significantly different in the two groups. This suggested that progestins may modify the effects of estrogens by shifting the increase in HDL to denser, less cholesterol-rich particles.

That the effects of specific progestins may differ was indicated by analysis of HDL cholesterol measurements in oral contraceptive users in the Walnut Creek study. Some hormone preparations (generally estrogenic) were associated with HDL cholesterol levels significantly higher in users than in non-users whereas others (containing progestins with anti-estrogenic and/or androgenic properties) were associated with a significant reduction in HDL cholesterol. When treatment with one of the progestins in the latter category, norethindrone acetate, was studied in detail in two female subjects with Type V hyperlipoproteinemia, reduction in total HDL, predominantly HDL_2, was observed. With all hormone preparations there was positive correlation between levels of HDL cholesterol and triglyceride, an opposite relation to that found between these lipids in the non-user population.

Estrogen-progestin effects have been investigated further in studies of serial changes in serum lipoproteins in women users of contraceptive vaginal rings. This protocol is being carried out in collaboration with D. Mishell of the University of Southern California. For the past several years, this group has been assessing the effects of these rings, which release controlled amounts of ethinyl estradiol and norgestrel that in turn are absorbed directly from the vaginal mucosa and thereby bypass the portal circulation. Serum HDL-cholesterol drops within two weeks of insertion of these rings, and this is associated with almost complete disappearance of the HDL_{2a} and HDL_{2b} subfractions. At the same time there are changes within the LDL distribution (increase in LDL of $S^{\circ}_f 0–7$ and decline in LDL of $S^{\circ}_f 7–12$) that conform to the reciprocal relationships we have found between HDL and LDL subfractions. It remains to be established whether these lipoprotein changes contribute to an increase in atherosclerotic risk in users of these contraceptive agents.

DIETARY EFFECTS ON SERUM HIGH DENSITY LIPOPROTEINS

Ronald M. Krauss, Virgie Shore,* Gail Butterfield and Frank T. Lindgren

The aim of this project is to determine the influence of various dietary factors on levels, composition, and metabolic interrelationships of serum high density lipoproteins (HDL) in healthy men. In the first year, studies using diets fed to outpatients assessed the effects of varying the ratio of polyunsaturated to saturated fat (P:S) and the effects of different types of protein (animal vs. vegetable); another study, performed in a human metabolic research unit, assessed the effect of varying energy flux.

With the assistance of a research dietitian, real food diets were formulated and prepared according to the specifications of the protocols. Macro- and micro-nutrient levels were analyzed directly, and any significant deviations from the specified values were corrected where possible. The initial (reference) diet contained approximately 17% of calories from protein, 52% from carbohydrate, and 31% from fat, with ratio of polyunsaturated to saturated fat (P:S ratio) of 1:1, and 150 mg of cholesterol per 1000 kcal.

In the first outpatient study, the reference diet was fed to a group of 6 healthy normolipemic men, and 5 of those subjects were then fed diets in which the P:S ratio of the reference diet was changed to 3:1 (high P:S) and 0.25:1 (low P:S), without any other change in diet composition. Each diet was fed for 4 weeks (with 4-week intervals between diets). Blood samples for lipoprotein analyses were obtained after overnight fast on days 0, 21 and 28 of each diet, and on day 28 samples were obtained between 3 and 6 hours after a standard fat meal.

Comparison of results on the high P:S vs. the reference diet revealed significant reductions in mean levels of total low density lipoprotein (LDL), LDL cholesterol, and LDL protein (19, 24 and 27% respectively). Levels of very low (VLDL) and intermediate (IDL) density lipoproteins did not change significantly. There was an insignificant reduction in mean HDL cholesterol (6%), but a significant reduction in total HDL (16%) and the HDL_2 subspecies (29%). In three subjects there was a reduction of HDL protein (mean 19%), and no change in the two other subjects. The ratio of the major HDL apolipoproteins (apoA-I and apoA-II) and the properties of the C-apolipoproteins varied considerably within 12 subfractions of HDL isolated by density gradient ultracentrifugation between the densities 1.061 and 1.205 g/ml, and the distribution of apolipoproteins was shifted in some individuals by diet. For example, there was little apoA-II in fractions 1 (least dense) and 12 (most dense) on the reference diet. On the high P:S diet apoA-II was reduced in fractions 2, 3, and 4 as well, and content of the C-apolipoproteins in HDL was increased.

With the low P:S diet, mean LDL cholesterol increased significantly compared with levels on the reference diet (18%), while total LDL and LDL protein levels were similar. Mean serum triglyceride levels also increased (45%), although interestingly there were no significant changes in VLDL, except for an increase in VLDL protein in one subject, who had very high levels of the Lp(a) lipoprotein. Mean HDL-cholesterol level was significantly reduced (13%), and levels of HDL_2 were reduced to the same levels found on the high P:S diet. This was accompanied by a shift in HDL protein to the higher density region except in the subject with high Lp(a). The reduction in HDL-cholesterol exactly paralleled the reduction in HDL total mass, as opposed to the case of the high P:S diet, where a relative enrichment in cholesterol content of HDL resulted in a minimal reduction in HDL cholesterol level despite a reduction in total HDL mass comparable to that on the low P:S diet. Finally, mean ratios (wt:wt) of HDL to LDL protein after the reference, high-P:S, and low-P:S diets were 2.54, 3.12, and 2.51 respectively. In comparison, the ratios of HDL to LDL cholesterol on these diets were 0.49, 0.60, and 0.36.

In summary, major influences of dietary P:S ratio on levels and composition of HDL were found in all subjects in this study. P:S ratio also influenced levels of HDL in relation to LDL, particularly with regard to lipoprotein cholesterol levels, and also with regard to apolipoprotein levels and total mass.

The second outpatient study involved varying the source of protein in the reference diet from 70% animal and 30% vegetable to (1) approximately 98% animal and 2% vegetable and (2) approximately 96% vegetable and 4% animal, all other parameters remaining constant. Analysis of the results of this study is in progress.

In the third study, carried out in the metabolic unit of the Department of Nutritional Sciences on the UC Berkeley campus, four highly trained runners were given the reference diet at two different levels of energy intake. One diet was sufficient to

*Lawrence Livermore Laboratory.

maintain body weight constant during 4 weeks of running 10 miles per day, and the other was sufficient to maintain the same weight during 4 weeks of running 5 miles per day. Preliminary analyses of the results indicate that levels of serum HDL (in particular the HDL_{2b} subclass) dropped significantly within one week of reducing energy intake, while levels of LDL increased.

The results to date indicate that levels of lipoprotein constituents known to influence coronary disease risk can be changed in normal men by modifications in dietary fat composition and total energy intake. Studies planned and in progress will provide further information on these and other dietary effects that will be required in making rational assessments of the potential risks and benefits of specific dietary interventions. Furthermore, the study of metabolic and hormonal factors governing the dietary responses will help in the understanding of mechanisms that may lead to improved therapies in the future.

EFFECTS OF PHYSICAL TRAINING ON SERUM LIPOPROTEINS AND HEPARIN-RELEASED LIPOLYTIC ACTIVITIES

Ronald M. Krauss, Peter D. Wood,* Frank T. Lindgren, and Christine Giotas

We have compared levels of serum lipoproteins in distance runners (15 men and 8 women currently running at least 15 miles/week for at least 3 mos) with levels in less active control subjects matched for sex, age and relative body weight. The findings have confirmed that runners have higher levels of high density lipoproteins (HDL), but analytic ultracentrifuge measurements have shown that the difference is confined to a specific HDL subclass (HDL_2). Levels of very low density (VLDL) and low density (LDL) lipoproteins are lower in runners; ultracentrifugal analysis shows that the difference in LDL is confined to lower molecular weight subspecies (S_f^0 0–8). Levels of VLDL and LDL were highly intercorrelated, while HDL and HDL_2 concentrations were independent of the levels of other lipoproteins. In this study population there was no significant inverse relationship between HDL and LDL levels; however levels of VLDL and LDL were found to be highly intercorrelated.

Much evidence has been obtained recently that levels of HDL, and specifically HDL_2, are strongly dependent on the metabolic flux of the triglyceride-rich lipoproteins, VLDL and chylomicrons, the latter derived from dietary fat and ordinarily not detectable in the fasting state. The clearance of these lipoproteins is mediated by the enzyme lipoprotein lipase, which is present in all extrahepatic tissues, and which can be measured in plasma after intravenous heparin administration. Using a standardized assay procedure, we have found that heparin-released plasma lipoprotein lipase activity is significantly higher in runners, confirming previous reports of enzyme measurements in adipose tissue and skeletal muscle biopsies. Furthermore, the activity of lipoprotein lipase in runners shows an inverse correlation with serum levels of triglyceride and VLDL; and in both runners and controls, there is a strong positive correlation between lipoprotein lipase activity and levels of HDL_2.

Another lipolytic enzyme, hepatic lipase, has also been measured in post-heparin plasma. We have found that its activity is significantly reduced in runners and that it is strongly correlated with relative and absolute body weight, and with levels of a specific HDL subclass (HDL_3).

These results suggest that lipoprotein lipase activity may be in part responsible for lower levels of VLDL in the runners and also for higher levels of HDL_2, while a possible metabolic role for hepatic lipase activity is less apparent. Our data, taken together with recent reports of others, suggest that this enzyme may favor formation of the HDL_3 subspecies at the expense of HDL_2.

We have recently completed an 18-month longitudinal study of exercise traning effects on serum lipoproteins and other metabolic parameters in 72 initially sedentary men, 48 of whom were selected at random for an exercise training program. The results indicate that in the subgroup of individuals who achieved the highest levels of exercise (in miles run per week), there were changes in HDL and other lipoproteins which paralleled the differences previously found in runners vs. sedentary controls. Further analysis of the results, including measurements of lipolytic activities, is now in progress.

*Stanford University.

TRANSPORT OF LIPID-SOLUBLE CARCINOGENS BY PLASMA LIPOPROTEINS

Helen P. Shu

The development of tumors at sites far from the site of initial carcinogen exposure suggests that carcinogens must be transported by the bloodstream. Early studies in which lipid-soluble carcinogen adsorbed on soot particles was eluted off by plasma but not by physiological saline indicated the presence of substances in plasma having affinity for the carcinogen. Later studies suggested that these substances might be plasma lipoproteins, but they did not fully characterize the interaction between the lipid-soluble carcinogen and blood elements. As part of our initial effort in understanding the fundamental mechanism for transport of lipid-soluble carcinogens, we have investigated in some detail the interaction between various blood components and benzo(a)pyrene (BaP).

One consistent finding has been that while the distribution of BaP among the lipoprotein classes differs from plasma to plasma, this distribution can be correlated with the total lipid volume of the lipoprotein particles. That is, when the distribution is calculated on the basis of lipoprotein lipid volume, a constant value is obtained regardless of the lipoprotein class or the plasma source (Fig. 1).

The observation that benzo(a)pyrene distribution is correlated with lipoprotein lipid volume is perhaps not surprising when one considers that BaP is an extremely lipid-soluble molecule. A more unexpected observation has been the apparent restriction of BaP uptake by lipoprotein particles with high apolipoprotein content.

The possible influence of apolipoproteins on BaP uptake by plasma lipoproteins was assessed in studies using the major high density lipoprotein (HDL) subfractions, HDL_{2b} and HDL_3. In Table 1, data on benzo(a)pyrene uptake by HDL_{2b} and HDL_3 are expressed per particle and per milliliter of lipoprotein–total lipid volume. Corresponding data for BaP uptake by isolated very low density lipoprotein (VLDL) and low density lipoprotein (LDL) are included for comparison. When BaP uptake is expressed on a per-particle basis, a range in uptake from 2400 BaP/VLDL to 7 BaP/HDL_3 is observed. Interestingly, the uptake per HDL_3 particle is significantly lower than that for HDL_{2b} (7 vs. 32). When BaP uptake by HDL_3 and HDL_{2b} is calculated on the basis of micromoles per milliliter of lipoprotein–total lipid volume, the uptake value of 121 μmol/ml for HDL_{2b}

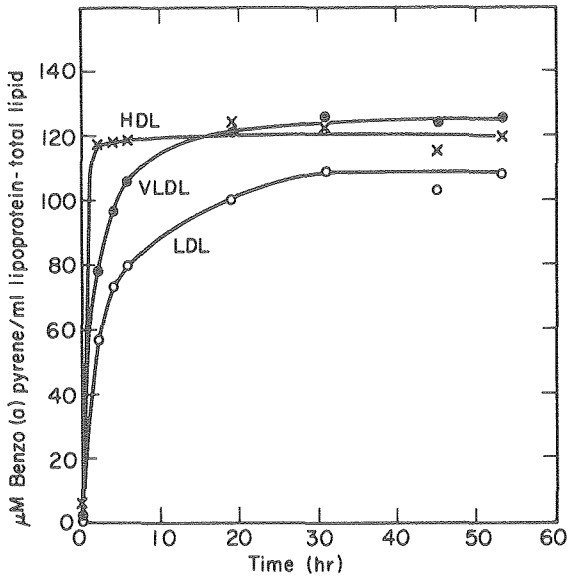

Figure 1. Molar benzo(a)pyrene uptake data for each lipoprotein fraction under saturation conditions were calculated with respect to the volume of lipoprotein–total lipids. Volume of deproteinated lipoprotein was estimated by subtracting the volume occupied by protein (molecular weight lipoprotein × percent protein × partial specific volume of protein) from total lipoprotein volume. Symbols: ●, VLDL; ○, LDL; x, HDL. XBL 7812-12405

Table I. Benzo(a)pyrene uptake by high density lipoprotein subfractions.

	VLDL	LDL	HDL_{2b}	HDL_3
Protein:phospholipid (weight:weight)	1:2	1:1	1:1	2:1
Benzo(a)pyrene uptake (mol/mol lipoprotein)	2400	200	32	7, 7
Benzo(a)pyrene uptake/lipoprotein-total lipid volume (μmol/ml)	120	110	121	89, 81

NOTE: Ratio of protein:phospholipid was obtained from chemical composition data. Uptake of mol benzo(a)pyrene per mol lipoprotein was determined from radioactivity and chemical composition data. The molar uptake data was then used, along with values of the lipoprotein–total lipid volume calculated from the chemical composition data, to calculate the μmol uptake per ml lipoprotein–total lipid volume.

agrees well with previously reported saturation values for isolated VLDL and LDL of 120 and 110 μmol/ml, respectively. The uptake values obtained for HDL_3 of 81 and 89 μmol/ml are substantially lower than values obtained for HDL_{2b}. These findings are consistent with the conclusion that in VLDL, LDL, and HDL_{2b} the lipoprotein–total lipid volume behaves as one compartment for benzo(a)pyrene uptake (with maximum uptake approximately 110–120 μmol/ml), while uptake by HDL_3 lipid volume is apparently restricted.

NEW PLASMA LIPOPROTEINS IDENTIFIED IN PEDIGREED BABOONS ON CHOLESTEROL DIET

Alex V. Nichols, Thomas Kuehl,* Elaine L. Gong, Patricia J. Blanche, and Henry McGill*

Diets high in cholesterol and saturated fat are generally considered to contribute to an increased risk from atherosclerosis and its clinical sequelae, such as coronary heart disease. A major link between consumption of such diets and atherosclerosis is their effect on the level of certain plasma lipoproteins that have been highly correlated with the incidence of the disease. In humans, it is well established that the low density lipoproteins (LDL) are the species primarily affected by diets high in cholesterol and saturated fat. The possible effects of such diets on plasma levels of the potentially "protective" high density lipoproteins (HDL) are under intensive investigation.

Recently it has been found that the levels of specific subspecies of HDL also increase in human plasma when cholesterol, in the form of eggs, is added to the normal diet. The properties of these lipoproteins are substantially different from those of the other normally observed HDL, particularly in the composition of their protein moeity. Unlike the usual HDL, they contain a protein designated as apolipoprotein E. This protein, similar to the apolipoprotein B of LDL, readily interacts with specific receptors on cell surfaces and thereby facilitates the incorporation of the lipid content of the HDL molecule into the cell. Elucidation of the role of HDL containing apolipoprotein E, in either the deposition or removal of cellular cholesterol, is clearly important to our understanding of the atherosclerotic process and is of considerable current interest.

In a collaborative study with H. McGill and staff at the Southwest Foundation for Research and Education (San Antonio, Texas), we have been investigating the response of a nonhuman primate, the baboon (*Papio cynocephalus*), to diets high in cholesterol and saturated fat. Baboon progeny, resulting from selective breeding for elevated as well as low concentrations of serum cholesterol, in response to the atherogenic diet, were sampled for determination of their lipoprotein profiles by analytic ultracentrifugation and gradient gel electrophoresis. In certain baboons, we have found new lipoprotein species (Fig. 1) with properties similar to the apolipoprotein E-containing HDL described in humans and in other experimental animals. This is the first

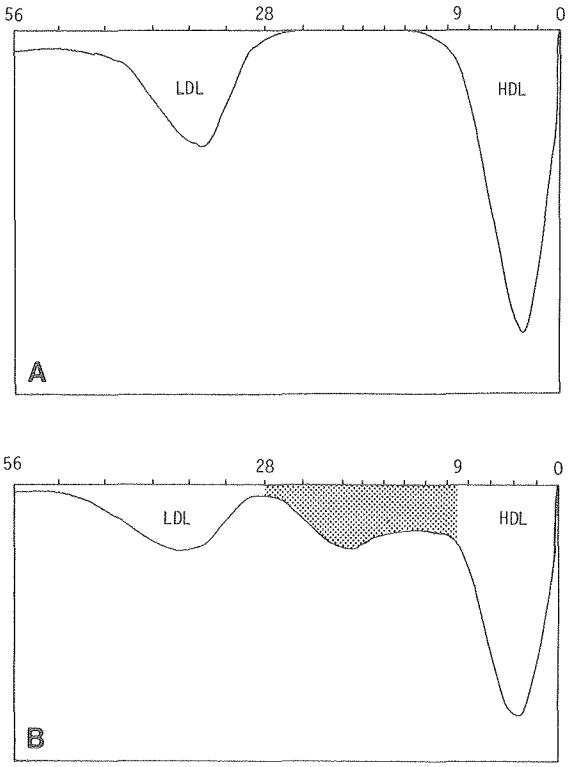

Figure 1. Representative concentration profiles of lipoproteins in the plasma of pedigreed baboons on (A) basal diet and (B) atherogenic diet; profiles were obtained by analytic ultracentrifugation. New cholesterol-rich lipoproteins (shaded region) exhibit ultracentrifugal flotation properties intermediate to those of the high density lipoproteins (HDL) and low density lipoproteins (LDL). XBL 8011-7448

*Southwest Foundation for Research and Education, San Antonio, Texas.

time that the levels of these species have been quantified in baboon plasma together with their particle-size distribution. We have characterized the major physical-chemical properties of these lipoprotein species and find them to be spherical particles, ranging in diameter between 120 and 220 Å (Fig. 2); these particles are rich in cholesteryl esters.

Our preliminary information suggests that this lipoprotein variant may be inherited through a single major gene. In projected studies, we plan to definitively establish the mode of inheritance, and the dietary and other environmental factors, that control the concentration of these lipoproteins in plasma. Furthermore, we plan to evaluate the contribution of these lipoproteins to the progression of atherosclerosis in baboons fed diets high in cholesterol and saturated fat.

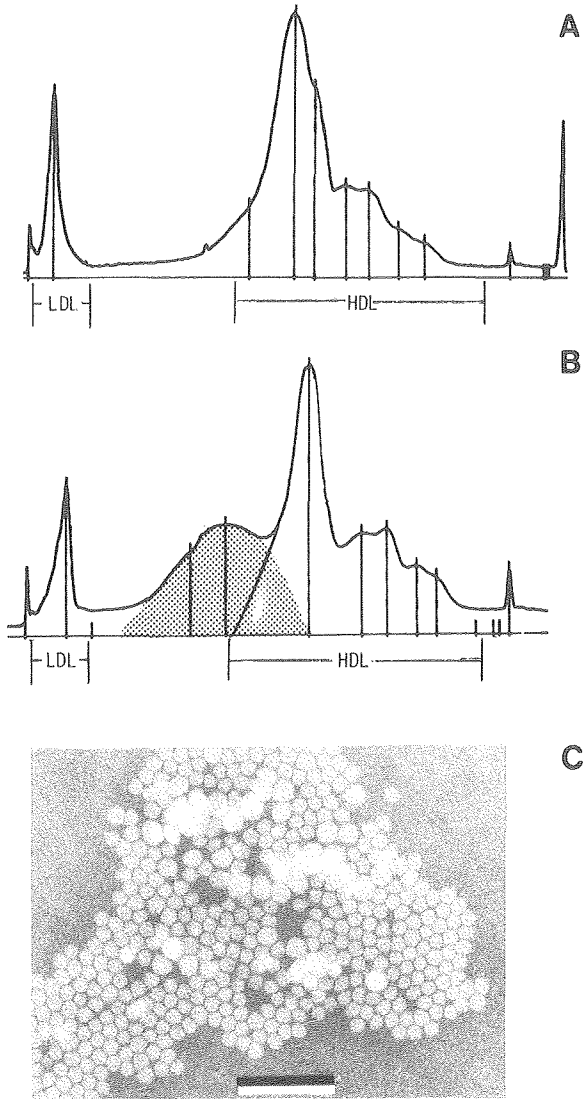

Figure 2. Representative concentration profiles of lipoproteins in the plasma of pedigreed baboons on (A) basal diet and (B) atherogenic diet. Profiles were obtained by a newly developed gradient gel electrophoresis procedure that resolves the lipoproteins according to particle size. New cholesterol-rich lipoproteins (shaded region) range in particle size from 120 Å to 220 Å, intermediate to LDL and HDL. Electron microscopy (C) of these particles in the mid-peak region of their distribution shows them to be spherical, with mean diameter of approximately 160 Å. Electron microscopy performed by T. Forte. (Marker represents 1000 Å.) *XBB 800-12468*

INTERRELATIONSHIPS BETWEEN LIPOPROTEIN SECRETION AND CULTURED HEPATOCYTE ULTRASTRUCTURE

Trudy Forte and Julia Bell-Quint

Studies with perfused rat livers have shown that the liver is able to synthesize and secrete both nascent very low density lipoproteins (VLDL) and high density lipoprotein (HDL) particles. Studies on avian and rat liver parenchymal cells in monolayer culture have demonstrated that cultured hepatocytes secrete VLDL into the culture medium. We have recently found that, in addition to VLDL, both low density lipoprotein (LDL) and HDL can be isolated from the culture medium of rat hepatocyte monolayers. Moreover, we noted that the rates of lipoprotein secretion, particularly VLDL, show time-related changes. In this article we correlate ultrastructural parameters of hepatocyte monolayer cultures with lipoprotein secretion as a function of time.

Parenchymal cells were isolated from the livers of male, WAG/rij rats and were suspended in Leibovitz L-15 medium including 8.3 mM glucose, 32 mU/ml insulin, penicillin-streptomycin and 20% fetal calf serum. The latter was excluded after overnight attachment of cells to the Petri dishes. Medium and cells were harvested separately, and lipoproteins were isolated from the culture medium by means of preparative centrifugation techniques: VLDL were isolated at d < 1.006 g/ml, LDL at d 1.006–1.063 g/ml, and HDL at d 1.063–1.21 g/ml.

For ultrastructural studies on cells, hepatocyte cultures were fixed *in situ* with 2.5% glutaraldehyde in 0.15 M sodium cacodylate buffer, pH 7.4; post-fixed in 1% osmium tetroxide in 0.15 M sodium cacodylate; and stained *en bloc* with 2% uranyl acetate for 30 min. Cultures were subsequently embedded in Araldite.

Rat hepatocyte cultures synthesize and secrete VLDL, LDL and HDL into the culture medium. As seen in Table 1, VLDL is the major lipoprotein isolated from the medium at early times (up to 6.5 hr). With prolonged incubation there is a notable decrease of VLDL so that after 48 hr VLDL concentration is reduced by 77%. Addition of sodium oleate to the medium resulted in the production of large quantities of VLDL (11.4 mg/g cell protein) during 48 hr incubation. Hence, fatty acids become rate-limiting substrates for triglyceride (TG) synthesis during prolonged incubation in unsupplemented medium. At early incubations substantial quantities of LDL and HDL (Table 1) can also be isolated from the medium. Unlike VLDL, these lipoproteins do not show a loss of concentration during prolonged incubation. The HDL are 110 Å spherical particles similar to rat plasma HDL. The LDL fraction at short incubation periods consists of a single population of particles; these structures are approximately 296 Å diam and contain only apolipoprotein B. Their rapid appearance in the culture medium suggests that they are synthesized *de novo*. Prolonged incubation results in the appearance of larger structures (400–800 Å) in the LDL fraction; since TG also increases in this fraction with time, this suggests that degradation of VLDL has occurred, thus producing an intermediate particle in the density range of LDL.

Table 1. Concentration of lipoproteins isolated from rat hepatocyte culture medium after 6.5 and 48 hours of incubation.

	mg lipoprotein/g cell protein		
Time	VLDL	LDL	HDL
6.5 hours	4.6 ± 0.8	1.2 ± 0.1	1.6 ± 0.1
48.0 hours	1.1 ± 0.3	2.9 ± 0.5	3.8 ± 0.2

The ultrastructure of rat hepatocytes in monolayer culture is in many respects similar to that of the intact liver; bile canaliculi with numerous short microvilli are present, and Golgi complexes are found in close proximity to the bile canaliculus. The lateral cell borders of adjacent hepatocytes are closely apposed, and osmiophilic particles are frequently trapped within the intercellular space. These particles have a mean diam of 609 Å (Table 2) and are presumed to be VLDL. Their presence suggests that during short incubation periods the rate of VLDL secretion into the medium is underestimated.

The Golgi complex appears to undergo changes dependent on the metabolic state of the cells. At early incubation times the Golgi complex contains cisternae and smooth-surfaced vesicles which enclose numerous VLDL particles 491 Å diam, range 300–883 Å [Table 2 and Fig. 1(A)]. After 24 and 48 hr incubation periods, only negligible amounts of VLDL are recovered in the medium; this is paralleled by a decrease in the number and size of particles found within the Golgi (Fig. 1B). The small size, 306 Å, of Golgi particles after prolonged incubation, suggests that they are LDL (Table 2). This suggestion is strengthened by the fact that substantial quantities

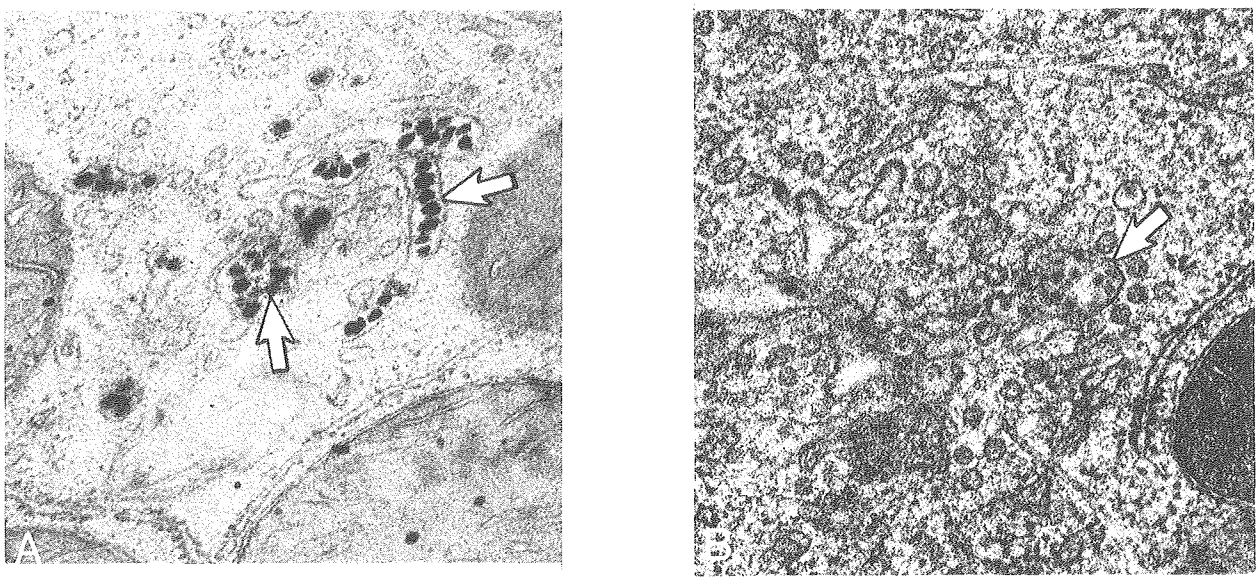

Figure 1. (A) Golgi region from 6.5 hr culture. VLDL within Golgi saccules and vesicles are indicated by arrows. (B) Golgi region from a 48 hr culture. Lipoprotein particles (arrow) are few in number and smaller than those from 6.5 hr incubation. *XBB 806-7546*

of LDL are isolated from the medium even after 48 hr. The presence of LDL within the Golgi and culture medium is evidence that the liver is able to synthesize and secrete LDL directly.

The disappearance of VLDL from the medium during prolonged incubation may also be accounted for by receptor-mediated uptake of particles into the cell; in fact, high-affinity VLDL binding sites on hepatocytes have been described by other investigators. Our ultrastructural studies revealed the presence of VLDL-containing coated vesicles (Fig. 2) in the apical portion of the hepatocytes. Similarly coated pits have been associated with receptor-mediated uptake of LDL by peripheral cells; thus it is likely that VLDL uptake and subsequent degradation steps are similar to those previously described for the LDL pathway.

Table 2. Comparison of electron microscopic size (diam in Å ± S.D.) of intracellular and extracellular lipoproteins.

	6.5 hr	48 hr
Golgi Saccules	491 ± 111	309 ± 39
Intercellular Space	609 ± 165	N.D.*
Culture Medium VLDL	797 ± 219	N.D.
Culture Medum LDL	296 ± 29	248 ± 38†

*N.D. = Not detectable.

†Approximately 20% of the total particles consist of structures 631 ± 203 Å diameter.

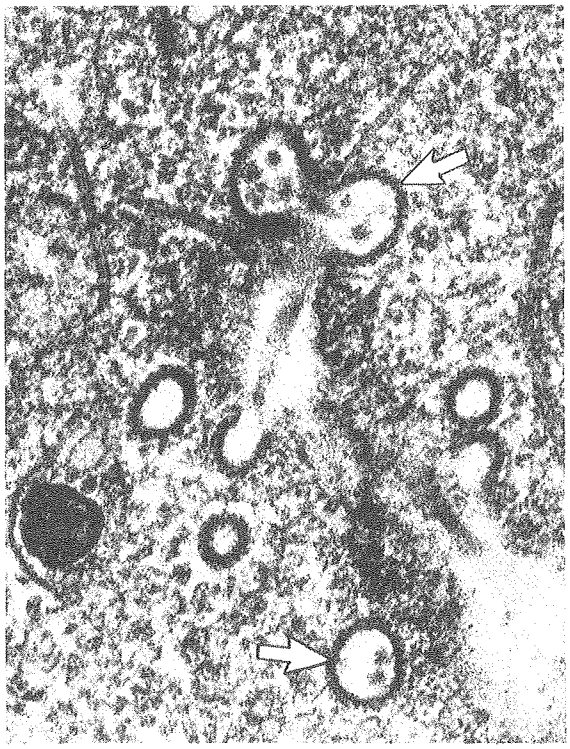

Figure 2. Coated pits and vesicles (arrows) within the cytoplasm of a cultured hepatocyte. VLDL-like particles are seen within some of the coated vesicles. *XBB 806-7544*

APPENDICES

Appendix A. List of Contracts and Grants Supporting Portions of Work Presented in this Annual Report

INVESTIGATOR	CONTRACT OR GRANT
E.J. Ainsworth	NASA P.O. # T 3516-G Life-Shortening Effects of HzE Particles on Mice/Heavy Ion Cell Transformation
E.L. Alpen	PHS Grant # CA 24789 Heavy Ion Radiation & Multicellular Spheroids
M.E. Bentfield-Barker	PHS Grant # HL 24577 Megakaryocyte Differentiation
G. Brecher	PHS Grant # CA 25133 Hemopoietic Differentiation, Macrocytic Anemia
T.F. Budinger	PHS Grant # HL 21697 Myocardium Infarct Sizing by ^{82}Rb Emission Tomography
T.F. Budinger	PHS Grant # HL 07367 Quantitative Cardiovascular Research, Training Grant
H.J. Burki	PHS Grant # CA 14310 *In Vitro* Study of Mammalian Cells Damaged by Tritium
H.J. Burki	PHS Grant # ES 01916 Alkylating-Carcinogens Mutagenesis in Mammalian Cells
J.R. Castro	PHS Grant # CA 19138 Treatment of Cancer w/Heavy Charged Particles
S.B. Curtis	PHS Grant # CA 17411 Response of Rat Rhabdomyosarcoma to Heavy Ions
K.H. Downing	PHS Grant # GM 27291 DNA Structure by Electron Diffraction & Microscopy
S.N. Ebbe	PHS Grant # AM 21355 Kinetics of Megakaryocyte and Platelet Turnover
S.N. Ebbe	PHS Grant # AM 07349 Hemopoietic Cellular Proliferation/Regulation
T.M. Forte	PHS Grant #HL 07279 Lipoprotein Methodology, Structure and Function Training Grant
J.F. Garcia	PHS Grant # HL 22469 Radioassay of Erythropoietin
R.M. Glaeser	PHS Grant # GM 23325 Biological Structure Analysis by Electron Microscopy
R.M. Krauss	PHS Grant # HL 24740 Dietary Effects on Serum High Density Lipoproteins

F.T. Lindgren	PHS Grant # HL 18574 Lipoprotein Methodology and Biomedical Applications
M.F. Maestre	PHS Grant # AI 08427 Physical Structure of Viruses, Chromosomes & Cell Nuclei
M.F. Maestre	PHS Grant # GM 25936 Studies on T4 Phase Gene Product 32 Protein-DNA Complexes
J. McCann	NASA P.O. # EPA 80-D-X0935 Plan for a Research and Information Center for the Analysis and Interpretation of Data from Short-Term Tests
M.S. Raybourn	PHS Grant # ES 01907 *In Vitro* Electrophysiology of CNS Toxicity
W. Schimmerling	PHS Grant # CA 23247 Physical Characteristics of Heavy Ion Beams
W. Schimmerling	NASA P.O. # L22395A To Measure the Production of Neutrons by High Energy Heavy Ions
H. Shu	EPA 79-D-X0533 Baseline Studies to Support Metabolism
H.S. Smith	PHS Grant # CA 25630 Studies of Malignant Progression Using Human Cells
M.R. Stampfer	PHS Grant # CA 24844 Characterization of Human Mammary Cells
C.A. Tobias	PHS Grant # CA 15184 Heavy Ion Radiobiology Related to Oncology
C.A. Tobias/J.I. Fabrikant	PHS Grant # CA 27021 Heavy Ion Radiography and Cancer
M. White	EPA 79-D-X0533 Cocarcinogenesis in Mice
E. Wiedemann	PHS Grant # CA 23382 Investigation of Human Beta-Lipotropin

Appendix B: 1979–1980 Publications

CONTRIBUTIONS TO JOURNALS

Aebersold, P. Mutation induction by 5-fluorodeoxyuridine in synchronous Chinese hamster cells. Cancer Research *39:*808–810 (1979).

Alpen, E.L., Powers-Risius, P. and McDonald, M. Survival of intestinal crypt cells after exposure to high Z, high-energy charged particles. Radiation Research *83:*677–687 (1980).

Anderson, L.W. and Smith, H.S. Premalignancy in vitro: Progression of an initially benign epithelial cell line to malignancy. Brit. J. Exper. Path. *60:*575–581 (1979).

Bissell, M.J., Bartholomew, J.C., Folkman, J., Smith, H.S. and Stampfer, M. Meeting report: culture systems for studying malignancy. Cancer Research *39:*4293–4295 (1979).

Black, J.A., Forte, T.M., and Forte, J.G. Structure of oxyntic cell membranes during conditions of rest and secretion of HDL as revealed by freeze-fraction. J. Anat. Rec. *196:*163–172 (1980).

Braun, U., Braun, G., and Sargent, T., III. Changes in blood-brain permeability resulting from d-amphetamine, 6-hydroxydopamine, and pimozide measured by a new technique. Experientia *36:* 207–209 (1980).

Budinger, T.F. Imaging technology; Part 1. Research versus clinical. Diagnostic Imaging *1(1):*4 and 8 (1979).

———. Physical attributes of single-photon tomography. J. Nucl. Med. *21:*579–592 (1980).

Burki, H.J. Ionizing radiation-induced 6-thioguanine resistant clones in synchronous CHO Cells. Radiation Research *81:*76–84 (1980).

———, **Lam, Chee-King, and Wood, Richard D.** UV-light-induced mutations in synchronous CHO cells. Mutation Research *69:*347–356 (1980).

Byers, V.S., LeCam, L., Levin, A.S., Johnston, J.O., and Hackett, A.J. Immunotherapy of osteogenic sarcoma with transfer factor. Cancer Immunol. Immunother. *6:*243–253 (1979).

Castro, J.R., Quivey, J.M., Lyman, J.T., Chen, G.T.Y., Phillips, T.L., Tobias, C.A., and Alpen, E.L. Current status of clinical particle radiotherapy at Lawrence Berkeley Laboratory. Cancer *46:*633–641 (1980).

———, **Quivey, J.M., Lyman, J.T., Chen, G.T.Y., Phillips, T.L., and Tobias, C.A.** Radiotherapy with heavy charged particles at Lawrence Berkeley Laboratory. J. Can. Assoc. Radiol. *31:*30–34 (1980).

Chapman, J.D., Doern, S.D., Reuvers, A.P., Gillespie, C.J., Chatterjee, A., Blakely, E.A., Smith, K.C., and Tobias, C.A. Radioprotection by DMSO of mammalian cells exposed to x-rays and to heavy charged-particle beams. Radiat. Environ. Biophys. *16(1):*29–41 (1979).

Char, D.H., Castro, J.R., Quivey, J.M., Chen, G.T.Y., Lyman, J.T., Stone, R.D., Irvin, A.R., Barricks, M., Crawford, J.B., Hilton, G.S., Lonn, L.I., and Schwartz, A. Helium ion charged particle therapy for choroidal melanoma. Ophthalmology *87:*565–570 (1980).

Chen, George T.Y., Singh, Rajinder P., Castro, Joseph R., Lyman, John T., and Quivey, Jeanne M. Treatment planning for heavy ion radiotherapy. Int. J. Radiation Oncology Biol. Phys. *5:*1809–1819 (1979).

Clemons, G.K., Russel, S.M., and Nicoll, C.S. Effects of mammalian thyrotropin-releasing hormone on prolactin secretion by bullfrog adenohypophysis *in vitro*. Gen. Comp. Endocrinol. *38:*62–67 (1979).

Creasey, A.A., Smith, H.S., Hackett, A.J., Fukuyama, K., Epstein, W.L., and Madin, S.H. Biological properties of human melanoma cells in culture. In Vitro *15:*342–350 (1979).

Curtis, S.B. and Tenforde, T.S. Assessment of tumour response in a rat rhabdomyosarcoma. Brit. J. Cancer *41 (Suppl. IV):*266–270 (1980).

Dorset, D.L., Jap, B.K., Ho, M-H., and Glaeser, R.M. Direct phasing of electron diffraction data from organic crystals: The effect of N-Beam dynamical scattering. Acta Cryst. *A35:*1001–1009 (1979).

Downing, K.H. and Chiu, W. Effect of stray magnetic field on image resolution in transmission electron microscopy. Ultramicroscopy *5:*351–356 (1980).

Durbin, P.W., Jones, E.S., Raymond, K.N., and Weitl, F.L. Specific sequestering agents for the actinides

4. Removal of $^{238}Pu(IV)$ from mice by sulfonated tetraminic catechoyl amides. Radiation Res. *81:*170–187 (1980).

Forte, T.M., Krauss, R.M., Lindgren, F.T., and Nichols, A.V. Changes in plasma lipoprotein distribution and formation of two unusual particles after heparin-induced lipolysis in hypertriglyceridemic subjects. Proc. Natl. Acad. Sci. *76:*5934–5938(1979).

Freeling, M. Maise *Adh1* as a monitor of environmental mutagens. Environ. Health Perspt. *27:*91–98 (1979).

Givens, J.R., Wiedemann, E., Andersen, R.N., and Kitabchi, A.E. Beta-endorphin and beta-lipotropin plasma levels in hirsute women:correlation with body weight. J. Clin. Endocrinol. Metab. *50:*975–976 (1980).

Glomset, J.A., Mitchell, C.D., King, W.C., Applegate, K.R., Forte, T.M., Norum, K.R., and Gjone, E. *In vitro* effects of lecithin: cholesterol acyltransferase on apolipoprotein distribution in familial lecithin: cholesterol acyltransferase deficiency. Ann. N.Y. Acad. Sci. *348:*224–241 (1980).

Goldring, D., Hernandez, A., Choi, S., Lee, J., Londe, S., Lindgren, F.T., and Burton, R.M. Blood pressure in a high school population: clinical profile of the juvenile hypertensive. J. Pediatrics *95:*298–304 (1979).

Gondos, B., Lai, C.E., and King, E.B. Distinction between atypical mesothelial cells by scanning electron microscopy. Acta Cytologica *23:*321–326 (1979).

Gong, Elaine L. and Nichols, Alex V. Interaction of human plasma high density lipoprotein HDL_2 with synthetic saturated phosphatidylcholines. Lipids *15:*86–90 (1980).

Goth-Goldstein, R. and Burki, H.J. Ethylnitrosurea-induced mutagenesis in asynchronous and synchronous Chinese hamster ovary cells. Mutation Research *69:*127–137 (1980).

Hayes, Thomas L., Pawley, James B., Fisher, Gerald L., and Goldman, M. A model for the exposure of individual lung cells to the foreign elements contained in fly ash. Environmental Research *22:*499–509 (1980).

Hayward, S.B. and Glaeser, R.M. High resolution cold stage for the JEOL 100B and 100C electron microscopes. Ultramicroscopy *5:*3–8 (1980).

Hilger, F. and Mortimer, R.K. Genetic mapping of arg1 and arg8 in *Saccharomyces cerevisiae* by trisomic analysis combined with interallelic complementation. J. Bacteriology *141:*270–274 (1980).

Hunter, J.A., Blanche, P.J., Forte, T.M., and Nichols, A.V. Interaction of HDL subclasses with phospholipid. Ann. N.Y. Acad. Sci. *348:*429–430 (1980).

Jap, Bing K. and Glaeser, Robert M. The scattering of high-energy electrons. II. Quantitative validity domains of the single-scattering approximations for organic crystals. Acta Cryst. *A36:*57–67 (1980).

Johnson, M.L., Romero, J.L., Subramanian, T.S., and Brady, F.P. Thick target corrections for charged particle spectra. Nucl. Instr. and Meth. *169:*179–184 (1980).

Kennedy, W.L., Alpen, E.L., Garcia, J.F. Regulation of red blood cell production by erythropoietin: normal mouse marrow *in vitro*. Exper. Hematol. *8:*1114–1122 (1980).

Kingsman, A.J., Clark, L., Mortimer, R.K., and Carbon, J. Replication in *Saccharomyces cerevisiae* of plasmid pBR313 carrying DNA from the yeast *trp 1* region. Gene 7:141–152 (1979).

Krauss, R.M., Lindgren, F.T., and Ray, R.M. Interrelationships among subgroups of serim lipoproteins in normal human subjects. Clinica Chimica Acta *104:*275–290 (1980).

Lawrence, J.H. Early experiences in nuclear medicine. J. Nucl. Med. *20:*561–564 (1979).

——— **and Linfoot, J.A.** Treatment of acromegaly, Cushing's disease and Nelson's syndrome. Western. J. Med. *133:*197–202 (1980).

Lücke-Hühle, C., Blakely, E.A., Chang, P.Y., and Tobias, C.A. Drastic G2 arrest in mammalian cells after irradiation with heavy-ion beams. Radiation Research *79:*97–112 (1979).

———, **Blakely, E.A., Ngo, F.Q.H., Chang, P.Y. and Tobias, C.A.** Survival and kinetic response of V79-spheroids after exposure to heavy-ion beams. Int. J. Radiat. Biol. *37:*483–492 (1980).

Magee, J.L. and Chatterjee, A. A spur unfolding model for the radiolysis of water. Radiat. Phys. Chem. *15:*125–132 (1980).

Malkin, R. and Bearden, A. Iron-sulfur centers of the chloroplast membrane. Coordination Chemistry Reviews *28:*1–22 (1979).

Mel, H.C. Academic tradition in clinical research—a commentary. Blood Cells *6:*101–102 (1980).

———. Ektacytometry and the measurement of cell physical properties. Blood Cells *6:*339–344 (1980).

Mitchell, C.D., King, W.C., Applegate, K.R., Forte, T.M., Glomset, J.A., Norum, K.R., and Gjone, E. Characterization of apolipoprotein E-rich high density lipoproteins in familial lecithin: cholesterol acyltransferase deficiency. J. Lipid Res. *21:*625–634 (1980).

Mohandas, N., Clark, M.R., Wyatt, J.L., Garcia, J.F., Eisenberg, P.D., and Shohet, S.B. Erythropoietic stress, macrocytosis, and hemoglobin switching in HbAA sheep. Blood *55:*757–761 (1980).

Ngo, F.Q.H., Utsumi, H., Han, A., and Elkind, M.M. Sublethal damage repair: is it independent of radiation quality? Intl. J. Radiat. Biol. *36:*521–530 (1979).

Nichols, A.V., Gong, E.L., Blanche, P.J., and Forte, T.M. Interaction of human plasma high-density lipoprotein HDL_{2b} with discoidal complexes of dimyristoylphosphatidylcholine and apolipoprotein A-I. Biochim. Biophys. Acta. *617:*480–488 (1980).

Peak, M.J., Webb, R.B., and Ainsworth, E.J. Survival of Escherichia coli strains differing in DNA repair capability after irradiation with fission spectrum neutrons. Radiat. Res. *81:*145–149 (1980).

Quivey, J.M., Castro, J.R., Chen, G.T.Y., Moss, A., and Marks, W.M. Computerized tomography in the quantitive assessment of tumor response. British J. Cancer *41(Suppl. IV):*31–34 (1980).

Roheim, P.S., Carey, M., Forte, T., Vega, G.L. Apolipoproteins in human cerebrospinal fluid. Proc. Natl. Acad. Sci. *76:*4646–4649 (1979).

Romero, J.L., Brady, F.P., Needham, G.A., Castaneda, C.M., Subramanian, T.S., Ullmann, J.L., and Zanelli, C.I. Electron capture by protons in a neutron beam facility. Nucl. Instr. and Meth. *171:*609–612 (1980).

Roots, R., Yang, T.C., Craise, L., Blakely, E.A., and Tobias, C.A. Rejoining capacity of DNA breaks induced by accelerated carbon and neon ions in the spread Bragg peak. Int. J. Radiat. Biol. *38:*203–210 (1980).

Sachs, M.M., Freeling, M., and Okimoto, R. The maize anaerobic proteins. Cell *20:*761–767 (1980).

Schaefer, E.J., Foster, D.M., Jenkins, L.L., Lindgren, F.T., Berman, M., and Brewer, H.B., Jr. The composition and metabolism of high density lipoprotein subfractions. Lipids *14:*511–522 (1979).

Schimmerling, W., Kast, J.W., Ortendahl, D., Madey, R., Cecil, R.A., Anderson, B.D., and Baldwin, A.R. Measurement of the inclusive neutron production by relativistic neon ions on uranium. Phys. Rev. Letters *43:*1985–1987 (1979).

———, **Todd, P., and Wood, J.C.S.** Analysis of cellular DNA distributions. II. Analytic solution for G2/G1 peak channel ratios. Cell Biophysics *1:*355–367 (1979).

Schooley, John C. Erythropoietin complexed with the F $(ab')_2$ fragment of anti-erythropoietin retains its biological activity. Exper. Hemat. *8:*830–836 (1980).

Scott, R.B. and Ainsworth, E.J. State-vector model for life shortening in mice after brief exposures to low dose of ionizing radiation. Mathematical Biosciences *49:*185–205 (1980).

Shu, H.P., Talcott, R., Rice, W., and Wei, E. Lipid peroxidation and paraquat toxicity. Biochemical Pharmacology *28:*327–331 (1979).

Smith, Helene S., Hackett, Adeline J., Riggs, John L., Mosesson, M.W., Walton, J.R., and Stampfer, Martha R. Properties of epithelial cells cultured from human carcinomas and nonmalignant tissues. J. Supramolecular Structure *11:*147–166 (1979).

———, **Riggs, J.L., and Mosesson, M.W.** Production of fibronectin by human epithelial cells in culture. Cancer Research *39:*4138–4144 (1979).

Springer, E. Louise. Comparative study of the cytoplasmic organelles of epithelial cell lines derived from human carcinomas and nonmalignant tissues. Cancer Research *40:*803–817 (1980).

Stampfer, M., Hallowes, R., and Hackett, A.J. Growth of normal human mammary epithelial cells in culture. In Vitro *16:*415–425 (1980).

Subramanian, T.S., Romero, J.L., and Brady, F.P. An experimental facility for measurement of charged particle continua arising from neutron-induced reactions. Nucl. Instr. and Meth. *174:*475–489 (1980).

Talcott, R., Shu, H., and Wei, E. Dissociation of microsomal oxygen reduction and lipid peroxidation

with the electron acceptors paraquat, diquat, and menadione. Biochemical Pharmacology *28*:665–671 (1979).

Tenforde, T.S. Thermal aspects of electromagnetic field interactions with bound calcium ions at the nerve cell surface. J. Theor. Biol. *83*:517–521 (1980).

———, **Curtis, S.B., Crabtree, K.E., Tenforde, S.D., Schilling, W.A., Howard, J., and Lyman, J.T.** *In Vivo* cell survival and volume response characteristics of rat rhabdomyosarcoma tumors irradiated in the extended peak region of carbon- and neon-ion beams. Radiat. Res. *83*:42–56 (1980).

Tinoco, I., Bustamante, C., Maestre, M.F. The optical activity of nucleic acids and their aggregates. Ann. Rev. Biophys. Bioeng. *9*:107–141 (1980).

Vaughan, W.J., Adamson, G.L., Lindgren, F.T., and Schooley, J.C. Serum lipid and lipoprotein concentrations following exposure to oxone. J. Environ. Path. and Toxicology *5*(1):87 (1980).

Wefel, J.P., Kidd, J.M., Schimmerling, W., and Vosburg, K.G. Differential fragmentation cross sections for 7.3 GeV nitrogen ions incident on protons. Phys. Rev. *C.19*:1380–1392 (1979).

Yang, T.C.H., Tobias, C.A., Blakely, E.A., Craise, L.M. Madfes, I.S., Perez, C., and Howard, J. Enhancement effects of high-energy neon particles on the viral transformation of mouse C3H1OT 1/2 cells *in vitro*. Radiat. Res. *81*:208–223 (1980).

Yano, Y., Budinger, T.F., Chiang, G., O'Brien, H.A., and Grant, P.M. Evaluation and application of alumina-based Rb-82 generators charged with high levels of Sr-82/85. J. Nuclear Medicine *20*:961–966 (1979).

Yao, J.K., Herbert, P.N., Frederickson, D.S., Ellefson, R.D., Heinen, R.J., Forte, T., and Dyck, P.J. Biochemical studies in a patient with a tangier syndrome. J. Neuropath. Exptl. Neurology *37*:138–154 (1978).

CONTRIBUTIONS TO BOOKS AND PROCEEDINGS

Alonso, J.R., Chatterjee, A., Tobias, C.A. High purity radioactive beams at the Bevalac. IEEE Trans. Nucl. Sci. *26*:3003 (1979).

Anderson, D.W., Nichols, A.V., Brewer, B. Ultracentrifugal characterization of the human plasma high density lipoprotein distribution. *In* Report of the HDL methodology workshop, San Francisco, May 1979, K. Lippel, ed. NIH Publ. 79–1661 (1979).

Bastacky, J., Sprague, L.M., Hayes, T.L. Positional microstructure of the human lung: microdissection and correlative microscopy techniques (LM, SEM, TEM). *In* 38th ann. proc. electron microscopy soc. Amer, San Francisco, pp. 774–775. G.W. Bailey, ed. (1980).

Braun, U., Braun, G., Sargent, T., III. Measurement of in vivo decarboxylation of dopa and tyrosine. *In* Catecholamines: basic and clinical frontiers, vol. 2, pp. 880–882. E. Usdin, I.J. Kopin, J. Barchas, eds. Pergamon Press (1979).

Budinger, T.F. Computed tomography: three-dimensional imaging with photons and nuclear magnetic resonance. *In* Biomedical pattern recognition and imaging processing: report of the dahlem workshop on biomedical pattern recognition and image processing, Berlin, May 14–18, 1979, pp. 179–212. K.S. Fu and T. Pavlidis, eds. Verlag Chemie, Weinheim (1979).

———, **Gullberg, G.T., Huesman, R.H.** Emission computed tomography. *In* Topics in applied physics, vol. 32: Image reconstruction from projections: implementation and applications, pp. 147–246. G.T. Herman, Ed., Springer-Verlag, Berlin, Heidelberg, New York (1979).

Burki, H.J. Mutations induced in synchronous CHO cells by ultraviolet light. *In* Proceedings VIth international congress of radiation research, Tokyo, Japan, May 13–17, 1979. S. Okada, M. Iamura, T. Terasima, H. Yamaguchi, Eds. Japanese Assoc. for Radiation Research., Tokyo (1979).

———, **Cleaver, J.E., Moustacchi, E.** Tritiated uracil, tritiated thymidine, and bromodeoxyuridine-induced mutations in eucaryotic cells. International Symposium on the Biological Implications of Radionuclides Released from Nuclear Industries. Int. Atomic Energy Agency, Vienna, Austria (1979).

Castro, J.R., Tobias, C.A., Quivey, J.M., Chen, G.T.Y., Lyman, J.T., Phillips, T.L., Alpen, E.L., Singh, R.P. Results of tumor treatments with alpha particles and

heavy ions at Lawrence Berkeley Laboratory. High LET radiations in clinical radiotherapy, supplement to the European Journal of Cancer, pp. 67–74. Pergamon Press, Oxford and New York (1979).

Chase, H.D., Ainsworth, E.J., Mobraaten, L.E., and Silvers, W.K. Laboratory animal management: Genetics. ILAR News, Vol. 23 (A1–A15) (1979).

Chen, G.T.Y. Treatment planning for charged particle radiotherapy. Treatment Planning (Amer. Assoc. Med. Dosimetrists) *3*:2–5 (1980).

———, **Pitluck, S.** Utilization of graphics in heavy ion radiotherapy treatment planning. IEEE Proc. Workshop on Picture Data Description and Management; pp. 172–175 (1980).

Curtis, S.B. The biological properties of high-energy heavy charged particles. *In* Proceedings of the Sixth International Congress of Radiation Research, Tokyo, Japan, May 13–19, 1979, pp. 780–787. S. Okada, M. Imamura, T. Terasima, H. Yamaguchi, eds.; Japanese Assoc. for Radiation Research, Tokyo (1979).

Curtis, S.B. Calculations of radiation quality of heavy-ion beams. *In* High LET radiations in clinical radiotherapy, supplement to European J. Cancer, pp. 218–219, G.W. Barendsen, J.J. Broerse, K. Breur, eds. Pergamon Press, Oxford and New York (1979).

———, **Schimmerling, W.** The BEVALAC: a source of high energy and high LET radiation for radiobiology, radiography, radiotherapy, and nuclear medicine. *In* Proceedings of the sixth international congress of radiation research; Tokyo, Japan, May 13–19, 1979, pp. 1004–1008. S. Okada, M. Imamura, T. Terasima, H. Yamaguchi, eds.; Japanese Assoc. for Radiation Research, Tokyo (1979).

———, **Tenforde, T.S., Schilling, W.A.** Review of the radiobiological response of a rhabdomyosarcoma irradiated with heavy ion beams: *in vivo* and *in vitro* results. *In* High LET radiations in clinical radiotherapy, supplement to European J. Cancer, p. 219 G.W. Barendsen, J.J. Broerse, K. Breur, eds. Pergamon Press, Oxford and New York (1979).

Davis, A., Devoret, R., Green, M., Hofnung, M., Kawachi, T., Matsushima, T., McCann, J. (Rapporteur), Mohn, G.R., Norpoth, K., Radman, M., Rosendranz, H.S., and Venitt, S. Mutagenesis assays with bacteria, *In* Long-term and short-term screening assays for carcinogens: a critical appraisal. IARC monographs on the evaluation of the carcinogenic risk of chemicals to humans. Supplement 2. IARC, Lyons, France pp. 85–106 (1980).

Derenzo, S.E. Precision measurement of annihilation point spread distributions for medically important positron emitters. *In* Proceedings of the fifth international conference on positron annihilation, Lake Yamanaka, Japan, April 8–11 (1979), pp. 819–823.

———, **Budinger, T.F., Cahoon, J.L., Greenberg, W.L., Huesman, R.H., Vuletich, T.** The Donner Laboratory 280-crystal high resolution positron coincidence tomograph. *In* Proceedings of the fifth international conference on positron annihilation; Lake Yamanaka, Japan, April 8–11, 1979, pp. 409–412.

Downing, Kenneth H. Electron diffraction from DNA crystals. Thirty-eighth ann. proc. Electron Microscopy Soc. Amer, San Francisco, Calif. G.W. Bailey, ed., pp. 536–537 (1980).

———, **Ho, Ming-Hsiu, Glaeser, Robert M.** A charge coupled device readout system for electron microscopy. *In* Thirty-eighth ann. proc. Electron Microscopy Soc. Amer. San Francisco, Calif. G.W. Bailey, ed., pp. 234–235 (1980).

Echlin, Patrick, Hayes, Thomas L., Pawley, James B. Freeze-fracture SEM of differentiating phloem parenchyma of Lemna Minor L. (Duckweed). Beitrage zur Electronemikroskopischen Direktabbildung von Oberflachen, Band 12; Verlag R.A. Remy, Munster, Germany (1979).

———, **Lai, C.E., Hayes, T.L., Hook, G.R.** Elemental analysis of frozen-hydrated differentiation phloem parenchyma in roots of *Lemna Minor L. In* SEM/1980/II; SEM, Inc. O. Johari, ed., pp. 383–394. Chicago (1980).

Fabrikant, J.I. Spermatogonial stem cell renewal following irradiation. *In* Proceedings of the sixth international congress of radiation research, Tokyo, Japan, May 13–19, 1979. S. Okada, M. Imamura, T. Terasima, H. Yamaguchi, eds. Japanese Assoc. for Radiation Research, Tokyo (1979).

———, **Tobias, C.A., Capp, M.P., Benton, E.V., Holley, W.R.** Heavy-ion imaging applied to medicine. *In* SPIE *233* Application of Optical Instrumentation in Medicine VIII (1980), pp. 255–263. Society of Photo-Optical Instrumentation Engineers, Bellingham, Wash. (1980).

Finch, G.L., Fisher, G.L., Hayes, T.L., Golde, D.W. Morphological studies of cultured human pulmonary macrophages. *In* Proceedings national scanning

electron microscopy symposium, SEM/1980/III, SEM, Inc. O. Johari, ed., pp. 315–326, Chicago (1980).

Fogel, S., Mortimer, R., Lusnak, K., Tavares, F. Meiotic gene conversion: a signal of the basic recombination event in yeast. Cold Spring Harbor Symposium on Quantitative Biology *43:*1325–1341 (1979).

Freeling, M., Woodman, J.C. Regulatory variant and mutant alleles in higher organisms and their possible origin via chromosomal breaks. *In* The plant seed: development, preservation, and germination, I. Rubenstein, et al., eds. Academic Press, New York (1979).

Grano, David A., Downing, Kenneth H. Modulation transfer functions of photographic emulsions. *In* Thirty-eighth ann. proc. Electron Microscopy Soc. Amer, San Francisco, Calif., G.W. Bailey ed., pp. 228–229 (1980).

Hayes, T.L. Biophysical aspects of scanning electron microscopy. *In* SEM/1980/I; SEM, Inc. O. Johari, ed. Chicago (1980).

———, **Lai, C., Bastacky, J.** Scanning electron microscopy and microanalysis of fly ash–lung cell interactions. *In* Pulmonary toxicology of respirable particles, 19th Annual Hanford Life Science Symposium, Richland, Wash. (1979).

———, **Lai, C.E., Fisher, G.L., Prentice, B.A.** Coordinated scanning electron microscopy and light microscopy for the evaluation of chemical element heterogeneity among individual fly ash particles. *In* Thirty-eighth ann. proc. Electron Microscopy Soc. Amer., San Francisco, Calif. G.W. Bailey ed., pp. 254–255 (1980).

Hayward, S.B. High resolution imaging of purple membrane at low temperature. *In* Thirty-eighth ann. proc. Electron Microscopy Soc. Amer. San Francisco, Calif. G.W. Bailey, ed., pp. 670–673 (1980).

Hermens, A.F., Curtis, S.B., Tenforde, T.S., Barendsen, G.W. Analysis of cell proliferation in a rat rhabdomyosarcoma irradiated with neon ions or with 300-kV x-rays. *In* High LET radiations in clinical radiotherapy. G.W. Barendsen, J.J. Broerse, K. Breur, eds., pp. 226–227. Pergamon Press, Oxford and New York (1979).

Holley, W.R., Henke, R.P., Gauger, G.E., Jones, B., Benton, E.V., Fabrikant, J.I., Tobias, C.A. Heavy particle computed tomography. *In* Proceedings, sixth computer radiology, IEEE Trans., pp. 64–70 (1979).

Hook, G.R., Lai, C.E., Bastacky, J., Hayes, T.L. Conductive coating studied on inflated lung in the frozen-hydrated and freeze-dried states. *In* Scanning electron microscopy/1980/IV; O. Johari, ed. Chicago, 1980.

Huesman, R.H., Cahoon, J.L. Data acquisition, reconstruction and display for the Donner 280-crystal positron tomograph. IEEE Trans. Nucl. Sci. *NS-27(1):*474–478 (1980).

Krauss, R.M., Lindgren, F.T., Wong, A., Anderson, B., Pan, S.S., Lewis, S.B. Measurement of HDL and other lipoproteins by quantitative electrophoresis. Report of the HDL Methodology Workshop San Francisco, Calif. March 5–7, 1979, pp. 114–124. K. Lippell, ed.; NIH 79–1661 (1979).

Lai, C.E., Hayes, T.L. Calibration of SEM frozen-hydrated analyses using standard salt solutions and peak to background measurements. Thirty-eighth ann. proc. Electron Microscopy Soc. Amer. San Francisco, Calif., 1980 G.W. Bailey, ed., pp. 800–801 (1980).

Lawrence, John H. History of pituitary therapy at the Donner Pavilion. *In* Proceedings of symposium on recent advances in the diagnosis and treatment of pituitary tumors, pp. 1–3. J.A. Linfoot, ed. Raven Press; New York (1979).

———, **Tobias, C.A., Chong, C., Lyman, J., Born, J.L., Linfoot, J.A.** The treatment of pituitary neoplasms with heavy particles. *In* Proceedings of first European workshop on treatment of pituitary tumors; pp. 266–272. Rottach Egern, Georg Thieme Publishers; Stuttgart (1978).

Li, F.C., Linfoot, J.A. Neurological examination in the diagnosis of pituitary adenomas. *In* Proceedings of symposium on recent advances in the diagnosis and treatment of pituitary tumors, pp. 119–129. J.A. Linfoot, Ed.; Raven Press, New York (1979).

Lindgren, F.T. The plasma lipoproteins: historical developments and nomenclature. Conference on lipoprotein structure. A.M. Scanu and F.R. Landsberger, eds. The New York Academy of Sciences *348:*1–15 (1980).

———, **Adamson, G.L., Krauss, R.M.** Automated quantitative lipoprotein microelectrophoresis. *In* Handbook of electrophoresis and chromatography. L.A. Lewis and J.J. Opplt, ed.; Vol. 1, Electrophoresis of lipoproteins pp. 229–247; Chemical Rubber Co., Cleveland, Ohio (1980).

———, **Shen, M.S., Krauss, R.M., Sargent, T.W.** Ultracentrifugation of HDL. *In* Report of the HDL meth-

odology workshop, San Francisco, Calif. March 5–7, 1979, K. Lippell, ed., pp. 45–52. NIH 79–1661 (1979).

Linfoot, J.A. Neuro-ophthalmological considerations in pituitary tumors. *In* Proceedings of symposium on recent advances in the diagnosis and treatment of pituitary tumors. J.A. Linfoot, ed., pp. 131–139. Raven Press, New York (1979).

———. Acromegaly. *In* Proceedings of symposium on recent advances in the diagnosis and treatment of pituitary tumors; J.A. Linfoot, ed., pp. 207–220. Raven Press, New York (1979).

———. Heavy ion therapy: alpha particle therapy of pituitary tumors. *In* Proceedings of symposium on recent advances in the diagnosis and treament of pituitary tumors; J.A. Linfoot, ed., pp. 245–267. Raven Press, New York (1979).

———. Acromegaly. *In* Current therapy 1980, Howard Conn, M.D., ed.; pp. 475–480. W.B. Saunders Co., Philadelphia (1980).

———. Alpha particle pituitary irradiation in the primary and post-surgical management of pituitary tumors. *In* Proceedings of the international symposium on pituitary microadenomas; Milan, Italy, October 12–14, 1978, pp. 515–529. Academic Press, Inc., London (1980).

———, **Nakagawa, J.S., Wiedemann, E., Lyman, J.T. Chong, C., Garcia, J., Lawrence, J.H.** Heavy particle therapy: pituitary tumors. Bull. Los Angeles Neurological Societies *42(3–4):*175–189 (1977).

Lloyd, R.D., Bruenger, F.W., Atherton, D.R., Jones, C.W., Weitl, F.L., Durbin, P.W., Raymond, K.N., Taylor, G.N., Stevens, W., Mays, C.W. Decorporation of Pu or Am in beagles by 3, 4, 3-LICAMS. Research Radiobiology, Annual Report Radiobiology Laboratory, University of Utah C00119-254, pp. 151–164 (1979).

Magee, J.L., Chatterjee, A. Chemical track effects in condensed systems and implications for biological damage. *In* Proceedings of the sixth international congress of radiation research, Tokyo, Japan, May 13–19, 1979, pp. 162–173. S. Okada, M. Imamura, T. Terasima, H. Yamaguchi, eds.; Japanese Assoc. for Radiation Research, Tokyo (1979).

Moccia, G., Miller, M.E., Garcia, J.F., Cronkite, E.P. The effect of plethora on erythropoietin levels. Proc. Soc. Exptl. Biol. Med. *163:*36–38 (1980).

Nichols, A.V., Blanche, P.J., Krauss, R.M., Gong, E.L. Gradient gel electrophoresis of HDL within the ultracentrifugal $d \leq 1.200$ fraction from human serum. *In* Report of the HDL methodology workshop San Francisco, May 5–7, 1979. K. Lippell, ed.; pp. 303–331. NIH 79-1661 (1979).

Peng, C.T., Horrocks, D.L., Alpen, E.L.(Eds) Liquid scintillation counting: Vol. I, Physical aspects; Vol. II, Sampling preparation and applications. Academic Press, New York (1980).

Raymond, K.N., Smith, W.L., Weitl, F.L., Durbin, P.W., Jones, E.S., Abu-Dari, K., Sofen, S.R., Cooper, S.R. Specific sequestering agents for the actinides. *In* Lanthanide and actinide chemistry and spectroscopy, N.M. Edelstein, ed., pp. 143–172. Proceedings of symposium, Washington D.C., Sept. 1979. ACS Symposium Series 131; Amer. Chem. Soc., Wash. D.C.

Sickles, E.A., Benton, E.V., Tobias, C.A., Woodruff, K.H. Mammography using Bevalac-accelerated heavy particles: a novel approach to dose reduction. In Reduced dose mammography; W.W. Logan and E.P. Muntz, eds., pp. 501–505. Masson Publ. Co., New York (1979).

Smith, H.S., Hackett, A.J., Riggs, J.L., Mosesson, M.W., Walton, J.R., Stampfer, M.R. Properties of epithelial cells cultured from human carcinomas and nonmalignant tissues. *In* Proceedings of the ICN-UCLA symposium on tumor cell surfaces and malignancy, pp. 93–112, R. Hynes, Ed.; Alan Less Inc., New York (1980).

Smith, J.M., Durbin, P.W., Jeung, N., VanWagenen, G., Jee, W.S.S. Measurement of some characteristics of trabecular bone of humerus, lumbar vertebrae, and calvarium, and of cortical bone of humerus of adult rhesus monkey (Macaca mulatta). Research in Radiobiology, Annual Report Radobiology Laboratory, University of Utah C00-119-254, pp. 33–54, (1979).

Sosinsky, G., Schekman, R., Glaeser, R. Enlarged crystalline patches on the plasma membrane of yeast protoplasts. *In* Thirty-eighth ann. proc. Electron Microscopy Soc. Am., San Francisco, Calif. pp. 686–687. G.W. Bailey, ed. (1980).

Tobias, C.A. Pituitary radiation: radiation physics and biology. *In* Proccedings of symposium on recent advances in the diagnosis and treatment of pituitary tumors; pp. 221–243. J.A. Linfoot, ed. Raven Press; New York (1979).

———, **Alpen, E.L., Blakely, E.A., Castro, J.R., Chatterjee, A., Chen, G.T.Y., Curtis, S.B., Howard, J., Lyman, J.T., Ngo, F.Q.H.** Radiobiological basis for heavy-ion therapy. *In* Prospects for treatment of radioresistant cancers, pp. 159–183. M. Abe, K. Sakamoto, T.L. Phillips, eds. Elsevier/North-Holland Biomedical Press, Amsterdam (1979).

———, **Blakely, E.A., Ngo, F.Q.H., Yang, T.C.H.** The repair-misrepair model of cell survival. *In* Radiation biology and cancer research, pp. 195–230. Proceedings, Thirty-second annual symposium on fundamental cancer research, Houston Texas, Feb. 26–Mar 1, 1979. A. Meyn and R. Withers, eds. Raven Press, New York (1980).

———, **Chatterjee, A., Malachowski, M.J., Blakely, E.A., Hayes, T.L.** Tracks in condensed systems. *In* Proceedings of the sixth international congress of radiation research, Tokyo, Japan, May 13–19, 1979, pp. 146–156. S. Okada, M. Imamura, T. Terasima, H. Yamaguchi, eds. Japan. Assoc. for Radiation Research, Tokyo (1979).

White, Margaret R. Nonmicrowave effects on health and environment. *In* Preliminary environmental assessment for the satellite power system (SPS); pp. 31–79. Revision 1, Department of Energy, DOE/ER-0036/2; (1980).

Wiedemann, E. Growth hormone and somatomedins. *In* Proceedings of symposium on recent advances in the diagnosis and treatment of pituitary tumors, pp. 93–110. J.A. Linfoot, ed. Raven Press, New York (1979).

———. Acromegaly: diagnosis and treatment. Present Concepts Internal Med. *13:*19–32 (1980).

Wilson, C.B., Linfoot, J.A., Sheline, G.E. The role of transsphenoidal microsurgery in the primary and secondary management of pituitary tumors. *In* Proceedings of symposium on recent advances in the diagnosis and treatment of pituitary tumors, pp. 419–428. J.A. Linfoot, ed. Raven Press, New York, 1979.

Yang, T.C.H., Tobias, C.A. Potential use of heavy-ion radiation in crop improvement. *In* Proceedings, international gamma field symposium, May 1979; Omiya, Japan. pp. 141–154, Gamma-Field Symposia No. 18 (1979).

LBL REPORTS ISSUED

Bauer, T., Glaeser, R.M., Yokoyama, H. Chemical induction of rubber biosynthesis in guayule—an electron microscopy study. LBL-9680 (October 1979) 14 p.

Burke, R.L., Alberts, B.M., Hosoda, J. Proteolytic removal of the carboxyl terminus of the T4 Gene 32 helix-destabilizing protein alters the T4 in vitro replication complex. LBL-11251 (July 1980) 48 p.

Castro, Joseph R. Progress report on heavy particle clinical radiotherapy trial at Lawrence Berkeley Laboratory July 1975–July 1979. LBL-9738 (1979) 13 p.

Chatterjee, A., Magee, J.L. Radiation chemistry of heavy particle tracks. II. The Fricke dosimeter system. LBL-10283 (March 1980) 37 p.

Curtis, S.B. The new particles and their application in medicine. LBL-9751 (Sept. 1979) 21 p.

Derenzo, S.E. Optimization of side shielding for circular positron emission tomographs. (Revision, LBL-9201, 1979.) LBL-9584 (October 1979) 17 p.

Fabrikant, Jacob I. The BEIR-III Report and the health effects of low-level radiation. LBL-10383 (January 1980) 30 p.

———. The BEIR-III Report and its implications for radiation protection and public health policy. LBL-10494 (March 1980) 24 p.

———. The BEIR-III controversy. Invited paper presented at the Plenary Session, Radiation Research Society, 28th Ann. Scientific Meeting, New Orleans, LA. June 1–5, 1980. LBL-11268 (June 1980) 24 p.

Feinberg, David Alan. Image processing of small protein crystals in electron microscopy. LBL-8413 (November 1978) 69 p.

Fisher, G.L., Chrisp, C.E., Hayes, T.L. Carbonaceous particles in coal fly ash. *In* Proc. Conference on Carbonaceous Particles in the Atmosphere. LBL-9037, pp. 229–232 (1979).

Goliaei, B. The kinetics of reversible-sequestration of leukocytes by the isolated perfused rat lung. (Ph.D. Thesis) LBL-11170 (August 1980) 145 p.

Gullberg, G.T. The attenuated radon transform—application to single-photon, emission computed tomography in the presence of a variable attenuating medium. LBL-10276 (March 1980) 73 p.

——— **and Budinger, T.F.** Single-photon emission computed tomography: compensation for constant attenuation. LBL-10713 (June 1980) 53 p.

Hosoda, J., Burke, R.L., Moise, H., Kubota, I., Tsugita, A. The control of T4 gene 32 helix-destabilizing protein activity in a DNA replication complex. LBL-10947 (May 1980) 10 p.

Kronenberg, S.S., Tenforde, T.S. Cell growth in a low-intensity, 60-Hz magnetic field. LBL-10056 (September 1979) 33 p.

Magee, J.L., Chatterjee, A. Radiation chemistry of heavy particle tracks. I. General considerations. LBL-10273 (March 1980) 42 p.

Mel, H.C., Reed, T.A. Red cell membrane biophysical response to very low concentrations of inorganic mercury. LBL-11671 (1980).

Ngo, F.Q.H., Blakely, E.A., Tobias, C.A. Sequential exposures of mammalian cells to low- and high-LET radiations. I. Lethal effects following x-ray and neon ion irradiation. LBL-7454 (April 1980) 41 p.

Pirruccello, M.C. and Tobias, C.A., Editors. Biological and medical research with accelerated heavy ions at the Bevalac, 1977–1980. LBL-11220 (November 1980) 419 p.

Rose, Keith A. Electron paramagnetic resonance saturation studies of $P700^+$ reaction-center chlorophyll in plant photosynthesis. (Ph.D. Thesis) LBL-9746 (November 1979) 105 p.

Schimmerling, Walter New sources of radiation. LBL-9961 (Sept. 1979) 41 p.

———. Heavy ion Dosimetry. LBL-9962 (March 1980) 30 p.

———, **Curtis, S.B., Gabor, G., Kaplan, S., Kast, J.W., Perez-Mendez, V., Sadoff, A., Subramanian, T.S., Tobias, C.A.** A particle identification spectrometer for heavy ion dosimetry. LBL-10551 (1980).

———, **Smith, A.R., Thomas, R.H.** Neutron flux density and secondary particle energy spectra at the 184-inch synchrocyclotron medical facility. Proceedings of the Vth International Conference of Medical Physics, Jerusalem, Israel, August 19–24, 1979 Vol. 3, Paper No. 57.4. LBL-6721-revised.

Subramanian, T.S., Romero, J.L., Brady, F.P., Watson, J.W., Fitzgerald, D.H., Garrett, R., Needham, G., Ullman, J.L., Zenelli, C. Charged particle continua from neutrons on carbon at 60 MeV. *In* Proceedings of the International Conference on Nuclear Physics, Berkeley, August 1980. LBL-11118, p. 887 (1980).

Tenforde, T.S. Dosimetry, instrumentation and exposure chambers for DC magnetic field studies. LBL-9554 (March 1979) 68 p.

———. Information on membranes derived from electrical surface charge measurements. LBL-10057 (May 1979) 8 p.

———, **Dols, C.G., Lake, A.A., Hay, R.D.** Design specifications for a large-volume, DC to 60 Hz, 0.1 Tesla (peak) magnet for primate experimentation. LBL-7485 (July 1979) 15 p.

Wiedemann, E. Adrenal and gonadal steroids. LBL-9355 (June 1979) 100 p.

Yee, J.P. Development and application of resistive pulse spectroscopy studies on the size, form and deformability of red blood cells. (Ph.D. Thesis) LBL-8840 (1979).

Appendix C: Biology and Medicine Division Staff

DIVISION HEAD

Edward L. Alpen
Thomas L. Hayes, Deputy

DIVISION ADMINISTRATION STAFF

Janice C. DeMoor
De A. Eggers
Laurie E. Graves
Wendell Hom
Allan W. Long
Georgia A. Newell
*Mark D. Sessler
Robert W. Springsteen
Baird Whaley
Herbert Wiener
Mary L. Worth

DIVISION SCIENTIFIC STAFF

E. John Ainsworth
Hal O. Anger

Mary E. Barker
John B. Bassel
S. Jacob Bastacky
Alan J. Bearden
Eugene V. Benton
Eleanor A. Blakely
James L. Born
George Brecher
Thomas F. Budinger
David J. Burke
H. John Burki
Gail E. Butterfield

Joseph R. Castro
Aloke Chatterjee
George T.Y. Chen
*William T. Chu
Gisela K. Clemons
Ruth A. Cohen
Gerald M. Connell
Stanley B. Curtis
Hunter O. Cutting

Jefferson W. Davis
Paul A. Davis
Stephen E. Derenzo
*Jonathan S. Dixon

Kenneth H. Downing
Patricia W. Durbin

Shirley N. Ebbe
Michael S. Esposito
Earl M. Ettienne

Jacob I. Fabrikant
Raymond S. Farinato
Trudy M. Forte
Michael Freeling

Cornelius T. Gaffey
Edward Ganz
Joseph F. Garcia
Walter George
Robert M. Glaeser
*Donald A. Glaser
Joseph D. Goldstein
Joan W. Goodman
Martin H. Graham
David A. Grano
*Grant T. Gullberg

Adeline J. Hackett
Stephen B. Hayward
Lester Hollander
William R. Holley
Junko Hosoda
Jerry Howard
Ronald H. Huesman

Kenneth L. Jackson
Bing K. Jap
Lin C. Jensen
*Russell L. Jones

Talwinder S. Kahlon
*John W. Kast
Esther H. Knudson
Robert L. Kong
Gerhard Kraft
Ronald M. Krauss
John C. Kroes

John H. Lawrence
Paul Licht
Frank T. Lindgren
John A. Linfoot

*Left Biology and Medicine Division prior to September 30, 1980.

Paul Lowinger
John T. Lyman

Marcos F. Maestre
John L. Magee
Chester A. Mathis
Joyce C. McCann
*William McGowan
Howard C. Mel
Robert K. Mortimer

Frank Q. Ngo
Alex V. Nichols

Jerry M. Owens

*Suzanne S.T. Pan
Theodore L. Phillips

Julia B. Quint
Jeanne M. Quivey

Michael S. Raybourn
Adrian Rodriguez
Ruth J. Roots
*Donald J. Rosenthal

Ahren J. Sadoff
Thornton W. Sargent, III
William M. Saunders
Walter Schimmerling
John C. Schooley
Lon G. Sherman
Helen P. Shu
Alexander T. Shulgin
Jerome R. Singer
Helene S. Smith
Lisa Snow
Charles A. Sondhaus
Harry G. Sperling
Martha R. Stampfer
Henry H. Stauffer
Harrison A. Stubbs
T.S. Subramanian
*Pauline Sun

Tom S. Tenforde
Gregory A. Threatte
Cornelius A. Tobias
Sylvanus A. Tyler

Robert J. Webber
Margaret R. White
*Eckehart Wiedemann
*Tokuko Wiedemann
*Priscilla D. Wong
Kay H. Woodruff
Larry D. Woods

Tracy C. Yang
Vivian V. Yang
Yukio Yano
James P. Yee
Chi-Kwan Yen

DIVISION SUPPORT STAFF

Frederick E. Abrams
Gerald L. Adamson
*Kuldip K. Ahluwalia
Steve P. Akeson
Hilda M. Alexander
Barbara M. Alford
Cathryne C. Allan
Arlette S. Atwater

*Keith R. Barber
Jacqueline J. Barnes
David O. Been
Kathleen A. Bjornstad
Patricia J. Blanche
Carol S. Bohlen
S. Kay Bristol
Philip Brodzinsky
Gerald L. Brooks

John L. Cahoon
Dorothy A. Carpenter
Betsy C. Carr
Emanuela N. Catena
Polly Y. Chang
Larry J. Chevez
Huey-Ling C. Chu
Colleen Cogorno
Paul J. Cogorno
Laurie M. Craise
Freddie L. Crenshaw, Jr.

Randy J. DeGuzman
Stephen J. Dentone
*Clardell L. Deuberry
James D. Dixon
Martha L. Dixon
*Virginia K. Docherty
Greta S. Duke
Dennis P. Duncan
Frank J. Durante

Diana J. Eibergen
*Peggy A. Eisenbach

Diana E. Fajardo
Michael B. Fizer
Brian L. Fletcher
*Marilyn J. Flynn

*Patricia A. Fobair
Carol A. Fong
Myrtle L. Foster
Roscoe Frazier
*Raymond G. Fredericks
*Helen M. Friend
*Thomas Fuerst
Charlie M. Fuller

Susan Garay
Patricia A. Garbutt
Christine Giotas
Queen E. Gipson
*Catherine R. Gisser
*Sally L. Glaser
Laura A. Glines
Bahram Goliaei
Elaine L. Gong
Sara P. Goolsby
Joan M. Graham
Mary R. Graham
*Paul J. Graham
*William L. Greenberg

Kathleen B. Hall
*Kathleen M. Harris
Linda D. Harrison
Helen F. Hart
Gloria J. Hathaway
Virginia C. Havens
Lilian E. Hawkins
Linda G. Hayashi
Lynn R. Hlatky
Minghsiu Ho
Gregory R. Hook
Laura J. Horn
Mildred K. Hughes
James A. Hunter

Jules S. Jaffe
*Barbara W. Jansen
Nylan M. Jeung
*Nancy Jo
Daniel M. Judd

John M. Kaldor
*Heroka Kasai
*Jonathan A. Kerner
*Barbara R. Komatsu
Natalia Kusubov

*Clifford E. Lai
*Lennetta G. Lai
Praveena K. Lal
*Joan Lawson
*Deborah A. Leach
Lynette L. Levy
Leora Lommel
Carole A. Lopez
*Judith A. Lowrie
Joan E. Luna
*Josephine A. Lundberg
Linda J. Lutgens

Bennett D. McAllister
*Beverly G. McCalla
*Mara A. McDonald
Tommy J. McKey
Velma B. McNeal
Ian S. Madfes
Lynn J. Mahlmann
*Tommie O. Mayfield
*Tamara B. Mihailovski
*Virginia Modica
Herbert W. Moise, III
Jerome A. Moore
Carol J. Mortensen
Brian R. Moyer
Ilene J. Mulry

Jeanette S. Nakagawa
Robert W. Nordhausen

Virginia I. Obie

Annie C. Pang
Shannon S. Parr
Charles C. Pattie
Theresa C. Peters
Elizabeth A. Phalen
Mary C. Pirruccello
Anne K. Poley
Patricia P. Powers-Risius
Bonnie J. Presson
John C. Prioleau

*Thomas A. Reed
Todd Richards
*Joanne Rogers
*Bohdan Roman

Thea B. Scott-Garner
Susan W. Shattuck
Andy Shih
Sarah G. Shinpock
*Theo H. Shock
Carla J. Simmons
Ester F. Solis
Gina E. Sosinsky
Dorothy S. Sprague
Lore S. Stein
*Nancy J. Steinhaus
*Jeffrey A. Stephenson

Linda L. Stimson
*Leslie Stopher
Daniel Straus
Stephen S. Sylvester

Tome Tanisawa
Susan D. Tenforde
*Vicki J. Truex
*Doris S. Tse
Julia A. Twitchell

Janet Uriu

*Nagammal Venkatesh

*Grace V. Walpole
Davie D. Wei
*Robert D. Wills
*Rod A. Wing
Wennie H. Wu

*Ann S. Yabusaki
Michael J. Yezzi
*Kenneth Yoskioka
*George Young

COMMITTEES

Division Advisory Committee

Edward L. Alpen
Eleanor A. Blakely
James L. Born
Thomas F. Budinger
H. John Burki
Joseph F. Garcia
Thomas L. Hayes
Alex V. Nichols
Cornelius A. Tobias
†Baird Whaley
†Laurie E. Graves

Division Staff Committee

H. John Burki
Stanley B. Curtis, Chair
Shirley N. Ebbe
Trudy M. Forte
John T. Lyman

Equipment Committee

Joseph F. Garcia, Chair
Shirley N. Ebbe
Aloke Chatterjee
Cornelius T. Gaffey
Thornton W. Sargent, III

Salary Committee

Edward L. Alpen
James L. Born
H. John Burki
Thomas F. Budinger
Joseph F. Garcia
Thomas L. Hayes
Cornelius A. Tobias
†Baird Whaley

Donner Library Committee

Robert M. Glaeser, Chair
Edward L. Bennett
Thomas F. Budinger
Gerald M. Connell
Thomas L. Hayes
Frank T. Lindgren
†Dorothy E. Denney
†Roy J. Nielsen

Human Use Committee

James L. Born, Chair
Thomas F. Budinger
Shirley N. Ebbe
William E. Siri
Henry H. Stauffer
†Janice C. DeMoor
†Baird Whaley

Radioactive Drug Research Committee

James L. Born, Chair
Edward L. Alpen
Aloke Chatterjee
Jacob I. Fabrikant
Henry H. Stauffer
Joseph D. Goldstein (Consultant)
†Janice C. DeMoor

Animal Welfare Committee

Herman Bonasch
Gerald M. Connell, Chair
Joseph F. Garcia
Joan W. Goodman
John C. Schooley

---

†Ex-officio, nonvoting member.